

## University of Southampton Research Repository ePrints Soton

Copyright © and Moral Rights for this thesis are retained by the author and/or other copyright owners. A copy can be downloaded for personal non-commercial research or study, without prior permission or charge. This thesis cannot be reproduced or quoted extensively from without first obtaining permission in writing from the copyright holder/s. The content must not be changed in any way or sold commercially in any format or medium without the formal permission of the copyright holders.

When referring to this work, full bibliographic details including the author, title, awarding institution and date of the thesis must be given e.g.

AUTHOR (year of submission) "Full thesis title", University of Southampton, name of the University School or Department, PhD Thesis, pagination

University of Southampton  
School of Engineering Sciences

Computational Engineering Design Group

**Finite element modelling of fatigue crack  
growth in multi-layered architectures**

by

**Allan Burke Veliz**

Thesis for the degree of Doctor of Philosophy

September 2009

## Supervisors:

**Dr. Stavros Syngellakis**

Computational Engineering Design Group

School of Engineering Sciences

**Prof. Philippa Reed**

Materials Research Group

School of Engineering Sciences

University of Southampton

Abstract

School of Engineering Sciences

Computational Engineering and Design Group

Doctor of Philosophy

by Allan Burke-Veliz

Crack growth analyses in multi-layered architectures used in the automotive industry for plain bearings, displaying elastic and plastic mismatches, were developed through automated meshing processes based on the Finite Element Method in the commercial code ANSYS. Two-dimensional FE analyses studied the effect of shielding and anti-shielding on crack growth in flat strip specimens subjected to three-point bending tests experiencing severe yielding and path deflections. This study was based on Crack Tip Opening Displacement estimates, the maximum tangential strain criterion and automatic step by step extensions to account for crack growth. The analysis of forecasted paths for deflected and bifurcated cracks showed the tendency of the crack to grow parallel to the layers orientation within the compliant interlayer, as observed experimentally, and following a path which maximised the crack driving force. The interaction of two-dimensional width-through cracks in co-linear, parallel-dominant and oblique arrangements was studied to compare their behaviour to independent growing cracks. The development of three-dimensional models was aimed to study the crack front evolution when more compliant or stiffer layers were placed ahead of the crack in flat strip specimens subjected to three-point bending tests experiencing severe yielding. The crack front growth was estimated according to the local values of the Crack Tip Opening Displacement and a fitted crack growth law, which accounted for the short fatigue crack behaviour observed experimentally. The comparison of Crack Tip Opening Displacements obtained with two-dimensional and three-dimensional models showed that the estimates obtained with the latter were affected to a lesser extent by shielding and anti-shielding. The estimation of cycles to propagate a crack to the interlayer, in addition to the initiation life obtained in previous experimental work at the University of Southampton, estimated that less than 40% of the total life was required for such a process and demonstrating the damage tolerance of the layered architecture. A detailed stress and strain analysis of the service conditions, based on the Elasto-Hydrodynamic Lubrication pressure, and manufacturing processes, mainly related to the forming of a concave shell, was developed for plain bearings as the initial step of a damage tolerance analysis.

# Declaration of Authorship

I, Allan Burke-Veliz, declare that the thesis entitled *Finite element modelling of fatigue crack growth in multi-layered architectures* and the work presented in it are my own. I confirm that:

- this work was done wholly or mainly while in candidature for a research degree at this University;
- where any part of this thesis has previously been submitted for a degree or any other qualification at this University or any other institution, this has been clearly stated;
- where I have consulted the published work of others, this is always clearly attributed where I have quoted from the work of others, the source is always given. With the exception of such quotations, this thesis is entirely my own work;
- I have acknowledged all main sources of help;
- where the thesis is based on work done by myself jointly with others, I have made clear exactly what was done by others and what I have contributed myself;
- parts of this work have been published in research journals as indicated in the list of publications provided with this manuscript.

Signed:

Date:

# List of publications

## Journal Papers:

"Fatigue Crack Shielding and Deflection in Plain Bearings under Large Scale Yielding". Engineering Failure Analysis. doi:10.1016/j.engfailanal.2009.03.032.

"A numerical study of crack shielding and deflection under extensive plasticity". Engineering Fracture Mechanics. doi:10.1016/j.engfracmech.2009.02.003.

"Plain bearing stresses due to forming and oil film pressure". Journal of Physics: Conference Series. doi:10.1088/1742-6596/181/1/012010.

## Conference Papers:

"Three-Dimensional Crack Growth in Multi-Layered Architectures for Automotive Plain Bearings". 12th International conference on Fracture. (NO ISBN YET) Ottawa, Canada, July 2009.

"Effects of Tangential Strains and Shielding in Large Scale Yielding in Multi-Layered Architectures for Bearings". 17th European Conference on Fracture. (ISBN 978-80-214-3692-3) Brno, Czech Republic, September 2008.

"Elasto-plastic finite element studies of fatigue crack shielding in multi-layered systems". 8th. World Congress on Computational Mechanics (WCCM8). (ISBN: 978-84-96736-55-9) Venice, Italy, July 2008.

# Index

List of Acronyms .....	x
List of Symbols.....	xii
Acknowledgments.....	xviii
List of Figures.....	xix
List of Tables.....	xxvii
1. Chapter One: Introduction .....	1
1.1. Background.....	1
1.2. Aim and Objectives.....	3
1.3. Thesis structure .....	6
1.4. Literature Review .....	7
1.4.1. Fracture mechanics .....	7
1.4.1.1. Linear Elastic Fracture Mechanics (LEFM) .....	7
1.4.1.2. Elastic Plastic Fracture Mechanics (EPFM).....	11
1.4.1.2.1. J integral.....	11
1.4.1.2.2. Crack Tip Opening Displacement.....	13
1.4.2. Damage tolerance approach.....	14
1.4.2.1. Growth of long cracks .....	16
1.4.2.2. Growth of short cracks .....	17
1.4.3. FE modelling of fatigue crack growth.....	19

1.4.4.	Plain journal bearings .....	20
1.4.4.1.	Architecture and manufacture of plain bearings.....	20
1.4.4.2.	Bearing Materials.....	22
1.4.4.3.	Damage in plain bearings .....	23
1.4.5.	Previous work at the University of Southampton .....	23
1.5.	ANSYS FEM software .....	31
1.6.	Summary.....	32
2.	Chapter Two: Shielding effects on straight cracks.....	34
2.1.	Introduction .....	34
2.2.	Background.....	34
2.3.	Model and methods.....	37
2.4.	Results.....	41
2.5.	Discussion .....	46
2.6.	Summary.....	48
3.	Chapter Three: Deflected and bifurcated cracks .....	49
3.1.	Introduction .....	49
3.2.	Background.....	49
3.2.1.	Crack deflection criteria.....	50
3.2.2.	Bifurcated cracks in multi-layered architectures.....	52
3.2.3.	Crack growth analysis using FE .....	54
3.3.	Assessment of crack deflection criteria .....	56

3.3.1. Results.....	57
3.3.2. Discussion .....	59
3.4. Deflected cracks in multi-layer architectures .....	59
3.4.1. Results.....	60
3.4.2. Discussion .....	64
3.5. Early bifurcation state.....	66
3.5.1. Results.....	67
3.5.2. Discussion .....	69
3.6. Bifurcated Branch Path.....	70
3.6.1. Results for bifurcated branch path .....	70
3.6.2. Discussion .....	73
3.7. Summary.....	74
4. Chapter Four: Crack interaction and coalescence.....	76
4.1. Introduction .....	76
4.2. Background.....	76
4.3. Model and methods.....	79
4.4. Results.....	81
4.4.1. Co-linear cracks .....	82
4.4.2. Parallel-dominant arrangements .....	83
4.4.3. Oblique arrangements.....	86
4.5. Discussion .....	87

4.6.	Summary.....	90
5.	Chapter Five: 3D crack growth modelling and characterisation.....	92
5.1.	Introduction .....	92
5.2.	Background.....	92
5.3.	Methodology for FE model creation.....	96
5.3.1.	Crack -elements generation.....	96
5.3.2.	Crack driving force post-processing.....	100
5.3.3.	Crack front advance and remeshing.....	102
5.4.	Crack front meshes comparison .....	103
5.4.1.	Convergence studies of CTOD estimates .....	105
5.4.2.	Spider-web crack tip model and exact solution .....	107
5.5.	Crack growth law .....	108
5.5.1.	Experimental crack growth data .....	112
5.5.2.	Linking experimental and numerical analyses.....	113
5.5.3.	Results.....	116
5.5.4.	Discussion .....	120
5.6.	Elasto-plastic analyses for the evaluation of shielding.....	123
5.6.1.	Results and discussion.....	123
5.6.1.1.	Crack driving force evolution and shielding.....	125
5.6.1.2.	Comparison to 2D analyses.....	128
5.6.1.3.	Plastic zone.....	129

5.7.	Discussion .....	132
5.8.	Summary.....	134
6.	Chapter Six: Fatigue life estimation and the effect of co-linear coalescence.....	136
6.1.	Introduction .....	136
6.2.	Background.....	136
6.3.	Elasto-plastic analyses replicating experimental data .....	139
6.3.1.	Total life experimental data.....	139
6.3.2.	Crack propagation phases within MAS-20S.....	140
6.3.3.	Crack growth analysis across the MAS-20S lining.....	142
6.3.4.	Lining life numerical estimations .....	145
6.4.	Co-linear cracks coalescence.....	148
6.4.1.	CTOD and crack front evolution.....	150
6.4.2.	Impact on fatigue life .....	154
6.4.3.	Development of the plastic zone.....	156
6.5.	Discussion .....	156
6.6.	Summary.....	160
7.	Chapter Seven: Stress analysis of plain bearings.....	161
7.1.	Introduction .....	161
7.2.	Background.....	161
7.2.1.	Bearing design procedures at MAHLE Engine Systems .....	163
7.3.	Residual stresses from forming operation .....	166

7.4. Full bearing analysis .....	172
7.4.1. Accelerated fatigue test conditions.....	174
7.4.1.1. Stress and strain results.....	178
7.4.1.2. Damage maps.....	183
7.4.2. Real engine conditions.....	187
7.4.2.1. Stress and strain analysis .....	188
7.4.2.2. Damage maps.....	189
7.4.3. Discussion .....	190
7.5. Summary.....	194
8. Chapter Eight: Conclusions, contributions and future work .....	196
8.1. Conclusions.....	196
8.2. Contributions .....	201
8.3. Future work.....	203
Appendix A.....	205
Proposed methodology for fatigue damage assessment.....	205
Appendix B .....	208
Sub-modelling stress analysis .....	208
1. Methodology.....	208
2. Results.....	210
3. Discussion .....	213
Appendix C .....	216

1. Two dimensional flat strip with single tip crack model under three-point bending.....	216
2. Two dimensional flat strip with bifurcated tip crack model under three-point bending.....	226
3. Three dimensional flat strip with quasi semi-elliptical crack under three-point bending ...	234
4. Three dimensional full bearing analysis .....	236
References .....	243

## List of Acronyms

APDL	Ansys Programming Design Language
ASTM	American Society for Testing Materials
BE	Boundary Element
BSI	British Standard Institution
CDF	Crack driving force
COD	Crack opening displacement
CTOD	Crack tip opening displacement
CTDV	Crack tip displacement vector
CTSD	Crack tip sliding displacement (CTSD)
CTTS	Crack tip tangential strain
DoE	Design of experiments
DoF	Degree of freedom
EHL	Elasto-hydrodynamic lubrication
EPFM	Elastic-plastic fracture mechanics
FD	Finite differences
FE	Finite Element
F&F RS	Forming and fitting residual stresses
GUI	Graphical user Interface
HRR	Hutchinson Rice Rosengreen
HVOF	High velocity oxyfuel
LEFM	Linear elastic fracture mechanics
LSY	Large Scale Yielding

MCDF	Maximum crack driving force
MCL	Modified Chen and Lankford
MM	Modified Miller relation
MPS	Maximum principal stress
MPSN	Maximum principal strain
MTS	Maximum tangential stress
MTSN	Maximum tangential strain
MERR	Maximum energy release rate
MSED	Minimum strain energy density
SSY	Small Scale Yielding

## List of Symbols

$A$	Crack front area
$a$	Crack length
$a_0$	Initial crack length
$a_{1,2}$	Interacting crack lengths
$B$	Specimen width in standard solution from ASME and BSI
$C$	Material constant for Paris Law
$C_m$	Correction factor for opening estimates
$C_{norm}$	Compliance of layered architecture in the direction normal to EHL pressure
$COD$	Crack opening displacement
$CTOD$	Crack tip opening displacement
$CTOD_{POST}$	Crack tip opening displacement post-coalescence
$CTOD_{PRE}$	Crack tip opening displacement pre-coalescence
$CTOD_{SINGLE}$	Crack tip opening displacement of a crack growing independently
$d_b$	Deformation at the casing-bearing interface
$d_c$	Deformation of the bearing casing
$d_f$	Deformation of the bearing caused by fitting operations
$d_n$	Deformation of the bearing strip due to normal loading

$d_r$	Distance between plastic zones
$d_t$	Deformation of the bearing thickness
D	Typical microstructural size or distance
$D_b$	Bearing diameter
$\frac{da}{dN}$	Crack growth rate per load cycle
$\left(\frac{da}{dN}\right)_i$	Crack growth rate at a given location on the crack front
$\left(\frac{da}{dN}\right)_{max}$	Maximum crack growth rate in extension step
$e$	Eccentricity between bearing and journal
$E$	Young Modulus
$E'$	Effective Young Modulus according to plane strain or stress conditions
$f_{ij}(\theta, r)$	Dimensionless function in terms of the angle $\theta$ and distance $r$ for the axial stress in the $ij$ direction according to the HHR relation
$f_{xx}(\theta, r)$	Dimensionless function in terms of the angle $\theta$ and distance $r$ for the axial stress in the $x$ direction
$f_{yy}(\theta, r)$	Dimensionless function in terms of the angle $\theta$ and distance $r$ for the axial stress in the $y$ direction
$h$	Distance between interacting cracks
$h_0$	Initial clearance between journal and bearing
$h_i$	Clearance at load step $i$
$K$	Stress intensity factor
$K_{I,II}$	Stress intensity factor in separation mode I or II

$k(\Phi)$	Function depending on the crystallographic orientation of the grain in Chan and Lankford model
$I_n$	Factor that is affected by the strain hardening exponent according to the HHR relation
$J$	J integral
$L$	Length between supports for three-point bending tests
$m$	Material property related to the Paris law relationship
$M$	Applied moment in standard solution from ASME and BSI
$N_f$	Number of cycles of total life
$N_i$	Number of cycles required for initiation process
$N_L$	Number of cycles required to propagate an initiated crack to the interface
$N_P$	Number of cycles required for a crack to initiate and reach the interface
$n$	Strain hardening exponent in Ramberg Osgood relation
$n_i$	Number of cycles at particular level of stress amplitude in Palmgren-Miner relation
$P$	Applied load in three-point bending test
$p$	Dimensionless factor to relate J integral and CTOD according to plane strain
$q$	Fitting parameter for Basquin relation
$r$	Radial coordinate in cylindrical system or fitting parameter for Basquin relation
$s$	Arc length around the integration contour for J integral
$T$	T stress
$\mathbf{T}$	Traction vector for J integral
$t_b$	Backing layer thickness for the MAS-20S system

$t_i$	Interlayer thickness for the MAS-20S system
$t_{L1}$	Lining layer thickness for the MAS-20S system
$t_{L2}$	Lining layer thickness for bi-layer system (no interlayer)
$\mathbf{u}$	Displacement vector for the J integral
$u_y$	Opening displacement
$w$	Strain energy for J integral or width for flat strip model
$W$	Specimen thickness in standard solution from ASME and BSI
$W_b$	Bearing width
$X$	Distance to typical microstructural feature in Chan and Lankford model
$x$	Cartesian coordinate
$y$	Cartesian coordinate
$\Gamma$	Integration contour for J integral
$\Pi$	Potential energy
$\gamma_s$	Surface crack energy per unit of surface area
$\delta$	Crack tip opening displacement
$\Delta a_i$	Crack extension at a given location on the crack front
$\Delta a_{max}$	Maximum crack extension per step
$\Delta CTOD$	Crack tip opening displacement difference between maximum and minimum load
$\Delta K$	Stress intensity factor difference between maximum and minimum load

$\Delta\gamma$	Shear strain amplitude at the crack tip in Miller model
$\varepsilon_{ij}$	Ongoing strain in direction $ij$
$\varepsilon_y$	Yield strain
$\sigma_a$	Stress amplitude in Basquin relation
$\sigma_f$	Critical far field stress that would cause crack extension
$\sigma_{ij}$	Ongoing stress in direction $i$ and $j$
$\sigma_{xx}$	Axial stress in the $x$ direction
$\sigma_{yy}$	Axial stress in the $y$ direction
$\sigma_{YS}$	Yield stress
$\sigma_\theta$	Tangential stress
$\sigma_\infty$	Far field stress
$\theta$	Coordinate in cylindrical system
$\mu$	Shear modulus
$\nu$	Poisson Ratio

*To my beloved wife and to the people I consider my family*

## **Acknowledgments**

The achievement of this degree was only possible due to the cooperation of private and public entities. I would like to thank the Mexican government and especially the National Council for Science and Technology (CONACYT) and the School of Engineering Sciences in the University of Southampton for funding this project. The support provided by MAHLE Engine Systems is also greatly acknowledged providing a great insight during the assessment of the case study.

I would also like to thank my colleagues who provided excellent feedback related to engineering and other less sophisticated but important matters. The environment under which this research was developed could not have been better and the time spent here will always be remembered with nostalgia and sometimes with relief.

The contribution to this work of my supervisors is unquestionable; the developed work would have been unreachable without their guidance and expertise in this field. However; the example given by Stavros and Philippa is the most valuable thing that I am taking with me and I can assure that my life has been marked by the time spent under their supervision.

These acknowledgements could not be complete without mentioning all the people that taught me so much during my stay in England. The time spent here showed me that it does not matter where you came from or where you are going, you will always find people eager to help you and worthy to be your friends.

Finally, I would like to acknowledge the long distance support of my family which deserves all the credit for any achievement obtained in my life. The greatest acknowledgment made here is to my wife whose support made possible to go through all this process without losing my mental health. Her example and sacrifices make me admire her more than anyone else. Her love has made me happier than I ever imagined and I will do my best to make her feel the same way.

## List of Figures

Figure 1. Bending tests for concave shells and flat strips.....	3
Figure 2. Material separation modes.....	10
Figure 3. $J$ integral contour.....	12
Figure 4. Geometrical definitions of CTOD. Crack tip position before loading, 45 degrees intersection and arbitrary distance from crack tip.....	15
Figure 5. Regimes $A$ , $B$ and $C$ of crack growth.....	16
Figure 6. Long and short crack fatigue growth.....	18
Figure 7. Roller element and plain bearing.....	20
Figure 8. Tri-layer architecture displaying backing, interlayer and lining layers.....	21
Figure 9. Manufacture operations sequence.....	22
Figure 10. Lining detachment caused by fatigue mechanisms.....	23
Figure 11. Crack propagation in MAS-1241 [7].....	25
Figure 12. Example of characteristic bifurcation and deflected crack in tri-layer architecture MAS-20S [7].....	26
Figure 13. Total life tests for different bearing architectures [8].....	27
Figure 14. Crack growth rate measurements in [8]. .....	28
Figure 15. True stress-true strain curves for the three-point bending model.....	29
Figure 16. Three dimensional optical micrographs of MAS-20S [7]. .....	30
Figure 17. Spider web and blunted crack tip configuration.....	36
Figure 18. Three-point bending and test specimen configuration.....	38
Figure 19. Estimated $K_s$ from British Standards, spider-web and blunted crack tip models.....	40
Figure 20. Finite element model of blunted crack before (a) and after deformation.....	41

Figure 21. Von Mises plastic strain contour in tri-layer architecture at 800 N with the crack tip positioned in the lining (Anti-shielding case).....42

Figure 22. Von Mises plastic strain contour in tri-layer architecture at 800 N with the crack tip positioned in the interlayer (Shielding case).....42

Figure 23. CTOD evolution with crack length in bi-layer system.....44

Figure 24. CTOD evolution with crack length in and tri-layer system.....44

Figure 25. Tangential strain variation around the crack tip at 600 N in the bi-layer system lining.....45

Figure 26. Tangential strain variation around the crack tip at 600 N in the tri-layer system lining.....46

Figure 27. Tangential strain variation around the crack tip at 200 N in the tri-layer system interlayer. ....46

Figure 28. Cylindrical coordinate system placed at crack tip. ....50

Figure 29. Estimations of path deflection according to  $K_{II} / K_I$  ratio [86].....51

Figure 30. Test specimen used by Mageed and Pandey [88].....57

Figure 31. Crack deflection predictions with corresponding fatigue test result [88] at 92.5 MPa.....58

Figure 32. Model generation methodology.....61

Figure 33. Predicted path and Von Mises stress contour of a single tip within the tri-layer system at 200 N.....62

Figure 34. Von Mises strain contour of a single tip within the tri-layer system at 200 N (a) and 800 N (b). ....63

Figure 35. CTTS evolution against extension steps. ....63

Figure 36. Comparison of CDF between straight and deflected paths at 200 N in the interlayer. ....64

Figure 37. Bifurcated model and analysed factors. ....67

Figure 38. Variation of CDF with kink angle in the tri-layer architecture at 200 N (CTOD values are normalised with respect to their maximum along each curve). .....68

Figure 39. Variation of CDF with kink angle in the bi-layer architecture at 400 N (CTOD values are normalised with respect to their maximum along each curve). .....69

Figure 40. Estimated paths for single tip deflected crack and bifurcated arrangements with only pure elastic and elasto-plastic materials. ....71

Figure 41. Accumulated deflection and CDF evolution in tri-layer architecture for single-tip deflected and bifurcated crack (bifurcated EP).....71

Figure 42. Equivalent plastic strain (Von Mises) in tri-layer architecture. ....72

Figure 43. Accumulated deflection and CDF evolution in tri-layer architecture using pure elastic (bifurcated E) and elasto-plastic (bifurcated EP) materials. ....72

Figure 44. Crack growth process in multi-layered architecture at initial crack growth stages. ....78

Figure 45. Crack growth process in multi-layered architecture at late crack growth stages. ....78

Figure 46. Interacting crack arrangements.....80

Figure 47. Distance between plastic zones for oblique (a), parallel (b) and co-linear arrangements.....81

Figure 48. Crack growth progression (a, b and c) in co-linear arrangement under 100% of yield stress showing Von Mises plastic strain contours. ....82

Figure 49. Co-linear arrangement results for  $CTOD_{COAL}/CTOD_{SINGLE}$  at equal crack lengths. ....83

Figure 50. Crack growth progression (a, b and c) in parallel arrangement under 100% of yield stress showing Von Mises plastic strain contours. ....84

Figure 51. Parallel cracks results for the CDF of shielded tips versus the shielded crack size (*a*, *b*, *c*) and the distance between plastic zones (*d*). ....85

Figure 52. Final stages of crack growth at crack separation equal  $1.7a$ ,  $3.5a$  and  $5.3a$  showing von Mises plastic strain contours in oblique arrangements under  $\sigma^\infty = \sigma Y$ . ....86

Figure 53. Oblique arrangement results for shielded tip deflection (*a*, *b*), CDF ratios of overlapped and single crack tips (*c*) and CDF ratios of overlapped and oblique tips (*d*) on the basis of the crack size (*a*, *c*) and the distance between plastic zones (*b*, *d*).....88

Figure 54. Cell mesh for a 3D crack propagation model. ....95

Figure 55. Three-dimensional elements and collapsed version.....98

Figure 56. Crack front mesh in cylindrical arrangement.....98

Figure 57. Crack block generation and interfaces in low-stress gradient and crack tip elements.....100

Figure 58. Typical mesh examples showing the lining surface (a) a cross section showing von Mises stress.....101

Figure 59. CTOD measurement in blunted tip mesh configuration. ....102

Figure 60. CTOD measurement in spider-web mesh configuration.....102

Figure 61. Relative crack extension along the front.....104

Figure 62. Numerical (left) and exact solution (right) for embedded crack under tension. 104

Figure 63. Convergence analysis with blunted tip (a) and spider-web (b) models. ....106

Figure 64. Crack opening profile using developed model and exact solution evaluated at 5 sampling points. ....108

Figure 65. Assumed behaviour by small fatigue crack growth models by Chan and Lankford and Miller. ....110

Figure 66. Crack growth law generation. ....111

Figure 67. Crack growth rate vs. crack length as reported in [10]. ....112

Figure 68. Predicted spread of plasticity under a load of 920 N (Von Mises strain contours are shown).....113

Figure 69. Spread of plasticity at 920 N. ....116

Figure 70.  $\Delta$ CTOD, CTOD at 920 N and CTOD at 92 N vs. crack length under three-point bending. ....117

Figure 71. Crack growth rate vs.  $\Delta$ CTOD under 920 N in 3D model. ....117

Figure 72. Fitted crack growth relationships illustrating the behaviour of on the relation described by Miller (MM) based on the cloud of data obtained experimentally. ....118

Figure 73. Fitted crack growth relationships illustrating the behaviour of the relation proposed by Chan and Lankford (MCL) based on the cloud of data obtained experimentally showing the effects of the selection of  $D$  (a) and the selection of initiation location between barriers (b). ....120

Figure 74. Crack front evolution in bi-layer and tri-layer architectures. ....124

Figure 75. Crack front evolution in tri-layer (a) and bi-layer (b) architectures at 200 N. ..125

Figure 76. Crack driving force evolution (a) and CDF ratio between values obtained at the deepest point and at the surface (b) in bi-layer and tri-layer architectures. ....126

Figure 77. Comparison between CDF estimates obtained from 2D and 3D models at both architectures. ....129

Figure 78. Plastic zone shape contained in the lining of a tri-layer architecture (Von Mises plastic strain contour). ....131

Figure 79. Plastic zone shape and low strain area next to the crack in tri-layer architecture (Von Mises plastic strain contour). ....131

Figure 80. Plastic zone broadening at the deepest point of the crack due to backing shielding in bi-layer architecture (Von Mises plastic strain contour). ....131

Figure 81. Co-linear (a), parallel-oblique (b) and parallel-aligned (c) crack arrangements. ....138

Figure 82. Total life tests of flat strips MAS-20S in parallel and perpendicular orientations of the loading axis to rolling. ....140

Figure 83. Crack driving force evolution in bi-layer (a) and tri-layer (b) architectures. ....143

Figure 84. Estimated crack driving force values evaluated at the free surface and deepest point of the crack in bi-layer and tri-layer architecture in 3D models. ....144

Figure 85. Estimated J-integral values along the crack front (a) and at particular positions for clarity (b) in bi-layer and tri-layer architectures in 3D models. ....145

Figure 86. Coalesced crack progression. ....149

Figure 87. Pre-coalescence CDF evolution in twin cracks beyond the effect of layered anti-shielding.....150

Figure 88. Post-coalescence CDF evolution in twin cracks beyond the effect of layered anti-shielding.....151

Figure 89. Post-coalescence cracks affected by shielding. ....152

Figure 90. CTOD estimates (a) and CDF ratio with half penny crack of equivalent depth. ....153

Figure 91. Post-coalesced plastic zone shapes at a crack depth equal to 0.12 mm under a load of 720 N (volume experiencing strains higher than  $4e-3$  is shown). ....156

Figure 92. Lining detachment caused by fatigue mechanisms. ....162

Figure 93. Design stages for MAHLE Engine Systems (Post-processing operations are only carried out in this research project, not currently required for MAHLE Engine Systems). ....164

Figure 94. Representative EHL pressure over bearing surface. ....165

Figure 95. Forming process components.....167

Figure 96. Circumferential stress evolution during the forming process. ....169

Figure 97. Cross Section of the bearing showing residual circumferential stresses resulting from forming (left) and residual circumferential stresses from 2D and 3D model showing the influence of friction (right). ....171

Figure 98. Evolution of the circumferential stresses when coining and broaching operations are included. ....171

Figure 99. Boundary conditions application. ....174

Figure 100. Sapphire rig. ....175

Figure 101. Specific load applied to upper top and bottom shell (a) and circumferential strain (MPa) in the bearing lining (neglecting fitting and forming operations and assuming linear elastic material models) at the cycle peak pressure (b). ....176

Figure 102. Bearing casing deformed shape (a) and EHL pressure evolution (b) during engine cycle (not to scale). ....176

Figure 103. Total circumferential stress vs. position at various crank angles (or time steps) assuming linear elastic material model neglecting (a) and accounting for F&F RS (b). .....180

Figure 104. Total circumferential (or tangential) strain vs. angular position at various crank angles (or time steps) assuming linear elastic material model neglecting (a) and accounting for F&F RS (b).....180

Figure 105. Total circumferential stress vs. crank angle at various angular position assuming linear elastic material model neglecting (a) and accounting for F&F RS (b). .....181

Figure 106. Total circumferential stress vs. crank angle at various angular positions assuming elastic-plastic model neglecting (a) and accounting for F&F RS (b).....182

Figure 107. Total circumferential strain vs. crank angle at various angular positions assuming elastic-plastic model neglecting (a) and accounting for F&F RS (b).....182

Figure 108. EHL pressure and clearance at 97 MPa at the cycle peak pressure. ....183

Figure 109. Amplitude maps of elastic and no residual stress analysis. Circumferential strain (a) and stress (b), principal strain (c) and stress (d) and Von Mises strain (e) and stress (f) .....184

Figure 110. Circumferential strain amplitude maps for elastic and no residual stress case (a), elastic and residual stress case (b), elasto-plastic and no residual stress case (c) and elasto-plastic and residual stress case (d).....185

Figure 111. Circumferential stress amplitude maps for elastic and no residual stress case (a), elastic and residual stress case (b), elasto-plastic and no residual stress case (c) and elasto-plastic and residual stress case (d).....186

Figure 112. Specific load variation with crankshaft position.....187

Figure 113. Bearing deformed shape (a) and EHL pressure (b) evolution along engine cycle for real case scenario (not to scale). ....188

Figure 114. Circumferential or tangential (a) and YZ shear strain (b) vs. bearing angular position in “Real A” .....189

Figure 115. Circumferential or tangential (a) and YZ shear strain (b) vs. crankshaft angular position in “Real A”.....189

Figure 116. EHL pressure (a) and clearance at peak load in “Real A”. ....190

Figure 117. Damage map based on circumferential or tangential (a) and XY shear (b) strain amplitude in “Real A”.....191

Figure 118. Proposed methodology for bearing design.....206

Figure 119. Sub-modelled analysis using EHL and deformations estimated from SABRE-EHL.....209

Figure 120. Circumferential strain comparison between full and sub-modelled analysis. .211

Figure 121. Circumferential strain comparison between sub-model and full analysis (using a cross Section defined as the sub-model border for the latter one).....211

Figure 122. Circumferential strain comparison between sub-model and full analysis (using a cross section at 180°) .....212

Figure 123. Strain ZZ (width direction) comparison between sub-model and full analysis (using a cross section at 180°) .....212

Figure 124. Principal strain comparison between sub-model and full analysis (using a cross Section at 180°).....213

Figure 125. Maximum strain reorientation as loading is applied (Full model used for clarity showing values at the lining surface). .....214

## List of Tables

Table 1. Previously investigated bearing architectures. Part I [10].	24
Table 2. Previously investigated bearing architectures. Part II [10].	25
Table 3. Elastic mechanical properties of MAS-20S [7].	29
Table 4. Finite body tessellation analysis of the MAS-20S lining [7].	31
Table 5. Ratios between elastic & plastic mechanical properties.	39
Table 6. Fitted values of $C'$ and $n'$ .	118
Table 7. Maximum absolute vertical deformation at various crack lengths.	141
Table 8. Life estimation using Tanaka and modified Chan and Lankford (MCL) relation with upper and lower bounds.	147
Table 9. Impact of crack initiation position in relation to hard intermetallics on fatigue life estimate.	147
Table 10. Comparison between single and coalesced crack growth based on the Modified Chan and Lankford (MCL) relation using a $D=28 \mu\text{m}$ initiated at the microstructural barrier.	155

# 1. Chapter One: Introduction

## 1.1. *Background*

Fatigue failure has been studied extensively to prevent components of engineering systems from going prematurely out of service or causing damage to the whole system. More demanding service conditions have been met with the introduction of tougher materials and complex architectures but they have also resulted in more severe plastic deformation around existing or fatigue-initiated flaws in the component. Multi-layered architectures can be found among those complex architectures. The combination of different material properties presents a new range of possibilities; especially when mechanical, thermal and electrical conductance properties are integrated to create new products. Most of the applications described in this work are related to the search for a compromise between material strength and damage tolerance on the one hand and additional vital features, such as thermal conductance, friction reduction, structural compatibility for joining and resistance to wear or corrosion, on the other.

The search for this compromise has been evident in various industrial applications. A compromise between heat conductance and strength can be found in the cooling system of compressor or blade buckets [1]. The circulation of coolant around bi-layered architectures consisting of an outer skin, intended to withstand wear and corrosion, and a copper inner part, intended to promote heat exchange. Other applications related to corrosion and wear can be observed in a range of industrial environments. Within the context of wear, applications related to the design of coins [2] and manufacture of hot drawing tools [3] have been developed. The latter is an interesting application, since not only wear is reduced but also the elimination of surface preparation is achieved, minimising operation times and costs. In the context of corrosion, the oil and gas industries have

also applied layered architectures in the transportation of fluids through piping systems [4]. Evidently, such fluids promote corrosion in structurally sound materials such as steel. Therefore, inner layers of nickel and copper alloys were added in order to minimise this effect. A more fundamental problem was addressed through the application of rolled steel-aluminium sheets with the aim of bonding incompatible materials [5]. The creation of layered inserts allowed welding between large structures of different materials such as in on-deck housings in ships. The popularity of this application in the last 30 years is a case in point of the importance of layered architectures. Commercial brands like DuPont still fabricate such inserts for state of the art yachts.

The examples presented above describe typical applications of layered architectures made of ductile materials. More recent applications in the microelectronics industry have introduced electrical conductivity as an additional feature to be considered in such architectures. Working towards current conduction efficiency but at reduced scales, ceramic and composite materials are used in these applications.

This work is mainly concerned with crack propagation occurring in layered architectures made up of ductile materials. The analysis developed in this thesis was applied to a layered architecture used for plain bearings in the automotive industry. These components are vital within the powertrain system. Their strategic position within the engine makes impossible to monitor visually damage evolution; this increases the importance of initial design methodologies that account for damage tolerance. The bearing design process is complex since manufacturing, assembly and service conditions affect the component performance. The study of service conditions is especially interesting and challenging since it is currently based on elasto-hydrodynamic lubrication (EHL) analyses whereby the oil film pressure is coupled with the elastic deformation of the housing and the journal.

Previous studies at the University of Southampton have characterised the material microstructure and crack propagation occurring in various bearing architectures [6-9]. The behaviour of growing cracks within these layered architectures was investigated in concave layered shells, as used in automotive bearings, and more extensively in flat strips, before the final forming process. These specimens were subjected to bending, as shown in Figure 1, in order to study a simpler and better known state of stress in contrast to complex bearing service conditions within an engine.

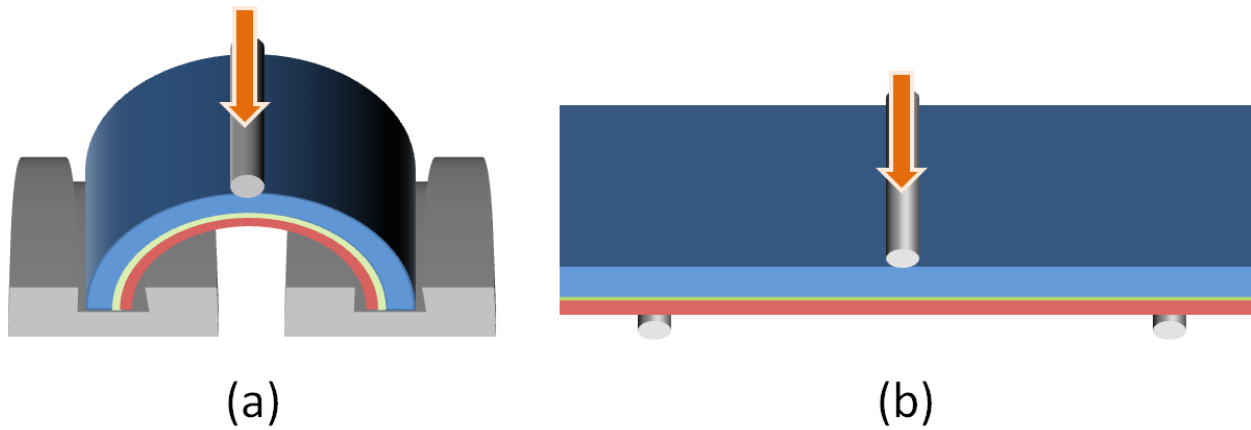


Figure 1. Bending tests for concave shells and flat strips.

The methodology followed here can also be applied to other mechanical components such as the examples described at the beginning of this Section. The methods followed here are also applicable to the study of ceramic layered architectures; although, suitable modifications should be made in applying these approaches to such very different mechanical systems.

## 1.2. *Aim and Objectives*

The aim of this research project is to model crack growth in multilayered material systems subjected to extensive elasto-plastic deformation. A damage tolerance approach and the finite element method are used to study crack propagation accounting for aspects such as deflection, bifurcation, coalescence, shielding caused by mechanical mismatch between layers, extensive elasto-plastic deformation and short-fatigue crack growth. The study of crack growth in multi-

layered architectures involves computational and modelling challenges related to the material's non linear deformation and the development of complex FE meshes that evolve as the crack extends, respectively.

This thesis is focused on the development of numerical models that could complement the extensive experimental work developed previously at the University of Southampton. Experimental work developed in the Materials Research Group has studied the crack growth mechanisms and behaviour in similar layered architectures promoting the selection of adequate modelling techniques. At the same time, this experimental work has provided the foundations for developing fatigue life estimations of layered architectures subjected to three-point bending and, in the near future, more complex loading conditions. Towards the latter, stress-strain fields are investigated in concave bearing shells subjected to service conditions

Particular objectives of this work are:

- Generation of efficient two and three dimensional finite element analyses for the simulation of three-point bending fatigue tests, including automatic mesh regeneration as the crack grows.
- Study of the consequences of shielding and anti-shielding in flat multilayered strips under three-point bending tests subjected to large scale yielding (LSY).
- Study of crack path instabilities such as deflection, bifurcation and coalescence focusing on their causes and their effects on the crack driving force (CDF).
- Comparison between the damage tolerance and total life approach through previous experimental work [10] in the University of Southampton with flat strip specimens under three-point bending tests.

In relation to bearing shells, the objectives are:

- Explore possibility of a damage tolerance approach through a detailed stress analysis of the big end bearing subjected to forming and fitting operations as well as hydrodynamic loading
- Use stress and strain output to determine the most likely crack initiation position.
- Propose a methodology to assess the fatigue performance of alloys used in the lining through numerical models and output from accelerated cyclic damage tests.

The methodology followed in this work focuses on appropriate use of parameters, laws and criteria for crack path and front prediction in 2D and 3D, respectively. Certain issues relevant to fracture and fatigue mechanisms such as residual strains and stresses and crack closure were not accounted for. Crack closure has been shown to have a smaller effect on fatigue crack growth under high levels of crack driving force and load ratio [11], justifying such a simplification. Capturing the change in the residual stress field as cracks grow is a complex analysis that exceeds the computational resources available to capture the component load history.

Micro-structural effects were not included within the developed finite element (FE) models since homogeneous material properties were assumed. It is recognised that the micro-structure plays a role in the crack growth process and understanding of the micro-mechanisms involved in such processes according to each particular alloy is important. Particular attention to those effects on crack initiation and propagation was made in previous experimental work at the University of Southampton. However, this work is centred on the macro or meso-mechanical behaviour of the component based on the mechanical mismatch found among the different layers. The material microstructure effect is only indirectly included in these numerical analyses through the development of a crack growth law based on experimental data. Data on typical microstructural features has thus been introduced into the analysis through a particular form of crack growth law.

More in depth studies of the microstructure effect on crack growth would require micro-mechanical approaches. The implementation of a coupled local-global approach would increase

significantly the complexity of the numerical analyses developed and require either the analysis of a particular microstructure or the introduction of stochastic variables related to the material. Such a study is beyond the scope of this project and the resources available.

### **1.3. Thesis structure**

The thesis comprises eight chapters that include relevant background, methodology, results, discussion and conclusions. The first chapter describes fundamental literature information on the application of the damage tolerance approach based on FE analyses. A further literature review on particular issues relevant to the analysis developed is provided in each subsequent results chapter. Two-dimensional FE analyses of multi-layered flat strips under three-point bending are developed in chapter two. Straight through-width crack models were validated against analytical solutions for monolithic specimens under three-point bending and evaluated shielding and anti-shielding effects in multi-layered ones. Deflected and bifurcated through-width crack arrangements in architectures of two and three layers are assessed in chapter three based on a validated crack deflection criterion. Single layered specimens under tension containing various arrangements of coalescing through-thickness cracks are analysed in chapter four to evaluate shielding and anti-shielding effects caused by crack interaction and their dependence on loading, crack size and configuration. Chapter five is focused on the development of a three dimensional crack growth modelling methodology and the generation of a crack growth law. The methodology is applied to bi-layer and tri-layer architectures under three-point bending loading to compare shielding and anti-shielding effects under moderate yielding. Chapter six simulates greater levels of plasticity and compares the numerical estimations of fatigue life against experimental data including possible effects of coalescence on total life. Chapter seven is dedicated to the stress and strain analysis of a bearing under service conditions accounting for previous deformation history from forming and fitting

operations. Chapter eight describes the conclusions obtained from this thesis and further areas of opportunity for future work.

## **1.4. Literature Review**

The framework for this thesis requires knowledge from several areas to provide an insight into fatigue crack propagation in multi-layered systems. This research involves machine elements, materials, solid mechanics and numerical modelling. The foundations of the approaches and their scope used in this work are described next. Further literature reviews at the beginning of each chapter are included describing previous work that is particularly relevant to the issues discussed.

### **1.4.1. Fracture mechanics**

The failure of a range of manufactured goods has led to much study of the causes and mechanistic processes involved in fracture. The costs emerging from fracture are difficult to quantify, however an economic study [12] in the United States estimated losses of approximately \$119 billion (4 % of the gross national product) related to this issue in 1978. This study also revealed that the application of the knowledge and technology available in 1983 could have saved more than \$35 billion in 1978. Initial efforts to understand field observations studied material conditions in cracked components using analytical solutions of plates that contained notches or holes (material flaws). These elastic solutions provided the basis to assess cracks as very sharp discontinuities in the material and initiated the study of linear elastic fracture mechanics (LEFM). Later, this approach was extended to problems where LSY was present leading to Elastic Plastic Fracture Mechanics (EPFM).

#### **1.4.1.1. Linear Elastic Fracture Mechanics (LEFM)**

The applicability of LEFM has provided a suitable framework to deal with the structural analysis of cracks and their resulting singular stress field behaviour. The foundations of this approach were established early in the twentieth century with significant developments in the 60s and 70s that

enhanced its applicability. Modern theories of fracture are based on the pioneering work of Griffith [13, 14] in 1921 who established a criterion for unstable extension of cracks in brittle solids. Based on the stress analysis in infinite solids by Inglis [15], Griffith postulated that the critical far field stress  $\sigma_f$  that would cause crack extension is given by

$$\sigma_f = \sqrt{\frac{2E'\gamma_s}{\pi a}} \quad (1)$$

where  $E'$  stands for the effective Young modulus,  $a$  for half of the crack length and  $\gamma_s$  for the surface crack energy per unit of surface area. The effective Young Modulus for plane strain conditions is equal to  $E/(1 - \nu^2)$  while for plane stress is equal to  $E$ .

Griffith's novel approach considered a brittle material exhibiting no plastic deformation containing a sharp crack. Irwin [16] modified Griffith's relationship into another form based on the energy release rate per crack extension  $dA$ . Irwin postulated that a crack extension under a constant stress would occur only if a decrement of the system potential energy was equal, at critical conditions, to the increment of surface energy caused by new surfaces created with a length  $dA$  and a unit width.

$$G = \frac{\sigma^2 \pi a}{E'} = 2\gamma_s = -\frac{d\Pi}{dA} \quad (2)$$

where  $G$  stands for energy release rate,  $\Pi$  for the potential energy and  $A$  crack front area.

The study of cracks was also developed in terms of linear elastic stress analysis with very sharp flaws or notches. Irwin [17], based on the stress analysis by Westergard [18], quantified the near-tip field in terms of the stress intensity factor  $K$ . The parameter  $K$  represented the crack tip local conditions while the energy release rate reflected the global energy balance. These parameters are used as a measure of crack driving force (CDF) which characterises the conditions around the crack

tip with a single value. Other crack driving force parameters have also been used in the context of EPFM and are described in subsequent sections.

The stress intensity factor has been related to different material separation modes. These separation modes are based on loading conditions: tensile opening mode or Mode I, in plane shearing mode or Mode II and out of plane shearing mode or Mode III; these modes are shown in Figure 2. Representative relations between stress and  $K_I$ , related to pure opening mode:

$$\sigma_{xx} = \frac{K_I}{\sqrt{2\pi r}} f_{xx}(\theta) + T + \text{terms that are negligible near the crack tip} \quad (3)$$

$$\sigma_{yy} = \frac{K_I}{\sqrt{2\pi r}} f_{yy}(\theta) + \text{terms that are negligible near the crack tip} \quad (4)$$

where  $\sigma_{xx}$  and  $\sigma_{yy}$  are the axial stress in the  $x$  and  $y$  direction (the latter being the loading direction),  $f_{xx}$  and  $f_{yy}$  are dimensionless functions,  $r$  and  $\theta$  are the polar coordinates with origin at the crack tip and  $T$  is the T stress. Similar relationships are available to describe stresses in other directions according to the material separation mode. CDF parameters are a representative measure of the conditions surrounding the crack tip and, therefore, an appropriate means to study fracture and fatigue problems.

$K$  has been used to investigate and compare the behaviour of cracks of different sizes and separation modes. However, it is important to recognise that  $K$  will only dominate the near-tip solution as shown by equations ( 3 ) and ( 4 ). As we move away from the crack tip second order terms gain more importance. On the other hand, the local failure processes that occur, usually designated as the process zone, depend on the scale of local failure and are not usually captured by  $K$  alone, bounding the dominance of the  $K$  solution to an annulus with maximum and minimum values of  $r$ .  $K$  solutions have also been shown to be applicable to problems exhibiting small plastic

deformation; however such plasticity should be well confined within the area of  $K$  dominance, usually referred to as problems with Small Scale Yielding (SSY).

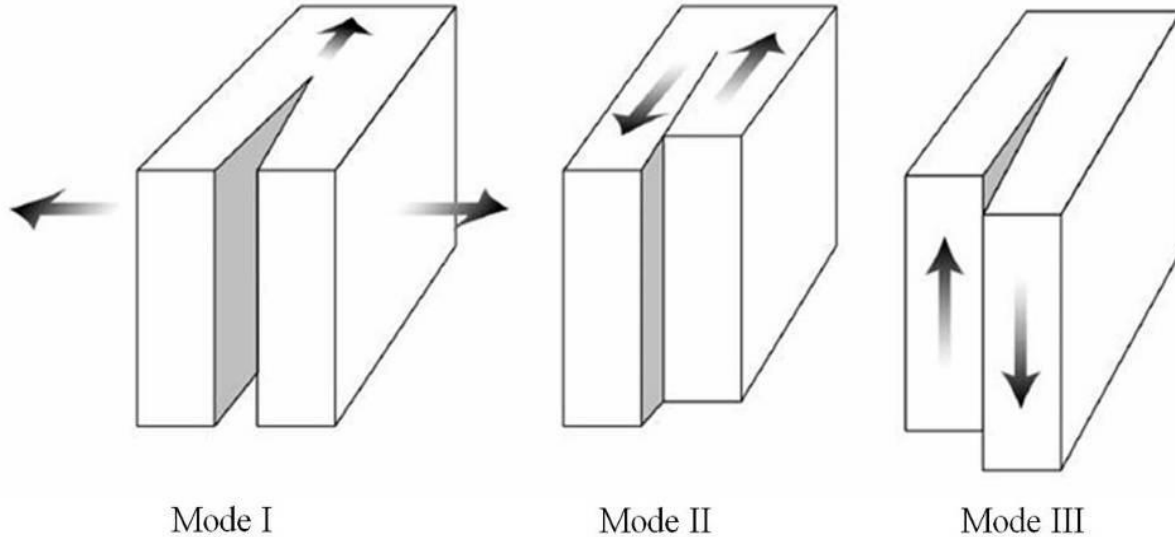


**Figure 2. Material separation modes.**

The definition of  $K$  and  $G$  led to the use of a new material property, the fracture toughness. This property is the critical value of stress intensity factor at which crack advance occurs. Codes of practice such as the British Standards Institution (BSI) [19] and the American Society of Testing Materials (ASTM) [20] provide some guidelines for the estimation of such a property considering the (limited) extent of plasticity that can be accommodated. According to ASTM, this plastic zone should be 25 times smaller than typical dimensions of the specimen (thickness, crack size and remaining ligament). Plastic zone size estimations by Irwin [17], Dugdale [21] and Barenblat [22] allowed this comparison, which in many ductile materials indicated a requirement for huge testing specimens. The introduction of a framework based on elasto-plastic fracture mechanics reduced these size requirements substantially and allowed the study of engineering problems where greater extents of plasticity develop.

Initial studies on fracture toughness, also known as critical CDF or  $K$ , showed that the specimen thickness played an important role in this process. Initial testing programs in the 1970s [23]

referred to plane stress or plane strain conditions to explain smaller estimates at thicker specimens. The constraint observed in thick specimens (assumed to lead to principally plane strain behaviour) reduces the material flow and leads to higher normal stresses when the yield stress is reached. In reality, the exact conditions of plane stress or plane strain do not hold across the whole thickness of the specimen and plane stress conditions are only observed at the free surface. The material constraint can be better related to stress tri-axiality which increases as the material analysed is located deeper in the specimen. Stress estimations by Narasimhan and Rosakis [24] showed this effect across the thickness of the plate and the distance from the crack tip.

#### **1.4.1.2. Elastic Plastic Fracture Mechanics (EPFM)**

Elastic Plastic Fracture Mechanics is applicable to tougher materials that are currently used in many engineering components. Plastic deformation allows materials to absorb energy after the yield stress is reached, allowing local material redistribution that may reduce stress concentrations and dissipate energy. As discussed previously, the validity of  $K$  to describe stress and strain fields around the crack tip is limited by the relation between the specimen and crack size to the plastic zone. Other CDF parameters have been used for the study of crack propagation under LSY conditions.

##### **1.4.1.2.1. J integral**

The  $J$ -integral was proposed by Rice [25], from energy concepts derived by Eshelby [26]. This parameter involves integration along a line around the crack tip involving the material's strain energy and the work done. Rice showed that  $J$  is the rate of change of potential energy with respect to crack propagation direction for a nonlinear elastic solid. The  $J$ -integral is given by

$$J = \int_{\Gamma} w \, dy + \mathbf{T} \frac{\partial \mathbf{u}}{\partial x} \, ds \quad (5)$$

where  $\mathbf{u}$  is the displacement vector,  $x$  and  $y$  are the co-ordinates in directions parallel and normal to the plane crack,  $s$  is the arc length around the integration contour  $\Gamma$ ,  $\mathbf{T}$  is the traction vector and  $w$  is the strain energy density. The integral representation is shown in Figure 3. The integral value is independent of the chosen contour. Its numerical computation may show path dependency but this would be due to inappropriate implementation or non proportional loading; conditions which are very rarely found when monotonic uniaxial loads are applied to stationary cracks [11, 23].

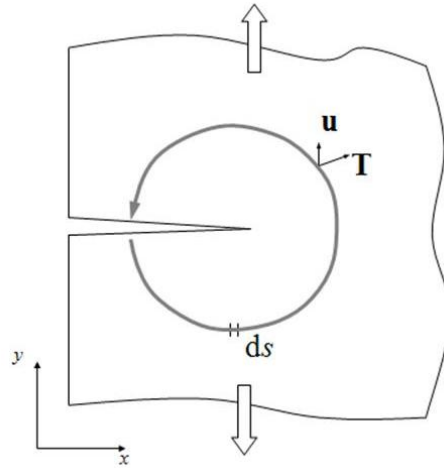


Figure 3.  $J$ integral contour.

The near tip stress fields can be determined through the Hutchinson Rice Rosengreen (HRR) singular equations [27, 28]. The analysis of elasto-plastic deformation requires the definition of rules related to yield, strain hardening and material flow. The Ramberg Osgood constitutive model [29] has been commonly used with HRR equations to fulfil the rules stated above.

$$\frac{\epsilon}{\epsilon_Y} = \begin{cases} \frac{\sigma}{\sigma_Y} & , \epsilon < \epsilon_Y \\ 1 + \alpha \left( \frac{\sigma}{\sigma_Y} \right)^n & , \epsilon > \epsilon_Y \end{cases} \quad (6)$$

where  $\epsilon$  represents the ongoing strain,  $\epsilon_Y$  the material yield strain,  $\sigma$  the ongoing stress,  $\sigma_Y$  the yield stress,  $\alpha$  is a material constant and  $n$  is the strain hardening exponent. The HRR singular fields for stress also showed a singularity when  $r \rightarrow 0$  as did  $K$  stress based solutions.

$$\sigma_{ij} = \sigma_Y \left( \frac{J}{\alpha \sigma_Y \varepsilon_Y I_n r} \right)^{\frac{1}{n+1}} f_{ij}(n, \theta) \quad (7)$$

where  $\sigma_{ij}$  represents stresses,  $r$  and  $\theta$  the distance and angle from the crack tip,  $I_n$  is a factor that is affected by the strain hardening exponent  $n$  and  $f_{ij}$  is a dimensionless function of stress.

The dominance of the HRR solution was also shown to be bounded by an annulus bounded by the process zone and an exterior radius dependent on the tested specimen and loading. The HRR fields under SSY conditions have been shown to hold over  $\sim 20\%$  of the plastic zone size in front of the crack tip. In contrast, the validity of these fields under LSY conditions appeared to be highly dependent on the tested specimen, ranging between 1% and 7% of the remaining ligament [23].

#### 1.4.1.2.2. Crack Tip Opening Displacement

The concept of crack tip opening displacement as a representative CDF is traced to Wells [30] who attempted to measure critical stress intensity values in steels. Wells observed that crack faces had moved apart prior to fracture as a result of plastic deformation, causing blunting at the crack tip. The intensity of this phenomenon was proportional to the toughness of the material. These attempts found that such a material could not be characterized by LEFM due to the excessive specimen size requirements. The aforementioned observations led Wells to propose the Crack Opening Displacement (COD) or Crack Tip Opening Displacement (CTOD) as a crack tip measure of fracture toughness. In his original work [30] Wells developed an approximate analysis that related the CTOD ( $\delta$ ) to the stress intensity factor at the limit of small scale yielding using Irwin [31] theory as shown in

$$\delta = \frac{4 K_I^2}{\pi \sigma_Y E} \quad (8)$$

where  $K_I$  is the stress intensity factor in its opening mode and  $\sigma_Y$  the yield stress. Burdekin and Stone [32] proposed an alternative analysis using the strip yield model. According to this analysis,

the size of the strip yield zone is related to the stress fields at the crack tip and the CTOD can be defined as the crack opening displacement at the end of the strip yield zone. The analysis of Burdekin and Stone provided the appropriate theoretical basis needed to use the CTOD as CDF.

They derived the relation

$$\delta = \frac{8\sigma_Y a}{\pi E} \ln \sec\left(\frac{\pi\sigma_\infty}{2\sigma_Y}\right) \quad (9)$$

where  $\sigma_\infty$  corresponds to the far field stress. According to Anderson [23] the limit of the previous equation when  $\sigma_\infty/\sigma_Y \rightarrow 0$  reveals a ratio of  $\pi/4$  between the strip yield model and the original postulate of Wells. A more general form of equation ( 8 ) can be obtained when a dimensionless factor  $p$  (which depends on  $I_n$  and  $n$ ) and effective Young's Modulus  $E'$  is used according to plane strain or plane stress conditions within the scope of LEFM, as follows

$$\delta = \frac{K_I^2}{p\sigma_Y E'} = \frac{J}{p\sigma_Y} \quad (10)$$

One of the most severe drawbacks of the CTOD is its ambiguous geometrical definition. According to the literature three different definitions can be applied: Crack tip position before loading [23], intersection at 45 degrees with deformed crack lines, proposed by Rice [25], and opening at arbitrary distance from crack tip [33]. These definitions are shown in Figure 4.

#### **1.4.2. Damage tolerance approach**

The estimation of a component life has been mainly developed through two different approaches. The first one, total fatigue life approaches, introduced by Wöhler [34], consist of the characterisation of the whole failure process as a single entity. Crack nucleation, stable and unstable crack growth are merged into a single event. This empirical characterization is based on experimental results and is aimed to estimate the number of cycles that a component can stand at a

determined stress or strain amplitude. The representative variables involved in this approach are the stress or strain ranges, the mean stress or strain and the environment.

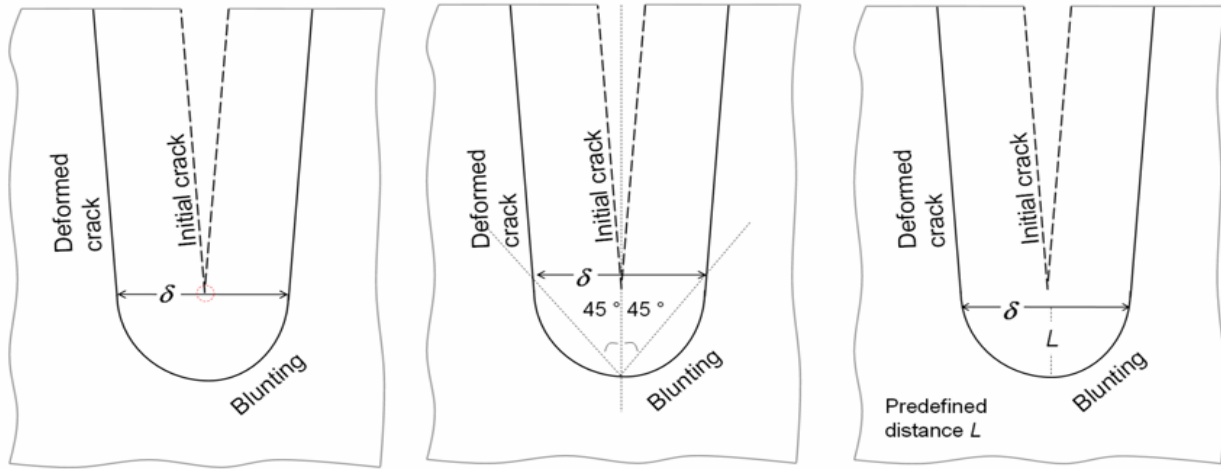


**Figure 4. Geometrical definitions of CTOD. Crack tip position before loading, 45 degrees intersection and arbitrary distance from crack tip.**

Total Life Approach works under the assumption of a defect free component. This assumes that crack initiation and failure would start at the location where the component receives a greater amount of damage. That is to say that the component would fail where the sum of damage caused by every single load at any point around the material is greatest.

The second approach, the damage tolerance approach is used to assess the rate of crack advance from an initial defect. Crack growth rate estimation, usually given in terms of crack growth per loading cycle, provides the means to assess the impact of a crack of a given size and determine a suitable inspection or replacement program to avoid failure. In contrast to total life approaches, the evolution of crack growth can be assessed identifying critical stages along the process. The estimation of the crack driving force gives a measure of possible crack growth and, as a result, a better understanding of the immediate consequences.

### 1.4.2.1. Growth of long cracks

Initial observations in crack growth identified three main regimes: initiation (or early stages of crack growth), stable growth and unstable growth. These regimes are shown in Figure 5 in a logarithmic plot of crack growth rate versus stress intensity factor amplitude. The near-threshold regime or regime A is related to the activation process of the crack growth; that is to say, that the crack growth state changes from being dormant or undetected to significant. Regime B exhibits a linear slope in the logarithmic plot. Identification of this regime is related to the work of Paris and Erdogan [35], also known as regime B and was the first to be studied. Finally, the unstable growth stage or regime C shows the transformation of the steady and moderate crack growth to an unstable rapidly accelerating growth that leads to total fracture, when the CDF parameter magnitudes are near to the fracture toughness.

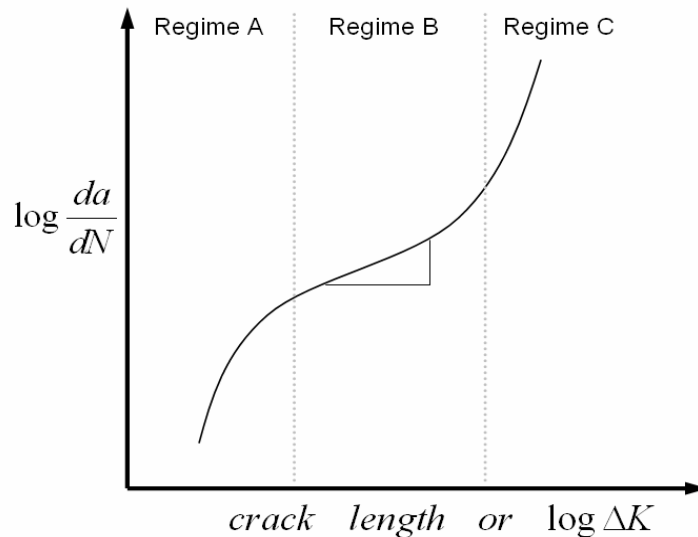


Figure 5. Regimes A, B and C of crack growth.

The first two regimes have been widely covered in the literature [16, 30, 35-38] due to their occurrence in different engineering materials and the generally insignificant influence of regime C on the overall fatigue life. The study of these regimes relates parameters such as crack driving force, crack size, loading ratio, frequency and others with a corresponding crack growth rate, given in

terms of the crack extension during a single cycle following a similitude principle. The similitude concept implies that any pair of cracks subjected to the same cyclic variation of CDF and sharing common material-environment conditions will exhibit similar crack growth rates, irrespective of the specimen geometry and loading conditions,

Regime B is characterised by a constant slope in logarithmic plots of crack growth rate against effective amplitudes of the crack driving force. Thus, Paris and Erdogan [35] described crack growth in this regime by

$$\frac{da}{dN} = C \Delta K^m \quad (11)$$

where  $da/dN$  is the change in the crack length per load cycle and  $N$  is the number of cycles,  $\Delta K$  the stress intensity range and  $m$  and  $C$  are material constants.

#### **1.4.2.2. Growth of short cracks**

Initial studies on fatigue cracks with a size below 1 or 2 mm showed uncharacteristic growth behaviour in particular materials and loading conditions. Pearson [39] was one of the first researchers to study short crack growth behaviour, observing growth rates up to a hundred times greater than the estimation provided by LEFM at a given level of effective stress intensity  $K_{\text{eff}}$  (difference between maximum  $K$  and  $K$  at which crack closure commences). These observations showed that the crack activation process observed in Regime A could be greatly influenced by other factors such as the material microstructure, loading level and environment conditions.

Lankford [40] and Tanaka *et al* [41] observed significant crack growth at crack driving forces well below the threshold levels where limited growth was expected under Regime A assumptions. The behaviour of short cracks has been shown to be dependent on typical microstructural features, such as grain size, the distance between second phase particles or similar microstructural features. This behaviour is shown schematically in Figure 6, where the distance between microstructural barriers

could dictate whether cracks at identical levels of  $K_{eff}$  arrest or keep growing. As cracks extend long crack behaviour is attained.

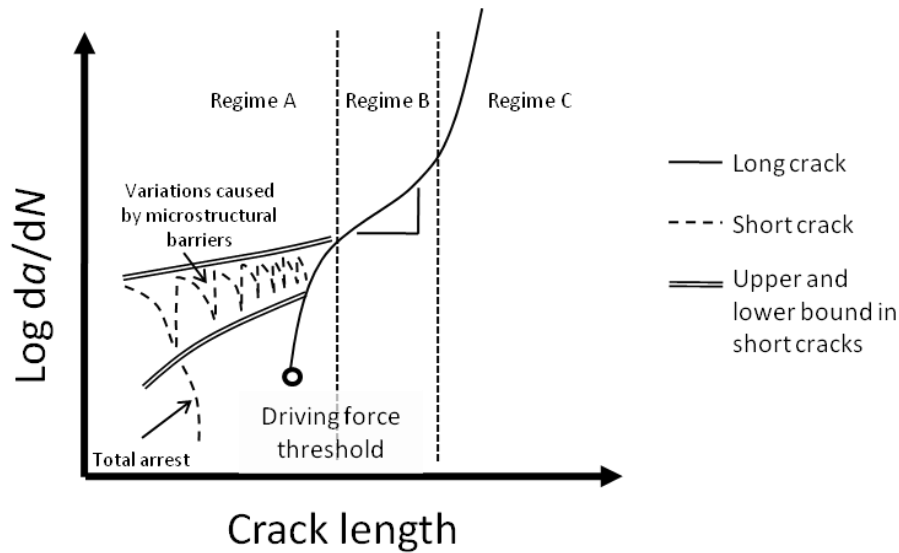


Figure 6. Long and short crack fatigue growth.

For the sake of simplicity, Suresh [11] categorised small cracks according to their typical features and behaviour as follows:

- *Micro-structurally short cracks*: Micro structure features have considerable effect due to their size similitude with the crack.
- *Mechanically short cracks*: Crack growth mechanisms differ from macro mechanical behaviour due to the different triaxial constraints. Deformations at the crack tip of short flaws within a grain are ruled by crystal plasticity instead of continuum mechanics, while the crystallographic orientation promotes local mixed mode loading conditions.
- *Physically short cracks*: Short crack growth is still not comparable to long cracks due to the retarding effect of crack wake on the latter due to closure, as the length increases this effect becomes more important.
- *Chemically short cracks*: Corrosion fatigue mechanisms may enhance short crack growth rates if crack length is not sufficiently long to produce steady-state crack tip corrosion conditions.

### 1.4.3. FE modelling of fatigue crack growth

The continuous development of computational power has led to a widespread use of numerical techniques such as Finite Element (FE) [42, 43] and Boundary element (BE) methods. FE analyses are extensively used in the assessment of cracked components. The development of a FE model for crack propagation analysis is a complex task that must consider relevant fatigue and fracture issues, such as appropriate crack tip meshing and crack extension tracking. Stress concentrations around crack tips generate excessive deformation that increase the complexity of the analysis and post processing calculations of stress, strain and crack driving force. To deal with these problems, mesh refinement and special crack tip mesh configurations [44, 45] have been used within LEFM and EPFM approaches. Simulation of crack extension is also necessary since the crack path and crack driving force values vary as the crack is extended; especially when mixed mode loading conditions, extended plasticity and other mechanisms take place. The development of crack growth analyses in FE or BE codes has been shown to be appropriate even for complex loading and sophisticated geometries [46-53].

The development of efficient FE models is indispensable in solving complex fatigue and fracture problems; at the same time, accurate computations of crack driving forces are essential. Many researchers have addressed this problem especially within a LEFM context. The numerical prediction of crack driving forces under EPFM received less attention in the past; however, work in this area has intensified in recent years. The computation of crack driving force parameters can be achieved through commercial packages, like ABAQUS [54] and ANSYS [55], which currently provide routines to obtain them. ABAQUS stands out in this matter since it provides estimations for three dimensional  $J$  integrals for non-linear analyses and  $T$  stress estimations for elastic isotropic analyses. However, ABAQUS modelling capabilities do not provide the overall flexibility available in ANSYS. Estimations of CTOD, as a CDF parameter, are obtained from basic results in FE analyses by measuring relative displacements between crack faces. For the sake of simplicity, CTOD has been

measured in previously published work [56, 57] at opposing nodes located at a specific distance from the crack tip.

#### 1.4.4. Plain journal bearings

Plain type bearings have been used in the assembly of journals and pistons in automotive engines in preference to roller element bearings despite the higher energy losses involved [58]. This is due to plain bearings being smaller, cheaper, and easier to assemble, making them more suitable to connect crankshafts, pistons and rods in modern automobiles. A rigorous design process is carried out for bearings to satisfy the structural, energetic, noise, vibration and harshness requirements under cyclic loads over long service intervals. Plain bearings' success is based on the ability of the elasto-hydrodynamic lubrication (EHL) layer to transmit the force between bearing and journal avoiding direct contact. By doing so, the EHL reduces energy losses and extends the life of mechanical components significantly. Sketches of a roller element and a plain bearing are shown in Figure 7.

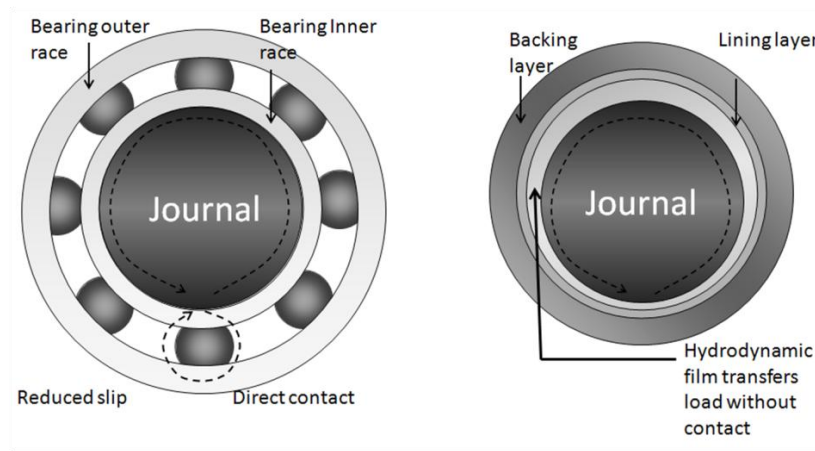


Figure 7. Roller element and plain bearing.

##### 1.4.4.1. Architecture and manufacture of plain bearings

Manufacturing processes for bearings have a strong influence on their performance. Each operation in the process affects the mechanical properties of the material and their variability. Thermal spray

coating, hot extrusion and roll bonding are manufacturing processes used to produce bi-layer and tri-layer bearing in strips which are then formed into concave shells. Layered architectures, shown in Figure 8, use a high strength material (such as steel) to provide rigidity and support while a thin interior lining with enhanced tribological properties is used to reduce the energy losses. Intermediate layers can also be used to strengthen the layers' bonding, reduce the constraint applied in the lining and prevent diffusion of other alloying elements into the backing.

An outline of the roll bonding process [59] carried out by MAHLE Engine Systems for the bearing manufacture is described next and shown in Figure 9. A continuous-casting process conveys lining billets to be reduced mechanically by successive rolling and heat treatment steps. The next operation consists of billet cladding and sealing of the lining by aluminium foil on both sides in order to reduce environment attack in one side and to form the interlayer with the backing on the other. Subsequently, another mechanical size reduction by rolling is carried out followed by a bonding process between steel backing and protected lining layers after being prepared in a cleaning solution. The final stage of the process forms the bearing shell into its final shape and broaches the internal face to the final specification of radius and required roughness removing the external layer of aluminium to reveal the lining.



**Figure 8. Tri-layer architecture displaying backing, interlayer and lining layers.**

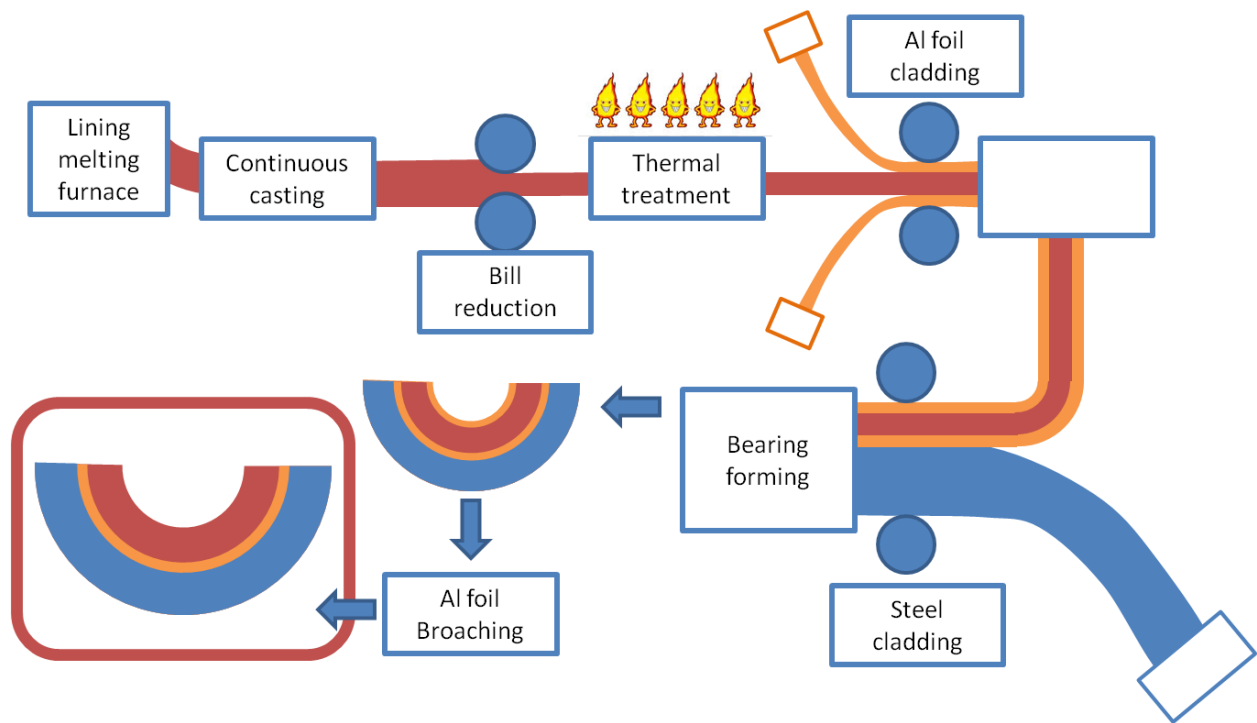


Figure 9. Manufacture operations sequence.

#### 1.4.4.2. Bearing Materials

The materials used in plain bearings have gone through continuous development for almost three centuries. These developments can be traced to the introduction of Babbitt metal in the nineteenth century to the enhanced alloys used nowadays. Copper and Aluminium alloys are widely used in automotive and industrial sectors for the fabrication of these components. Several alloying materials are used in these alloys such as Antimony, Zinc, Manganese, Nickel, Vanadium, Zirconium and Strontium while Lead, Silicon and Tin are particularly used in the automotive sector [60]. Aluminium alloys based on Al-Si and Al-Sn systems are of particular importance to this study due to their general applicability in the automotive industry and the availability of test data to support numerical modelling [61]. The materials mentioned above are mainly used in the lining due to their tribological and shock absorbing capabilities. The backing of the bearings analysed is usually made of a stronger alloy having suitable bonding properties to lining and/or interlayer. A frequently used material for these backing layers is a low to medium carbon steel of low cost.

### 1.4.4.3. Damage in plain bearings

A typical damage observed in bearings during extended service is the lining detachment into the hydrodynamic film. This lost lining causes further damage to the bearing and the journal affecting the original EHL profile. The lining detachment occurs through a three-dimensional crack growth process that is influenced by the layered architecture and EHL pressures. The principal trend observed in this process is the alignment of the crack path to run parallel to the layers orientation, shown in Section 1.4.5. At the same time, characteristic interaction mechanisms between cracks and mixed mode loading may cause coalescence in the plane parallel to the bearing surface. An example of lining detachment can be observed in Figure 10 [62].



Figure 10. Lining detachment caused by fatigue mechanisms.

### 1.4.5. Previous work at the University of Southampton

The study of multi-layered architectures based on automotive plain bearings has been pursued at the University of Southampton for approximately the last 10 years [6-9, 63]. Some numerical and extensive experimental research has been carried out to gain a better understanding of the crack propagation mechanisms observed. The architectures investigated had linings based on aluminium alloys and were mainly processed by roll bonding. Later studies also assessed a multilayer architecture manufactured through high velocity oxyfuel (HVOF); however, the current thesis uses

the data and results from the architecture MAS-20S; for this reason, more detailed information is provided in this chapter on this system in comparison to other tested architectures.

The materials and geometrical features of the investigated architectures are shown in Table 1 and Table 2. In general terms, the bearing architectures studied consisted of a medium carbon steel backing layer that is rigid enough to support the journal and an alloy layer or lining to resist wear and fatigue. A thin intermediate layer, which improves the bonding between the lining and backing, and an overlay layer, which reduces wear even further, have been often used in these automotive bearings.

The studies on these architectures have principally been dedicated to the investigation of fatigue crack initiation and crack propagation through the different layers [7]. The MAS-1241 flat strip architecture subjected to three-point bending showed crack propagation patterns that initiate on the lining surface and propagate towards the backing; then, the crack deflects and grows parallel to the layers orientation once it penetrates the more compliant interlayer, as shown in Figure 11. Numerical analyses in this architecture also studied the influence of the bifurcation angle and proximity to a dissimilar layer on the CDF [7].

**Table 1. Previously investigated bearing architectures. Part I [10].**

		MAS-1241	MAS-16	HVOF
Lining layer	Thickness (mm)	0.15—0.35	0.15—0.35	0.20—0.35
	Composition (Weight %)	Al-12Sn-4Si-1Cu	Al-20Sn-1Cu-0.25Mn	Al-20Sn-1Cu
Interlayer	Thickness (mm)	0.04—0.05	0.04—0.05	N.A
	Composition (Weight %)	Al	Al	N.A
Backing layer	Thickness (mm)	1.5—1.6	1.5—1.6	1.82—1.9
	Composition (Weight %)	Medium Carbon steel	Medium Carbon steel	Low Carbon steel (annealed)

**Table 2. Previously investigated bearing architectures. Part II [10].**

		MAS-20S	MAS-20	RB-168
Overlay-layer	Thickness (mm)	N.A	N.A	0.005—0.008
	Composition (Weight %)	N.A	N.A	Sn Ni
Lining layer	Thickness (mm)	0.15—0.38	0.15—0.38	0.2—0.30 N.A
	Composition (Weight %)	Al-6-8Sn-2.5Si-1Cu-1Ni-0.25Mn-0.06V	Al-6-8Sn-2.5Si-1Cu-1Ni-0.25Mn-0.06V	Cu-8Sn-1Ni
Interlayer	Thickness (mm)	0.04—0.05	0.04—0.05	N.A
	Composition (Weight %)	Al	Brazed sheet Al-1.2Mn-0.6Cu-0.7Fe Al-6Si-0.8Fe-0.25Cu	N.A
Backing layer	Thickness (mm)	1.8—1.82	1.8—1.82	1.5—1.55
	Composition (Weight %)	Medium Carbon steel	Medium Carbon steel	Carbon steel

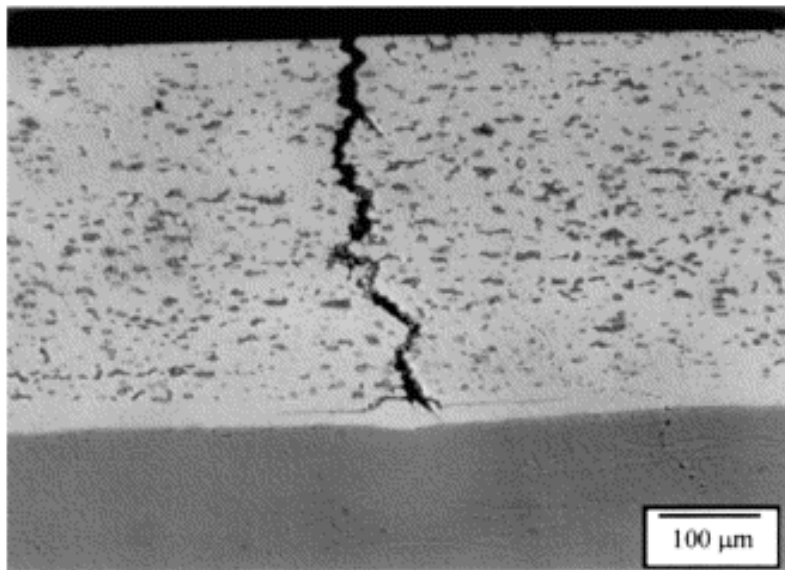


**Figure 11. Crack propagation in MAS-1241 [7].**

Further fatigue crack initiation assessments conducted on MAS-1241 and MAS-16 [6, 9] showed that Si particles with preferential orientations along the tensile axis would maximise the hydrostatic stress leading to decohesion between particles and the matrix. On the other hand, total life tests with three-point bending configurations showed that ambient conditions were more favourable for crack propagation than oil and vacuum, the latter proving to be the most beneficial environment for extended lives.

Additional studies on crack initiation were carried out on architectures, MAS-20, HVOF, RB168 and MAS-20S [63] the latter being the one with a greater initiation resistance. Further studies on these architectures [8], but especially on MAS-20S due to its superior performance, were carried out in order to estimate the growth rate of cracks on the lining surface in three-point bending fatigue tests. The crack propagation pattern observed in architecture MAS-1241 was also identified in MAS-20S, as shown in Figure 12. In the context of bearings, propagation through the thin interlayer appeared to be responsible for the release of small fragments into the EHL film and subsequent damage to the bearing and journal. This release is expected to occur when two cracks reach the interlayer and coalesce.

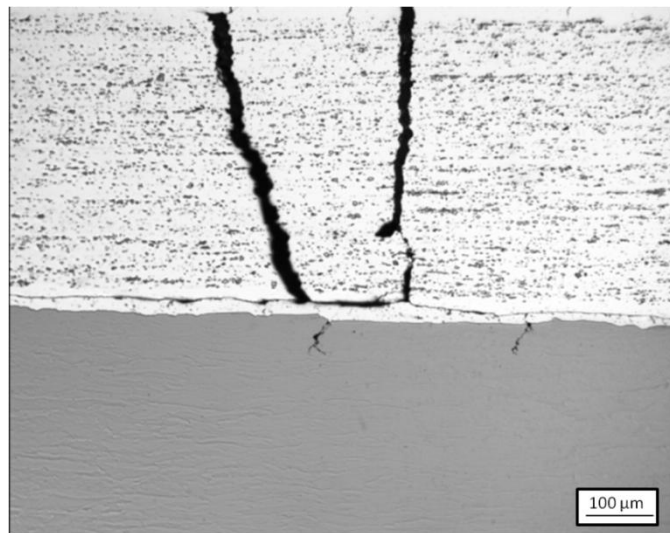


**Figure 12. Example of characteristic bifurcation and deflected crack in tri-layer architecture MAS-20S [7].**

Total life tests were also carried out with the MAS-20S and other architectures such as MAS-16, HVOF, MAS-20 and MAS-1241 [8]. These tests involved flat strips subjected to three-point bending tests and were compared on the basis of the plastic strain measured at the surface of the lining, within a loading range between 660 N and 920 N, using a load ratio of 0.1 and a frequency of 10 Hz. Life experiments continued until a maximum absolute vertical displacement of the loading cross-head 0.5 mm greater than the maximum absolute vertical displacement in the first loading cycle (approximately 0.18 mm) observed at the undamaged specimen. This amount of deflection was defined as the failure criterion in such experiments indicating that the crack had propagated substantially into the backing layer reducing the specimen stiffness and promoted the detachment of lining fragments. Total life data is presented in Figure 13.

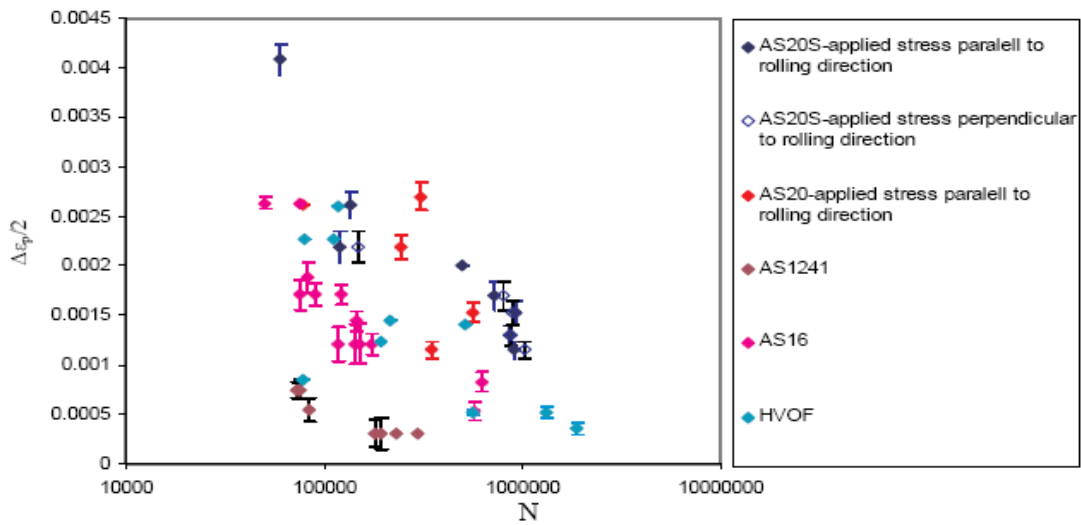


Figure 13. Total life tests for different bearing architectures [8].

Crack growth measurements were also carried out in MAS-20S, MAS20 and HVOF architectures through interrupted fatigue tests under three-point bending [8] at  $\Delta \epsilon = 0.0063 \pm 0.0002$ , which corresponds to a maximum load of 920 N for MAS-20S. Acetate strips of 20x40mm were used to replicate the surface after dipping them in acetone for about 15-20 seconds. These acetate strips became soft enough to be manually pressed against the polished surface of the flat bar in order to

record the current length of growing cracks. Loading was stopped every 1000 cycles to apply and remove the replicas. Further details on these tests can be found in [10]. The crack growth plot, shown in Figure 14, was developed through the obtained replicas under the optical microscope relating the observed crack size to the elapsed number of cycles through the secant method.

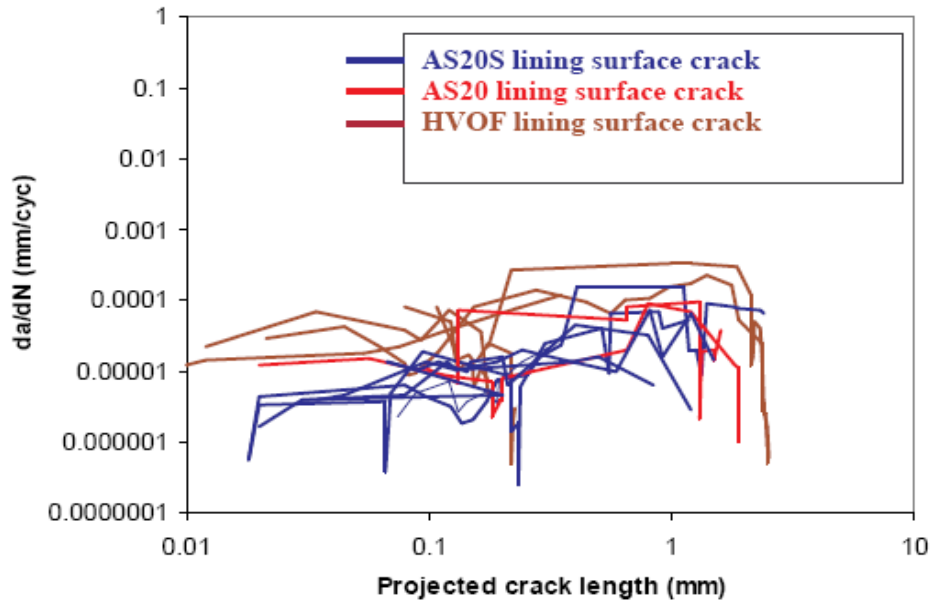


Figure 14. Crack growth rate measurements in [8].

Crack growth rate measurements of the tested architectures showed significant scatter. This scatter was most notable in the architectures MAS-20 and MAS-20S, which share the same lining alloy. The crack growth observed in the latter architecture suggested that short crack fatigue growth could be occurring; a condition that was consistent with the size of the assessed cracks.

Numerical simulations based on the MAS-20S architecture are developed in this thesis. Therefore, previous work concerned with the material characterisation of this architecture was essential. This characterisation involved the assessment of mechanical properties and microstructural features. True-stress true-strain curves, shown in Figure 15 were obtained for every layer through monotonic tensile tests with specially prepared single-layer specimens [10]. The relative stiffness and strength of the layer materials is shown in Table 3.

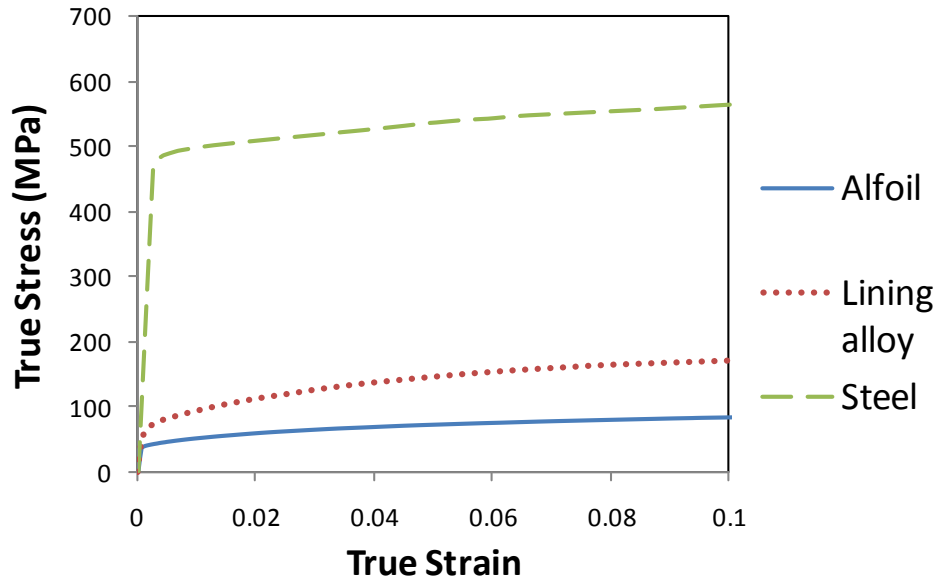
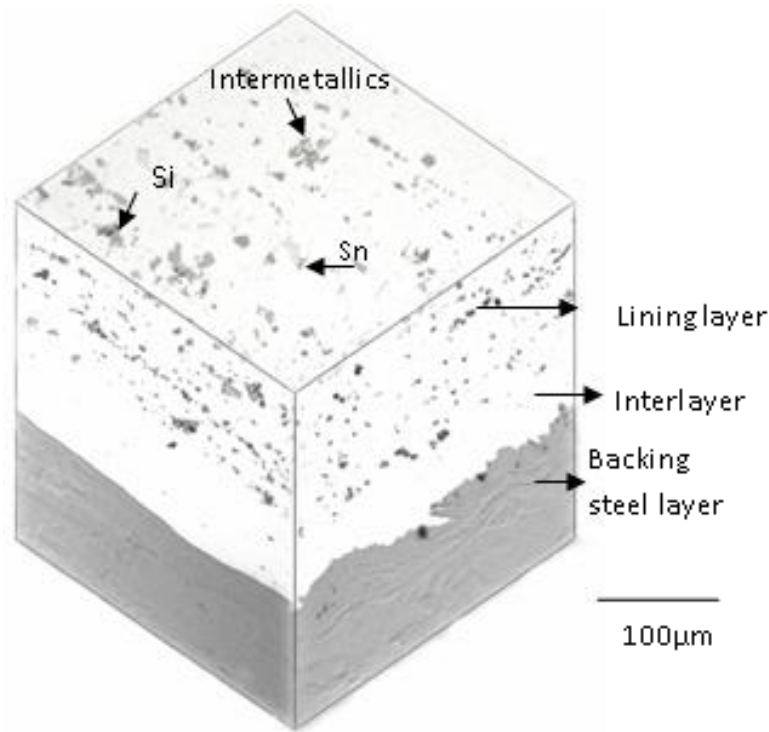


Figure 15. True stress-true strain curves for the three-point bending model.

The investigations on the MAS-20S microstructure, which is shown in Figure 16, were mainly focused on the lining of this architecture due to the location of crack initiation processes. Electron backscattering diffraction on the lining material revealed a typical grain size of  $9 \pm 1.5 \mu\text{m}$  and that mainly three types of secondary particles were found within the alloy: Si, Sn and hard intermetallic particles ( $\text{CuAl}_2$  and  $\text{NiAl}$  or  $\text{NiAl}_3$ ). These second phase particles had a sparse distribution and wide particle size range. The medium-carbon steel, used for the backing, was formed by elongated ferrite grains and pearlite regions in the direction of rolling.

Table 3. Elastic mechanical properties of MAS-20S [7].

	Material description	Yield stress	Young Modulus	Poisson Ratio
Lining	Aluminium alloy	53 MPa	70 GPa	0.33
Interlayer	Pure aluminium	37 MPa	67 GPa	0.33
Backing	Medium-carbon steel alloy	459 MPa	198 GPa	0.3



**Figure 16. Three dimensional optical micrographs of MAS-20S [7].**

Finite body tessellation analyses on a 2 mm area provided statistical information on the object area and mean near neighbouring distance (as defined in [61]) for the second phase particles. Hard intermetallics appeared to be the most abundant second phase particle closely followed by Sn. The number of particles found, object area and mean near neighbouring distance are presented in Table 4; more detailed information can be found in [10].

Additional work related to the second phase particles [10] involved nano-hardness tests using a calibrated diamond probe (Berkovich indenter) to obtain relevant mechanical properties. This study showed a great variability on the taken measurements and such variability was attributed to uncertainty of boundary conditions under which the second phase particle is deformed. These estimations showed very similar values for stiffness between intermetallics and Si particles while Sn showed lower values. According to the number of particles and their hardness, it appears that the intermetallics are the most influential second phase particle in the lining of the MAS-20S

architecture. Studies on crack initiation showed that such particles appear as preferential sites for such a phenomenon in the MAS-20S architecture. On the other hand, the existence of such particles may lead to drops in local crack growth due to their higher stiffness and work as effective microstructural barriers.

**Table 4. Finite body tessellation analysis of the MAS-20S lining [7].**

Particle	Number of particles	Object area ( $\mu\text{m}^2$ )	Mean near neighbouring distance	Estimated Young modulus from Nano-hardness (GPa)
Sn	356	27.55±21.85	30.29±15.32	78±26
Si	98	14.71±14.21	43.88±16.47	109±41
Intermetallics	501	26.05±16.64	28.88±12.63	117±25

### **1.5. ANSYS FEM software**

ANSYS Multiphysics software is a comprehensive coupled physics tool combining structural, thermal, computational fluid dynamics, acoustic and electromagnetic simulation capabilities in a single engineering software solution. This research project has only worked with ANSYS structural simulation capabilities to study the crack's surrounding material and its mechanical response.

ANSYS simulations consist of three main steps: pre-processing, solution and post-processing. Pre-processing operations are focused on specifying component information (such as geometry, materials), discretising component volume or volumes into smaller elements and applying loading conditions (displacement constraints and forces). The solution step creates a stiffness matrix, inverts this matrix and multiplies it by the force vector to obtain the displacement vector [64]. Post-processing operations yield values for relevant parameters such as deformation, stress and strain.

ANSYS can be operated using a graphical user interface (GUI) or in a command-based manner. Command-based modelling offers small file storage, parametric modelling to facilitate the development of design of experiments (DoE) and faster solution times when used in batch mode (only results files are stored and preprocessing files including the mesh are deleted). On the other hand, command-based modelling requires a deeper understanding of the software processes and the creation of initial models is time consuming.

ANSYS Programming Design Language (APDL) is a tool that enhances its modelling capabilities. Arithmetical operations and data storage using this tool facilitate geometry creation, load application and crack tip positioning. The main disadvantage of APDL is its computation speed and command limitation. More powerful programming packages such as MATLAB provide more commands and speed up some post-processing operations. Linking MATLAB and ANSYS is a sound option when post-processing operations become complex or computationally expensive.

## **1.6. Summary**

Layered architectures aimed to withstand cyclic deformation allow the combination of different material properties and present a new range of possibilities; especially nowadays where mechanical, thermal and conductance properties are integrated to create new products. Plain journal bearings, compressor buckets, drawing tools, pipes and even coins have benefited from these architectures.

The use of a damage tolerance approach assessing fatigue life provides a better understanding of failure processes through the evolution of CDF parameters. In contrast to total life approaches, the evolution of crack growth can be assessed identifying critical stages along the process. The estimation of the crack driving force gives a measure of the possible crack growth and, as a result, a better understanding and insight of the immediate consequences. Crack driving force parameters such as the CTOD and  $J$  integral have been applied successfully to problems subjected to LSY.

Because of its suitability to study fatigue problems and simple numerical implementation, the CTOD appears to be a sound option for relating the near-tip material conditions to crack growth rate.

The development of FE analyses in the context of the damage tolerant approach has assessed complex problems through sophisticated models. Relevant implementation issues of FE analyses must be considered; such as specialised crack tip meshes and crack extension tracking.

The current project aims to contribute to a better understanding of how cracks propagate in multi-layered systems formed of ductile materials. Phenomena such as shielding, multi-crack interaction and large scale deformations will be analysed to understand their impact on the crack driving force and effects on the crack path estimation, which in essence control the crack growth rate. These phenomena have been widely studied under small scale yielding conditions; however their influence on the path estimation and crack driving force under LSY and cyclic loading are issues where further contributions can be made. The following chapters deal with these topics through 2D and 3D analyses. A more detailed literature review on these specific topics is provided in the relevant chapters.

## 2. Chapter Two: Shielding effects on straight cracks

### 2.1. Introduction

The objective of the work developed in this chapter is the assessment of CTOD for straight through-width cracks of variable length as the crack tip approaches a stiffer or more compliant layer in bi-layer and tri-layer architectures under three-point bending loading. The applied load was varied to cause different extents of plasticity in the analysed material system. Conditions around the crack tip that may cause path deflection or bifurcation were also investigated here. The 2D analyses developed in this Section do not represent accurately the stress conditions that arise in the growth of a quasi semi-elliptical surface crack under three-point bending. However, such simplified models may resemble to the stress conditions and shielding effects experienced at the deepest point of a long transverse crack when a longitudinal cross section is analysed. This simplification allows the study of the aforementioned factors and their impact on the crack driving force at lower computational costs and higher levels of loading promoting greater extents of plasticity, with crack tips at short distances from the layers' interface

### 2.2. Background

The rise and drop of growth rates due to the mechanical properties mismatch in front of the crack path has been the subject of many studies. This mismatch may take place due to the presence of second phase particles or layers, as in the present case. These perturbations of crack growth behaviour are often labelled as crack shielding or anti-shielding. Pioneering studies by Suresh and co-workers [65-67] investigated shielding and anti-shielding effects on the crack growth rate in plastically mismatched layers when the crack tip approaches a stiffer or more compliant layer, respectively, using the  $J$  integral as CDF. Experimental and numerical studies by Joyce *et al* [7] in

three-layer architectures also used the  $J$  integral in a parametric study evaluating the influence of layer thickness and yield strength on the CDF and its consequent shielding trends. Joyce *et al* thus found that a thick and stiff interlayer would result in enhanced shielding effect that may lead to longer fatigue life, as observed in Al-Sn and bronze bearing systems. Shielding effects caused by the mismatch of mechanical properties were also shown to affect the crack path despite the application of far-field pure mode I loading conditions. Crack path instabilities such as crack deflection and bifurcation have been observed in brittle [68] and ductile materials [7, 69] when shielding occurs; nevertheless stable paths have also been observed [70] in architectures consisting of ductile materials.

Pippan and Riemelmoser [71] developed a theoretical model for bi-layer architectures with plastic mismatch only to study the CTOD evolution as the crack tip approaches the interface through analyses based on the Dugdale model. Pippan and Riemelmoser also extended their analyses to cyclic loading and concluded that as the ratio between cyclic amplitude CTOD ( $CTOD_{max} - CTOD_{min}$ ) and maximum CTOD is increased, crack closure could increase as well leading to greater shielding.

However theoretical work has provided essential foundations of modern methodologies that have extended the reach of fracture mechanics to more complex situations, the application of damage tolerance approaches to engineering applications cannot always be based on direct implementation of analyses that provide closed-form solutions for infinite bodies, based on homogeneous and elastic materials. Tailor-made materials with functional gradients or layered architectures provide excellent performance for specialised applications at the cost of using sophisticated analyses to assure the component reliability. Numerical tools have become indispensable in such assessments and propelled the implementation of damage tolerance approaches.

The Finite Element Method is based on approximations by polynomial functions that cannot represent the singular stress field behaviour predicted by the Fracture Mechanics with

conventional element formulations. Henshell & Shaw [72] and Barsoum [73], independently, developed quarter-point elements that could be used in spider-web arrangements to characterise the stress field singularity  $r^{-1/2}$  within LEFM, shown in Figure 17. However, such elements have shown very limited application to LSY problems [23] since as plasticity occurs stress and strain values are overestimated. Barsoum [73] also worked with collapsed second order elements which show a strain singularity  $r^{-1}$  observed in fully-plastic analysis (quadrilateral element collapse into a triangular shape leaving its mid-side nodes in their original positions). Collapsed 8-noded elements, and their 3D counterpart 20-noded bricks, are well suited to analyse fully-plastic and elasto-plastic analyses, especially when small deformations are analysed (i.e. strains below 0.1).

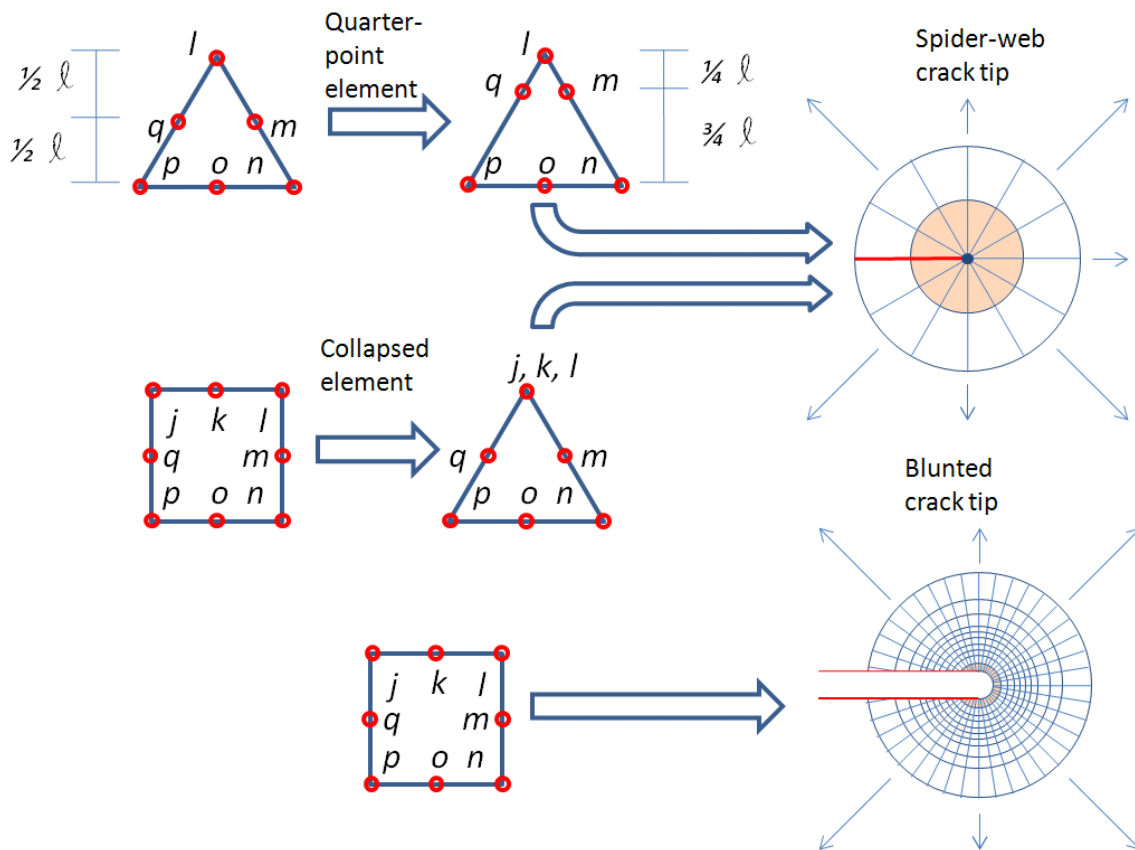


Figure 17. Spider web and blunted crack tip configuration.

The analysis of finite strains usually requires a more refined crack mesh that assumes that the crack is already blunted as observed experimentally [30, 74, 75] and allows a more precise stress

and strain estimation. Crack tip blunting is consistently observed in LSY problems and FE meshes including an initial small radius at the crack tip are a sound option for simulating such problems. Unfortunately, no commercial or in-house software known to the author exists to develop such crack tip meshes in FE models. This is in contrast to spider-web configurations which are available in specialised packages such as WARP3D, FEACrack and FRANC2D. McMeeking [45] used blunted meshes in his work and recommended that the final size of the blunted crack radius to be five times greater than that of the initial profile to prevent size dependency of the results. Anderson [23] suggests using 1 element every  $15^\circ$  for spider-web tips and at least every  $9^\circ$  for blunted tips.

### **2.3. Model and methods**

The tri-layer architecture MAS-20S described in Section 1.4.5 was analysed here. The test arrangement is schematically drawn in Figure 18. The specimen consisted of a backing steel layer of thickness  $t_b = 1.80$  mm, a lining aluminium alloy layer of thickness  $t_{L1} = 0.38$  mm and an aluminium foil interlayer of thickness  $t_i = 0.04$  mm. The bi-layer model was a hypothetical one, consisting of the same backing layer as that of the tri-layer model and an aluminium alloy lining layer of thickness  $t_{L2} = t_{L1} + t_i = 0.42$  mm. The strip had a width  $w = 19.5$  mm and length between supports  $L = 40$  mm. Two-dimensional models assuming plane-strain conditions were developed and solved in ANSYS 11.0 (using the Sparse Direct Solver) using second order elements and a multi-linear isotropic hardening material model (the implemented routines are shown in Appendix C). Current CDF estimations were obtained through monotonic loading simulations assuming that such estimations were representative of the trends and results obtained for cyclic loading, as assumed in previous work [7]. Kinematic hardening models, which include the Bauschinger effect, are more appropriate in simulating cyclic loading. However, such material models in ANSYS have proven to be unsuitable for large deformations [55]. Isotropic hardening models implemented in ANSYS have shown to be better suited for the extent of anticipated

plasticity in this problem and, theoretically, the impact of using any material model is greatest when unloading cycles are simulated. The compliance matrix is re-calculated at each iteration in non-linear solution processes accounting for the effect of large deformations developed in the simulations.

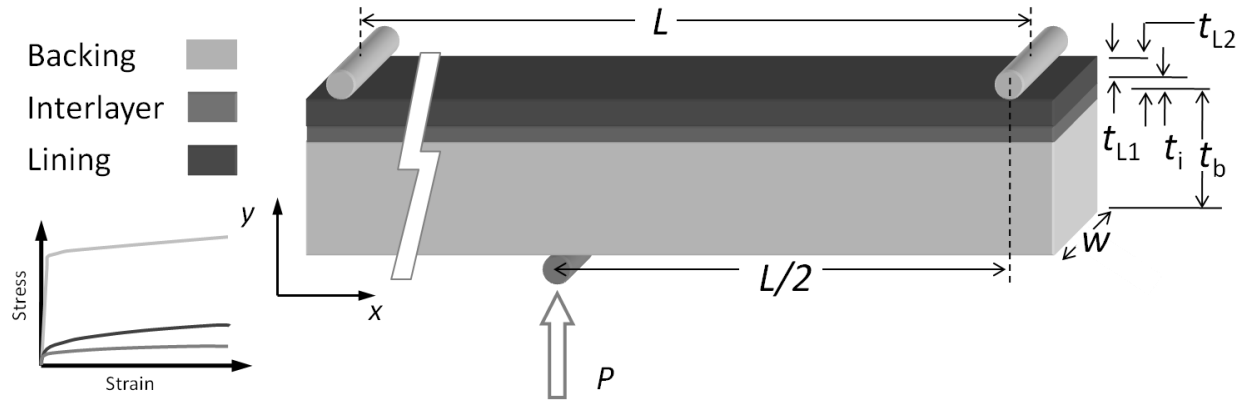


Figure 18. Three-point bending and test specimen configuration.

Based on experimental observations as well as preliminary numerical tests, LSY conditions were dominant at the higher range of the applied loads; therefore, the mechanical properties of each layer material are entered in the form of the true stress-strain curves, shown in Figure 15. The material characterisation of each layer material was carried out through monotonic tensile tests with specially prepared single-layer specimens corresponding to the materials of the architecture MAS-20S, as described in Section 1.4.5. The relative stiffness and strength of the layer materials is shown in Table 5 with respect to the lining alloy properties.

Spider-web and blunted crack tip models using elastic material models were initially developed here to assess the validity of each methodology. Blunted crack tip configurations have not been used widely in elastic analysis, which seems logical due to its greater computational expense when compared to quarter-point elements in spider-web configurations that model efficiently the stress singularity observed at the crack tip. Nevertheless, blunted crack tip configurations provide a more

detailed description of stresses and strains around the crack tip and appear as a sensible choice when large deformations and blunted crack tips are observed experimentally.

**Table 5. Ratios between elastic & plastic mechanical properties.**

Layer	Material description	Yield stress ratio	Young Modulus ratio
Lining	Aluminium alloy	1 (57/57)	1 (70/70)
Interlayer	Pure aluminium	0.66 (37/57)	0.96 (67/70)
Backing	Medium-carbon steel alloy	8.05 (459/57)	2.82 (198/70)

Empirical solutions for  $K_I$  from common specimen geometries and loading are available in British [76] and American [77] standards. The approximate solution to estimate the  $K_I$  for an edge crack in a beam under three-point bending is given by

$$K_I = \frac{M}{BW^{3/2}} \frac{6 \sqrt{2 \tan\left(\frac{\pi a}{2W}\right)}}{\cos\left(\frac{\pi a}{2W}\right)} \left[ 0.923 + 0.199 \left\{ 1 - \sin\left(\frac{\pi a}{2W}\right) \right\}^4 \right] \quad (12)$$

where  $M$  is the applied moment,  $B$  the specimen width,  $W$  the thickness and  $a$  the crack length.

Spider-web and blunted tip configurations were created in a flat strip specimen subjected to three-point bending, as shown in Figure 18, assuming a single material across the thickness for the analysis to be consistent with the approximate solution. The results from the two models were compared at different crack lengths, in a range from  $0.1 t_{L1}$  to  $0.97 t_{L1}$  in  $0.03 t_{L1}$  intervals, comparing the computed values of  $K$  against the solution given by Eq. ( 12 ) found in fracture testing standards. The stress intensity factor is plotted against the crack length in Figure 19. The difference between analytical and spider-web  $K$  estimations was difficult to distinguish, while models with blunted crack tip configurations overestimated the  $K$  values by between 1.5 % and 3.5 %.

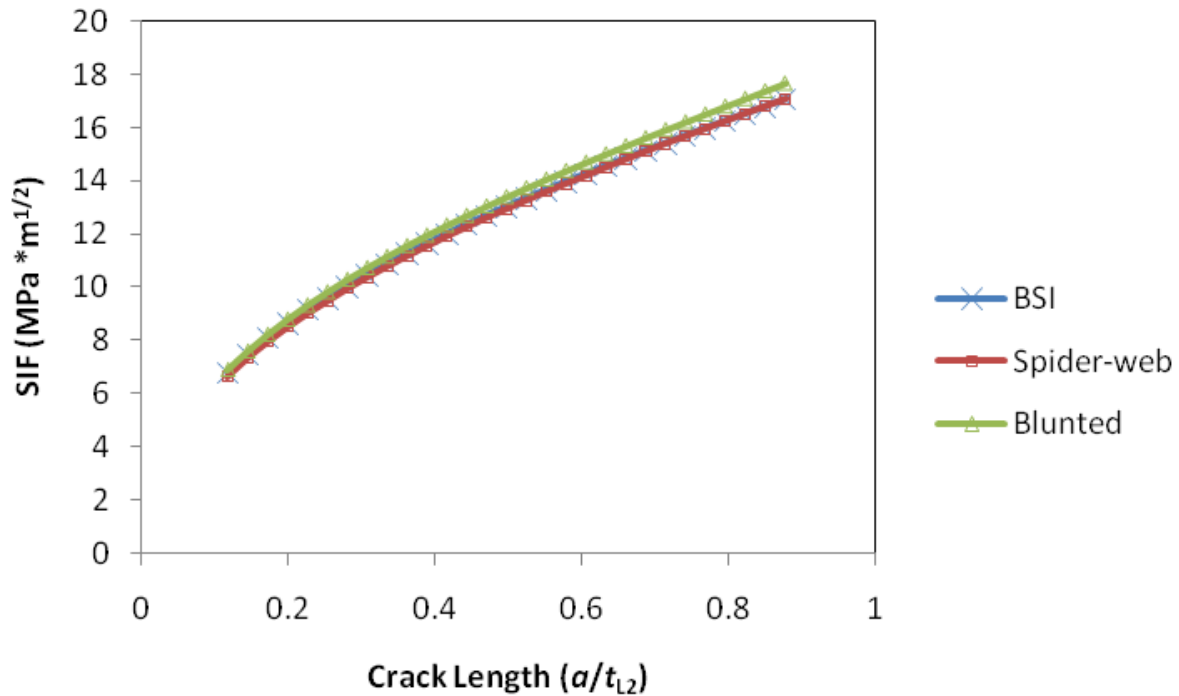


Figure 19. Estimated  $K_s$  from British Standards, spider-web and blunted crack tip models.

The use of elasto-plastic material models to test the suitability of both crack tip configurations showed that spider-web crack tip profiles produce poor-shaped elements in a mesh size that would allow the study of cracks located at  $0.01 t_{L2}$  from the interface. Excessive element deformation occurred as crack opening increases and crack tip elements are reduced in size to fit the crack tip as close as possible to the layers interface, especially in the interlayer where preliminary analyses showed crack openings of  $0.25t_i$  and bifurcation was expected to occur. Blunted crack tips, shown in Figure 20, were computationally more expensive, but can be modelled to fit narrow spaces closer to interfaces and study in greater detail stresses and strains around blunted crack tips. The typical radius size was set to 120 nm with an element size of 10 nm. Relevant stress and displacement values were read relative to a local polar frame of reference with origin at the centre of the semi-circle.

The developed numerical analyses are based on the assumption of homogeneous materials for all the architecture layers. It should be noted that element and blunted crack tip sizes, which show a

similar size to typical microstructural features found in the lining of the architecture MAS-20S. The generation of such refined meshes is not aimed at accounting for heterogeneous mechanical properties of each individual layer, but at the modelling of extensive plasticity and the positioning of crack tips at small distances from the layers' interface.

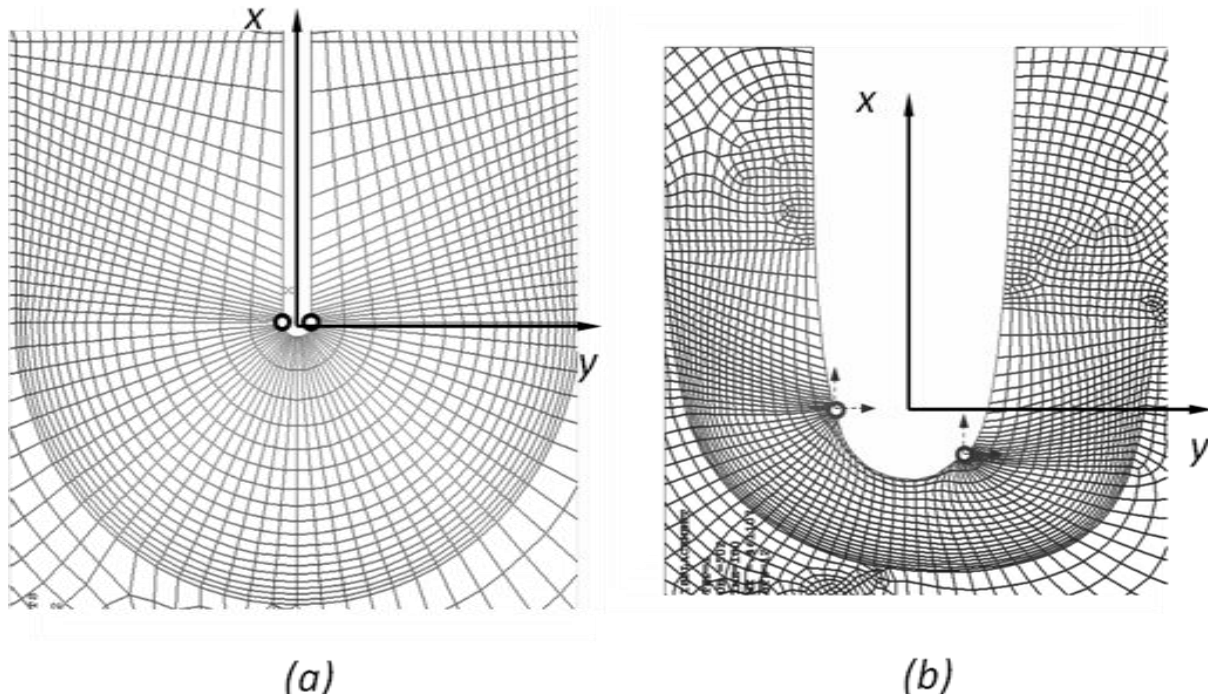


Figure 20. Finite element model of blunted crack before (a) and after deformation.

## 2.4. Results

The predicted plastic zones that developed in multi-layer architectures showed characteristic patterns associated with shielding and anti-shielding. The von Mises plastic strains, when the crack propagates towards a more compliant layer, were strongly discontinuous across the interface and reached greater values in the interlayer despite being at greater distance from the crack tip as shown in Figure 21. Figure 22 shows the opposite trend, where the stiff steel backing limited the size of the plastic zone surrounding the crack tip leading to greater constraint on the interlayer material.

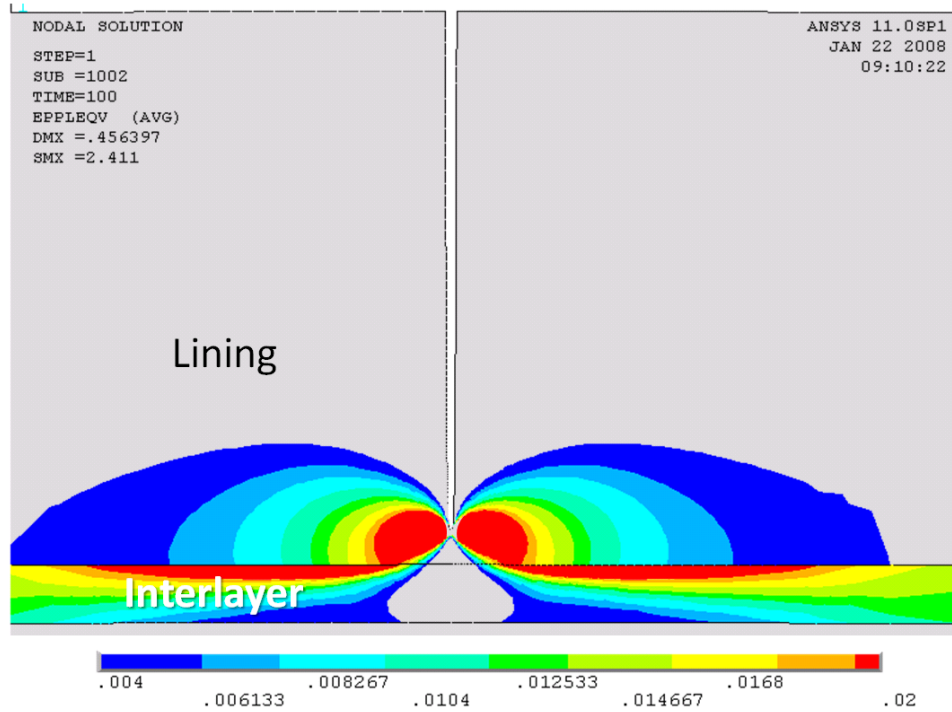


Figure 21. Von Mises plastic strain contour in tri-layer architecture at 800 N with the crack tip positioned in the lining (Anti-shielding case).

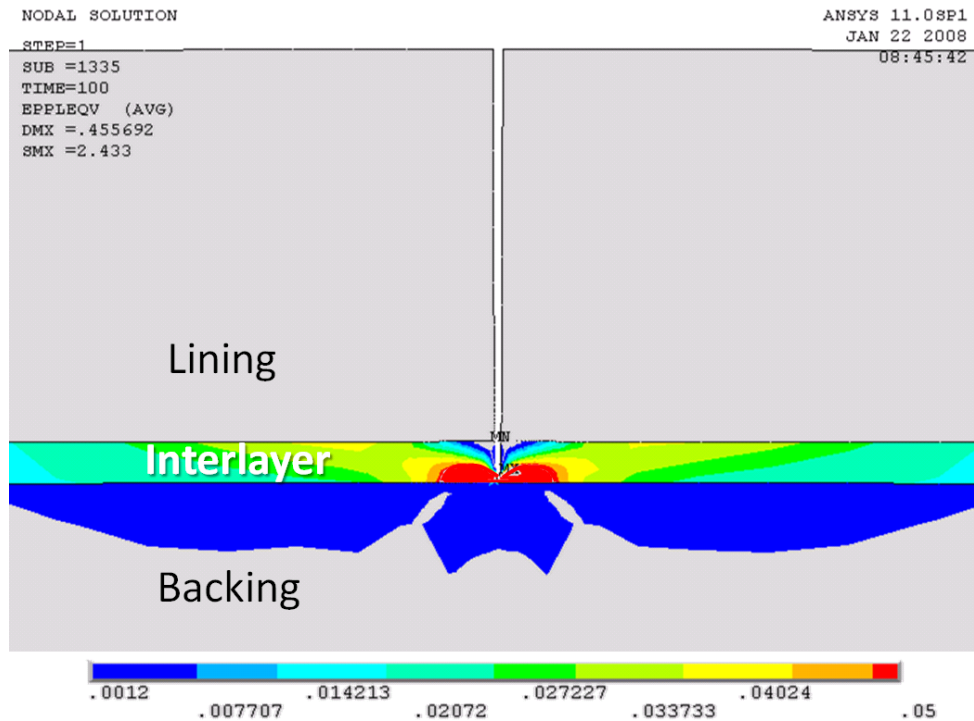


Figure 22. Von Mises plastic strain contour in tri-layer architecture at 800 N with the crack tip positioned in the interlayer (Shielding case).

The variation of CTOD with crack length in both the bi-layer and tri-layer system under 5 levels of loading is shown in Figure 23 and Figure 24, respectively. In this as well as all subsequent graphs, the CTOD results were plotted against the ratio of the crack length  $a$  to the lining thickness  $t_{L2}$  of the bi-layer system. The shielding and anti-shielding trends observed in Figure 23 and Figure 24 were consistent with those reported in similar previous investigations based on  $J$ -integral and stress intensity factor estimates of systems with principally plastic [65, 69] but also elastic [7] mismatch.

In the bi-layer architecture, the shielding effect was indicated by the decrease in CTOD as the crack approached the stiffer steel layer. In the tri-layer architecture, the anti-shielding effect is noted when the crack approached the more compliant interlayer, and the shielding effect when the crack approached the stiffer backing from the interlayer. The materials mismatch effect and crack tip proximity to the interface is shown by the CDF reduction: in the tri-layer, CDF drops by 37 % at  $P=800$  N, and in the bi-layer architecture, by 19 % at  $P=800$  N. The spread of plasticity into the backing layer of the bi-layer strip at the highest two load values reduced the mismatch between the layers and, as a consequence, shifted the maximum CTOD closer to the aluminium/steel interface.

Initial assessments of tendencies for crack deflection were performed in this chapter for the evaluation of straight path stability under pure mode I loading conditions. The maximum tangential strain (MTSN) criterion, proposed by Chang [78] was used for this purpose. Other crack deflection criteria and the validity of the MTSN are discussed in greater extent in Section 3.3. The implementation of this criterion was based on FE strain estimates around the blunted crack tip at intervals of  $5^\circ$ . More detailed information about the implementation of this criterion is also discussed in Section 3.3.

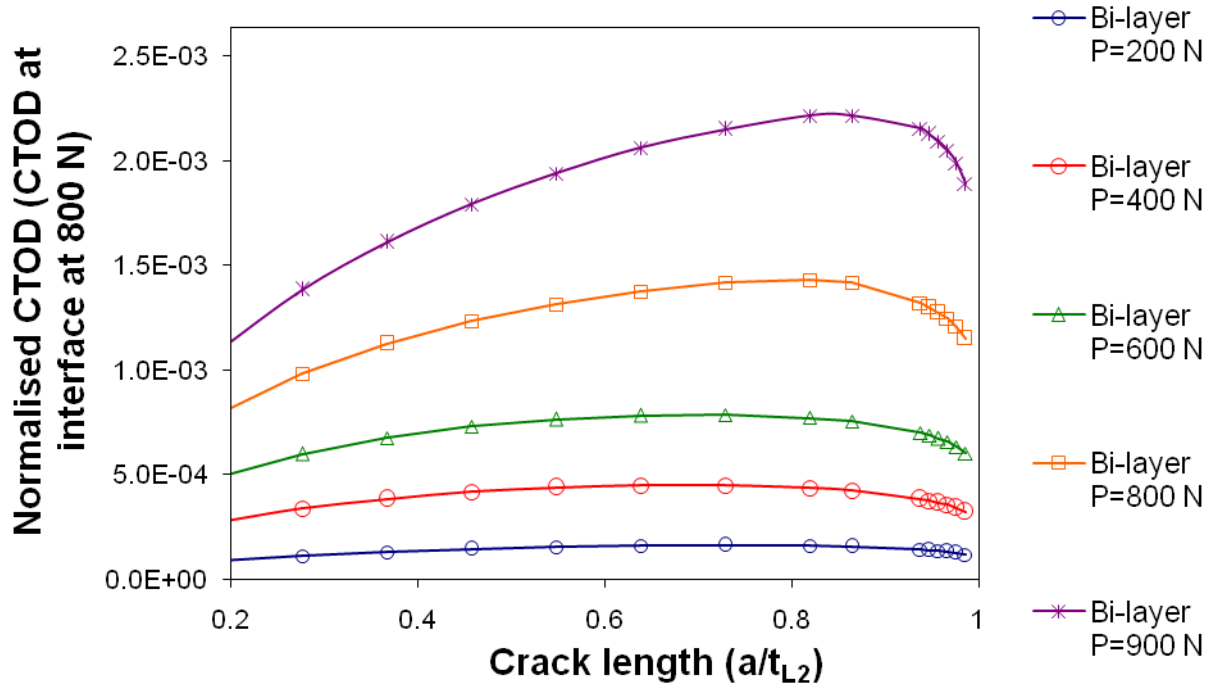


Figure 23. CTOD evolution with crack length in bi-layer system.

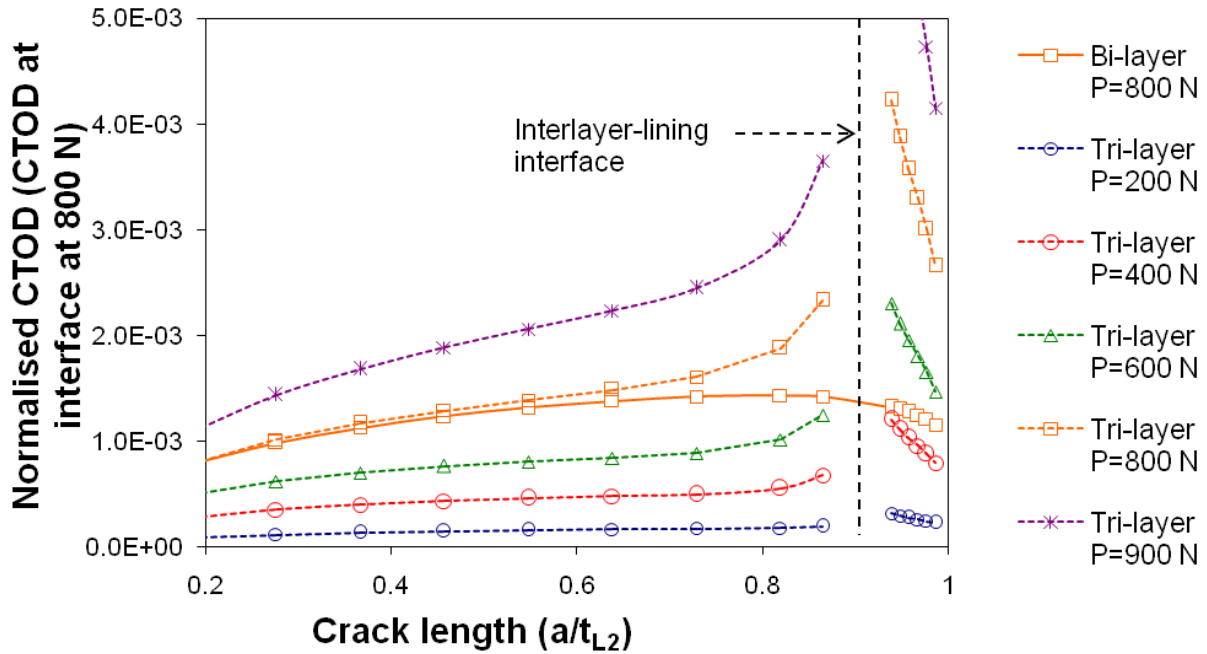


Figure 24. CTOD evolution with crack length in and tri-layer system.

The evaluated crack tip tangential strains (CTTS) showed different patterns depending on the applied load, crack length, layer in which the crack tip is located and architecture analysed. At crack

lengths below  $0.45t_{L2}$  and  $0.54 t_{L2}$  in the bi-layer and tri-layer strips, respectively, the CTTS had a clear maximum (MTSN) when plotted against the angular position around the blunted tip; this clearly indicated the normal to the interface as the preferred direction of propagation as observed experimentally. Greater crack lengths showed a steady reduction of curvature that caused a more difficult identification of the maximum value. This curvature reduction was observed to have greater intensity in the bi-layer architecture when the crack grew in the lining, as shown in Figure 25 with  $P=600$ . A less significant curvature reduction can be observed when the crack grows in the lining of a tri-layer architecture. This curvature reduction is visible, but the maximum value is clearly identified as shown in Figure 26.

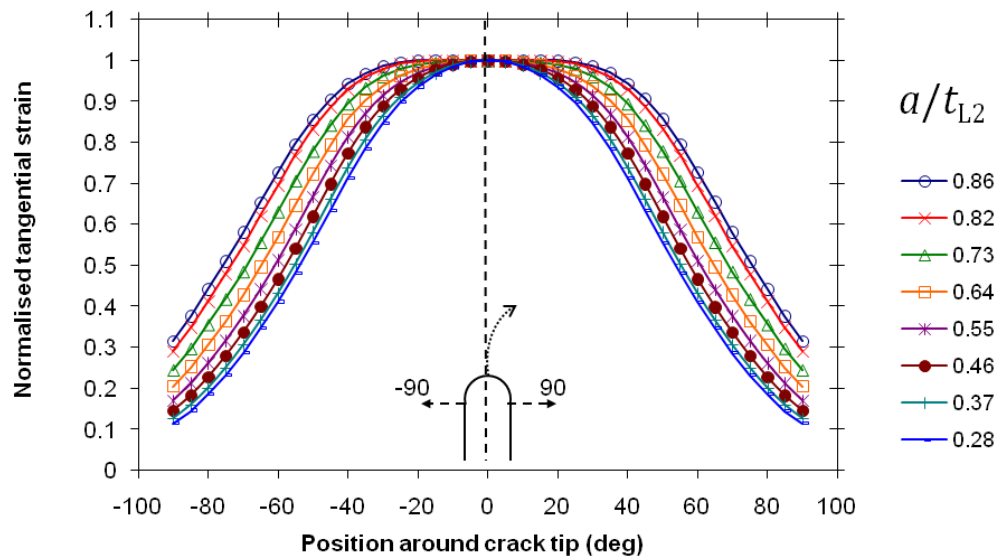


Figure 25. Tangential strain variation around the crack tip at 600 N in the bi-layer system lining.

Crack growth within the interlayer shows this phenomenon at its highest intensity due to the proximity to the stiff backing. As soon as the crack penetrates the interlayer the CTTS curves show a very significant curvature reduction that spread the maximum tangential strain into a range of values around the crack tip. Further crack growth produced a symmetrical profile where two maximum values can be observed away from the original direction, as shown in Figure 27 for a

$P=600$  N. As the load is increased, these symmetrically located peaks grow and their difference from the tangential strain obtained at  $0^\circ$  is increased.

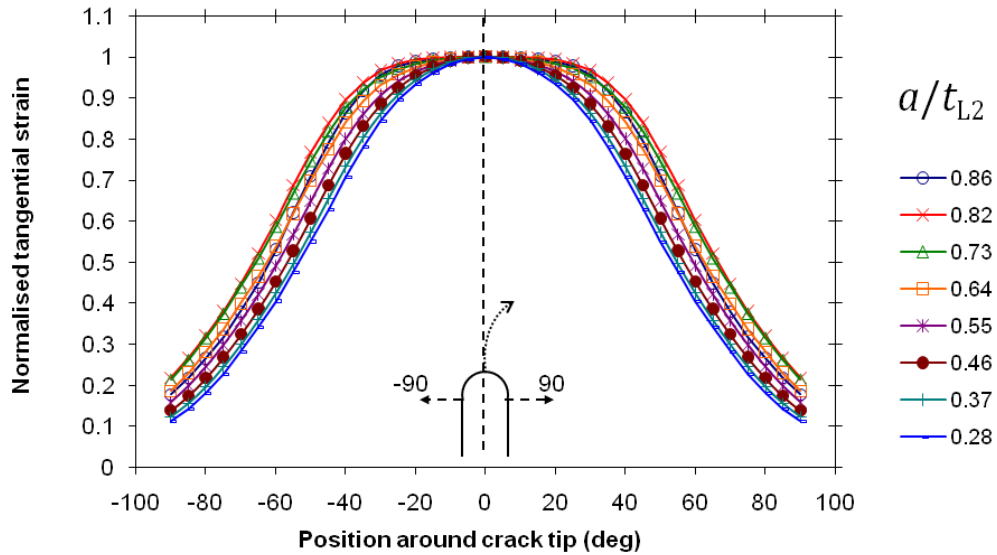


Figure 26. Tangential strain variation around the crack tip at 600 N in the tri-layer system lining.

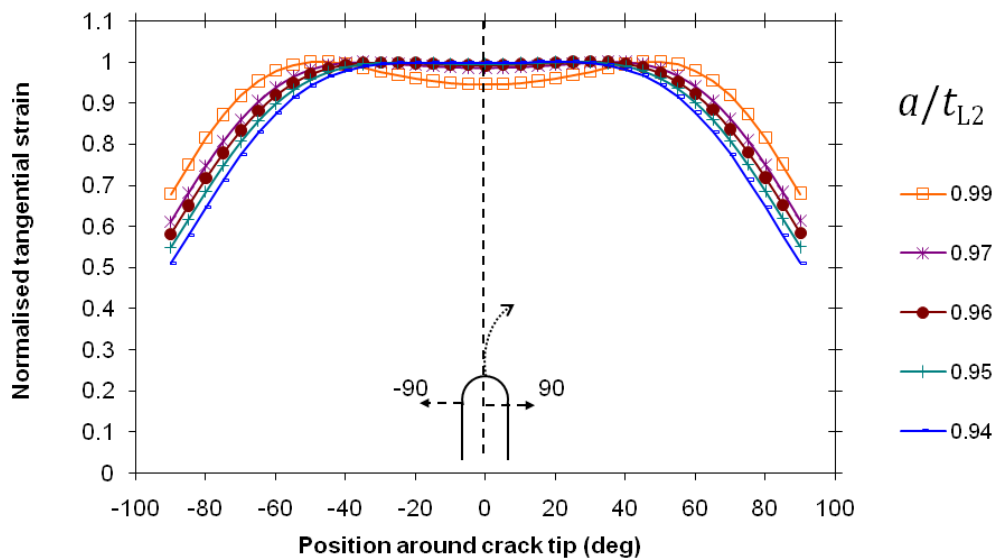


Figure 27. Tangential strain variation around the crack tip at 200 N in the tri-layer system interlayer.

## 2.5. Discussion

Mechanical property mismatches across layers led to the prediction of interesting trends in crack tip deformation, crack driving force evolution and potential for crack growth. Shielding and anti-

shielding effects in multi-layered architectures are shown to be influenced by the elasto-plastic properties of the materials involved. Elastic analyses may be representative of main shielding and anti-shielding trends at low loads. However, this behaviour is not scalable to service conditions near the proportional limit and above as demonstrated by the shift of the CDF maximum value in the analysed bi-layer architecture.

The CTOD as CDF parameter obtained from blunted tip meshes was shown to be well suited for investigating crack shielding and anti-shielding in multi-layered systems under LSY conditions. The results obtained with CTOD are consistent with those previously published [65-67, 79], based on a different CDF parameter. The CTTS results hint at possible crack deflection or bifurcation as the crack tip approaches a layer interface.

The maximum tangential strain, proposed by Chang [78] as the basis of a crack deflection criterion, is clearly identified for low crack lengths but as the crack approaches the stiffer and stronger backing layer, the existence and location of a maximum CTTS becomes less obvious. This was the first indication that the shielded crack may follow a deflected or bifurcated path. Bifurcation and deflection issues will be addressed in later chapters.

One of the limitations of this work in the fatigue context is the use of the CTOD at maximum load as CDF representation. However, nominal CDF values to explain shielding and anti shielding effects have also been used previously in the literature [7]. A more suitable measure of the crack tip conditions could be the  $\Delta$ CTOD, obtained from the maximum and minimum load case. Modelling attempts to incorporate the unloading process into the simulation were carried out; however, such attempts faced the fact that the extent of plasticity and recovery phase generate highly distorted elements that exceed the computational resources available. As an alternative, the CDF value at the minimum load could be estimated by applying a monotonic load. Efforts to include the minimum loading effect and obtain a  $\Delta$ CTOD estimate were carried out in further life estimation studies.

## **2.6. Summary**

Two-dimensional FE models that incorporate elasto-plastic hardening material models and blunted crack tip representations were implemented to evaluate the CDF as cracks grew approaching stiffer and stronger or more compliant layers and thus studied shielding and anti-shielding effects. These effects were shown through the CDF evolution as cracks approach stiffer and more compliant layers. At the same time von Mises plastic strain contours showed characteristic patterns where a stiffer layer limited the size of this region while more compliant ones extended it, especially in the direction perpendicular to crack growth. CTTS values may show a direction change potential as cracks approach a stiffer layer despite the application of far-field pure mode I loading. A clear CTTS maximum indicating a straight growth is estimated at small crack lengths in both architectures. However, as the crack approached a stiffer layer, the maximum CTTS value spread over a range of possible crack growth directions, hinting at the possibility of deflection or bifurcation.

## 3. Chapter Three: Deflected and bifurcated cracks

### 3.1. *Introduction*

The objective of the work described in this chapter is to gain a better understanding of deflection and bifurcation events observed in previous experimental work on the MAS-20S architecture, shown in Figure 12. To achieve this, two tasks were performed: the evaluation and selection of an appropriate deflection criterion for the analysed numerical models and the tracking of CDF evolution as the shielding and anti-shielding identified in the previous chapter developed. Events of both deflection and bifurcation were investigated here since it was difficult to confirm unequivocally that the observed paths were formed through one or another.

### 3.2. *Background*

The analysis of propagating cracks with deflected patterns has been of interest since the 1970s [80, 81] as observed in most engineering applications. Cotterell and Rice [82] studied the orientation effects of deflected kinks on  $K$  through an elastic analysis.

The implementation of FE analyses to growing cracks requires models that follow the CDF and path evolution. In order to do so, it is possible to create an adaptive model that evolves modifying the tip as the crack extends or generate a number of models, which do not share a common material discretisation, that analyse different stages of the crack propagation. In both cases, the models rely on post-processing standard FE results to determine the CDF and the direction of growth as cracks propagate.

### 3.2.1. Crack deflection criteria

One of the first approaches to predicting the crack path direction was proposed by Erdogan and Sih [83], who postulated the Maximum Tangential Stress or Opening Stress Criterion (MTS). According to this criterion, the crack would propagate in the direction associated with the greatest tangential stress  $\sigma_\theta$  relative to a polar co-ordinate system with origin at the tip of the crack, as shown in Figure 28.

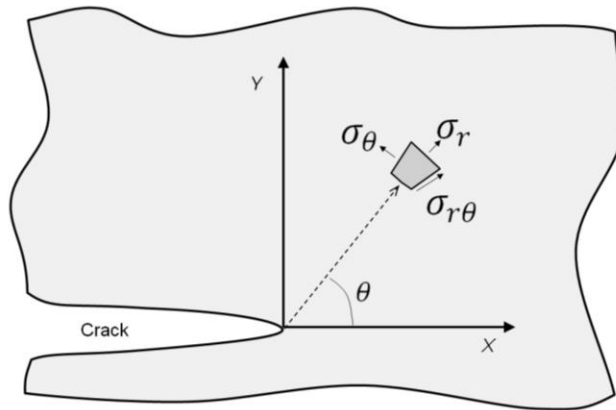


Figure 28. Cylindrical coordinate system placed at crack tip.

The most common application of this criterion uses the tangential stress closed-form solution in terms of the stress intensity factors:

$$\sigma_\theta = \frac{1}{\sqrt{2\pi}} \cos \frac{\theta}{2} \left( K_I \cos^2 \frac{\theta}{2} - \frac{3}{2} K_{II} \sin \theta \right) \quad (13)$$

to determine the tangential stress and the direction of the angle  $\theta$  that maximises this stress. An alternative criterion is the Maximum Crack Driving Force (MCDF), which can be considered as a general principle, since it can be applied with different crack driving force parameters. This principle states that the crack will propagate in the direction that maximises the crack driving force. It can be said that this criterion was formally introduced as the Maximum Energy Release Rate (MERR) by Hussain [84] and Palaniswamy and Knauss [85], independently, by assessing the influence of a small virtual extension on an existing crack over a range of possible deflection angles.

Its numerical application is not straightforward but rather time consuming since it requires model modifications and tests at each single sub step. Each model modification estimates the crack driving force for a crack extension in a particular direction and through direct comparison obtains the most suitable direction (This criterion was applied by Joyce *et al* [7] using the  $J$  integral)

The CTOD has also been used with this principle by Sutton [56] under elastic conditions correlating reasonably well with experimental results under static loading and small scale yielding. Sutton also stated that the material separation mechanism dictates whether the CTOD or crack tip sliding displacement (CTSD) should be used, extending its applicability to Mode II dominant conditions. Fracture toughness values for the CTOD and CTSD control which mechanism occurs in the material.

Ramulu and Kobayashi [86] evaluated the differences in the context of LEFM among the MTS, Minimum Strain Energy Density Criterion (MSED) and MCDF (MERR) and the various deflection angles predicted are plotted versus the ratio  $K_{II}/K_I$  in Figure 29. Three different Poisson's ratios were used with the MSED, showing agreement among the criteria when dominant opening separation modes are analysed.

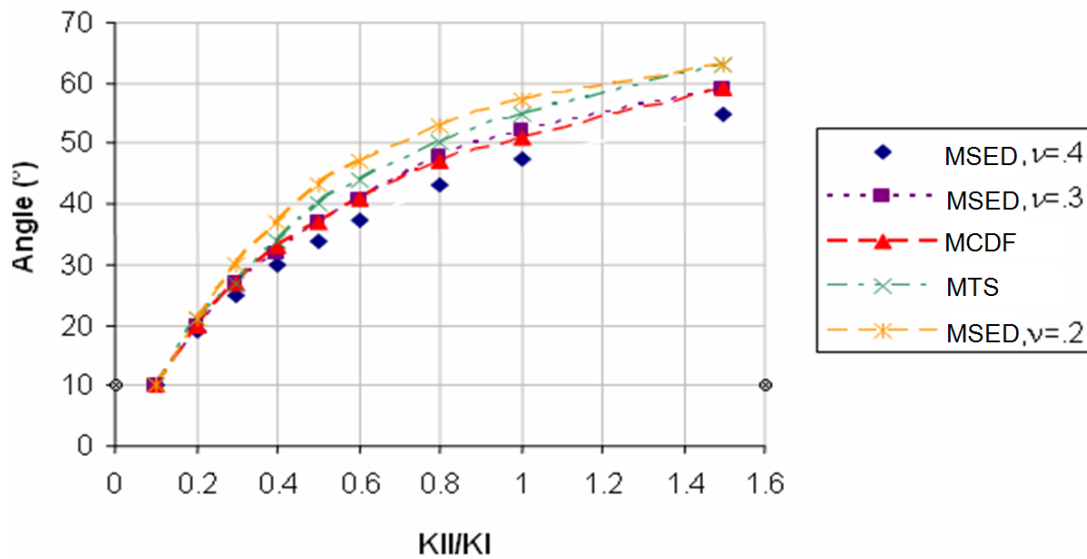


Figure 29. Estimations of path deflection according to  $K_{II} / K_I$  ratio [86].

The Maximum Tangential Strain (MTSN) criterion was introduced by Chang [78] based on similar principles to those adopted for the MTS. Due to its strain-based nature, the MTSN seems to be a more suitable option to estimate the crack deflection angle under LSY conditions. Strain measurements reflect more emphatically the state of the material under LSY conditions, since for a given load increment a greater sensitivity is observed in plastic strain than stress estimates. The MTS and MTSN were compared by Chambers [87] for stainless steel under cyclic loading, showing a minor difference at the beginning of the propagation under mixed mode conditions. Chambers also observed that crack deflection was aimed to reach an orientation where pure opening loading was experienced. Mageed and Pandey [88] also implemented the MTSN in aluminium plates with inclined cracks subjected to fatigue loading obtaining identical results to the estimations provided by the MTS.

### ***3.2.2. Bifurcated cracks in multi-layered architectures***

The occurrence of bifurcation has been often explained [89] in terms of material resistance and energy release rate. It is evident that no crack growth would occur when the material resistance is much greater than the energy release rate. In the opposite case, the material is incapable of dissipating that amount of energy through a single tip leading to bifurcation. The mismatches between energy release rate and material resistance can be traced to increments of energy release rate, through a sudden overload and associated CDF increment, or drops in the material resistance, similar to the crack growth from strong to weaker layers.

Bifurcation, along with other crack propagation mechanisms, has been observed to influence the evolution of the CDF and crack growth rate. Bifurcation has been widely investigated in brittle materials [68, 90-92], where these mechanisms appear more consistently. Various authors [93-95] have reported how the CDF in bifurcated cracks is reduced significantly and its dependence on the

bifurcation angle in elastic solids. Bifurcated cracks in multi-layered architectures composed of ductile materials have also been studied to a lesser extent [96].

Experimental and numerical studies by Joyce *et al* [7] in layered systems consisting of steel and aluminium alloy layers under three-point bending corroborated previous shielding and anti-shielding observations [66, 67] and reported that the bifurcation angle that yields the greatest CDF value increases as the crack tip approaches a stiffer layer. Jiang *et al* [70] studied experimentally plastically mismatched steels under four-point bending tests showing no signs of bifurcation or deflection as the crack tip approached a stiffer layer, suggesting that the existence of negative values of  $T$  stress was responsible for this effect. Hbaieb *et al* [68] studied bifurcation in ceramic multi-layered systems under four-point bending loading investigating the  $T$  stress, the energy maximisation principle and the interaction with other cracks to detect possible causes for bifurcation and path deflection. From their FE analyses they suggested that a spontaneous crack within the compliant layer was formed as the specimen was loaded, attracting the crack to a path parallel to the layers orientation. Criteria for brittle materials that determine the occurrence of crack bifurcation have been proposed by Ho *et al* [97] and extended by Lugovy *et al* [90] in multi-layered architectures based on loading, elastic material properties and layers thickness. Criteria involving ductile materials and the identification of the position of bifurcation have not been found in the literature.

The bifurcation or branching caused by overloads has also been studied due to its retarding effect on crack growth. Suresh [79] studied the effect of overloads on the crack path and observed that bifurcations may occur with the application of an overload; however, this bifurcated arrangement only remains for a few cycles since one of the branches shields the other's growth leading again to a single tip crack growth. Similarly, the occurrence of deflections due to the application of an

overload were observed by Katz et al [98] followed by the return to its original growth direction and speed as it separated from the application point of the overload.

### **3.2.3. Crack growth analysis using FE**

Previous numerical work studying crack propagation has used adaptive FE models through node release [99] or element erosion [100]. Node release and element erosion algorithms have been used extensively in fracture problems. These techniques, usually based on physical variables (strain, stress, energy, etc.) at a single point or node, have difficulties representing the whole material separation process. Its application to fatigue problems is limited to a reduced number of cycles if the physical variables are to be used to guide the propagation process. An extended number of cycles can be simulated by eroding or releasing at different crack lengths to estimate the CDF as the crack extends artificially since the application of this technique at each loading cycle leads to prohibitive computational costs. The main disadvantage of this process is the mesh dependency of such crack growth and path prediction. Prior knowledge of the crack path certainly helps to construct an adequate mesh that forces the crack to propagate along such a path, and obtain CDF estimations consistent with experimental observations. Numerical works based on previously known crack paths can be found in two [101] and three dimensions [102, 103].

The introduction of cohesive elements to different commercial packages provides a tool to extend cracks based on parameters that describe the material separation process more accurately, altering the local material compliance as appropriate according to a traction separation law [104]. Previous knowledge of the crack path also helps substantially this analysis implementation, since the global existence of such cohesive elements may modify the overall stiffness of the component when the operating conditions of the material are near to the proportional limit. Cohesive elements have been applied to a greater extent in fracture than to fatigue applications since only a few cycles can be fully simulated; however, the progression of damage around the crack tip can be assessed [105].

An alternative option is remeshing as the crack grows, based on the ability to create or successively modify efficient and reliable models. Across this literature review two different techniques have been noted: block shifting and non-structured remeshing. The block shifting technique [106] uses parametric element blocks that already contain the crack tip. This technique used by Zencrack (mesh generator created by Zentech [107]) has as evident advantages the reduced computational costs of its elements and transitions, its major drawbacks are the poor element shape before a block is shifted and poor adaptability to sudden crack path changes or irregular surface cracks. This method has proved to be extremely cost efficient for the  $J$  integral and stress intensity factor computation in elastic analyses.

Non-structured remeshing, as shown by Bittencourt [46], regenerates the elements around the crack tip to incorporate each crack extension, thus creating a new crack tip and allowing the meshing algorithm to generate an appropriate transition between the permanent elements. Development of meshing algorithms and software has facilitated this task considerably. Its major disadvantage is the compromise required between the number of elements to be remeshed and mesh quality. Very small remeshing areas usually create low quality elements to couple the new crack tip with the previously stored elements. As the remeshing area is increased, element-generation algorithms create elements with higher quality at a higher computational cost. In the long term, high quality elements are more desirable since the solution process, compared to the remeshing operations, requires more computational power according to preliminary numerical tests in this chapter.

The complexity involved in the analysis of extended cracks has led to the development of other areas such as X-FEM [108, 109] which allows the introduction and extension of discontinuities within the material without remeshing. This method adds degrees of freedom to introduce a discontinuity and as this discontinuity grows more degrees of freedom must be added. This method

has been applied successfully to complex out of plane crack simulations [110] and current research is being developed to link this method to commercial codes such as ABAQUS [111]. The application of this method so far appears focused on elastic and mildly plastic problems where stress fields are well known. The study of problems with singularities that have been studied to a lesser extent is also under development. At the same time, the existence of two discontinuities of differing kinds i.e., the crack and different material layers, has not been developed yet but is an interesting area where progress should be made.

### **3.3. Assessment of crack deflection criteria**

Mageed and Pandey [88] tested 2024-T3 aluminium plates, shown in Figure 30, under tension with centre cracks at various angles to the loading axis to study the initial direction of the deflected crack under the generated mixed-mode loading conditions. Plates with initially straight 9-mm cracks at inclination angles of 30°, 45°, 60 and 75°, measured from the axis normal to the loading direction, were tested under a cyclic tension ranging between 18 and 92.5 MPa. The specimen thickness, length and width are 1.27 mm, 250 mm and 180 mm, respectively. The Young's modulus, Poisson's ratio, yield stress, ultimate stress and elongation to fracture of the material were reported to equal 73.1 GPa, 0.33, 370 MPa, 440 MPa and 11%, respectively. A true stress- strain curve that fitted these data was constructed and entered into the FE model.

Two-dimensional models of the reported specimens were built assuming plane stress conditions using blunted tip mesh configurations. Relevant stress and displacement values were read relative to a local polar frame of reference with origin at the centre of the blunted tip semi-circle

The crack deflection criteria tested were the maximum tangential stress (MTS) [81], maximum tangential strain (MTSN) [87], maximum principal stress (MPS) [112], maximum principal strain (MPSN) and crack tip displacement vector (CTDV) [113]. It should be noted that none of these criteria has shown a better performance for every loading scenario, including LSY and cyclic

loading. Rather than relying on  $K$  calculations, the implementation of MTS and MTSN in this study was based on nodal FE results obtained around the blunted crack tip. The MPS, MPSN and CTDV criteria were implemented in a similar manner. The required parameters for each criterion were estimated at  $5^\circ$  intervals around the blunted tip. The maximum stress or strain value and its angular position were obtained using a quadratic interpolation based on the greatest value of stress or strain found on the blunted tip nodes and the values corresponding to the adjacent nodes in each tangential direction around the blunted tip.

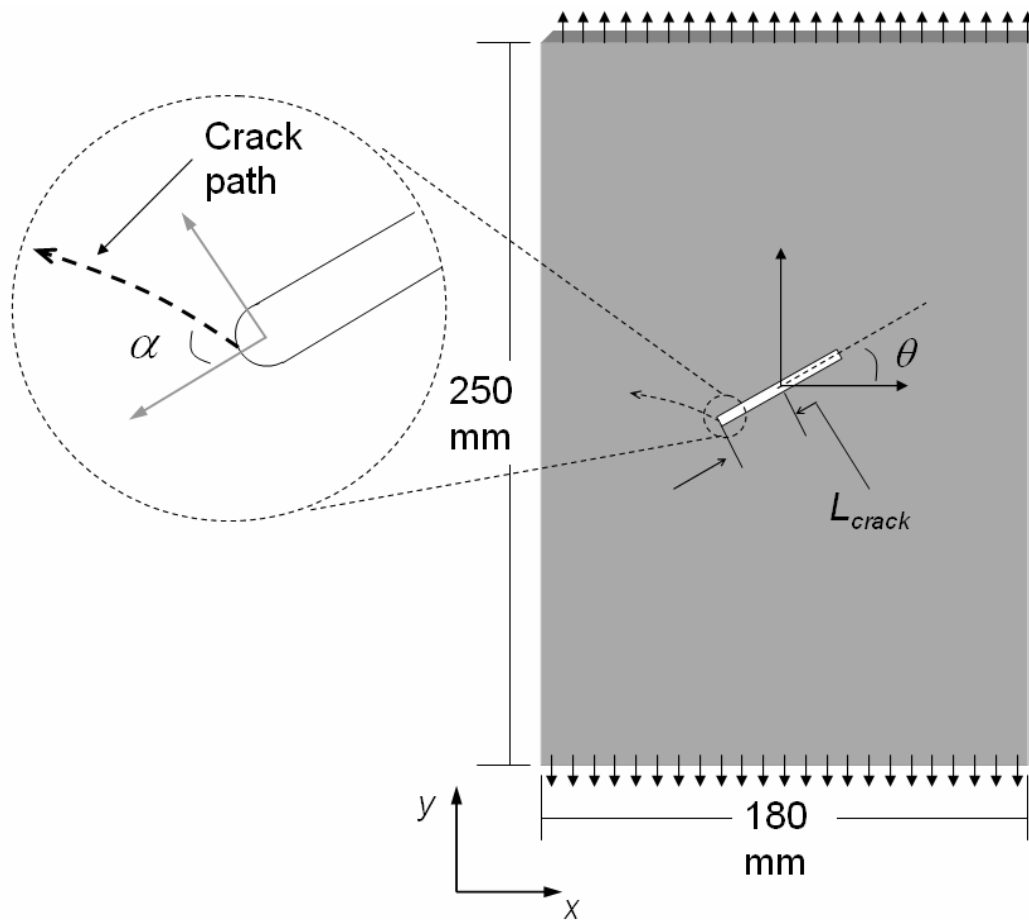


Figure 30. Test specimen used by Mageed and Pandey [88].

### 3.3.1. Results

The FE results are presented together with the experimental measurements in Figure 31 for the four inclination angles of the remote tensile stress of 92.5 MPa relative to the crack opening

direction. Estimations of the deflected direction of propagation by the CTDV, MTSN and MPSN criteria of an inclined crack at 30°, which corresponded to the most dominant mode-I loading conditions considered, were almost identical and consistent with the reported experimental result [88]. The agreement of MTSN and MPSN predictions with experimental results was slightly reduced with increasing inclination angles while those based on CTDV follow an opposite trend.

The MTS and MPS criteria appeared to underestimate initially the deflection angle but their predictions become more consistent with MTSN and MPSN as the inclination angle increases. The FE analyses also simulated the minimum applied tensile stress of 18 MPa and, in the case of MTSN, MPSN and CTDV, the respective deflection angle predictions were slightly greater (around 4%) than those obtained under maximum load. The MTS and MPS criteria showed an identical behaviour to their strain counterpart when the model is subjected to the minimum load. It is also noteworthy that the deflection estimates obtained from principal stress criteria (MPS) was identical to that of tangential stress criteria (MTS); condition which also appeared on strain based criteria (MTSN and MPSN)

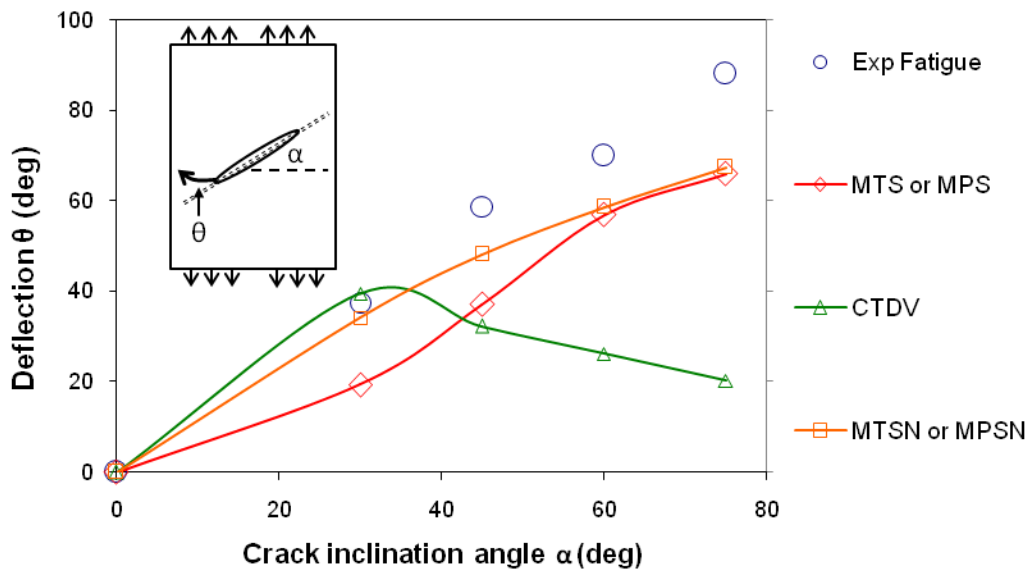


Figure 31. Crack deflection predictions with corresponding fatigue test result [88] at 92.5 MPa.

### 3.3.2. Discussion

Identical estimates of MPS and MTS led to further analysis of these criteria and it was found that the application of blunted tips at this particular level of loading led tangential stresses and strains to coincide with their respective principal values. A strain-based approach provided estimates of crack deflection angles more consistent with experimental evidence than those obtained using a stress-based criterion for this particular implementation. For this reason, the MTSN criterion would be used in subsequent stages of this study in order to estimate the crack path.

It was expected that crack propagation would occur along a direction bounded by the deflection angle estimates obtained at the maximum and minimum load. Since the difference between these two values is found to be small, the analyses per crack increment developed next were performed only under maximum load thus saving computational effort. The application of MTSN criterion was monitored in subsequent analysis so that it is limited to mode-I dominant, mixed-mode loading for which the crack deflection estimates are found to be most reliable by any of the assessed criteria as suggested by Ramulu and Kobayashi [86].

### 3.4. *Deflected cracks in multi-layer architectures*

The test specimen geometry, materials and FE analysis features were identical to the ones described in the previous chapter. The generation of previous FE models is carried out through a parametric design that adjusted the model mesh according to the predicted crack size and direction. In order to fulfil the objectives described in this chapter, a remeshing scheme was chosen to extend the crack according to the applied loading conditions and layered structure. The implementation of this scheme required the generation of a number of models, a time consuming task for any analyst. Therefore, the creation of algorithms to auto-regenerate this models and minimise the analyst effort as described by Wawrzynek [114] is desirable.

The created routine followed the structure described in Figure 32, creating short crack extensions along the predicted direction according to the near-tip stress state at the previous step; as described by Colombo and Giglio [115] for a remeshing scheme. The concatenation of short crack extensions forms the path along which the values of the crack driving force were obtained. The model generation for this analysis was carried out using the tools provided by ANSYS APDL (Ansys Parametric Design Language). The implemented routines are shown in Appendix C.

Most of the stages presented in Figure 32 are executed in a standard way for an FE analysis. The key parts of the modelling process are to establish an appropriate element size transition between the crack tip and the permanent elements, and the definition of a new crack tip that is able to merge with the crack path formed before. This task can be performed easily in an interactive way; however, for the user tasks to be eliminated from this process it is necessary to use the APDL and meshing tools to modify the mesh features as the crack grows.

### 3.4.1. Results

Deflected crack propagation was studied in both bi-layer and tri-layer architectures starting from straight flaws of a length equal to  $0.6 t_{L2}$  and  $0.92 t_{L2}$ , respectively. These cracks were again placed at the centre of the specimen surface as observed experimentally under three-point bending loading (see Figure 18). Two different load magnitudes,  $P = 200$  N and  $P = 800$  N, were applied corresponding to conditions of moderate and large-scale yielding.

Results from the tri-layer architecture indicated distinct trends of crack propagation in different layers. At both load levels, the crack growth direction within the lining remained unaffected as the crack tip approached the more compliant interlayer. CTOD increased with crack extension as previously observed with stationary straight cracks (see Figure 23). The curvature of the CTTS curves became slightly smaller as the tip approached the compliant interlayer, especially at high

loads. However, the maximum CTTS value (according to MTSN criterion) could still be identified as the one forecasting a straight crack path normal to the interface.

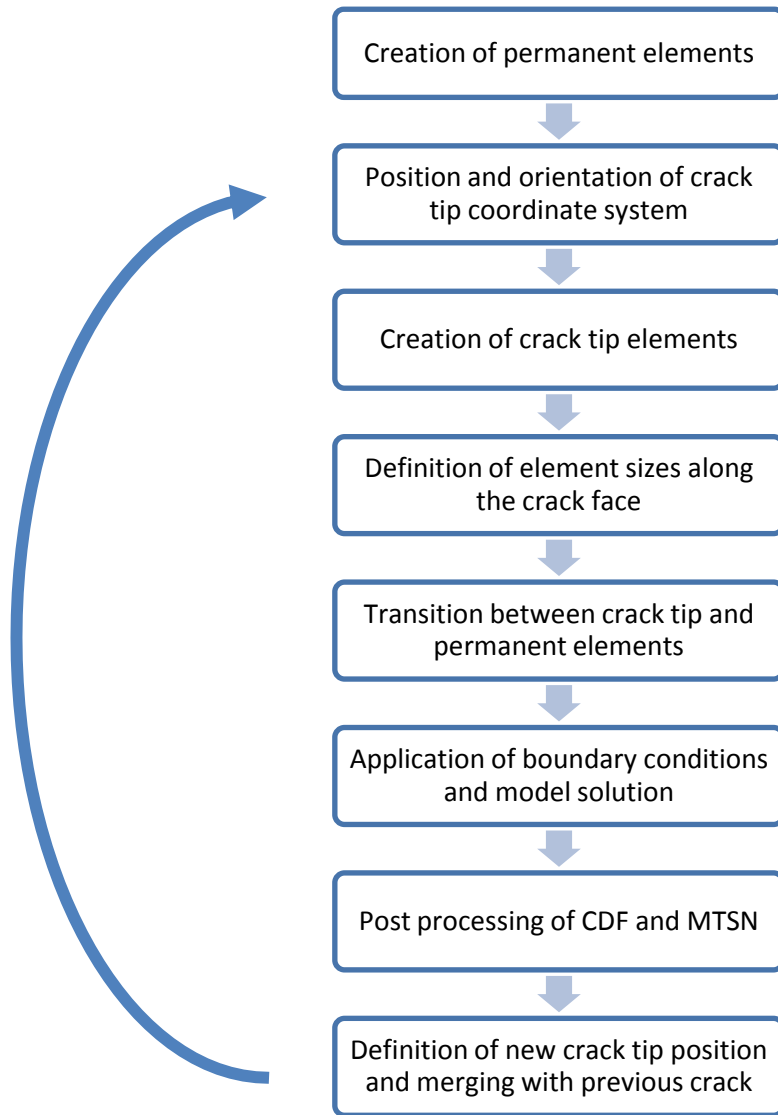


**Figure 32. Model generation methodology**

As soon as the tip penetrated into the interlayer, it was not possible to identify a single maximum along the obtained CTTS curves; the extent of this curve flattening depended on the applied load. This meant that almost identical CTTS values emerged symmetrically located with respect to the original direction of propagation corresponding to polar angle  $\alpha$ . Despite the small variation of CTTS within a wide range of polar angles, an MTSN value was numerically identified at  $\alpha = 16.4^\circ$ . It

was assumed that a small deviation from loading or geometric symmetry would cause the crack to deflect at this angle, which was thus used to define the orientation of the introduced short kink deflection with a value  $\alpha$  was adopted in the initial extension; smaller subsequent deflections are forecasted automatically, according to the crack deflection criterion, so that the crack path approached asymptotically the interlayer-backing interface as shown in Figure 33 according to the MTSN estimations. The CTTS variation along the blunted crack tip at various deflected crack extensions is plotted in Figure 35. It is interesting to notice that the MTSN becomes progressively more distinguishable and uniquely identifiable immediately after the first deflection.

The CTOD estimates obtained from the straight and deflected cracks as well as the accumulated deflection angle in the interlayer are presented in Figure 36 for  $P = 200$  N. This figure clearly shows that the predicted CDF was greatest along the deflected path; this was consistent with the principle of crack propagation in the direction of least resistance, corresponding to maximum CDF [84]. Similar path deflections in the interlayer were predicted by the analysis performed under  $P = 800$  N. Apart from the expected increase in CDF estimates, the main difference was a slightly more pronounced initial deflection, as shown in Figure 34.

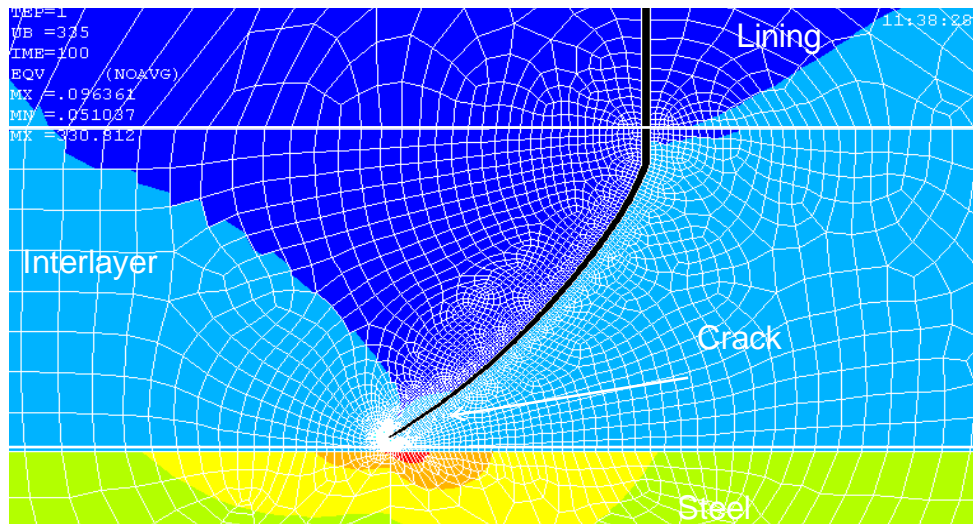
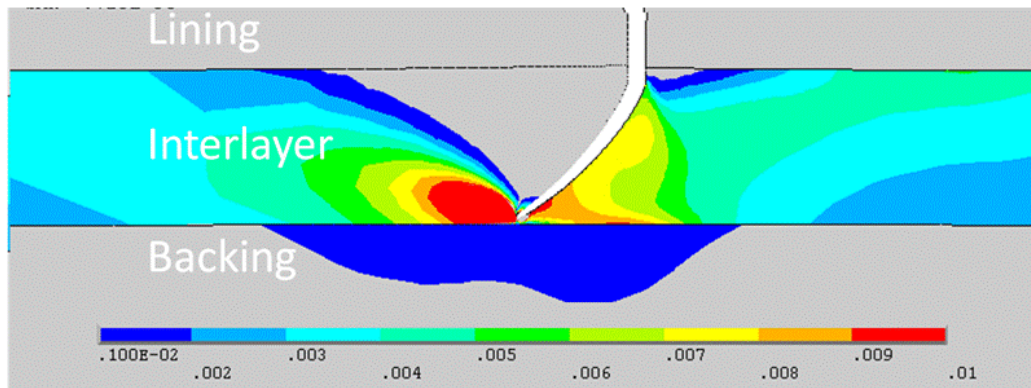
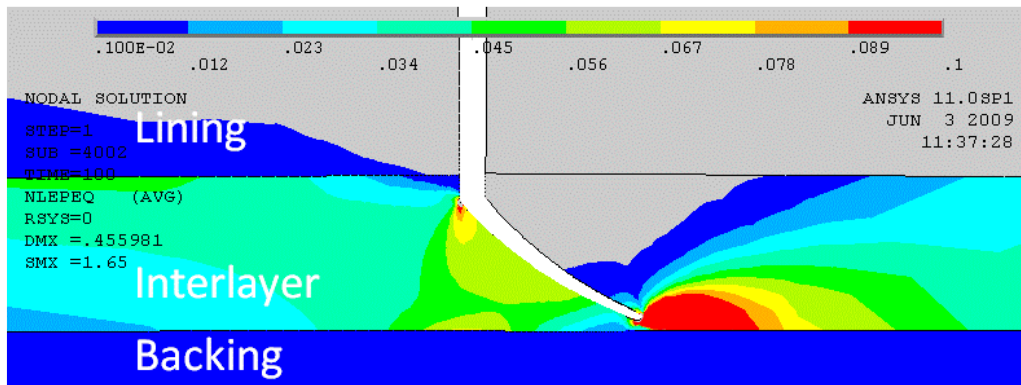


Figure 33. Predicted path and Von Mises stress contour of a single tip within the tri-layer system at 200 N.



a)  $P= 200\text{ N}$



b)  $P= 800\text{ N}$

Figure 34. Von Mises strain contour of a single tip within the tri-layer system at 200 N (a) and 800 N (b).

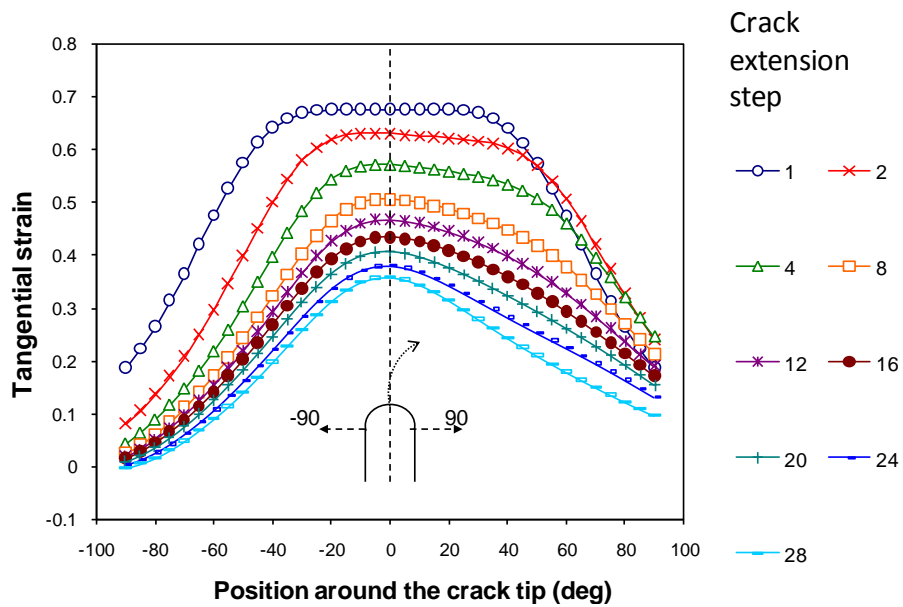


Figure 35. CTTS evolution against extension steps.

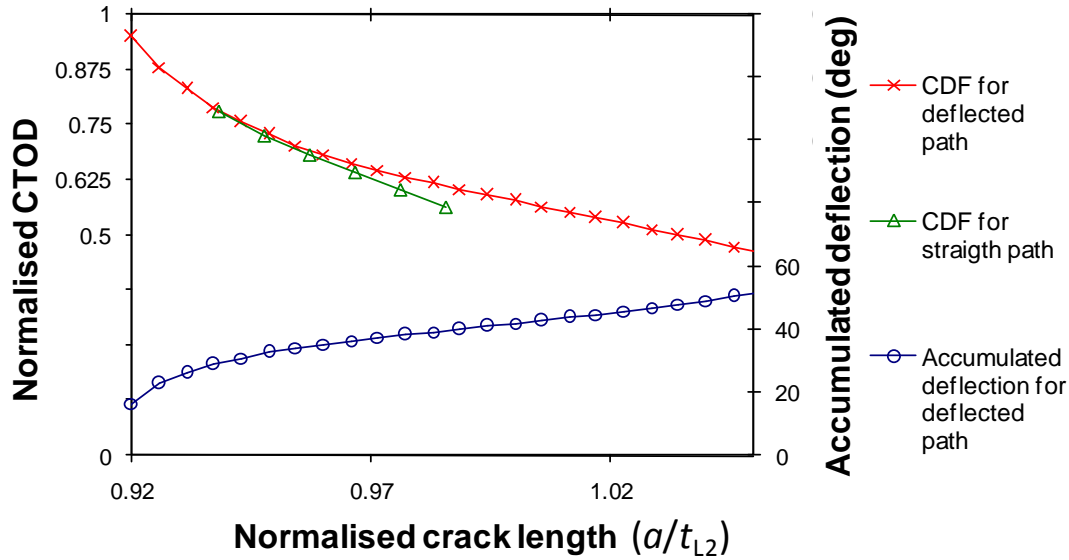


Figure 36. Comparison of CDF between straight and deflected paths at 200 N in the interlayer.

Crack deflection in the bi-layer system within the interlayer was found to be influenced to a greater extent by the intensity of the applied load. For  $P = 200$  N, initial 1 degree-deflections appeared very close to the steel layer (at  $a=0.95t_{L2}$ ); in contrast, an equivalent deflection appeared at  $a=0.61t_{L2}$  for  $P=800$  N. The CDF estimates in the bi-layer system were also slightly greater along the deflected direction than the straight path at both load levels, in qualitative agreement with the findings from the tri-layer architecture shown in Figure 36.

### 3.4.2. Discussion

Previous work [66, 67] on shielding and anti-shielding in layered architectures has usually explained these phenomena in terms of differences between the materials' yield stress. However, the yield stress only reflects part of the material state since it is not fully responsible for the post-yield deformation and the state of stress. An additional factor would be the difference between the materials' strain hardening rate represented by the gradient of the  $\sigma$ - $\epsilon$  curves since this is also directly related to the material resistance to deformation. This relation is simple when elastic or fully plastic analyses are carried out. Nevertheless, elasto-plastic analyses result in a widely ranging gradient depending on the stress concentration patterns developing around the crack tip.

The assessment of layered architectures with different elasto-plastic properties was developed by Joyce [61] in the analysis of preferential bifurcation orientations. However, a mechanistic approach to test the impact and correlation of factors such as the yield stress and the strain hardening exponent was not fully developed. Such an approach could clarify the impact of shielding in a broader sense.

CTOD estimations within the interlayer showed single-tip deflected cracks despite the absence of far-field mixed-mode loading, which is in contrast to previous work in monolithic components which applied the MTSN [87, 116] and other criteria [81, 83, 113, 117]. Such a condition in the bi-layer lining appears to be confined to higher loads. It is worth noting that the CTTS curvature is reduced as the crack approaches the interface and the applied load is increased. This curvature reduction may enhance the effects of local material heterogeneities to disturb the perfect symmetry of the problem and thus initiate deflection. This sensitivity is reduced as the deflected crack propagates away from the plane of symmetry gradually reaching a more stable state. Chambers *et al* [87] also observed that cracks deflected towards an orientation where pure opening loading was experienced. For this particular case, the crack deflected to extend parallel to the layers orientation where a combined state of shear and opening existed.

The assessment of crack path sensitivity to a perturbation was limited to confirming whether the whole process would ultimately predict a crack orientation approximately at  $+90^\circ$  or  $-90^\circ$  to the original straight path, that is, parallel to the layers' orientation. Path perturbations of sizes comparable to the scale of typical material micro-structural features, such as the hard intermetallics with a mean near neighbouring distance of  $28\ \mu\text{m}$  shown in Section 1.4.5, are expected to be re-oriented so that crack growth complies with the far field loading conditions and the multi-layered architecture. This hypothesis was tested by introducing an arbitrary initial deflection at  $30^\circ$  to the straight crack path in the lining and the interlayer. In both cases, the

perturbed crack path gradually returned to the path predicted without perturbation based on the adopted deflection criterion. The quick re-alignment of the path showed the predominance of far-field loading and specimen properties over the effect of a local perturbation in this particular example.

Crack deflection in zig-zag patterns has been linked to service life extension through the lengthening of the crack path and the CDF reduction when compared to straight cracks. In this particular study, the estimated deflections did not cause any CDF reduction, but slight increments in comparison to a straight path. These CDF increments showed that the principle of CDF maximisation introduced by Hussain [84] and Palaniswamy and Knauss [85] was fulfilled. The CDF increments caused by this deflection were not as significant as the possible path extension obtained if the crack propagates parallel to the layers orientation.

Material homogeneity has been assumed in this work focusing on the mesoscopic property mismatches among layers in the architecture. It is evident that the material microstructure will have a significant impact on the CTOD estimates; however, the estimations based on only the mesoscopic properties provide a clearer view of the layered architecture effects. The localised heterogeneity may lead to a more tortuous crack path in comparison to perfect homogeneous materials. Nevertheless, it is expected that layered architectures would have a similar overall effect over homogeneous and heterogeneous layers. At the same time, the crack growth behaviour of the analysed heterogeneous lining, shown in Section 1.4.5, can be included into the analysis through the development of a crack growth law based on experimental data.

### **3.5. Early bifurcation state**

Crack bifurcation occurred in the tri-layer architecture interlayer under three-point bending tests when the crack tip approached the backing layer. Based on this observation and on previous CTTS results, the possibility of bifurcation was investigated in the lining of the bi-layer system and the

interlayer of the tri-layer system. Initially, bifurcated cracks with very small branches were studied focusing on the CDF at the onset of bifurcation to determine the initial kink angle at which bifurcation occurs. Other parameters considered in this study are the straight crack length before bifurcation  $a$  kink length. Taking advantage of the problem symmetry, only half of the strip specimen was modelled and analysed as shown in Figure 37. A parametric study was performed involving bifurcated crack kinks of length between 1% and 5% of the thickness of the layer containing the crack tip.

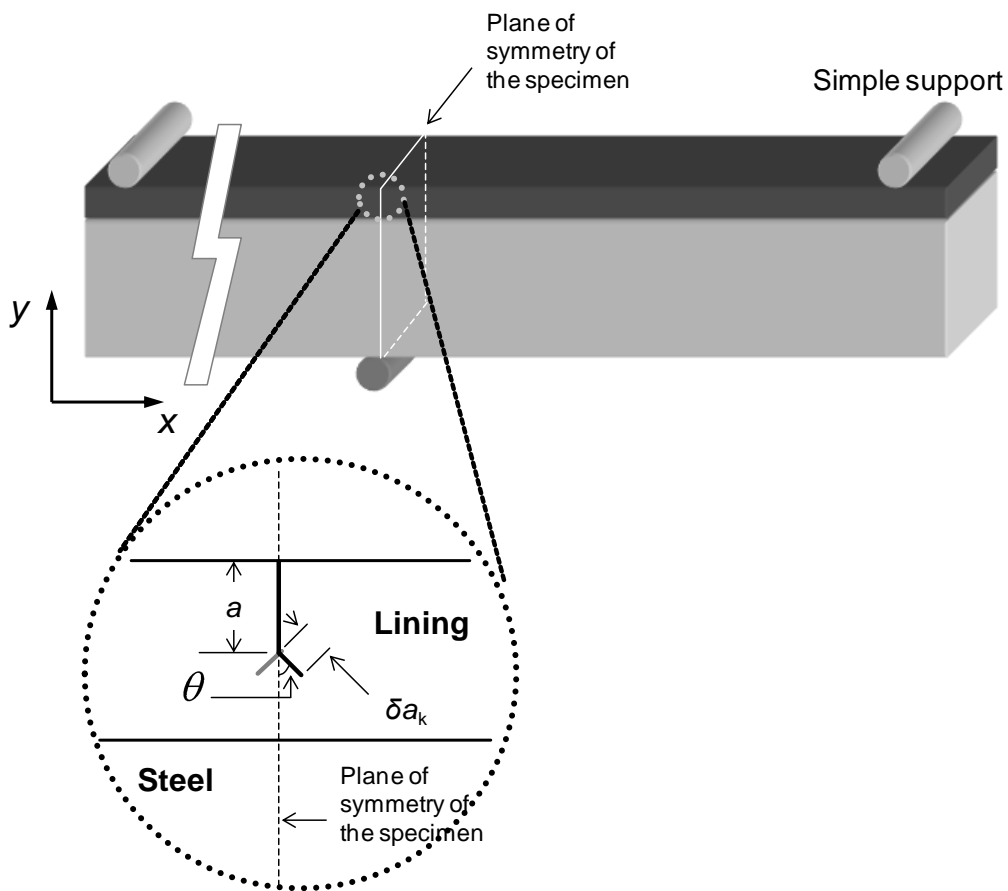


Figure 37. Bifurcated model and analysed factors.

### 3.5.1. Results

The results from both layered systems showed that for any given straight crack length before bifurcation there exists a kink angle that maximises the CDF, which can be interpreted as the most

likely deflection direction. The CTOD ratio between bifurcated and straight cracks of equal length ranged between 32% and 50% in the bilayer architecture and 44% and 51% in the trilayer one. The variation of kink length within the limits mentioned above did not have any significant effect on the predicted deflection angle. The CDF estimates obtained in the case of the tri-layer architecture are shown in Figure 38. A gradual shift of the maximum to greater kink angles can be observed as the bifurcation point approaches the interface. The last case analysed, corresponding to a straight crack length of  $0.993t_{L2}$ , resulted in a steep increment in the angle that corresponds to a maximum CDF value. As shown in Figure 39, no such steep increments were found in the case of the bi-layer model up to a crack length before bifurcation of  $0.95t_{L2}$ .

As noted with the straight cracks presented in the previous section, the CDF estimates were also affected by the proximity to a stiff layer (largely dependent on the crack length before bifurcation). Due to the thinness of the interlayer, shielding in the tri-layer architecture was observed as soon as the bifurcation point crossed into the interlayer while shielding in the bi-layer architecture became apparent only after the straight crack length grew above  $0.7t_{L2}$ .

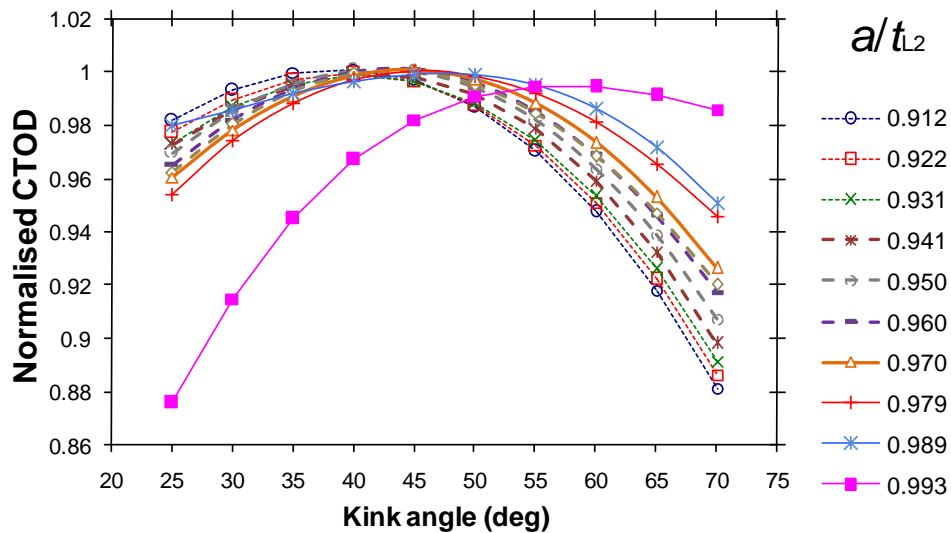


Figure 38. Variation of CDF with kink angle in the tri-layer architecture at 200 N (CTOD values are normalised with respect to their maximum along each curve).

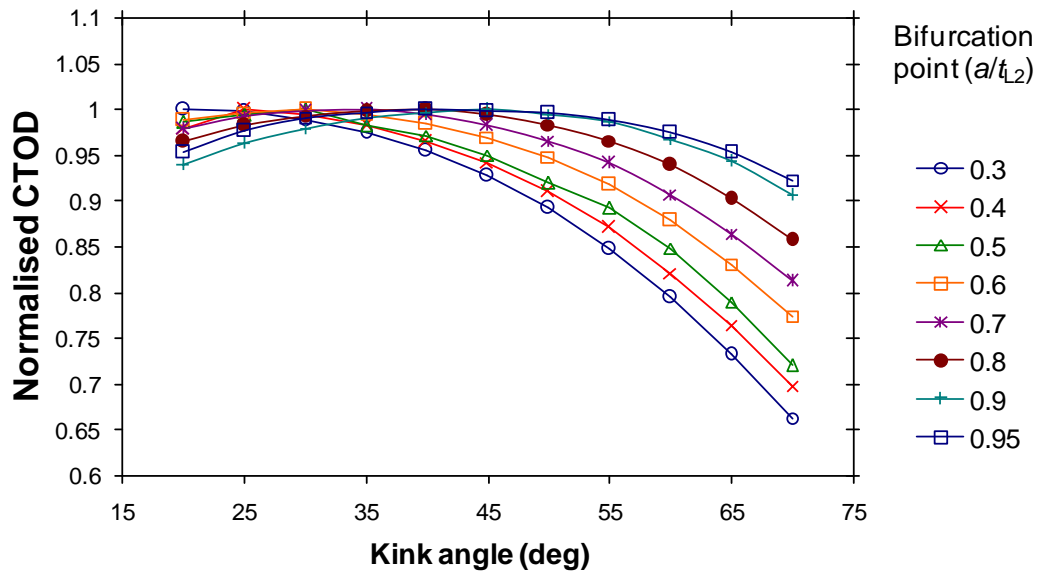


Figure 39. Variation of CDF with kink angle in the bi-layer architecture at 400 N (CTOD values are normalised with respect to their maximum along each curve).

### 3.5.2. Discussion

The study of the CDF estimates of different bifurcated cracks showed the importance of the kink angle in the early bifurcation stage. The kink angle corresponding to a CDF maximum value rises as the bifurcation point approaches a stiff layer. The predicted direction of the bifurcated path depends on the extent of property mismatch and the proximity of the crack tip to the layer interface, as reported previously by Joyce *et al* [61]. In this earlier work, the kink angle corresponding to the maximum CDF, represented by the  $J$ -integral, reached the value of  $90^\circ$ . The maximum CTOD values obtained in this work do not correspond to such high deflections despite the assessment of cracks closer to the interface. This difference may arise due to the preferred CDF parameter or different material models used for the backing layer. Joyce *et al* assumed an elastic material for this layer, while an elasto-plastic model is used in this work. Such a model reduced the local constraint at the interlayer-backing interface arising from the yielding caused by loading and stress concentration.

### **3.6. Bifurcated Branch Path**

Experimental work in tri-layer architectures has shown that bifurcation occurs as soon as the crack penetrates the interlayer; an event that was expected due to the sudden drop of material crack growth resistance. The initial kink angle used for the bifurcated branch was selected according to the kink angle that yielded a maximum CDF in the early bifurcation state analysis, obtained through quadratic interpolations. The bifurcated path analysis is initiated with a kink angle of  $37.15^\circ$  in the interlayer. Subsequent crack growth was simulated according to the MTSN criterion.

Experimental observations of crack propagation in the architecture MAS-20S did not show signs of arrest after a bifurcation event. This is in contrast to the findings by Suresh [79] and Katz et al [98] which describe how longer kinks shield smaller kinks leading to an eventual arrest. The propagation after bifurcation in the analysed tri-layered architecture remained bifurcated and kept deflecting towards an orientation parallel to the layers.

#### **3.6.1. Results for bifurcated branch path**

The comparison between results for deflected and bifurcated crack analyses showed two clear differences in the tri-layer architecture. Firstly, the predicted crack path deflections were greater for bifurcated than single-tip deflected cracks at lower values of crack depth  $c$ , shown in Figure 40. As crack tips approach the backing-interlayer interface, deflections of both crack configurations appeared closer, as shown Figure 41; which also shows the difference between the CDF values in both crack configurations. Secondly, the CDF estimates along single tip deflected cracks are greater than those along their bifurcated counterparts. A typical generated and plastic strain estimates for the latter are shown in Figure 42.

The application of an elasto-plastic analysis involves computational difficulties arising from the more demanding material characterisation and requires extensive computational resources. For this reason, simpler analyses, within the scope of LEFM, are usually applied. The difference between

results from elastic and elasto-plastic analyses was studied by considering a bifurcated crack growing in the interlayer. The Young modulus used for the lining, interlayer and steel are 70 GPa, 67 GPa and 197 GPa, respectively, as shown in Table 3. Figure 43 shows the CDF evolution and cumulative deflection for both material models for a bifurcated crack growing in the interlayer at a load  $P = 200$  N, which causes extensive yielding in this particular layer.

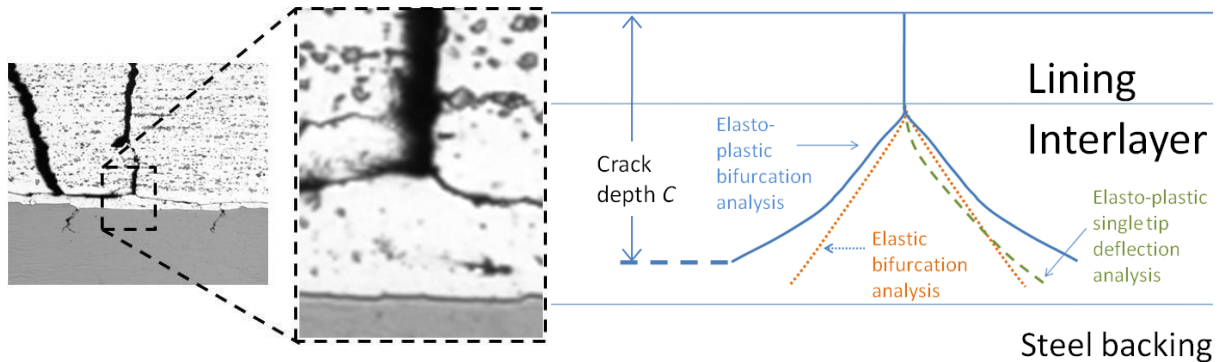


Figure 40. Estimated paths for single tip deflected crack and bifurcated arrangements with only pure elastic and elasto-plastic materials.

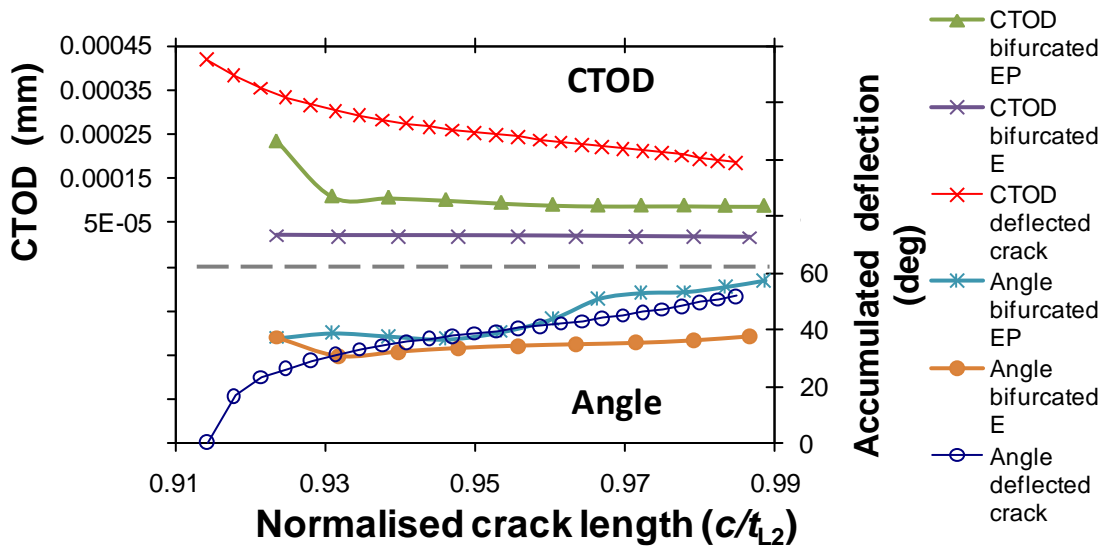


Figure 41. Accumulated deflection and CDF evolution in tri-layer architecture for single-tip deflected and bifurcated crack (bifurcated EP).

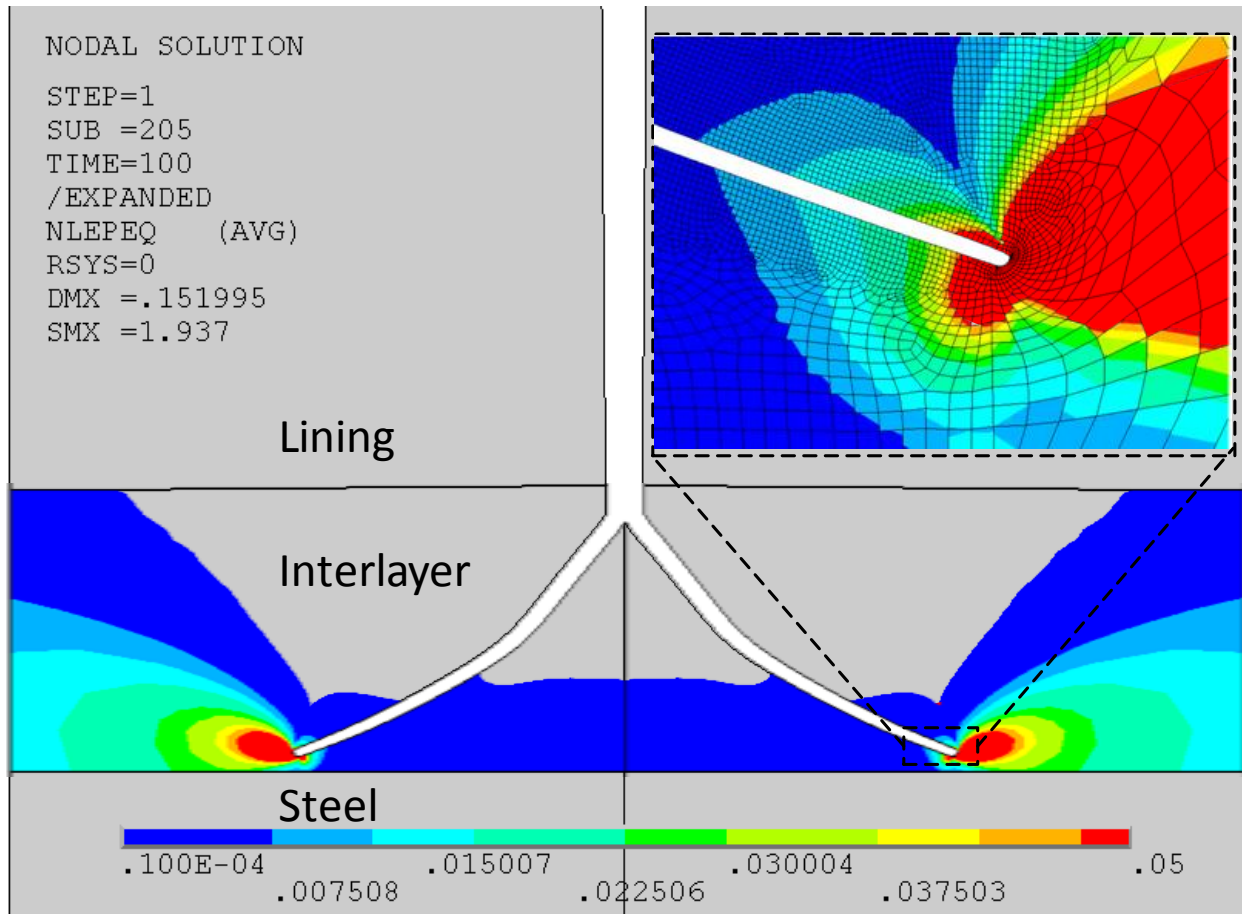


Figure 42. Equivalent plastic strain (Von Mises) in tri-layer architecture.

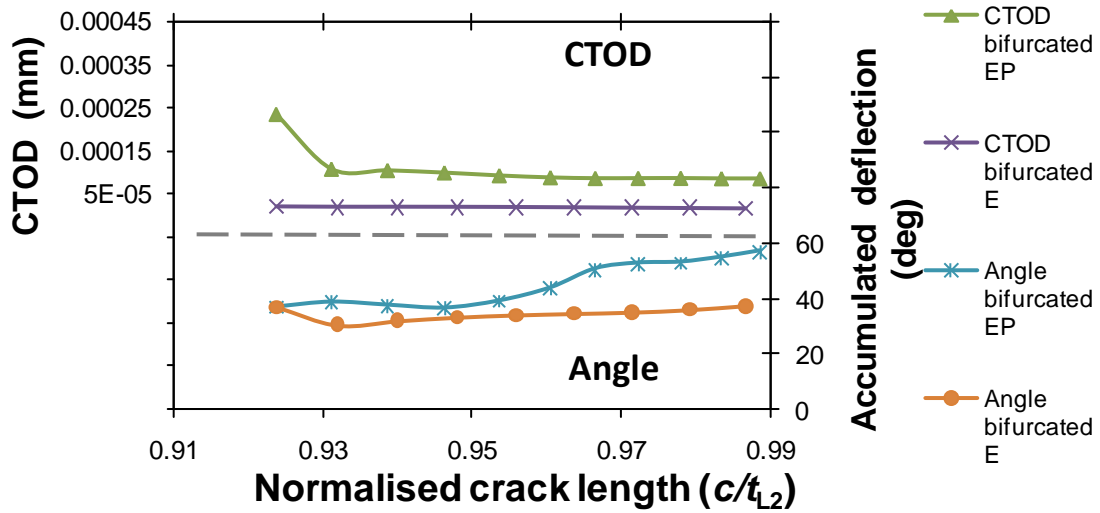


Figure 43. Accumulated deflection and CDF evolution in tri-layer architecture using pure elastic (bifurcated E) and elasto-plastic (bifurcated EP) materials.

Figure 40 also shows the comparison between the estimated paths using elastic and elasto-plastic material models. The path forecasted using elastic properties showed a very limited deflection; in contrast to its elasto-plastic counterpart that estimates greater estimations which, visually, appear to be more consistent with experimental crack paths. Despite estimating greater values for deflection, predicted paths obtained through elasto-plastic analyses still showed a significant difference to experimental observations.

### 3.6.2. Discussion

The simulation of bifurcated growing cracks showed a characteristic trend of progressive deflection that aligns the crack growth direction with the layers interface, as shown experimentally in Figure 12. This is in agreement with Joyce *et al* [61] findings that forecasted a bifurcation angle of  $90^\circ$  as the bifurcation point approaches the stiff backing.

Studies on crack bifurcation have shown its impact on the values of CDF and, as a consequence, on crack growth rate, presumably leading to longer service life. Deflection and smaller crack growth rates led to this assumption; however, it is also noteworthy that bifurcation close to the lining free top surface may lead to a faster detachment of lining fragments in multi-layered bearing systems as the lateral crack growth, parallel to the layers orientation, is more likely to coalesce with other cracks.

The estimated CTOD values after bifurcation dropped between 49% and 68% for the analysed architectures and loading conditions, this may appear to be in contrast to the work of Meggiolaro *et al.* [95], with  $K$  reductions up to 37%, and Kitagawa [93], with reductions ranging between 30% and 40%, in very short kinks at similar kink angles. The range of reductions found by Kitigawa would represent CTOD drops between 51% and 64% which is consistent with the drops found with more complex elasto-plastic models. The most relevant difference between elastic and elastoplastic analyses can be found as crack branches extend. Models with elastic material models showed that

the initial bifurcation angles remained almost unchanged despite approaching the backing layer in contrast to elasto plastic orientation. In conclusion, the initial CDF drop can be well characterised by elastic analysis; however, as the branches extend elastic material models cannot model the change of orientation of the branches. The application of a methodology within the scope of EPFM is indispensable when LSY conditions are analysed since the estimation of the CDF parameter from FE analyses show a significant variation, clearly illustrated in Figure 43.

The difference observed between the numerically estimated paths and experimental observations was attributed to the significant shear experienced by blunted crack tips. The mixed mode loading experienced at the crack tip could have reached levels under which the MTSN criterion does not provide accurate results, as discussed previously in Section 3.3.2, along with excessive deformation which could have affected its implementation. However, the MTSN criterion provided a reasonable estimation of the path and allowed a comparison with other modelling techniques available.

### **3.7. Summary**

Various criteria are available to estimate the crack tip direction according to fatigue or constant loading and mixed-mode loading conditions. No single criterion has proven a superior performance for every single scenario especially when fatigue and mixed-mode loading conditions are present. The crack tip displacement vector (CTDV), maximum principal stress and strain (MPS and MPSN) and the maximum tangential stress and strain (MTS and MTSN) were implemented for the conditions experimentally assessed by Mageed and Pandey [88]. The maximum tangential strain provided a more consistent estimation of the deflection angle, in this particular implementation, with the experimental results obtained under fatigue loading, especially at dominant mode I mixed-mode loading conditions.

Automated growth analyses for deflecting cracks in bi-layer and tri-layer systems were created using a remeshing scheme that generates short crack extensions along the predicted direction

according to the near-tip state of stress at the previous step. The concatenation of these short cracks forms the path along which the values of the crack driving force are obtained.

The cracks under such a severe shielding process show tangential strain curves with a flat profile, or no curvature, around the maximum value. This profile suggested the crack extension could occur in any direction over this range. Subsequent deflections using the maximum numerical value of this range showed that the flat profile disappeared gradually until a single clear maximum could be identified again. The predicted crack profile obtained from this extension tends to self-align with the layers orientation. The cracks under anti-shielding conditions were not forecasted to suffer any deflection. The CDF estimates along the forecasted paths showed greater values than straight cracks with equivalent crack lengths, showing that the estimated path maximises the CDF.

The crack growth conditions that appeared after bifurcation were studied together with the subsequent growth at each branch. At the same time, parametric studies revealed that for every given straight crack length, a single kink angle value that maximises the CDF estimates existed. These values were used as initial deflected growth values to observe the evolution of the CDF as it approaches the materials' interface at different bifurcation angles. CDF reductions up to 68 % are observed and were also dependent on the proximity of the layers interface as observed in straight cracks.

The occurrence of deflected or bifurcated cracks promoted by shielding conditions appears to be possible according to the assumptions that the CTTS profile reflects the deflection and bifurcation likelihood. The symmetrical CTTS profile with two maxima and paths, which are visually more consistent with experimental observations, suggest that bifurcation would be a more natural occurrence in a homogeneous material while heterogeneous material features may lead to single-tip deflected cracks.

## **4. Chapter Four: Crack interaction and coalescence**

### **4.1. Introduction**

The objective of the finite element analyses described in this chapter is to identify possible effects of the presence of various cracks in the same body on crack growth. Previous work has shown the importance of multiple cracks and their possible shielding and anti-shielding effects according to size and orientation. At the same time, this analysis is intended to provide information on the minimum distance between cracks to be considered independent for further 3D analyses and the magnitude of the observed effects according to the studied material properties and in relation to the applied loads.

The analysis of interacting and coalescing cracks in three dimensions demands extensive computational power. Therefore, 2D models under tensile stresses were here modelled as a simplified representation of the material conditions at the lining surface under three-point bending conditions. Such 2D models require substantially less computational power allowing the crack growth simulation of different crack arrangements and levels of loading.

### **4.2. Background**

One of the main advantages of damage tolerance over total life approaches is its ability to account for the perturbation of stress and strain fields caused when a flaw is already present in the material. This idea suggests the importance of multiple cracks contained in the material since each crack evolves according to its near stress fields and these fields depend on other flaws nearby. Identifying the possible interactions between cracks and their consequences is vital to avoid failure or overdesign.

Crack interaction and coalescence have been observed in the crack propagation study of multi-layered architectures under three-point bending [10, 61, 63] and bearing working conditions [7, 61]. According to these observations, a dominant crack located at the lining surface is formed by the coalescence of various short cracks after the specimen is cyclically loaded. These cracks are initiated in the proximity of a line across the lining surface where the maximum stress develops under three-point bending conditions. The initiation of these cracks occurs preferentially along this line; however, microstructural features such as grain boundaries, secondary phase particles and the distribution of defects influence slightly the location of such initiation sites [9]. Multiple cracks initiate simultaneously and grow on the plane perpendicular to the layers orientation. As these cracks approach each other, the crack growth rate accelerates until coalescence occurs. Coalescence and shielding effects caused by a stiffer layer contribute to the formation of shallow cracks that grow perpendicular to the layers interface as shown in Figure 44 for initial crack growth stages and Figure 45 for late crack growth stages.

Interacting and coalescing cracks have been of interest due to their mutual shielding and anti-shielding effects, which are detected through the CDF estimates evolution, and depend on particular crack arrangements [11, 23]. Co-linear crack configurations have shown anti-shielding effects in previous work [118] with  $K_I$  increasing by up to 60 % in analytical solutions of through-thickness cracks in plates of infinite length. Murakami [118] also developed a similar analytical solution that showed the opposite effect on the crack growth of parallel cracks, where  $K_I$  reductions of up to 40% were found. Meyer *et al.* [119] investigated through thickness cracks at different orientations with FE models that assumed elastic and elastic-perfectly plastic material behaviour. The latter showed greater anti-shielding effects.

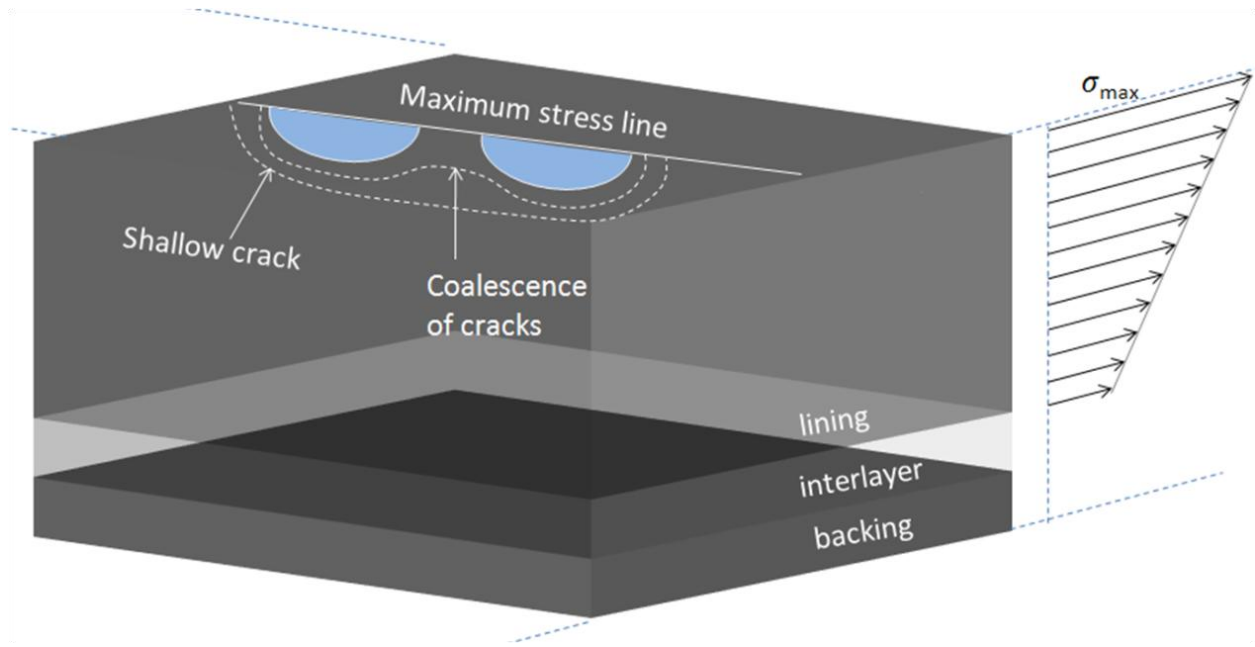


Figure 44. Crack growth process in multi-layered architecture at initial crack growth stages.

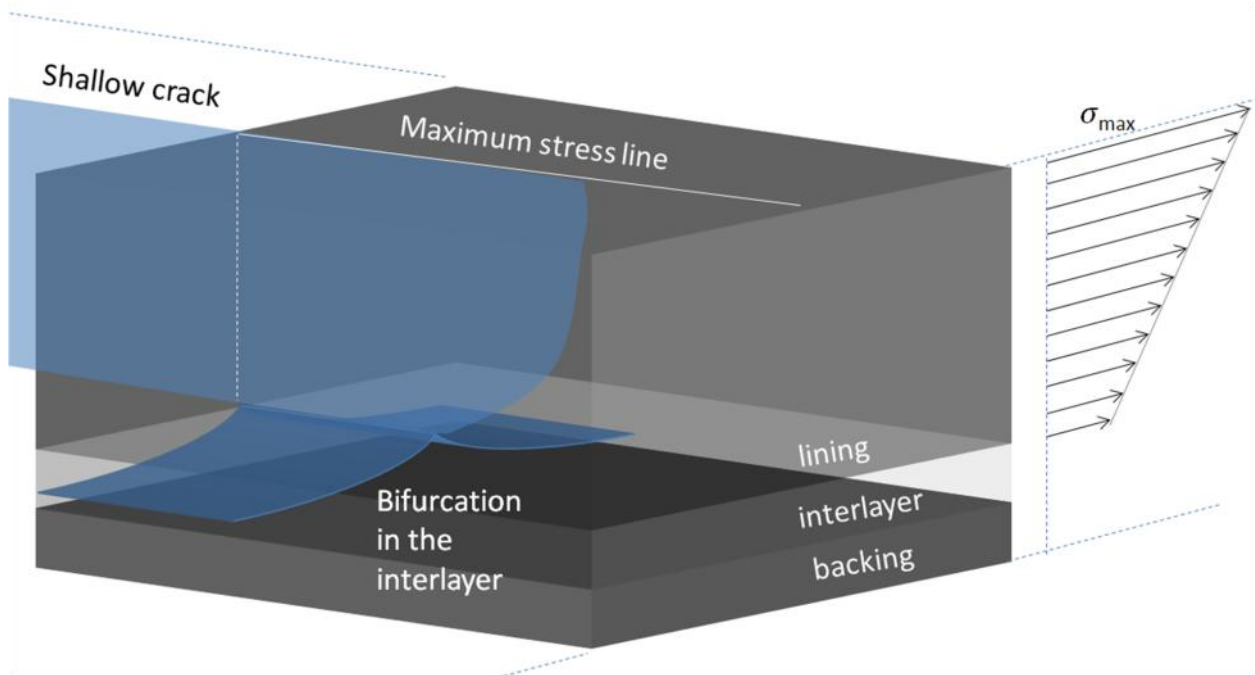


Figure 45. Crack growth process in multi-layered architecture at late crack growth stages.

Studies on coplanar cracks [120] examined Forsyth's findings [121] related to the existence of a critical distance  $h$  between cracks that would cause coalescence from a particular set of loading conditions; this is given by the relation

$$h \propto \left( \frac{\sigma_{\infty}}{\sigma_Y} \right)^2 (2a_1 + 2a_2) \quad (14)$$

where  $a_1$  and  $a_2$  the lengths of interacting cracks. In contrast, Wang *et al* [120] found that coalescence does not depend on the material strength according to their studies of two steels leading to a simpler relationship:

$$h \leq 0.14(2a) \quad (15)$$

The influence of different crack arrangements assuming an elastic material behaviour has been studied extensively in the literature; the impact of elasto-plastic behaviour has been assessed to a lesser extent. However, the extension of such cracks and CDF evolution in numerical analyses with elasto-plastic material models in two dimensions can be further developed, especially for oblique and parallel cracks since the study of coalescence of co-linear cracks has been extensive, even in the 3D case [122-125].

### **4.3. Model and methods**

Four different configurations are analysed using two-dimensional finite element models. These configurations, shown in Figure 46, are labelled as: (a) oblique, (b) parallel-dominant, (c) co-linear and (d) single, the latter for comparison purposes only. The response to the loading magnitude and distance between cracks was also assessed in a model geometry linked to the specimen used in three-point bending tests carried out in previously [10] in the University of Southampton. The modelled specimen consisted of a single layer made of the architecture MAS-20S lining material, whose properties are shown in Figure 15 and Table 3, assuming plane stress conditions. The initial crack length  $a_0$  analysed for oblique, dominant (from parallel dominant arrangement) and single cracks was equal to  $W/10$ . Shielded and coalescing co-linear cracks had an initial length  $a_0=W/20$ . The initial distance between coalescing tips in co-linear arrangements in the direction of  $W$  was

equal to  $8 a_0$  or  $2W/5$ , while the distance between overlapped and oblique tips in oblique arrangements was equal to  $2a_0/3$  or  $W/15$ .

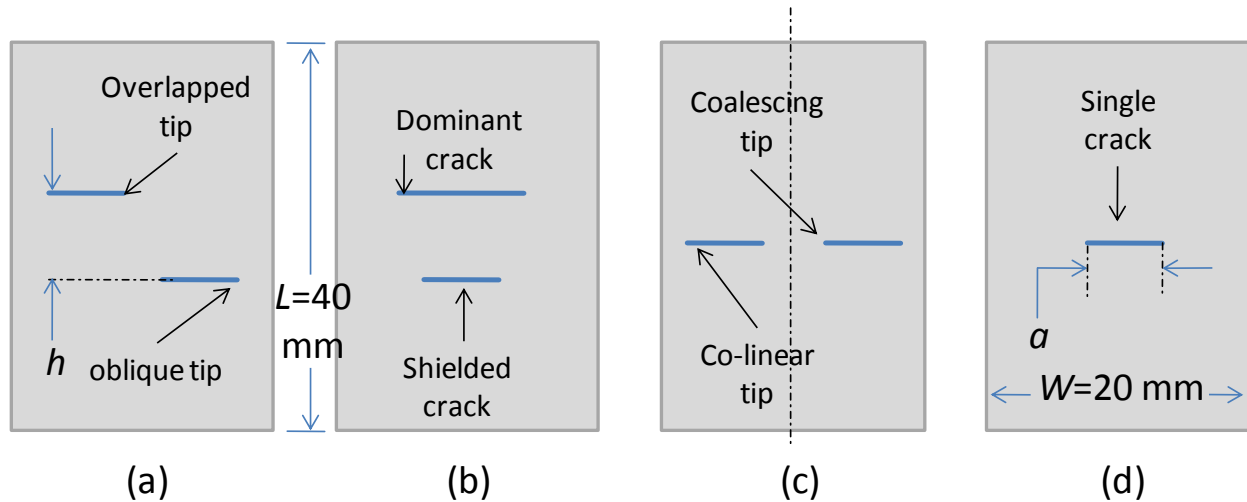


Figure 46. Interacting crack arrangements.

The study of coalescence and crack interaction through these 2D numerical models used the crack extension methodology described previously in Figure 32 in order to analyse the impact of the stress field modifications introduced by a second crack. By analysing step by step extensions based on the MTSN deflection criterion, it is possible to track the changes in the crack path and assess the combined effect of deflection and crack interaction on the CDF estimates.

The analysed specimen is subjected to uniform tensile stresses in the longitudinal direction (normal to the cracks). The existing flaws propagated by estimating the relative growth according to the assumption that crack growth rate varies linearly with the CTOD [126], that is,  $da/dN = b CTOD$  where  $b$  is a fitting parameter. Later stages of this project involved a crack growth law linked to experimental data [10]. The interacting cracks were extended and deflected using remeshing algorithms based on the MTSN path criterion. The far-field load levels applied in these analyses correspond to 40%, 70% and 100% of the stress that would cause yielding in undamaged specimens. The crack separation levels are set at  $h/a_0 = 1.7, 3.5$  and  $5.3$ . The analysed cracks were extended until the elements that form the blunted crack tip configuration touched the border of the

specimen or each other as done previously in [127] for fatigue modelling assuming that coalescence occurred. Other criteria to define coalescence are available mainly in the context of fracture as shown in [128, 129].

The CTOD estimations are plotted against two parameters: dominant crack length ( $a$ ) and distance between plastic zones ( $d_r$ ), as shown in Figure 47. Both parameters are normalised with respect to either the plate length ( $L$ ) or width ( $W$ ), depending on the growth direction of the interacting crack. The crack length was measured from the centre of each blunted crack arc while the plastic zone size was estimated through the area with non-zero von Mises plastic strain values.

#### 4.4. Results

The general trends described in the literature for parallel and co-linear cracks were confirmed by the CDF estimates in this work. The application of loading levels that generated LSY conditions required large amounts of computational resources; however, the analysis of such conditions indicates the importance of non-linear numerical analyses.

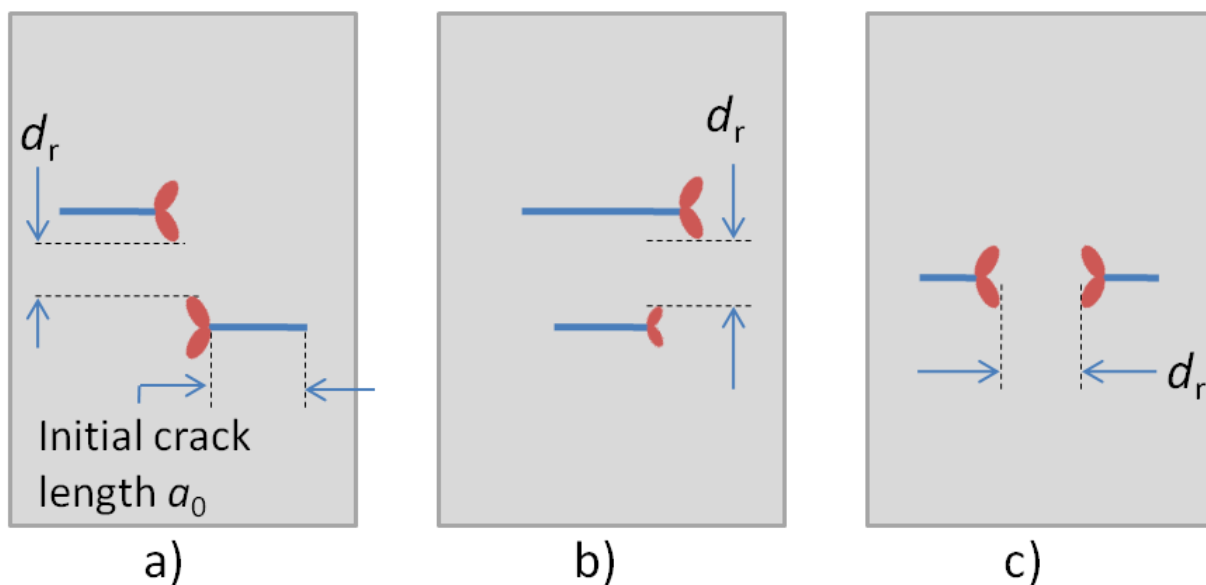
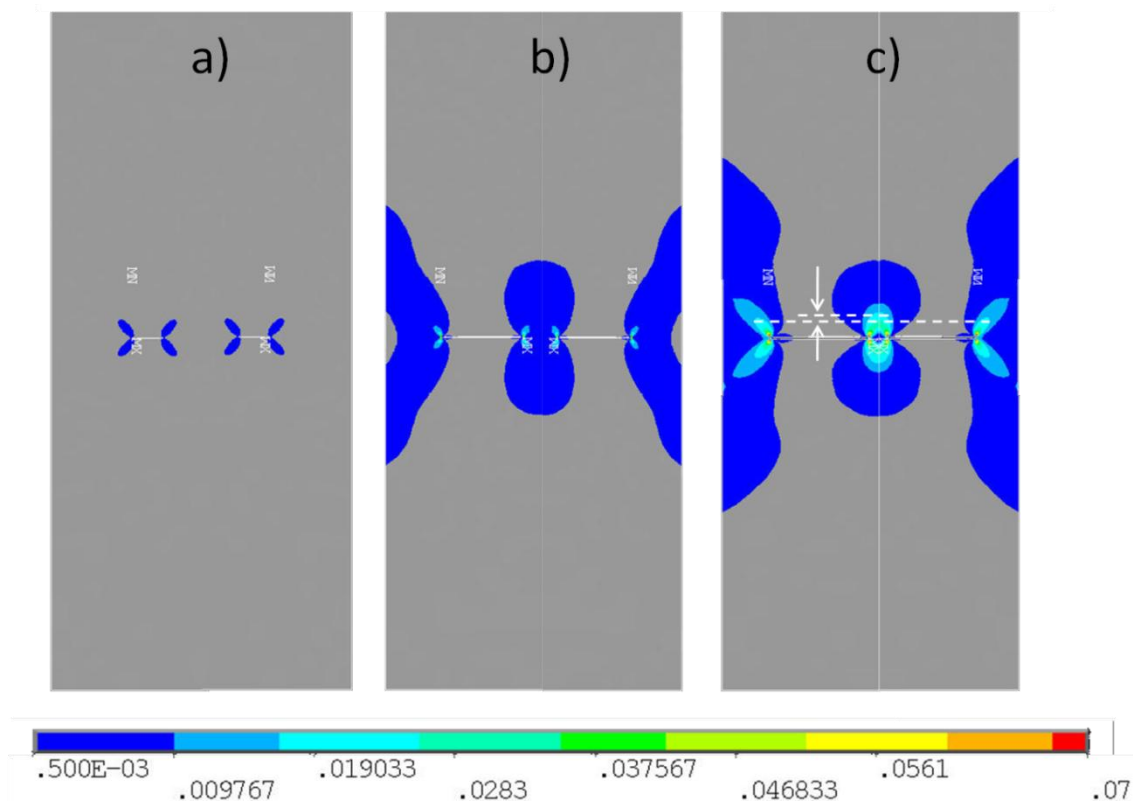


Figure 47. Distance between plastic zones for oblique (a), parallel (b) and co-linear arrangements.

#### 4.4.1. Co-linear cracks

The evolution of von Mises strain as the co-linear cracks grow showed the impact of multiple cracks that interact with each other. Figure 48a shows the plastic strain contours when  $a = 0.1W$  and the characteristic plastic zone butterfly pattern at coalescing and co-linear tips without any indication of interaction between them. As cracks started to grow, it is evident from Figure 48b that the plastic zones of coalescing tips merged distorting the original characteristic pattern. As cracks continued approaching each other as shown in Figure 48c, plastic strains between both crack tips became more intense.



**Figure 48. Crack growth progression (a, b and c) in co-linear arrangement under 100% of yield stress showing Von Mises plastic strain contours.**

The anti-shielding effects in co-linear arrangements are shown in Figure 49, where coalescing co-linear  $CTOD_{COAL}$  and single crack  $CTOD_{SINGLE}$  ratios are plotted against the crack size. The  $CTOD_{COAL}/CTOD_{SINGLE}$  values were computed based on cracks of equal lengths.  $CTOD_{COAL}/CTOD_{SINGLE}$

from cracks with sizes close to  $a_0$  showed values close to one, confirming that the initial separation was sufficient to cause little or no interaction. The estimated  $CTOD_{COAL}/CTOD_{SINGLE}$  shows a rising trend with crack size and load level as expected. Very little interaction can be observed between cracks at the smallest crack length analysed where the distance between tips is close to  $8 a_0$ .

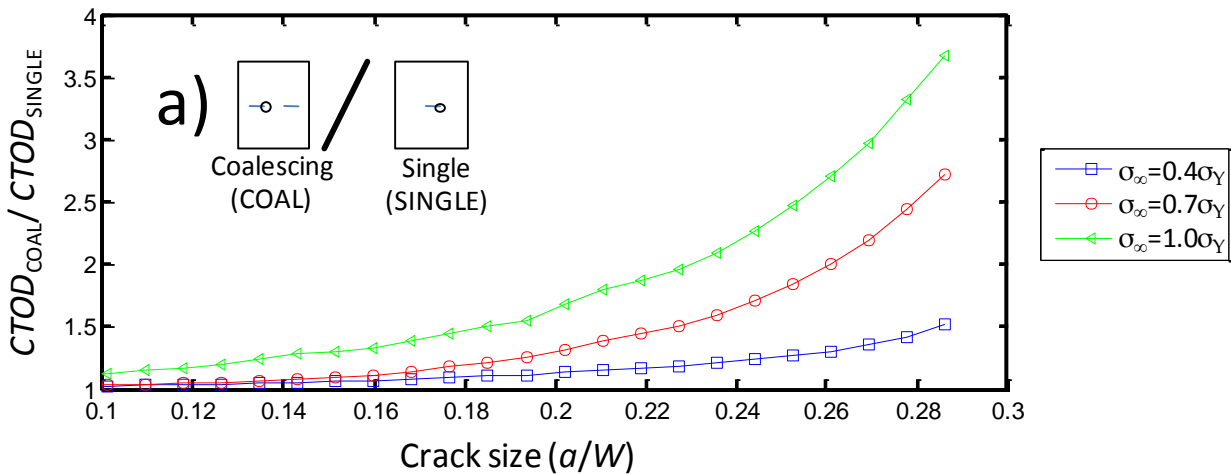
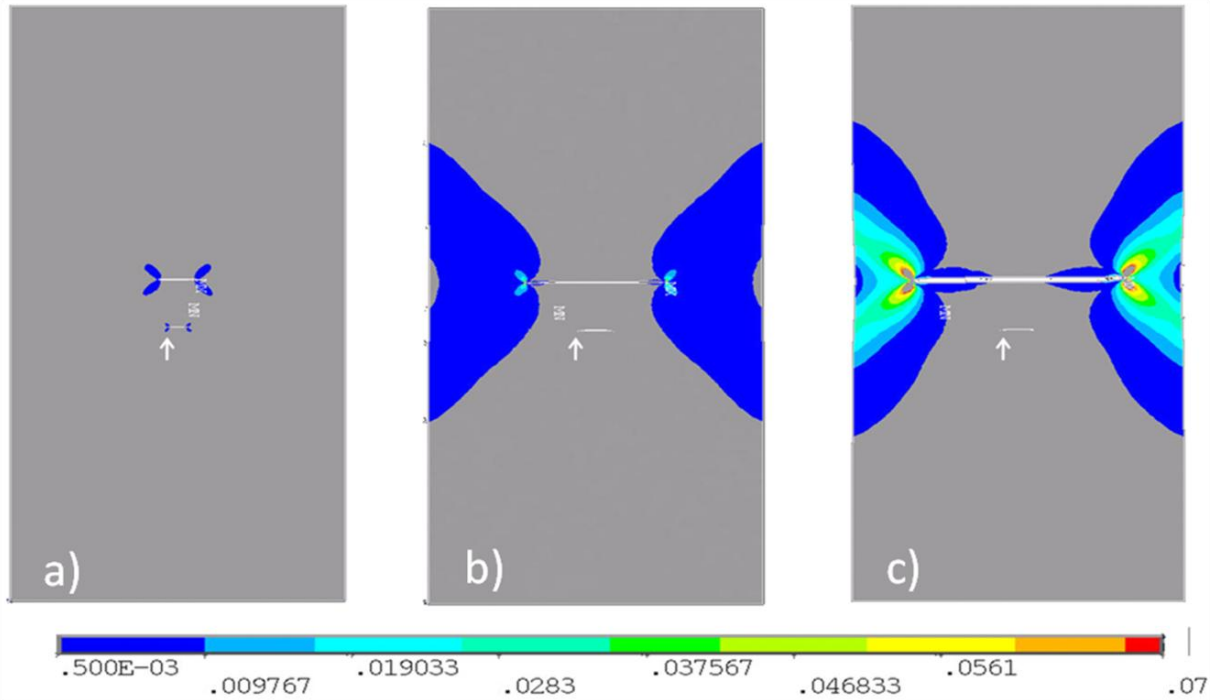


Figure 49. Co-linear arrangement results for  $CTOD_{COAL}/CTOD_{SINGLE}$  at equal crack lengths.

#### 4.4.2. Parallel-dominant arrangements

The crack extension analyses of parallel cracks produced the characteristic plastic zone butterfly pattern observed in the first simulation of the analysis, shown in Figure 50a. At this initial stage, a significant difference between the sizes of both plastic zones is visible in the plot. The lines of force were redirected away from the crack tip of the shielded crack reducing its plastic zone size and propagation speed. The shielding process over the smaller crack became more evident as the dominant crack extended. Figure 50a shows that the plastic zone was initially visible while the crack size ratio between cracks is comparable. As the dominant crack extended, the plastic zone disappeared in the shielded crack tips, shown in Figure 50b and Figure 50c, and the effect of the crack size difference became more obvious. No deflection tendencies were forecasted in parallel arrangements.



**Figure 50. Crack growth progression (a, b and c) in parallel arrangement under 100% of yield stress showing Von Mises plastic strain contours.**

Shielding effects in parallel arrangements are shown in Figure 51. Figure 51a shows the estimation of  $CTOD_{SHI}/CTOD_{SINGLE}$  against their crack size; these ratios showed the influence of loading and separation between cracks. Initial CDF ratios between 0.5 and 0.9 were observed at crack sizes close to  $a_0$  and shrank to values as low as 0.1 at later stages of crack growth as the difference between their crack size increased. Figure 51b shows the evolution of the normalised CDF in the shielded crack (with respect to the CTOD estimate at a crack size  $a_0$ ) against the respective crack size. CDF estimates in this plot grew initially and then dropped quickly since the dominant crack grew faster and increased the shielding effect. The distance between cracks  $h$  and higher loading levels influenced the shielding process in the small-parallel crack. Greater separation and low loads resulted in a lower shielding rate. Figure 51c shows the estimations of  $CTOD_{SHI}/CTOD_{DOM}$  against their respective crack size ratio. CDF ratios dropped as the size ratio increases with values as low as 0.1 around a crack size ratio of 3 irrespective of load level or separation distance. Figure 51d shows the values of  $CTOD_{SHI}/CTOD_{DOM}$  against the distance between plastic zones; these values showed

that shielding at low load levels,  $\sigma_\infty = 0.4 \sigma_Y$ , occurred despite a fairly constant distance between the plastic zones. At higher load levels,  $\sigma_\infty = 1.0 \sigma_Y$ , the shielding process occurred while the plastic zones approach one another and even merge.

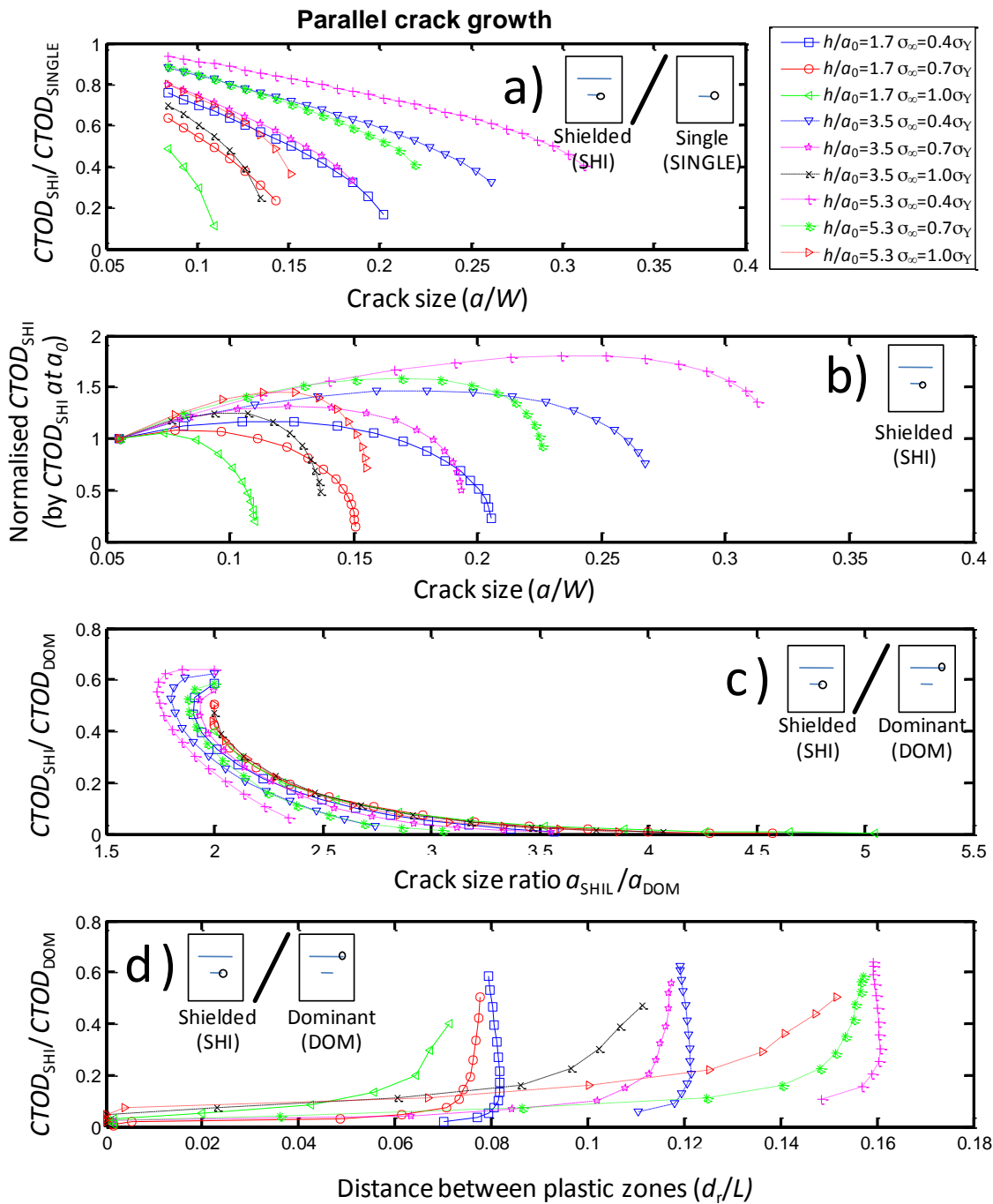


Figure 51. Parallel cracks results for the CDF of shielded tips versus the shielded crack size (*a*, *b*, *c*) and the distance between plastic zones (*d*).

### 4.4.3. Oblique arrangements

The crack growth in oblique arrangements showed a clear coalescing trend of the overlapping crack tips. This coalescing process developed slowly as the crack tips overlap and a progressive deflection occurred leading each tip towards the crack face of the other crack. Figure 52a shows coalescence developing at the smallest level of crack separation  $h/a$ . Milder signs of coalescence were observed at the medium level of crack separation (Figure 52b) while small deflections occur at the highest level (Figure 52c). Greater loading levels spread the extent of plasticity significantly and reduced the distance that cracks overlap. Figure 52 also shows that a high strain area ( $\sim 0.019$ ) formed between the overlapping crack tips irrespective of the distance or separation level analysed. A second high strain area ( $\sim 0.028$ ) of smaller size could be also identified between the overlapped tips and the opposite crack face.

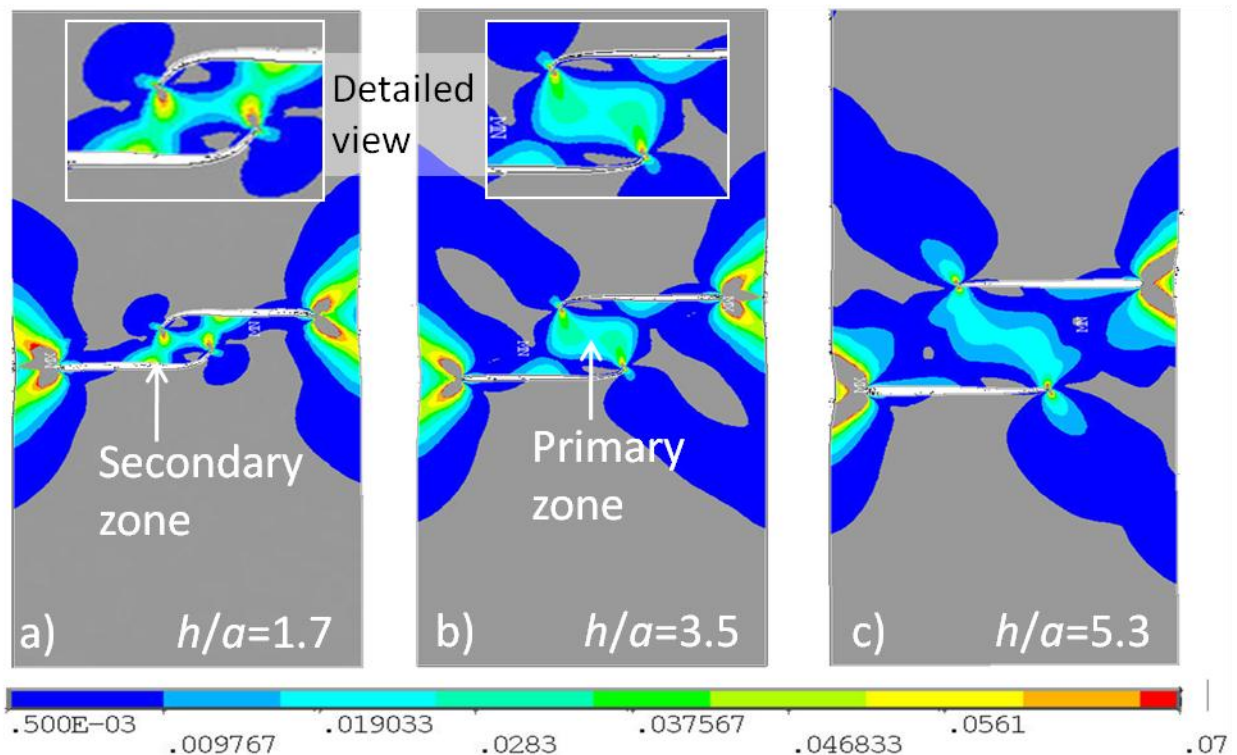


Figure 52. Final stages of crack growth at crack separation equal  $1.7a$ ,  $3.5a$  and  $5.3a$  showing von Mises plastic strain contours in oblique arrangements under  $\sigma_{\infty} = \sigma_{\gamma}$ .

The shielding and deflection effects in oblique arrangements are shown in Figure 53, where the shielded tip deflection ( $a$ ,  $b$ ), the ratios of overlapped and single crack tip CDF ratios  $CTOD_{OVE}/CTOD_{SINGLE}$  ( $c$ ) and overlapped and oblique tip CDF ratios  $CTOD_{OVE}/CTOD_{OB}$  ( $d$ ) are plotted against the crack size ( $a$ ,  $c$ ) and the distance between plastic zones ( $b$ ,  $d$ ). It can be observed that crack deflection (Figure 53a and b) behaved in different ways with respect to the reduction of distance between plastic zones and crack size. Deflection increased with crack size at values of  $h$  equal to  $1.7a_0$  and  $3.5a_0$ . At the maximum separation value considered,  $h$  equal to  $5.3a_0$ , a maximum deflection (below  $12^\circ$ ) was reached and then dropped irrespective of distance between plastic zones or crack size. The  $CTOD_{OV}/CTOD_{SINGLE}$  (Figure 53c) dropped at initial stages of crack growth, later on these ratios increase above 1. The  $CTOD_{OV}/CTOD_{OB}$  (Figure 53d) showed shielding trends that reduced their slope as the distance between the plastic zones is shortened.

#### **4.5. Discussion**

As shown by the results of the numerical analyses in this chapter, various factors such as material properties, loading, crack position and orientation combine to develop conditions for shielding and anti-shielding effects. The initial value assigned to factors of interest, such as crack tip position, orientation and plastic zone separation, change through the propagation process leading to the idea that the consideration of a parametric study involving only straight cracks [119] was not sufficient to evaluate possible drops and accelerations of crack growth rate.

With respect to co-linear cracks, the obtained  $CTOD_{COAL}/CTOD_{SINGLE}$  values showed a rising trend as both tips approached each other as reported by Murakami [118] based on LEFM analyses.  $CTOD_{COAL}/CTOD_{SINGLE}$  equal to 1.3 and 1.6 times at  $\sigma_\infty=0.7\sigma_Y$  and  $\sigma_\infty=1.0\sigma_Y$ , respectively, even at a considerable distance between cracks ( $\sim 4a_0$  between coalescing crack tips) were observed. Evidently, this ratio only increases as cracks approach each other.

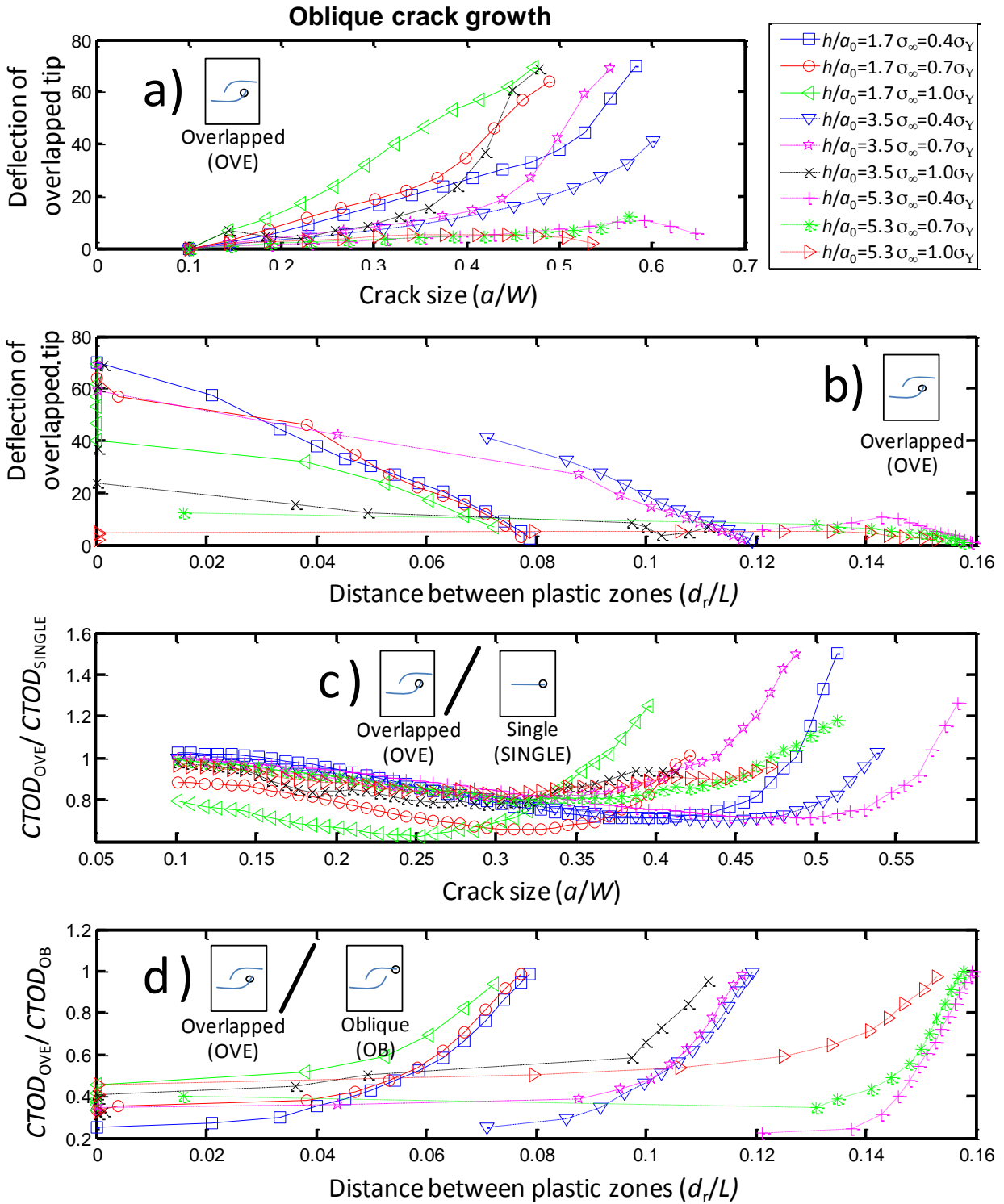


Figure 53. Oblique arrangement results for shielded tip deflection (*a*, *b*), CDF ratios of overlapped and single crack tips (*c*) and CDF ratios of overlapped and oblique tips (*d*) on the basis of the crack size (*a*, *c*) and the distance between plastic zones (*b*, *d*).

The analyses performed showed the importance of shielding processes occurring in parallel crack arrangements, even to the point of causing full arrest since CDF reductions of 90% (for  $a_{\text{DOM}}/a_{\text{SHI}}=3$ , as shown in Figure 51c) were forecasted at high loads and short distances between cracks ( $\sim 1.7 a_0$ ). The variation of  $\text{CTOD}_{\text{SHI}}/\text{CTOD}_{\text{DOM}}$  was evaluated with the distance between plastic zones showed that considerable shielding occurred independent of the interaction between plastic zones (Figure 51d), in contrast to the effect of the size ratio (Figure 51d). It was also observed that as the load was increased, greater shielding effects were predicted by the analyses developed. This process can be understood as disruption of the lines of force that existed in elastic materials and, within the plastic range, a material softening around the dominant crack that causes the lines of force to be directed even further away from the shielded tip.

The evaluation of shielding and anti-shielding when compared to the distance between plastic zones  $d_r$  in oblique arrangements revealed a different scenario (see Figure 53b). Linear slopes could be observed when  $\text{CTOD}_{\text{SHI}}/\text{CTOD}_{\text{DOM}}$  was plotted against  $d_r$  (at least for a distance equal to 3 times the original crack length). At later stages of propagation the relation between  $\text{CTOD}_{\text{SHI}}/\text{CTOD}_{\text{DOM}}$  and  $d_r$  became non-linear. At the same time, the values of  $\text{CTOD}_{\text{SHI}}/\text{CTOD}_{\text{DOM}}$  in Figure 53c showed a combined effect of shielding, while both tips overlap, and then anti-shielding, when coalescence with the middle part of the opposite crack became imminent in the secondary strain zone (as shown Figure 52). The extent of plasticity and proximity between crack tips governed the deflection rate and CDF. The crack paths observed in oblique arrangements suggested that similar trends can be involved in the fragment detachment process that occurs in the lining during bearing service conditions. Coalescence deflections, along with bifurcations, caused by the mechanical mismatch between layers, govern the lining detachment process.

The determination of coalescence based on the distance between cracks  $h$  is the most important factor. Higher levels of loading also promoted the coalescing process to a lesser extent since the

deflection of the coalescing tip increased and also CDF values grew faster as the overlapping tips approached the opposite crack face. The Forsyth criterion [121], shown in Eq. ( 14 ), revealed that the most likely conditions to promote coalescence are related to higher levels of loading. In this research project, deflections based on the MTSN criterion grew higher with increased loading levels; however, it was evident that coalescence would occur. On the other hand, at the highest separation between cracks, initial trends towards coalescence disappeared eventually, irrespective of the level of loading (Figure 53).

The relationship proposed by Wang *et al.* [120], shown in Eq. ( 15 ), indicated that coalescence would not occur in any tested scenario with values of  $h$  greater than  $0.28 a_0$ , while in this work even values of  $3.5 a_0$  resulted in clear signs of coalescence). This was expected since Wang *et al.* [120] worked with a different material and loading conditions; however, the suggestion that loading played a less significant role than the separation between cracks in this process was corroborated here. The analyses performed for oblique arrangements indicated that a separation distance  $h$  larger than 3.5 times the original crack size would be sufficient to avoid coalescence under any level of loading.

The effect of crack tip closeness to the specimen border is a topic for future work; with regard to the validity of the obtained results at late stages of crack extension where the proximity to the specimen edge could have influenced the CDF estimates.

#### **4.6. Summary**

Oblique, parallel and co-linear arrangements were studied in propagating analyses based on the MTSN criterion which extended the crack through automated procedures. Through these analyses, the evolution of CDF and the crack path were studied. Shielding and anti-shielding effects were observed in parallel and co-linear arrangements, respectively. A combination of both shielding and anti-shielding was observed in oblique arrangements.

Co-linear cracks confirmed typical CDF rises as coalescing tips approached as discussed in previous work.  $CTOD_{COAL}/CTOD_{SINGLE}$  equal to 1.3 and 1.6 times at  $\sigma_{\infty}=0.7\sigma_Y$  and  $\sigma_{\infty}=1.0\sigma_Y$ , respectively, even at a considerable distance between cracks ( $\sim 4a_0$  between coalescing crack tips) were observed. Parallel arrangements showed that a dominant crack would reduce the crack growth of smaller cracks if they were placed at a relatively small distance. Even at distances equivalent to  $5.3a_0$ , an initial CDF reduction of 10% was observed and as the difference between crack sizes increased, this initial value rose 50%. The separation distance  $h$  between oblique cracks played a more important role in promoting coalescence than the applied loading in the analyses developed. At the same time, oblique arrangements showed a trend towards coalescence through the deflection of the overlapped tips at distances between cracks below  $3.5a_0$ .

## **5. Chapter Five: 3D crack growth modelling and characterisation**

### ***5.1. Introduction***

The objective of the work described in this chapter is to study the evolution of a 3D crack front in the architecture MAS-20S under three-point bending. In order to fulfil the stated objective, two secondary essential tasks must be carried out: validation of 3D models created through automated meshing processes that incorporate subsequent crack growth and the introduction of a crack growth law based on the numerical estimations of CTOD and previous experimental work that characterised the lining fatigue crack growth behaviour of the architecture MAS-20S.

The analysed cracks originate from the lining surface and grow perpendicularly to the layers orientation under pure mode-I loading conditions. Crack growth analyses are performed in both bi-layer and tri-layer architectures. The simulation of crack growth is limited to the lining due to the excessive computational cost required to place such a 3D crack in the interlayer and the lack of data regarding the crack growth behaviour in this layer.

### ***5.2. Background***

Most surface cracks observed in engineering problems show crack growth rate variations along their crack front according to the specimen geometry, loading and environment conditions. These variations can be found in the literature for the most common loading conditions and have been assessed through analytical or FE solutions.

The FEM analysis of crack propagation in three-dimensions is based on respective two-dimensional methodologies. A case in point is the generation of specialised mesh configurations around the

crack tip that facilitates the estimation of the CDF. In contrast to 2D analyses, the crack tip becomes a front in 3D that expands according to the local CDF values, which may not be uniform along the front. The FEM model along this front usually consists of a structured mesh looking like an extrusion of the original 2D crack tip mesh configuration, as shown by Riddell [47]. The high mesh density around the crack tip in 2D problems increases the computational cost of such analyses; furthermore, the extension of this high density area along the front often persuades analysts to limit their scope to 2D and/or elastic materials modelling.

The effect of elliptical cracks on the surrounding material was initially investigated through analytical solutions for infinite solids [130-132] consisting of elastic and isotropic materials. Later works based on FE analyses [133, 134] obtained expressions for the CDF (represented by  $K$ ) for finite solids and specific loading configurations. A major issue arising in these works is the constraint applied to the front shape, which is assumed to be perfectly elliptical. Crack surfaces were thus defined by only the ellipse major and minor axis and the CDF values at the ends of these axes dictate the crack surface extension. The work by Lin and Smith [135] based on FE elastic analysis compared predictions of semi-elliptical and quasi semi-elliptical crack fronts (formed by a number of points where the CDF is evaluated) concluding that the crack aspect ratio could differ up to 20%, especially for bending cases.

The greatest challenge in the development of crack propagation analyses in 3D may be the extension or evolution of the surface crack and the numerical model representing it. The extension of the surface crack depends on the crack growth conditions that the crack front experiences locally. Therefore, the more sampling points distributed along the crack front, the more accurate the estimation of the front shape will be. Evidently, each sampling point results in additional degrees of freedom (DoF) and computational cost leading to a trade-off between accuracy and mesh density. The adoption of a suitable crack growth law to correlate the growth along the front

requires reliable and systematic experimentation. Combined with an appropriate crack growth law, different techniques such as node release [136], element erosion [137], cohesive zone modelling [105], remeshing [50, 138] and lately X-FEM [110] has been used to address 3D crack growth modelling, as mentioned in Section 3.2.3.

The results obtained through node release, element erosion and cohesive elements were shown to be significantly improved by the implementation of a “cell mesh”, shown in Figure 54, which predefines the direction of propagation and precise form of subsequent crack fronts. The success of the “cell mesh” relies on previous knowledge of the crack surface extension. For instance, every time a group of nodes is released, the next crack front form will have a pre-defined shape that is consistent with experimental results. Developing a mesh that does not include the front evolution leads to crack fronts with spiky shaped and with out of plane deflections defined by the irregular position of the nodes generated by the meshing process. Spiky crack fronts usually lead to local increments on the crack driving force to generate a smooth crack front shape, especially when homogeneous materials are assessed. This effect is greatly reduced when high mesh densities are used, leading to greater computational costs.

X-FEM and remeshing techniques do not depend on any previous knowledge of the crack growth and estimate the surface cracks growth according to the values of CDF among other factors (depending on the chosen crack growth law [47]). In both techniques, CDF will mainly dictate the extension of the crack in and out of plane according to the mode mixity [139]. The estimation of the crack growth direction in 3D problems is currently based on the approaches developed for simpler 2D analyses, discussed in Section 3.2.1. The overall shape of the crack surface is gradually formed by individual extension steps, in or out of plane, leading to complex crack fronts and surfaces.

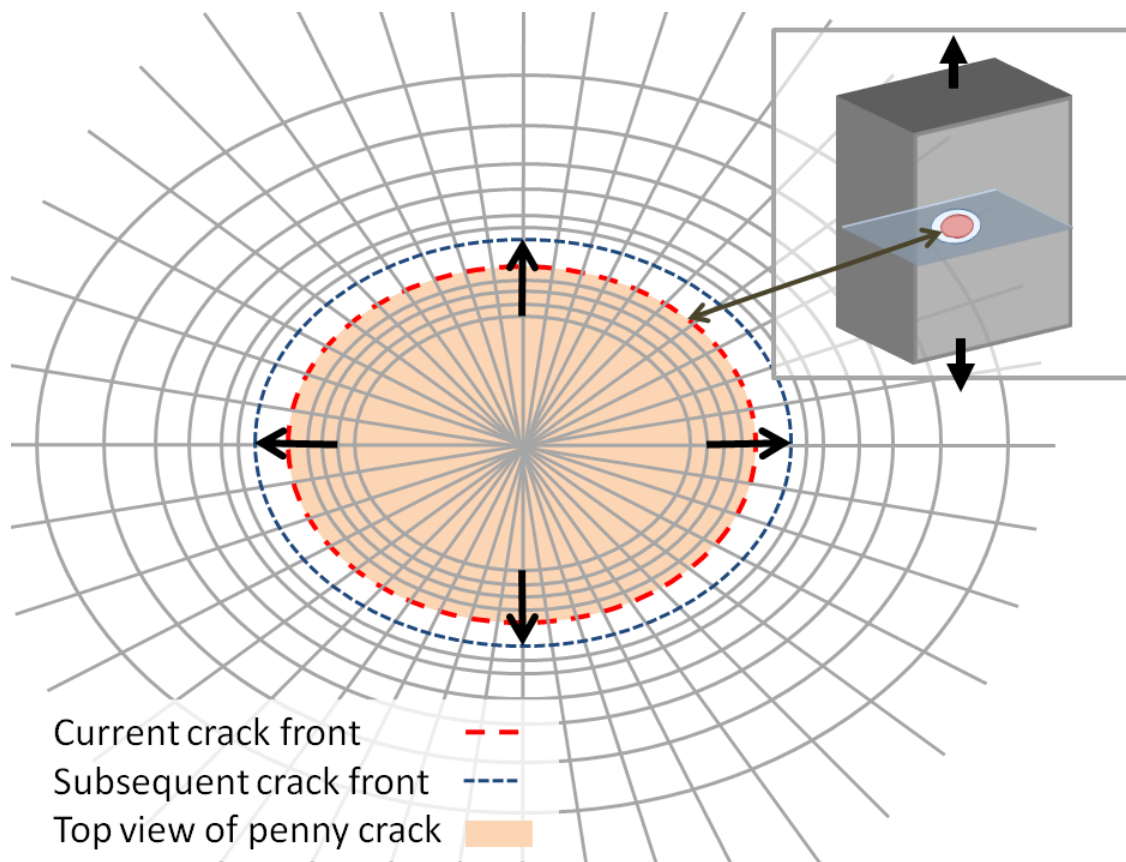


Figure 54. Cell mesh for a 3D crack propagation model.

Another issue of interest in the development of crack propagation analyses are the effects of tri-axiality and the free surface. It has been observed that initially straight crack fronts in compact tension specimens curve as propagation occurs. This curved front shows slower crack propagation at the free surfaces. These effects have been numerically studied under the LEFM scope where it has been argued that a weaker constraint of the material exists, in comparison to the middle of the specimen, that delays crack growth [140] and a weaker stress singularity is present at the free surface [141]. Furthermore, the study of this problem faces the tri-axiality transition from deep into the material to the free surface. The computation of  $K$  and  $J$  depend on assumptions of plane stress or strain, which do not represent the tri-axiality evolution along the front.

Lin and Smith [135] proposed to address the free surface effect by assuming plane stress conditions at the crack front end, where it coincides with the free surface of the specimen, and plane strain

conditions along the rest of the front. At the same time, they proposed a lower value of  $C$ , the material constant for the Paris law shown in Eq. ( 11 ), for assessing growth at the surface. This value (corresponding to  $0.9^m C$  at greater depths) appears to be related to the Poisson ratio effect on CDF estimates under plane strain conditions and showed an excellent correlation to experimental results [142].

### **5.3. Methodology for FE model creation**

Three dimensional analyses of fatigue problems through FE modelling have shown their potential to assess the crack growth process. This work, in general terms, adopts the methodology proposed by Lin and Smith [143] based on remeshing schemes to extend the crack. This methodology consists of the generation of crack front elements that are suitable for post-processing leading to CDF values (standard crack mesh configurations to calculate  $J$ -integral,  $K$  or CTOD), estimating the crack front advance according to a crack growth law and re-meshing until a critical or pre-defined crack size is reached. The time or cycles to reach a given crack length can be computed at the end of the crack extension analysis using the CDF estimates and the adopted crack growth law.

#### **5.3.1. Crack -elements generation**

The generation of FE models developed here to study crack growth due to fatigue or fracture adopted many concepts explained by Carter *et al.* [50] in great detail. Key issues identified by Carter *et al.* are the volume decomposition into smaller entities and modification of the volume containing the crack elements, so that the crack front and the boundaries of the containing volume are sufficiently separated to generate a good quality mesh. A similar decomposition into volumes comprising three main element groups was carried out here according to the element functionality as described below.

Firstly, elements with low-stress gradients are created using coarse meshes to reduce the computational time. These coarse meshes may take the form of 10-node tetrahedrons, 15-node

triangular prisms and 20-node bricks. Very thin volumes, such as the interlayer and the lining, are modelled using 20-noded bricks and 15-noded prisms to avoid ill-shaped 10-node elements. The transition between coarse and fine elements using ANSYS meshing technology is better achieved using 10-node tetrahedrons. Therefore, the steel layer consisted of the latter to facilitate the meshing process. The collapsed 20-noded brick used in spider-web crack front configurations is the 3D version of the regular brick element shown in Figure 55.

Secondly, crack tip elements (collapsed bricks at the front and patterned surrounding elements) are created in a direct manner by specifying each of the coordinates of nodes that form the elements and their position within the element according to its type. In this way, it is possible to develop the desired pattern and connectivity among elements like the spider-web tip with collapsed elements, for instance. The crack front elements are usually created so that they form a solid cylinder structure with easily identifiable sections or planes, as shown Figure 56. The section with the desired crack pattern is created perpendicular to the path to improve the computation accuracy of CDF, usually based on 2D methods [47, 50, 143].

The creation of the crack tip elements is based on ANSYS modelling tools that allow the use of local coordinate systems. Such local coordinate systems are positioned and oriented according to the CDF results at the previous step post-processed through the MATLAB routines developed for that purpose (listed in Appendix C). The MATLAB routines post-process the FE results to provide estimations of CDF, compute the proportional extension along the crack front, generate a new crack front and define the position of the 2D crack sections at a perpendicular orientation to the crack front arc.

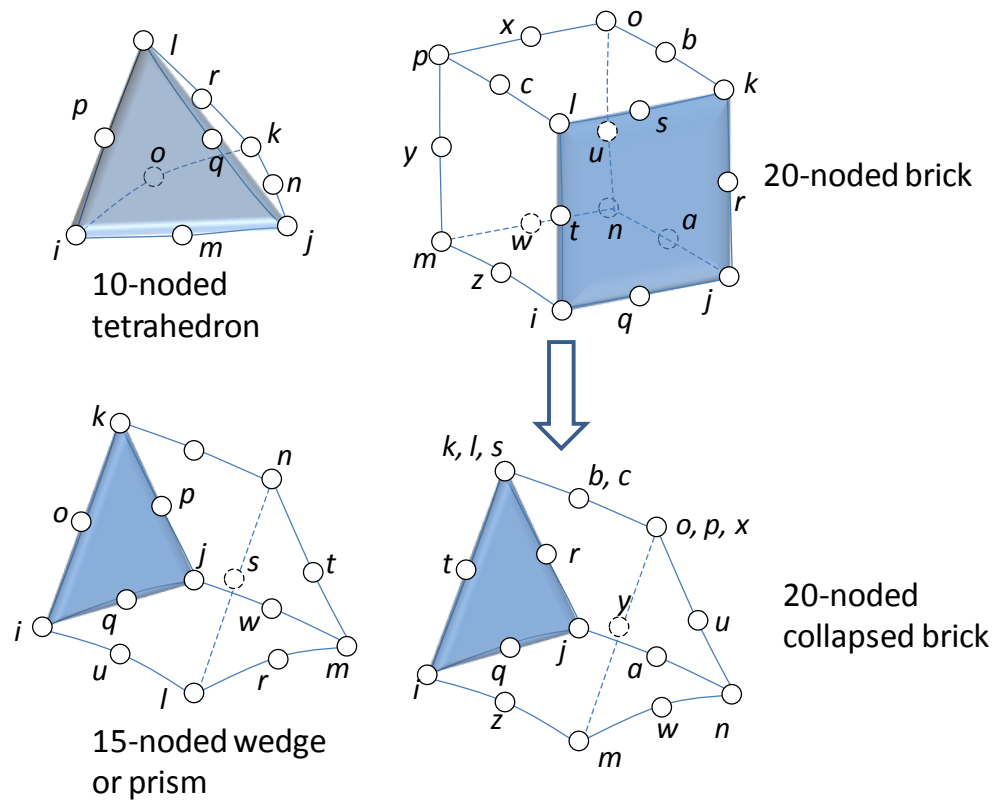


Figure 55. Three-dimensional elements and collapsed version.

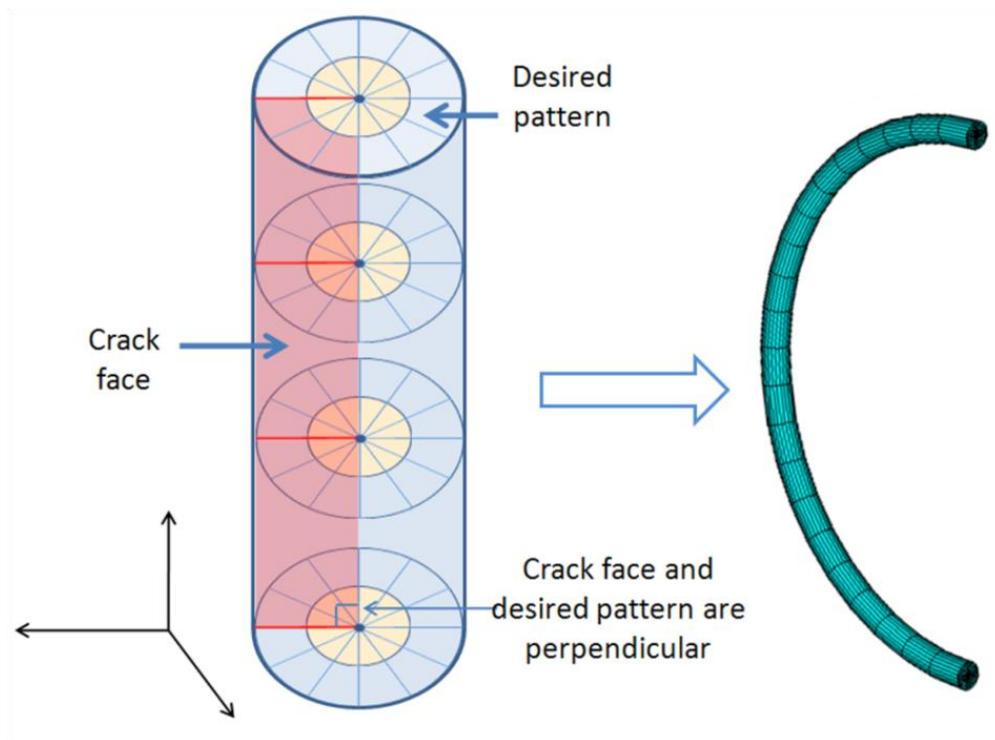
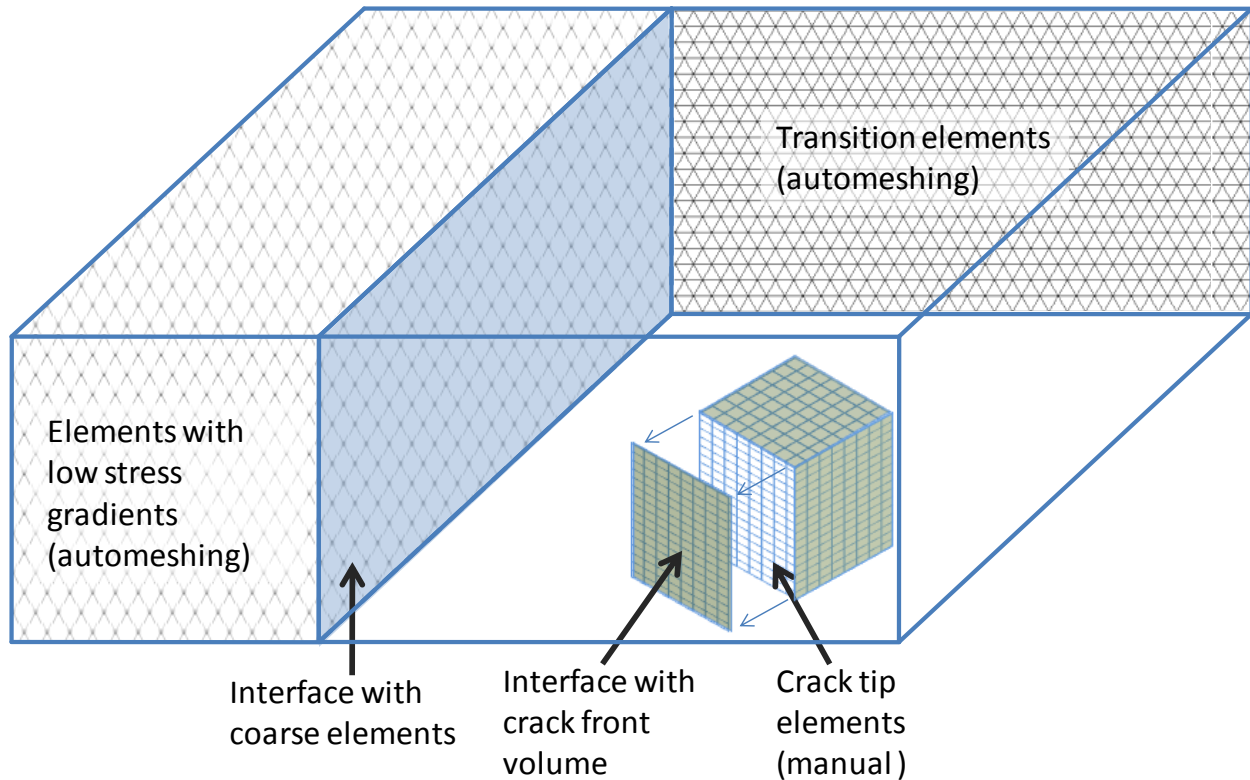


Figure 56. Crack front mesh in cylindrical arrangement.

The generation of blunted tip or spider-web element arrangements in two-dimensions is a cumbersome task that can be based on geometrical entities such as points, lines and surfaces using auto-meshing tools in ANSYS, for instance. However, the generation of crack front elements in three-dimensional models using such geometrical entities is a rather unstable process due to the need for Boolean operations, whose execution was not successful on a regular basis. Initial attempts to perform the meshing process indicated that a mixed approach, which entails direct element creation and automatic meshing, provides the best results. Direct element creation and its coupling with the rest of the model are implemented through additional MATLAB routines that generate ANSYS input files, shown in Appendix C. This implementation places local 2D coordinate systems along the pre-defined initial crack front and orients each local coordinate system to be orthogonal to the crack front arc at its origin. The coordinates of nodes that form the 2D sections are also predefined with the possibility to be scaled up or down to obtain the best compromise between accuracy and computational cost. The size of these sections determines the transition zone, which represents the most expensive part of the model, computationally speaking. A fixed numbering system is used in the node generation facilitating the assembly of the crack tip elements using programming loops in MATLAB.

Thirdly, the transition elements, which surround the crack tip elements inside the crack block, link crack tip and low-stress gradient volumes (regions). These transition elements are created through an automatic meshing process based on and constrained by an interface that consists of surfaces surrounding the crack tip and the low stress gradient elements. The three main element groups are schematically illustrated in Figure 57.



**Figure 57. Crack block generation and interfaces in low-stress gradient and crack tip elements.**

It is particularly important for the implementation of this methodology to construct crack fronts according to the CDF values obtained at the end of each solution step. This implementation is capable of creating blunted and spider-web configurations using quarter-point wedges or collapsed brick elements. At the same time, circular, elliptical or user-defined shapes can be adopted for the initial crack front while the subsequent front shapes are determined by the CDF and the adopted crack growth law. An example of the created mesh is shown in Figure 58.

### 5.3.2. Crack driving force post-processing

The post-processing operations for generating CDF values is carried out following the approach proposed by Lin and Smith [143] where planes that include a blunted tip or spider-web configuration are formed normal to the crack front; the CTOD is used as CDF parameter in this work instead of  $K$ . Blunted tip and spider web configurations have opposite nodes at the crack faces, thus

allowing efficient calculation of the opening and sliding displacement between the faces. The CTOD estimation is based on the relative movement of opposed nodes at a particular distance away from the crack tip. The selected opposed nodes were positioned at a distance  $d_{\text{blunt}} = 960 \text{ nm}$  and  $d_{\text{spid}} = 900 \text{ nm}$  away from the tip, schematically shown in Figure 59 and Figure 60. These node pairs were chosen due to their proximity. Typical minimum element sizes for the blunted tip in the radial and circumferential direction are  $e_{\text{blunt-rad}} = 300 \text{ nm}$  and  $e_{\text{blunt-circ}} = 26.1 \text{ nm}$ , respectively; while for the spider-web elements to  $e_{\text{spid-rad}} = 300 \text{ nm}$  and  $e_{\text{spid-circ}} = 82.1 \text{ nm}$ .

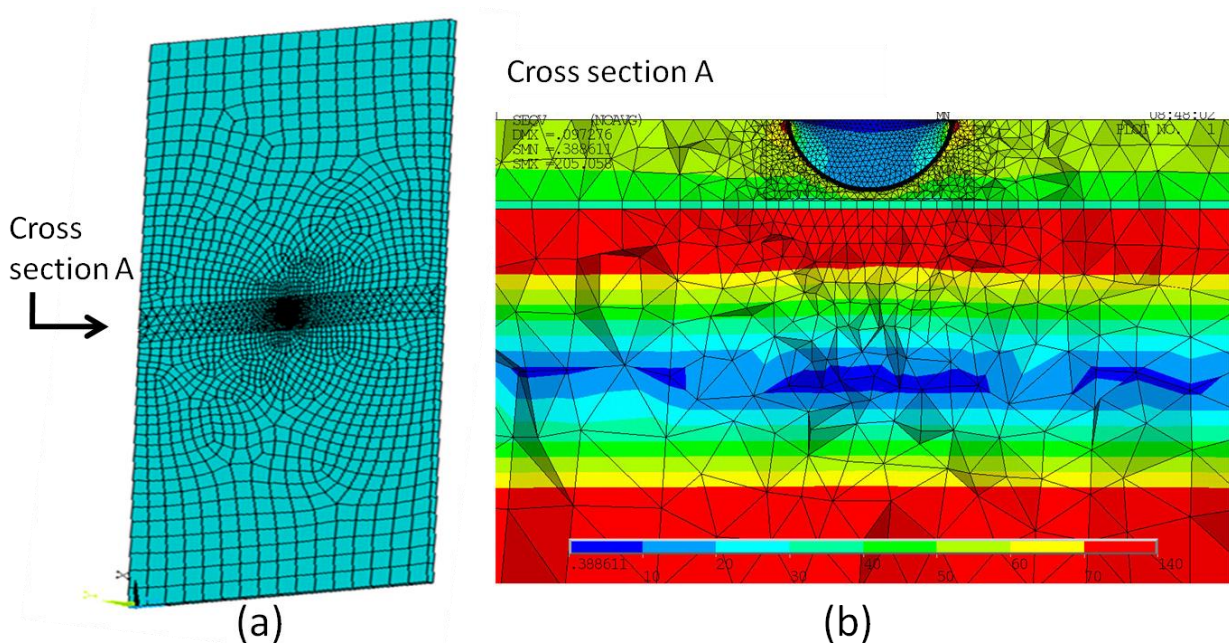


**Figure 58. Typical mesh examples showing the lining surface (a) a cross section showing von Mises stress.**

The element size used for 3D analyses is slightly larger than that used for the 2D counterpart. Nevertheless, the generated elements still had a comparable size to that of microstructural features found in the lining of the architecture MAS-20S. Similar to 2D analyses, 3D assessments are not intended to account for any heterogeneity in each individual layer, but to the modelling of extensive plasticity and the positioning of crack tips at small distances from the layers' interface.

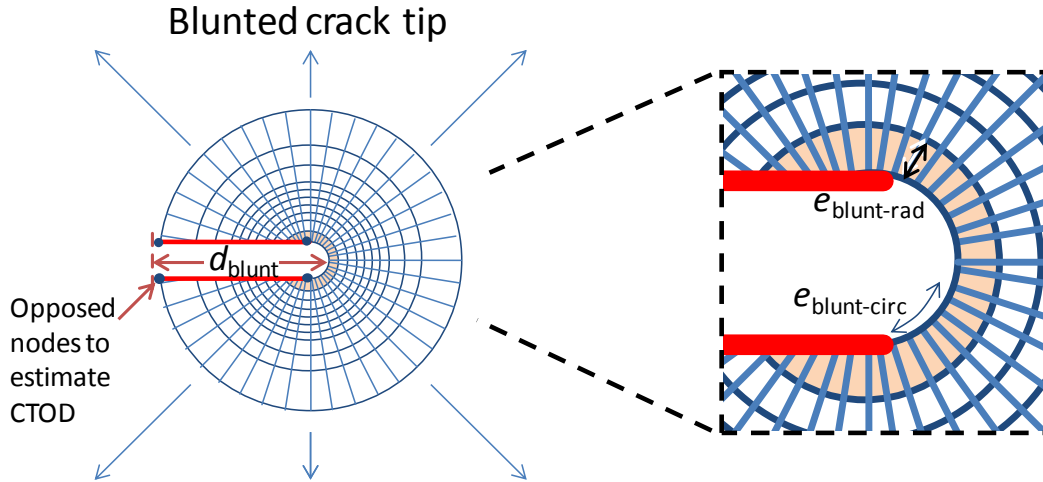


Figure 59. CTOD measurement in blunted tip mesh configuration.

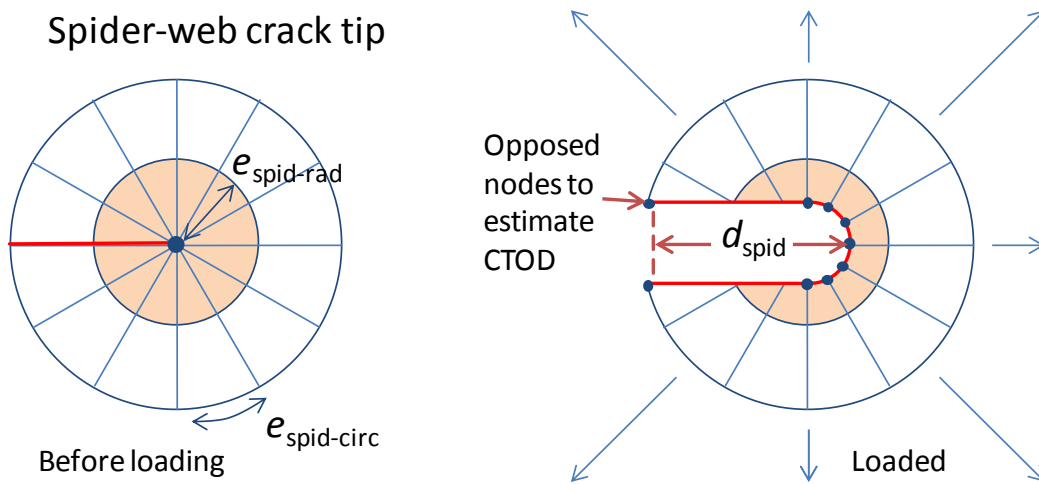


Figure 60. CTOD measurement in spider-web mesh configuration.

### 5.3.3. Crack front advance and remeshing

The crack front advance was based on the relative growth around the crack front and the definition of a maximum extension step  $\Delta a_{\max}$ , corresponding to the  $CDF_{\max}$ , according to Riddell *et al.* [47]

$$\Delta a_i = \frac{\left(\frac{da}{dN}\right)_i}{\left(\frac{da}{dN}\right)_{\max}} \Delta a_{\max} = \frac{f(CDF_i)}{f(CDF_{\max})} \Delta a_{\max} \quad (16)$$

where  $\Delta a_i$  refers to advance at the location  $i$ ,  $(da/dN)_i$  to the expected growth rate at the location  $i$ , and  $(da/dN)_{max}$  to the maximum growth rate along the crack front. The use of small values of crack advance is recommended for problems with sudden crack front changes, deflections that cause out of plane crack growth and other factors that contribute to the formation of irregular crack surfaces.

Remeshing operations in this methodology only require the generation of a new crack front and transition elements. The new crack elements created along the crack front were created according to the CDF estimates at the previous step. As the crack front length grows, the number of elements is automatically increased so that a fairly constant element size is maintained throughout the crack propagation analysis, as shown in Figure 61.

#### ***5.4. Crack front meshes comparison***

The accuracy of the estimated CTOD and its sensitivity to mesh refinement along the crack front are assessed in models with two different crack tip arrangements, namely, spider-web and blunted, applied to the specimen under the loading schematically shown in Figure 62. The dimensions of the analysed plate are the same as those of the flat strip specimen shown in Figure 18 but with a reduced thickness equal to  $2 t_{L2}$ , for the purpose of assessing a mesh representative of the ones to be used in the multi-layered system. The surface crack took the shape of a penny crack and symmetry conditions replaced free-of-traction conditions on the open face of the lining. The crack is oriented perpendicular to this face with a radius of  $0.266 t_{L2}$ , resulting in an embedded crack subjected to remote tensile stresses. Firstly, a sensitivity study on the mesh refinement along the crack front was carried out using an elastic material model, and secondly, a comparison with an exact solution for a penny-crack in an infinite solid was made using blunted and spider-web meshes with quarter-point elements. The material used for these analyses correspond to the MAS-20S

lining elastic properties, with a Young's modulus equal to 70 MPa, subjected to a far field tension of 20 MPa.

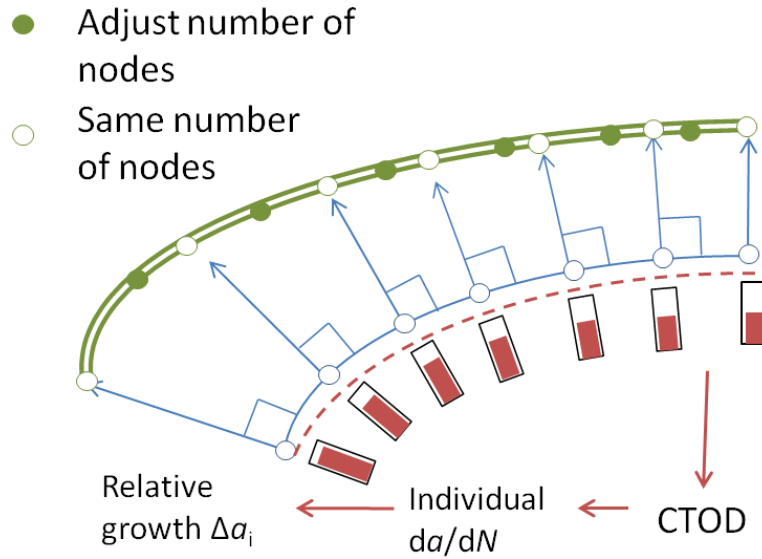


Figure 61. Relative crack extension along the front.

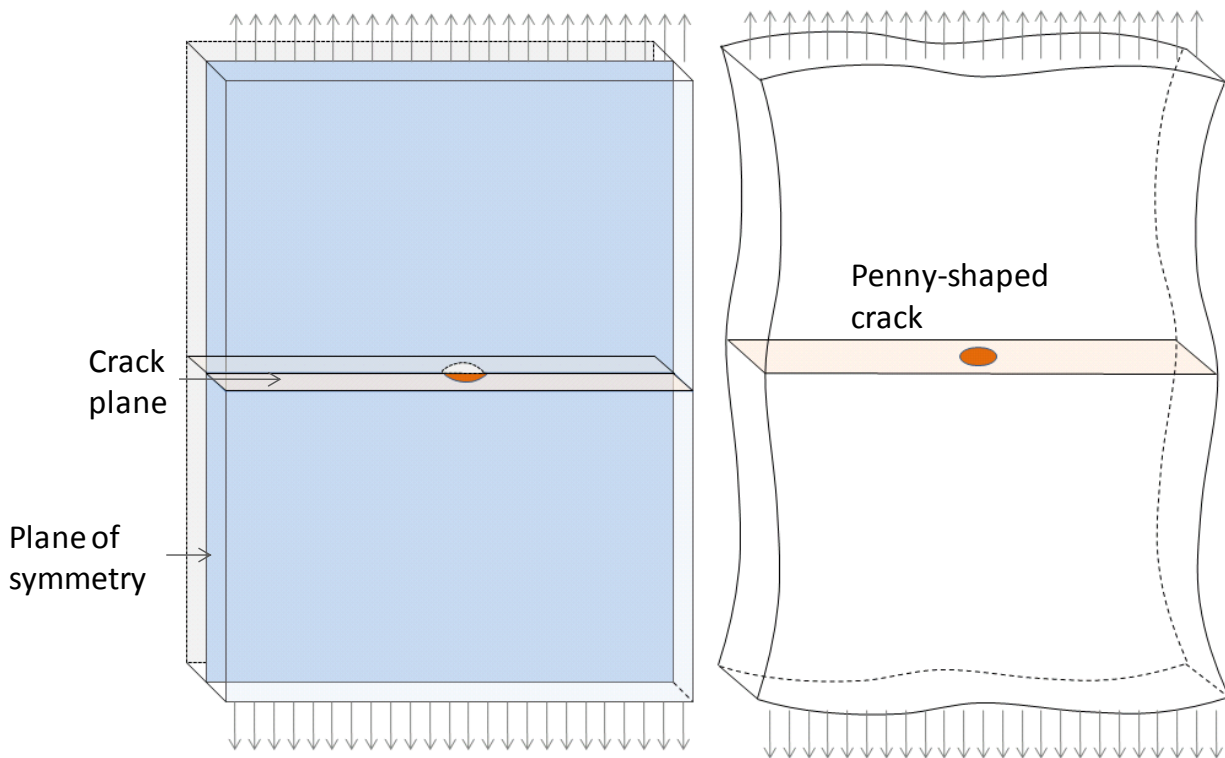


Figure 62. Numerical (left) and exact solution (right) for embedded crack under tension.

### 5.4.1. Convergence studies of CTOD estimates

A convergence study is carried out for both crack tip meshing configurations to determine the effect on CTOD estimates of the number of elements that form the crack front of an embedded crack. This number was varied from 18 to 54 elements obtaining CTOD estimates of around 9 nm at  $d_{\text{spid}} = 900$  nm. Convergence tests carried out in this section provided a good idea of the computational costs expected from subsequent elasto-plastic analyses. According to preliminary numerical tests, each elastic analysis using the ANSYS Sparse Direct Solver required from 1 to 3 hours of computing time using a four-Intel Xeon processors with 8 GB of RAM memory analysing between 60,000 and 120,000 nodes. The computational cost required to solve a non-linear FE model can be divided into two parts: iteration cost and number of steps and iterations per step. The iteration cost is mainly driven by the number of DoFs used in the analysis and how much time is required to form and invert the stiffness matrix. The total number of iterations is controlled by the non-linearity of the problem and is greatly affected by high stress gradients over the material, as occurs around the crack tip. The computational cost in terms of each iteration was much greater in 3D in comparison to 2D models; this was expected due to the higher number of DoFs used in the analysis. However, the number of iterations may drop since elements of greater size are used in 3D (compared to previous blunted tip models in 2D) leading to the use of fewer elements in high gradient areas. Efficient FE models are indispensable for the tasks planned due to the significant computational cost required.

Figure 63b shows that spider-web configurations, which use quarter-point elements suitable for elastic analyses, provide crack tip opening estimates that are more or less constant along the crack front. A single crack tip opening value is expected along the crack front of a circular embedded crack in infinite solids due to the axisymmetric nature of the problem. The created FE model has finite dimensions, one of which is a small thickness equal to  $2 t_{L2}$ , and a reduced separation between the crack and the volume boundary which contrasts with the infinite solid dimensions. Therefore,

the results obtained from the slim FE model should reflect the same axisymmetric trend to ensure that its boundaries did not influence its predictions.

Higher scatter was observed in CTOD estimations from blunted tip models, shown in Figure 63a, attributed to the higher aspect ratio of the used elements, in comparison to that of spider-web models, in the circumferential and the crack front direction. Models with higher mesh refinement along the crack front showed a significant improvement towards a more uniform CTOD value. It is also noteworthy that the requirement on the undeformed blunted tip radius to be at most one fifth of the estimated CTOD [45] was not fulfilled. The analysis of smaller blunted tips would lead to even larger aspect ratios since the tip elements would have a smaller size. The evident alternative to solve this problem is a mesh refinement in the radial and crack front direction leading to greater computational cost.

Spider-web configurations provided a more uniform estimation along the front, visually detected, of CTOD values when compared to those obtained from blunted tip meshes at the same level of refinement along the front. Less scatter can be achieved from blunted tip meshes with greater mesh refinements but also computational costs.

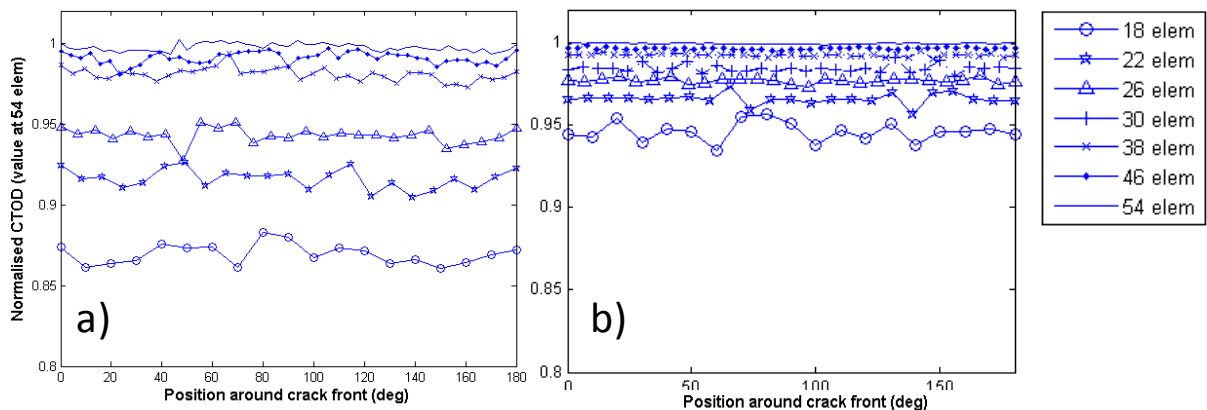


Figure 63. Convergence analysis with blunted tip (a) and spider-web (b) models.

The use of quarter-point and collapsed elements in spider-web arrangements seems a better choice for elastic and elasto-plastic analyses, respectively. Collapsed elements, whose formulation shows a similar singularity to perfectly plastic deformation at the crack tip, are suitable for simulations with extensive plastic deformation. The fourth level of mesh refinement (30 elements in Figure 63b), which corresponds to an average element size of 5.85  $\mu\text{m}$  along the crack front, provides the best initial compromise between accuracy (97.7 %) and time spent per analysis (1.1 hrs at small crack lengths) considering that as the crack extends computational demands would increase.

#### 5.4.2. Spider-web crack tip model and exact solution

An exact solution for stress and displacements in an infinite solid containing a flat ellipsoidal crack was developed by Green and Sneddon [132] in the 1950s. This solution provides the means to obtain the crack opening for penny-shaped or ellipsoidal cracks. The crack opening for a penny shaped flaw is reduced to an axis-symmetric problem which yields

$$COD = \frac{4 \sigma_{\infty} (1 - \nu^2)}{E \pi} \sqrt{r (2a - r)} \quad (17)$$

where  $a$  is the crack radius and  $r$  to the normal (radial) distance from the crack front.

The specimen geometry used for this comparison is shown in Figure 62. The specimen, material models and loading conditions are those used in the convergence analyses on the previous section. These analyses revealed that the crack openings were slightly underestimated (around 5%) using an average element size of 5.85  $\mu\text{m}$  along the front, especially at  $d_{\text{spid}} < 1 \mu\text{m}$ . The agreement of the results obtained from the FE model in comparison to those of the exact solution varied between 95% and 99%. Such underestimations are consistent with results from the convergence analysis in Section 5.4.1 and, according to Figure 64, the agreement of the FE model grew as  $d_{\text{spid}}$  is increased. The obtained level of accuracy appears to be adequate for the proposed research, especially at  $d_{\text{spid}} > 1.5 \mu\text{m}$ .

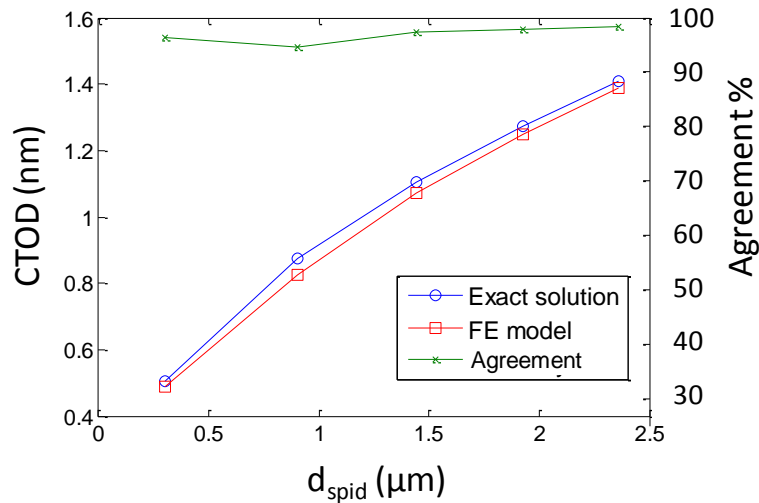


Figure 64. Crack opening profile using developed model and exact solution evaluated at 5 sampling points.

### 5.5. Crack growth law

Fatigue crack propagation modelling is based on a crack growth law. This law relates the most representative parameters in a crack growth process to the crack growth rate. In this way, it is possible to estimate the number of cycles necessary to reach a critical or desired crack size for 2D and 3D problems and estimate the proportional growth along the front of 3D cracks, as shown in Figure 61.

The development of a fatigue crack growth law for any given material requires relevant experimental data capturing the physical behaviour of the near-tip material as it separates. Evidently, the law to be proposed should include the most significant factors in the process and provide good approximation to the values obtained experimentally. The relationship, shown in Eq. ( 11 ) in Section 1.4.2.1, proposed by Paris and Erdogan [35] allows the estimation of long crack growth within the designated Regime B, as shown in Figure 5.

Crack growth observed in the lining of the MAS-20S architecture was previously associated [8] with short fatigue crack behaviour. The study and prediction of small fatigue crack growth through traditional LEFM methods has showed significant differences leading to total life overestimations.

The differences between the behaviour of long and short cracks have been previously related to effect of closure, different separation mechanics and microstructural features [144], as described previously in Section 1.4.2.2.

Various models have been proposed to represent small fatigue crack growth based on experimental data [145, 146], statistical approaches involving the microstructural barriers [147, 148], the plastic zone interaction with grain boundaries [149] and the crack tip strain [150]. The latter one combined the resolved shear stresses in different grains and the distance to typical microstructural features with a typical crack growth law.

Within the scope of this work, it is believed that a statistical approach as described by Miller [147] is consistent with the available experimental evidence and modelling techniques. This approach has modelled this growth behaviour based on the crack length  $a$  within a material with a typical microstructure feature size  $D$  according to

$$\frac{da}{dN} = C(D - a)(\Delta\gamma)^\beta \quad (18)$$

where  $C$  and  $\beta$  are constants and  $\Delta\gamma$  cyclic shear strain. This relationship [147] shows that crack growth is only affected by the position of the first microstructural barrier; further growth could be modelled with established relations for long cracks.

In contrast, the approach proposed by Chan and Lankford [150] assumes that the effect of the microstructural barrier remains irrespective of the crack size. The distance  $X$  between the crack tip and the microstructural barrier as well as a crystallographic function  $k(\Phi)$ , ranging from 0 and 1 and expressed in terms of the resolved shear stress, dictate the crack growth reduction at a given level of CDF according to the relation

$$\frac{da}{dN} = C \left( 1 - k(\Phi) \left( \frac{D - 2X}{D} \right)^m \right) (\Delta K)^n \quad (19)$$

where  $m$ ,  $n$  and  $C$  are fitting parameters related to the material behaviour. The form of the assumed crack growth rate is shown schematically in Figure 65.

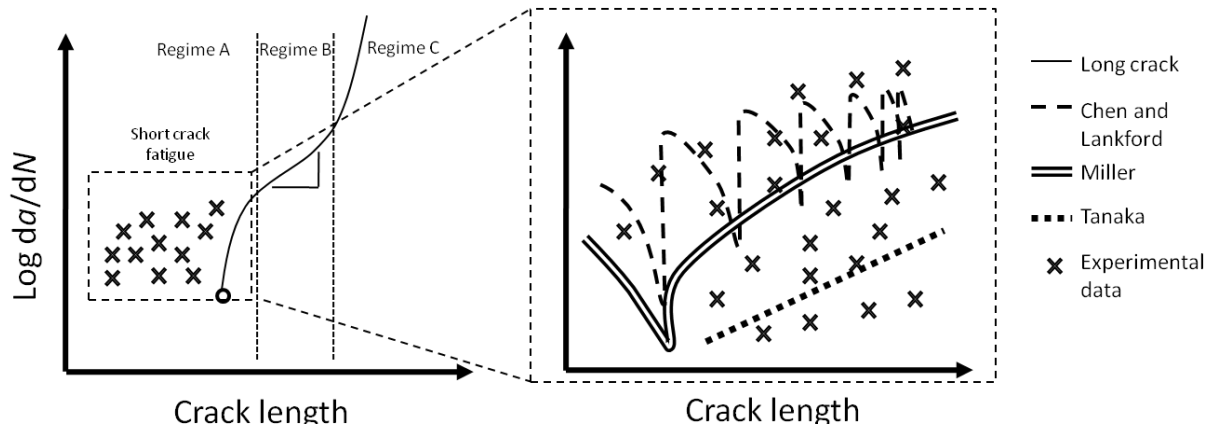


**Figure 65. Assumed behaviour by small fatigue crack growth models by Chan and Lankford and Miller.**

Other typical CDF parameters such as the CTOD have also been used for the study of short cracks. Tanaka *et al* [145] studied ductile materials under cyclic loading and proposed a crack growth law based on CTOD estimations leading to satisfactory results when compared to experimental data. The form of the relationship proposed by Tanaka *et al* [145] is

$$\frac{da}{dN} = C'(\Delta CTOD)^{n'} \quad (20)$$

where fitting parameters  $C'$  and  $n'$  accounted for the material behaviour. The  $n$  exponent values obtained for materials such as copper and steel ranged between 2.29 and 1.39. Such a form of crack growth law has also been used to characterise the behaviour of physically small cracks with crack lengths between 0.05 and 1 mm [151].

The relationships proposed by Chan and Lankford [150] and Miller [147] require the selection of a typical microstructural size that would work as a barrier to crack growth under a simplified

distribution within the material. Accounting for the position of every single barrier along the crack path from a particular characterised specimen would represent a complex task beyond the scope of this project. Therefore, it was assumed here that these barriers are homogeneously distributed within the material according to the material characterisation of the MAS-20S architecture, described in Section 1.4.5. The material characterisation presented in [10] considered that hard intermetallics were the most representative barrier among the existing second phase particles. These barriers appear to be located at a mean distance equal to  $28.88 \pm 12.63 \mu\text{m}$ . The mean distance and two other representative values, located at a separation equal to one standard deviation on each side, were used to assess the impact of this variability.

The crack growth law development was only possible due to material characterisation data from [10], three-point bending experiments [10] and their simulation through three-dimensional FE models in this thesis. The process is schematically outlined in Figure 66.

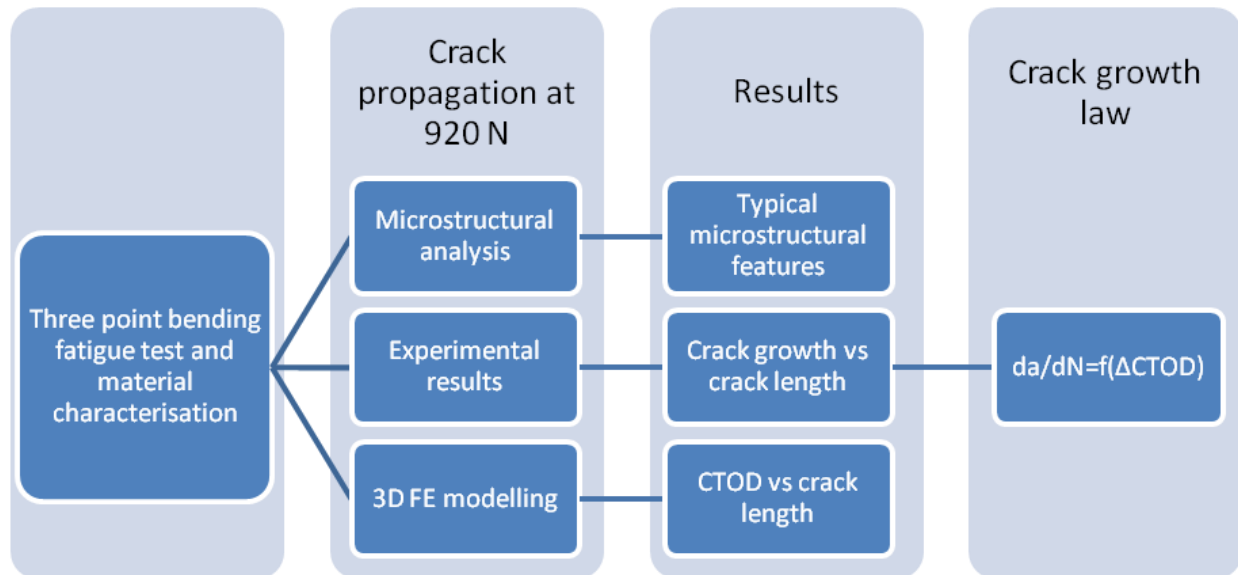


**Figure 66. Crack growth law generation.**

### 5.5.1. Experimental crack growth data

Interrupted fatigue tests were performed on a tri-layer flat strip specimen (designated MAS-20S) under three-point bending as shown in Figure 18 [10]. This study was conducted using a maximum load of 920 N, corresponding to top lining plastic strain of approximately 0.006, a load ratio of 0.1 and a frequency of 10 Hz. More details related to these tests can be found in Section 1.4.5 or in Reference [10]. Only data obtained from cracks smaller than 0.3 mm, equivalent to an estimated depth of 0.15 mm, was used for the growth law development in order to minimise the shielding and anti-shielding effects on the crack growth and CDF. Furthermore, since a large number of cracks of such a small length existed, the overall impact of individual coalescing events would be reduced. These events occur less frequently in longer cracks; however, greater crack length increments can arise under these circumstances. Additional effort was directed to accounting for coalescence effects in later sections of this thesis. The experimental results of crack growth are shown in Figure 67; indicating clearly that long crack behaviour did not control the growth.

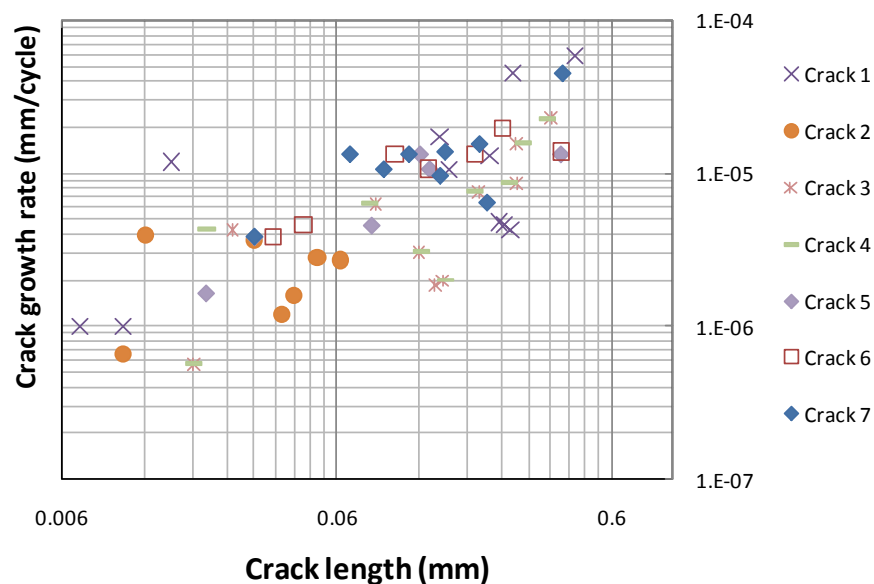


Figure 67. Crack growth rate vs. crack length as reported in [10].

The existence and growth of flaws in the material amplifies stresses and strains significantly. The 2D model assuming plane strain conditions provided an initial estimation of the expected spread of plasticity in the lining. The applied load caused a significant extent of plasticity, as shown in Figure 68, covering the entire surface of the lining and the central part of the backing.

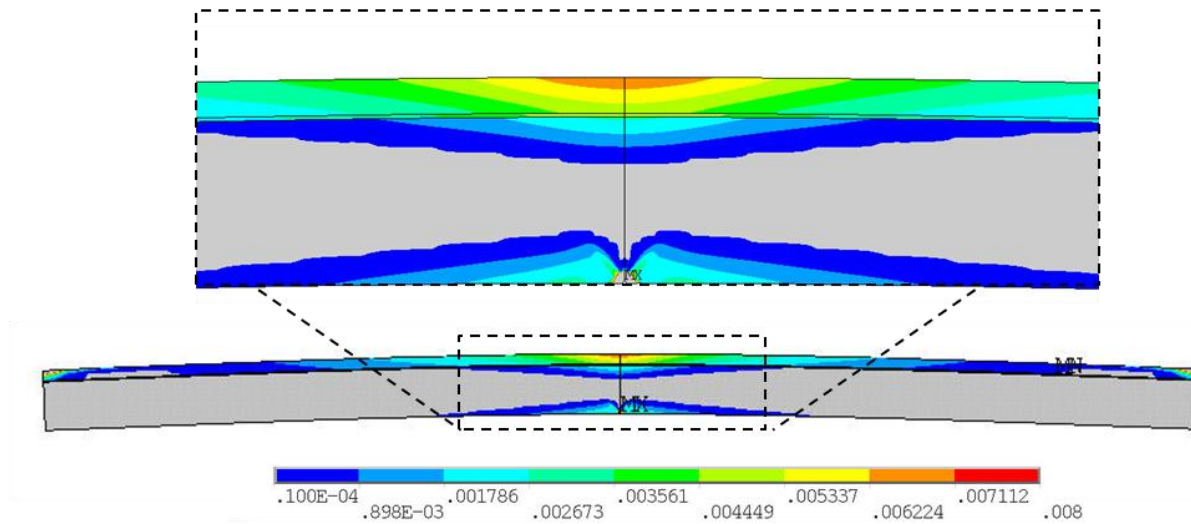


Figure 68. Predicted spread of plasticity under a load of 920 N (Von Mises strain contours are shown).

### 5.5.2. Linking experimental and numerical analyses

The experimental set-up presented in Section 1.4.5 set the foundations for the development of numerical models for the estimation of crack growth. The conditions under which the fatigue experimental data was obtained were replicated through 3D FE models that assumed elasto-plastic material behaviour, shown in Figure 15 and Table 3. The replication of these experiments enhanced the understanding of stress and strain states evolution and provided estimated values of CDF along the crack front.

The replication of experimental conditions was intended to yield a relationship between the conditions experienced by the crack tip and the consequent crack growth rate. The size of the analysed cracks corresponded to micro-structurally short fatigue crack regime [11] and their

experimental growth rate assessment, shown in Figure 67, also presented characteristic short crack behaviour. At the same time, a crack growth law that reflects local crack tip conditions is required for the future assessment of shielding and anti-shielding mechanisms caused by layered architectures.

Short fatigue behaviour and local crack tip conditions can be linked through the relationships described by Miller [147] or Chan and Lankford [150]. The extent of the influence, in terms of crack length, of microstructural barriers on crack growth rate remains to be evaluated. The choice between the two relationships was to be decided according to their ability to represent the crack growth rate behaviour obtained experimentally.

At the same time, the CTOD was used as the CDF parameter as previously done by Tanaka *et al* [145]. The new forms of the crack growth laws, that is, the modified Miller (MM) and modified Chan and Lankford (MCL), are, respectively:

$$\frac{da}{dN} = C'(D - a)(\Delta CTOD)^{n'} \quad (21)$$

$$\frac{da}{dN} = C' \left( 1 - \omega \frac{(D - 2X)}{D} \right) (\Delta CTOD)^{n'} \quad (22)$$

The values of the material property  $m$  was assumed to be equal to 1 as reported in other works [10]. The crystallographic function  $k(\Phi)$  was replaced by the variable  $\omega$  that would indicate the maximum reduction of CDF at the microstructural barrier ( $\omega = 1$  would lead to crack growth arrest). The intention of these analyses is principally to evaluate the layer heterogeneity effect rather than the local heterogeneity within the analysed alloy. The relationship proposed by Tanaka *et al* [145] was also originally meant to describe the cyclic behaviour of the material through the  $\Delta CTOD$  as CDF parameter. A rigorous estimation of  $\Delta CTOD$  through FE analyses involves the application of loading and unloading processes while the crack is extended and the collection of

stress deformation history accounts for crack closure [152]. However, such analyses do not seem to be feasible for crack growth analyses where more than 100,000 loading cycles are to be applied.

Such simulations face the complexity of modelling reverse plastic flow and initial attempts to do so found that the large deformations generated by the high loads applied caused instabilities to the solution process when the maximum load was released. Similar results were obtained in 2D analyses with blunted cracks; the use of spider-web configurations also presented such challenges. A simplified alternative assumed that the CTOD corresponding to the minimum load during the cyclic analysis approximates to the CTOD value obtained when an equivalent load is applied monotonically. This assumption, according to LEFM theory [11], is expected to provide overestimated values of the  $\Delta$ CTOD depending on the extent of crack closure through the propagation process. However, a more extensive analysis to determine more accurately the  $\Delta$ CTOD involves computational costs entailing resources beyond the available capacity. At the same time, it is believed that such an overestimation would not affect the total life estimates provided that the generation of a crack growth law and subsequent total life assessments follow a consistent methodology.

The difference between cyclic and monotonic estimations of  $\Delta$ CTOD was assessed using a 2D model subjected to 4 cycles without crack extension under a load of 200 N. This model also considered contact between the crack faces in order to account for the possibility of closure. This simulation showed that the application of a load ratio of 0.1 did not lead to crack closure and the difference at the minimum load between the CTOD value obtained monotonically and cyclically only was 1%. This discrepancy was assumed to remain small at higher loads; however, more caution should be exercised when smaller, or negative, load ratios or longer cracks are assessed since crack closure would influence the estimation of  $\Delta$ CTOD to a greater extent.

### 5.5.3. Results

As mentioned earlier, the FE analyses providing the aforementioned correspondence between crack size and  $\Delta$ CTOD were based on elasto-plastic material models. Two different load cases were applied in this study since the computation of  $\Delta$ CTOD required the values of the maximum and minimum crack opening at 920 N and 92 N, respectively. The solution required an iterative process where the number of iterations and time required for individual iterations depended on the crack front size. Between 20 and 100 total iterations were necessary to achieve convergence while individual iterations consume between 1 and 2 hours. Twelve different crack lengths were considered for this analysis involving  $\sim$ 1320 hours of processing on a workstation with 4 Intel Xeon processors and 8 GB of RAM. Very expensive runs were necessary to simulate the process at the load level applied experimentally, showing that almost the whole lining is in the plastic regime and significant plasticity also spreads into the backing layer causing large deformations as shown in Figure 69. The extent of plasticity observed in this 3D model was similar to the one observed in its 2D version under the same loading.

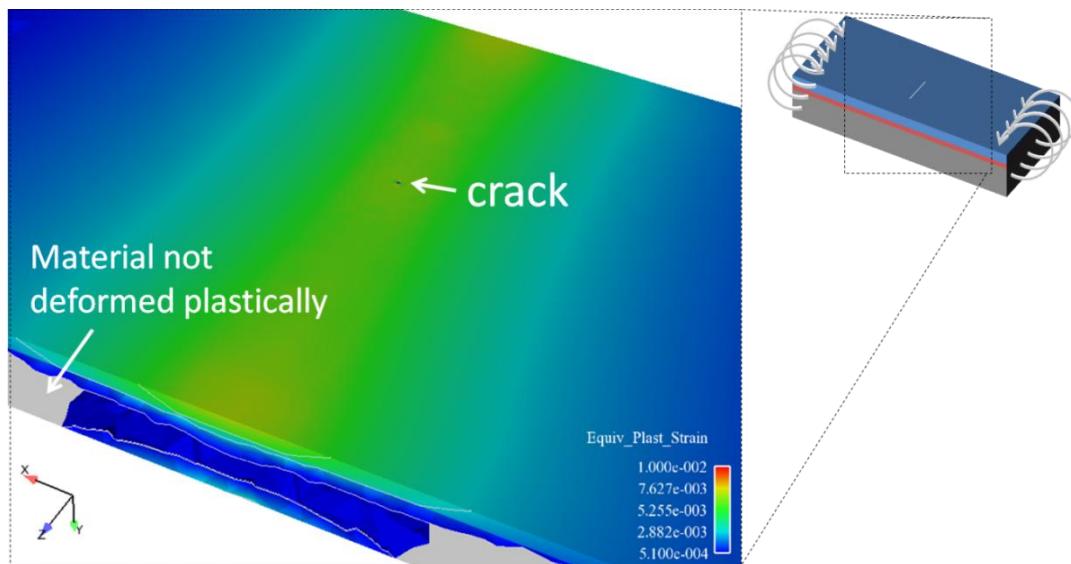


Figure 69. Spread of plasticity at 920 N.

The numerically obtained relationship between  $\Delta CTOD$  and crack length is shown in Figure 70 for the tested loading cycle. A power relationship was fitted to these data and, in this way, it was possible to obtain  $\Delta CTOD$ -crack growth rate pairs leading to a crack growth law. The crack growth rates obtained experimentally are shown in Figure 71 plotted against the numerically obtained CDF.

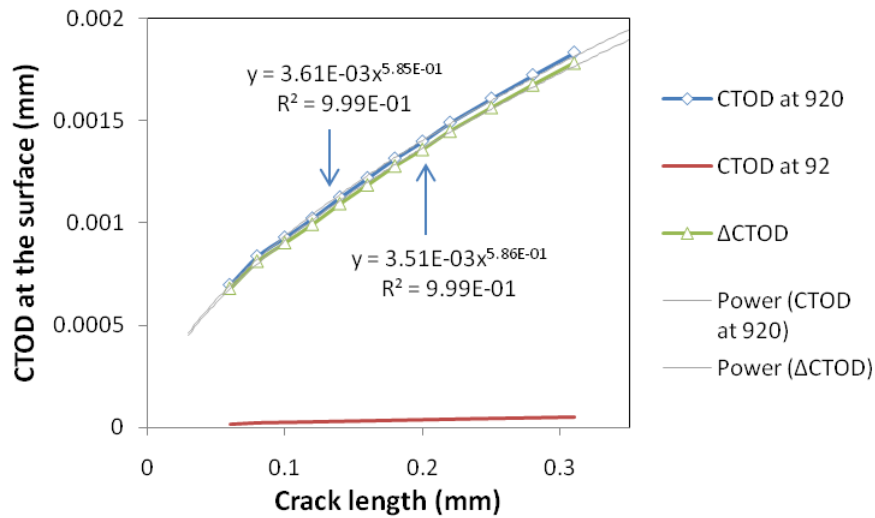


Figure 70.  $\Delta CTOD$ ,  $CTOD$  at 920 N and  $CTOD$  at 92 N vs. crack length under three-point bending.

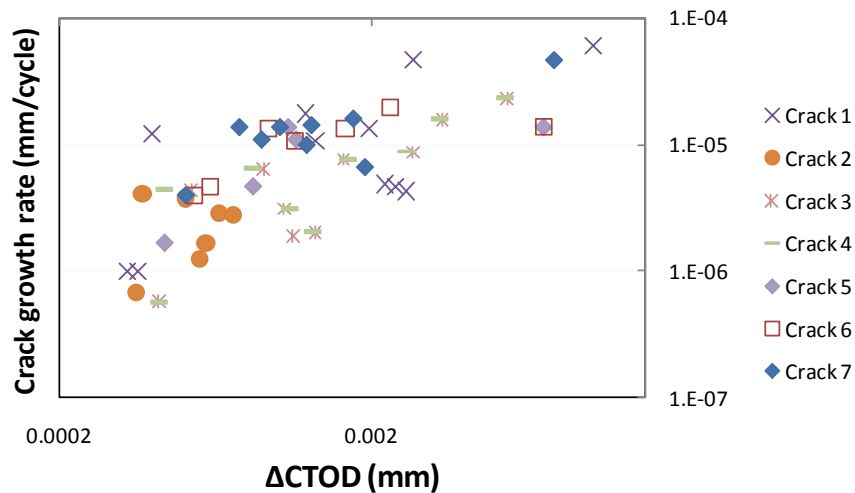


Figure 71. Crack growth rate vs.  $\Delta CTOD$  under 920 N in 3D model.

Equations ( 20 ) and ( 22 ) were fitted to experimental data presented in Figure 67 and Figure 70 using the least square method. It is evident that the MM, represented by equation ( 20 ), is

dependent on the chosen value of  $D$ . Therefore, three different sets of values for  $C'$  and  $n'$  laws were fitted according to characteristic values of  $D$  (based on previous data on hard intermetallics for the MAS-20S). The values selected for  $D$  were the mean of the near neighbour distance, equal to 28.88  $\mu\text{m}$ , and two other values separated from the mean by one standard deviation, that is, equal to 41.15  $\mu\text{m}$  and 16.15  $\mu\text{m}$ . The power trend line based on the relationship proposed by Tanaka was also obtained. The estimated parameters from these fits are shown in Table 6 and their plots in Figure 72. From this figure it can be observed that the Tanaka line goes through the middle of the cloud of points obtained experimentally; however, it is noteworthy that this law did not account for any microstructural effect.

**Table 6. Fitted values of  $C'$  and  $n'$ .**

	$D$	$C'$	$n'$
Tanaka	-	0.019	1.129
Modified Miller	$D=28 \mu\text{m}$	7.33-e7	-1.042
	$D=16 \mu\text{m}$	3.78e-8	-1.213
	$D=41 \mu\text{m}$	4.83e-7	-0.822
Modified Chan and Lankford	Upper level	4.000e-2	1.000
	Lower level	1.538e-3	1.000

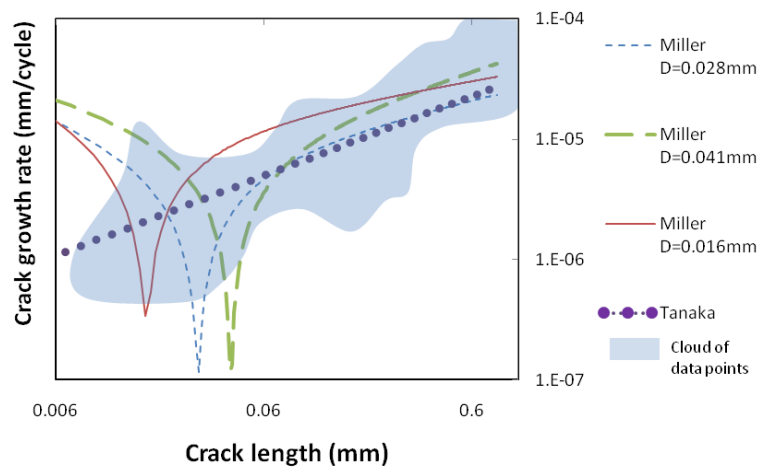


**Figure 72. Fitted crack growth relationships illustrating the behaviour of on the relation described by Miller (MM) based on the cloud of data obtained experimentally.**

The lines obtained for the MM relation showed its characteristic behaviour consisting of a single and significant drop in crack growth rate at crack size equal to  $D$ . The variation of this parameter also had a significant influence on the estimation of the fitting parameter  $C'$ , shown in Table 6. The trends obtained showed that the variability observed in the cloud of experimental points with a crack size smaller than 0.06 mm could be explained by the presence of a microstructural barrier. However, a similar variability was observed at cracks with a size greater 0.06 mm where a less significant variability is forecasted by the MM law.

In contrast, the periodicity observed in the MCL relationship led to a different approach due to the periodicity effects on the fitting process. It was considered that the estimation of a power law relationship (identical to the proposed at Tanaka *et al* [145]) bounding the experimental data would be more representative of the crack growth process. These upper and lower boundaries would provide information of extreme behaviour and, at the same time, facilitate the development of a law of this form assessing the importance of the typical distance between microstructural barriers, as previously described for the MM relationship, and the crack initiation position between barriers. The estimation of such upper and lower levels was done by proposing different values for the constants  $C'$  and  $n'$  and comparing them visually to the cloud of data obtained experimentally. The estimated parameters for upper and lower levels are shown in Table 6 and plotted in Figure 73 along with a typical behaviour. At the same time, Figure 73a shows the differences between laws based on  $D = 41 \mu\text{m}$  and  $D = 16 \mu\text{m}$  while Figure 73b shows the impact of the position of initiation site within barriers (initial distance to first barrier, subsequent barriers were assumed to appear at equidistant separations of magnitude  $D$ ). The effect of these differences on the total life was evaluated in the next chapter.

The form of the MCL relation shows that the values chosen for  $C'$  and  $n'$  determine the maximum values of growth rate obtained for any given level of CDF (when  $D = 2X$ ). In contrast, the selection

of  $\omega$  determines the maximum reduction. Therefore, the values chosen for  $C'$  and  $n'$  were those of the upper boundary; on the other hand, the reduction required for the estimates obtained from the upper boundary to match those of the lower boundary was approximately 96%, leading to the selection of  $\omega = 0.96$ .

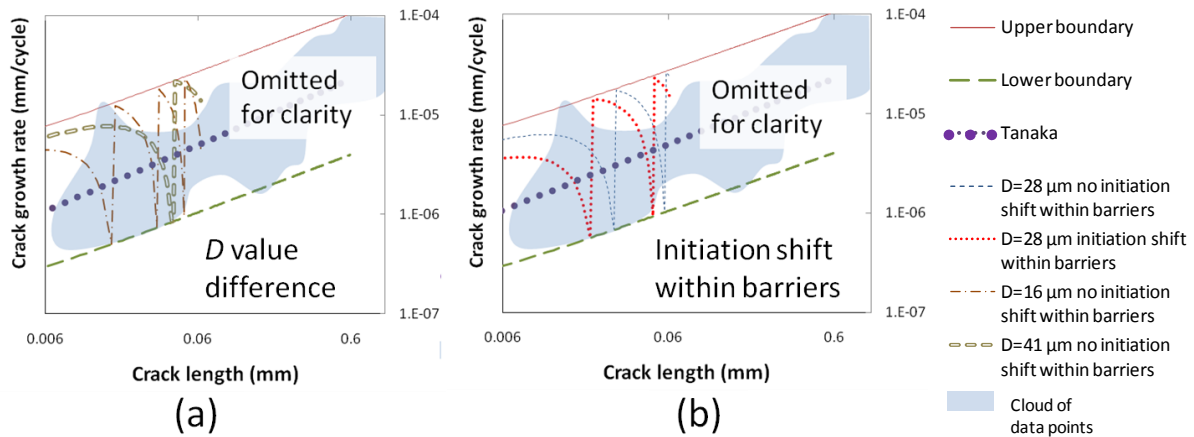


**Figure 73. Fitted crack growth relationships illustrating the behaviour of the relation proposed by Chan and Lankford (MCL) based on the cloud of data obtained experimentally showing the effects of the selection of  $D$  (a) and the selection of initiation location between barriers (b).**

#### 5.5.4. Discussion

The selection of the crack growth law has an important effect on the total life estimates. According to the results shown in Figure 72 and Figure 73, it is not possible to determine unequivocally which value of  $D$  would provide more conservative or accurate estimates of crack growth. Therefore, further assessments on the impact of this variable are made in later sections. However, particular trends are discussed next.

The model proposed by Tanaka appears to provide a representative measure of the average crack growth conditions for the range of crack sizes analysed, as shown in Figure 72 and Figure 73 since it went through the cloud of experimental data points. However, the absence of microstructural insight may cause significant life overestimations especially when a crack growth law developed from long crack data is extrapolated to the small crack range.

The estimated exponent  $n$ , equal to 1.13, for the Tanaka relation was of the same order of magnitude as the estimations made in previous work [145] in other ductile materials such as steel and copper (1.13 and 1.17, respectively) with a low content of second phase particles. The trend presented by these different materials showed that higher values of yield strength corresponded to lower values of  $n'$ . The crack propagation law obtained for the lining aluminium alloy did not follow this trend since the lining exhibited a higher yielding stress (51 MPa in comparison to 40 MPa for the copper) but an identical value for  $n'$ . This discrepancy may be attributed to the different loading configurations and, especially, to the different extents of plasticity exhibited in both studies. However, it is believed that the obtained values of  $n'$  are consistent with previous work.

The trend lines obtained from the MM relation appeared to reflect more closely the nature of experimental data cloud (inspected visually) near the position of the micro-structural barrier, in comparison to Tanaka's. Experimental data at greater crack lengths (larger than 0.06 mm) also showed that the crack growth rate variability was not represented by the laws based on Tanaka nor Miller relations. At the same time, further analysis of the fitting parameters revealed that the CDF in the Miller model would have an unusual effect on the crack growth rate. The negative values obtained for  $n'$  indicate that as the CDF is increased, as a result of higher levels of loading, for instance, smaller crack growth rates would be expected. This trend cannot be correlated nor justified by any physical observation. These results were attributed to the application of a single load and the use of another variable that is closely related to the CDF, the crack size. The information entered into the model was not sufficient to allow the separation of these two variables.

The trend lines obtained from the MCL relation appeared to correlate better with the cloud of experimental data, inspected visually. Accounting for microstructural barriers at crack lengths could explain the existence of crack growth rate variability at cracks 10 times larger than  $D$ .

The proportional growth along the crack front can be calculated through equation ( 17 ) and the adopted crack growth law. This is expressed as the ratio between local and maximum crack growth. Assuming that a single value of  $D$  would be used for every particular crack length and along any direction of crack growth, the Tanaka, MM and MCL relations would yield the same result for relative crack growth. Evidently, this would imply that microstructural and crack size parameters remained constant along the front and would only change as the crack extends.

$$\Delta a_i = \frac{\left(\frac{da}{dN}\right)_i}{\left(\frac{da}{dN}\right)_{\max}} \Delta a_{\max} = \frac{\Delta CTOD_i^{n'}}{\Delta CTOD_{\max}^{n'}} \Delta a_{\max} \quad ( 23 )$$

The value of  $n$  equal to 1.13, obtained from the law based on Tanaka relationship, was used in the next crack front estimations. This value was used due to its better overall consistency to experimental data ( $R^2=0.56$ ).

Additional steps to avoid early service failures according to the British Standards [153] consist of the use of  $C'$  values equal to the average plus two standard deviations as safety factor. According to these recommendations, the value of the  $n'$  parameter remains unchanged, which in practice facilitates the fatigue life calculations since any modifications to the  $C'$  parameter only has an inverse proportional effect to the number of cycles estimated but would not modify the estimated crack fronts due to the proportional growth represented by equation ( 23 ). In the particular case of this study, any modification to the  $n'$  parameter requires the re-calculation of the crack front succession. A safety factor applied to the  $C'$  parameter appears a convenient option for the generation of a safe design; however, more caution should be exercised as the variability in the factor  $n'$  increases due to its exponential effect on the crack growth rate.

## **5.6. *Elasto-plastic analyses for the evaluation of shielding***

The analysis of propagating cracks using elasto-plastic material models was carried out on the MAS-20S architecture (tri-layer) and a hypothetical one for which the interlayer was assumed to be part of the lining (bi-layer), as previously done in Section 2.3. The proportional crack growth along the front was modelled here based on Eq. ( 23 ) as discussed in Section 5.5.4. The crack growth study under moderate yielding, using a load of 200 N, facilitates the modelling of cracks reaching a small distance from the layers' interface, where shielding and anti-shielding effects are most intense.

### **5.6.1. Results and discussion**

Three-dimensional crack growth simulation under moderate yielding caused by three-point bending was found to be a computationally expensive process in terms of processing time and results storage. The models developed to account for various crack sizes ranged from 60 000 elements and 120 000 nodes to 140 000 and 240 000 nodes. This significant increase on the DOFs occurs due to the need for keeping the element size constant as the crack grows.

The processing time of the analysis of each crack model required between 12 and 26 hours using computational facilities with 4 cores and a total of 4 GB of RAM memory. The number of degrees of freedom used in these simulations required extensive amounts of in-core memory for the solution, that is, between 3.5 and 10 GB. The RAM memory usage varied from 700 MB and 2.2 GB, which seemed to be the maximum allowed in the computational facilities used for a single process. Reaching this limit caused the solution process to slow down significantly. Overall, the storage of result files for both architectures exceeded 50 GB of hard disk. The computational cost of tri-layer and bi-layer architectures was comparable despite the greater propagation depths of 0.4 mm for the latter one in comparison to 0.36 mm for the former. Crack front proximity to the layers' interface in the tri-layer resulted in slow convergence rates due to the more compliant interlayer.

The crack extension step was varied during the analysis reducing gradually in order to achieve crack growth assessment near the layers' interface and capture the effects of shielding and anti-shielding. The starting extension step was set at 0.04 mm and was reduced to 0.01 as the crack depth exceeded a value of 0.27 mm at both architectures. The step was further reduced at a crack depth of 0.34 mm and 0.37 mm in the tri-layer and bi-layer architecture, respectively.

The crack front evolution in bi-layer and tri-layer architectures was almost identical below a crack depth of 0.27 mm, as shown in Figure 74. Small differences can be observed at greater depths, which were consistent with the CDF trends obtained from two-dimensional analyses where bi-layer and tri-layer architectures provided almost identical outcomes until the crack tip approached sufficiently the layers interface, as shown in Figure 23. The difference between the predicted crack fronts in tri-layer and bi-layer was only visible when the distance between fronts was compared at the surface and the deepest point at depths greater 0.3 mm. The crack front forecasted in the tri-layer architecture showed an almost unnoticeable greater depth, or smaller aspect ratio, than that of the bi-layer architecture, as expected due to shielding and anti-shielding effects.

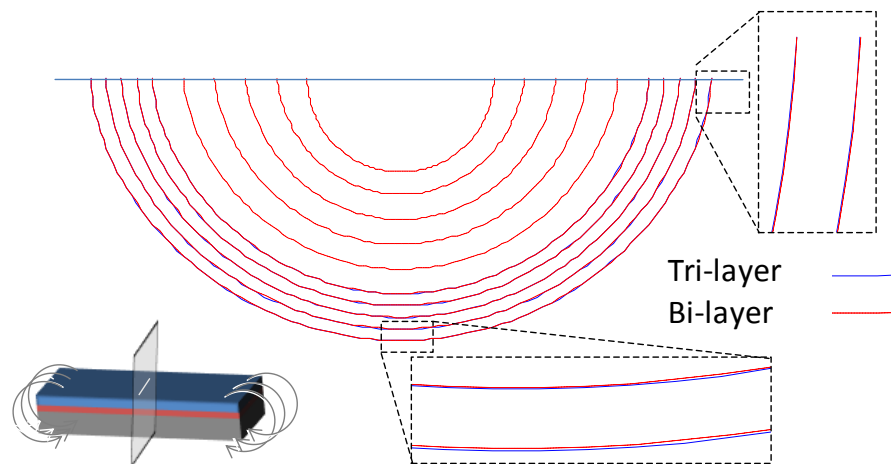


**Figure 74. Crack front evolution in bi-layer and tri-layer architectures.**

### 5.6.1.1. Crack driving force evolution and shielding

The crack front evolution in both architectures showed notable similarities at the estimated values of CTOD and their pattern along the crack front, shown in Figure 75. This pattern had maximum values at the surface while the minimum was located at the deepest point of the crack front as observed by previous authors when bending stresses are applied [135, 143, 154]. The sampling points at which the CTOD was estimated along the front were positioned at equal distances (based on coordinates related to the normalised length of the front); similar 3D plots presented later in this work are arranged in the same manner.

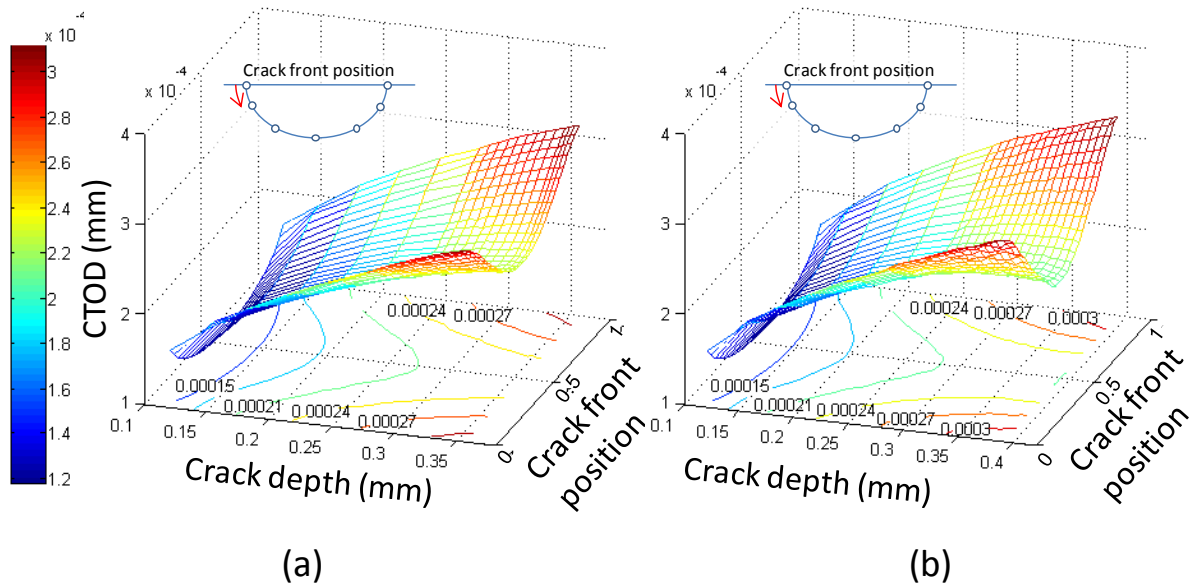
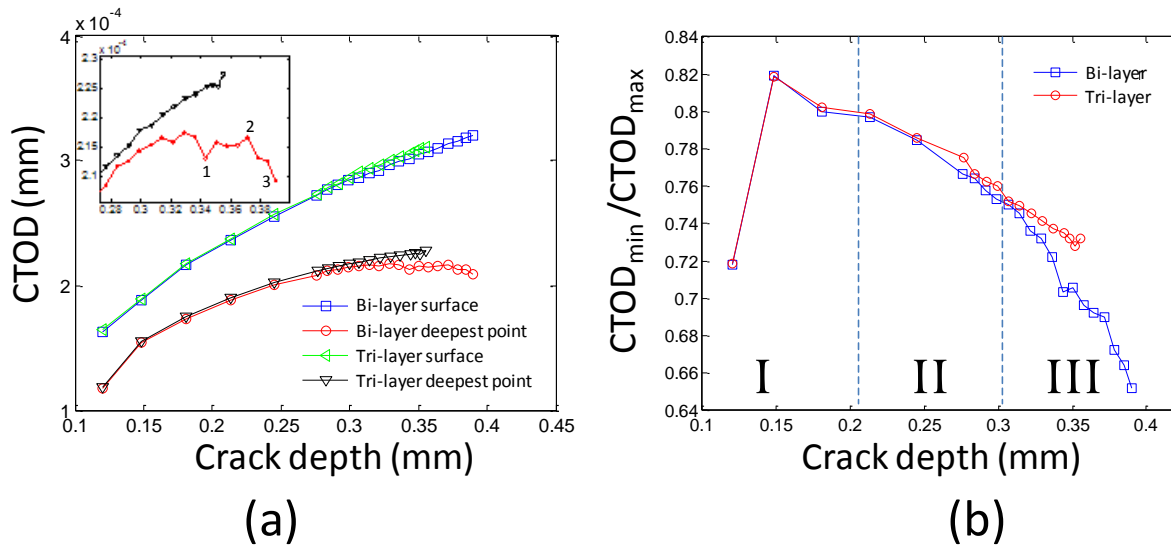


Figure 75. Crack front evolution in tri-layer (a) and bi-layer (b) architectures at 200 N.

The evolution of CTOD distribution along the crack front with crack depth for both architectures is shown in Figure 76. In both architectures, the CTOD estimates at the surface showed very similar values and rising trends. In contrast, the estimates at the crack's deepest point showed a significant difference as the crack front approached the layers' interface. The CTOD estimates obtained below crack depths of approximately 0.31 mm were almost identical irrespective of the analysed architecture with rising trends of a lesser slope than those observed at the surface.

As expected, shielding and anti-shielding effects were only visible at the deepest point of the crack front at depths greater than 0.31 mm. Crack growth beyond this point showed accelerating and decelerating trends according to the adjacent layer stiffness. However, it could be observed that these trends did not affect to a great extent the magnitude of the estimated CTOD.



**Figure 76. Crack driving force evolution (a) and CDF ratio between values obtained at the deepest point and at the surface (b) in bi-layer and tri-layer architectures.**

The evaluation of  $CTOD_{min}/CTOD_{max}$ , which represents the ratio of CDFs at deepest point along the front and at the surface at each simulation step, showed more clearly the evolution of these two parameters, as shown in Figure 76b. Through this plot it is possible to identify three different growth phases: initial transition from circular to quasi semi-elliptical (I), crack growth under pure bending conditions (II) and start of shielding and anti-shielding mechanisms (III). The initial form transition phase consisted of the changes that the crack front must undergo to achieve a more natural shape according to the loading conditions. The rate of change depended on the difference between current and natural shape. In this particular case, a slightly elongated crack in the direction of the flat strip length developed due to the deformation caused by three-point bending.

The second phase showed the typical results of crack growth in a monolithic specimen subjected to tension-bending with maximum values of CDF at the free surface where the bending moment achieves its maximum value. As the crack front grew progressively deeper into the strip, lower CDF ratios were estimated. This behaviour has been previously observed [135] in the crack growth in monolithic strips and it is associated with significant change of the crack aspect ratio as the crack front approached the neutral axis of the strip. However, the loading conditions and multi-layer architecture produced a different stress distribution to the ones observed in pure bending conditions in a monolithic strip. The stress distribution through the lining thickness in an undamaged specimen at 200 N corresponded to a combined tension-bending loading case in a monolithic strip where tensile stresses are dominant (tension of about 53.5 MPa and maximum bending stress of about 8.5 MPa). The ratio between tension and bending stresses is a key indicator of how the crack front deforms; however, it is important to consider that these conditions may vary as the crack extends and plasticity spreads over the material.

The third phase shows the clearest signs of the appearance of shielding and anti-shielding. Shielding appeared to increase the rate at which  $CTOD_{min}/CTOD_{max}$  decreased in the bi-layer architecture, as shown in Figure 76b. In contrast, anti-shielding kept almost constant the rate at which  $CTOD_{min}/CTOD_{max}$  decreased and, possibly, closer to the layers' interface this ratio may stop decreasing or even go up. However, the small separation between the front and the interface would not allow a significant crack change before the crack penetrates the interlayer. The crack growth in the interlayer offers interesting prospects for future work. The modelling challenges of a front placed within two different materials and the computational challenges offered by even greater deformations in the interlayer hints at the complexity of this assessment.

The crack growth analyses developed in the bi-layer architecture with a crack depth greater than 0.34 mm showed sudden drops and rises in the evolution of CDF, as shown by the enlarged view in

the inset of Figure 76a (Points 1, 2 and 3). The existence of these peaks may indicate that the extension steps used here were not sufficiently small to capture the changes of CDF and, in consequence, reproduce the correct front shape due to the addition of shielding effect to that of the overall deformation state governing the crack front extension. Despite the existence of these peaks, the overall shielding trend was clear. Therefore, a further crack extension refinement was not considered necessary.

### ***5.6.1.2. Comparison to 2D analyses***

The development of two-dimensional analyses has been preferred over its three-dimensional counterpart when possible due to the evident difference in modelling complexity and solution time. Despite their shortcomings, two-dimensional models may provide an initial estimate before developing more complicated models or a good approximation when a quick response is required. It is evident that the two-dimensional simplification made to the three-point bending simulation reduces the stiffness of the specimen more dramatically by modelling a width-through crack instead of half-penny type crack.

The CDF estimates from 2D and 3D analyses subjected to a load of 200 N showed a clear difference in magnitude, as shown in Figure 77. Higher CDF estimates are expected from the 2D model since a through crack along the width was assumed. The acceleration and deceleration effects on the CDF caused by shielding and anti-shielding in 3D models did not show the strength observed in two-dimensional analyses. This difference can be attributed to the constraint that the surface crack shape causes as it expands as a whole.

Shielding and anti-shielding are localised effects that only affect small segments of the crack front. The small separation between front and layers' interface would affect the CDF values locally causing disproportional growth that modifies the surface crack profile. The segments affected most intensively by shielding and anti-shielding accelerate or decelerate, respectively, the crack growth

of the neighbouring crack front material. At the same time, the neighbouring material obstructs the disproportional growth of the most affected areas. In other words, shielding and anti-shielding effects are averaged or diluted into a greater portion of material.

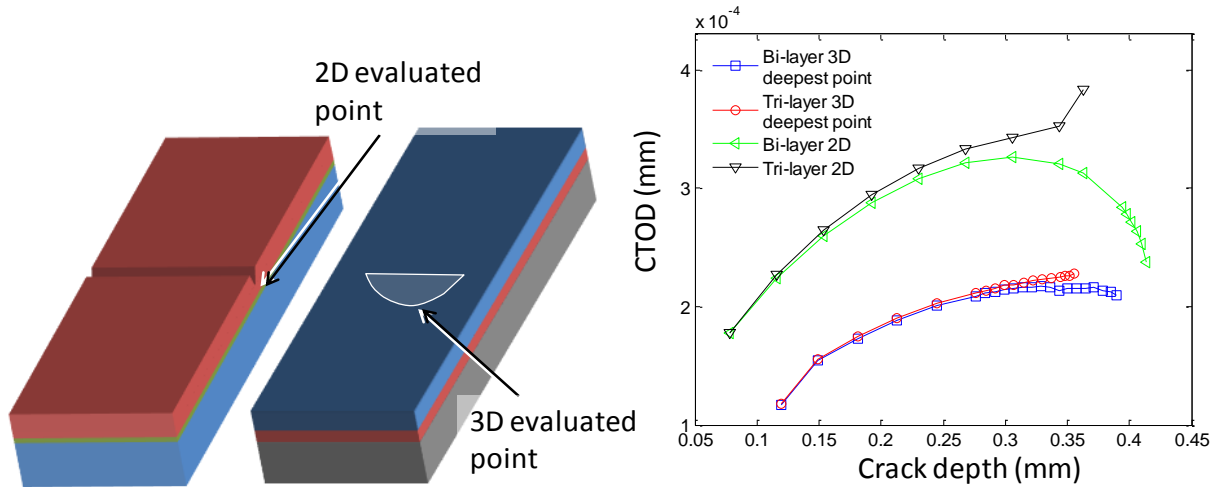


**Figure 77. Comparison between CDF estimates obtained from 2D and 3D models at both architectures.**

### 5.6.1.3. Plastic zone

The plastic zone has been extensively studied in test specimens with through-width cracks. Tri-axiality effects have been of interest in these specimens, often accounted for assuming plane strain or plane stress conditions according to the location in the specimen. The shape of the plastic zone around half penny-type crack is more complicated, especially when loading conditions differ from uniform remote tension normal to the crack surface. Figure 78 shows how the plastic zone located deeper into the material is smaller in comparison to the one observed at the surface. This effect has been explained [11, 23] through the difference between the tri-axial state of stress and strain around the evaluated points at the crack front and the loading conditions applied.

The shape and size of the plastic zone are key elements in determining how initiated cracks will develop, leading to coalescence or full arrest as shown in the 2D analysis presented in Section 4.4.2. The material volume shown in Figure 78 is undergoing a plastic strain equal to or greater than  $5e-$

4, for clarity purposes, since the volume around the crack front and a substantial portion of the lining undergoes plastic deformation in the bi-layer architecture even at low loads such as 200 N and for cracks with a depth equal to 70% of the lining thickness.

As the crack front approaches the interlayer, in the tri-layer architecture, high values of plastic strain can be observed in this intermediate layer. The higher compliance and lower yield strength of the interlayer produced a protuberance in the plastic zone shape. This protuberance expands through the interlayer forming a secondary plastic zone that promotes faster crack propagation as shown in Figure 79 in a tri-layer architecture with a crack of depth equal to 93% of the lining thickness.

Figure 79 also shows the formation of a low strain area located next to the crack faces. Evidently, the intensity of these low strain areas was diluted as we move away from the cracks. However, the presence of low strain areas influences the propagation of new cracks, especially of smaller size and oriented in a parallel plane. Cracks in an oblique orientation are particularly harmful to the performance of plain bearings since they may lead to early lining detachment into the hydrodynamic film.

In contrast, propagating cracks in a bi-layer architecture are shielded by the stiffer backing. This condition was simulated by not extending the crack into the backing and specifying a maximum depth for the crack front points. This forced the crack into an irregular shape, similar to a truncated circle as shown in Figure 80, which is not consistent with the previous crack front forms. The crack irregular shape appeared to promote the development of a broader plastic zone in this region with higher levels of plasticity than a quasi semi-elliptically shaped crack. It was expected that this plastic zone broadening may facilitate the crack initiation process in the backing layer.

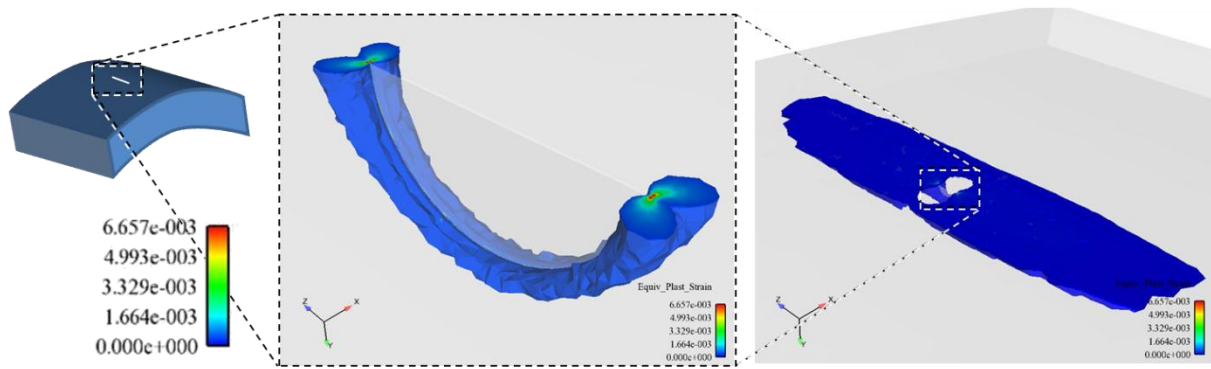


Figure 78. Plastic zone shape contained in the lining of a tri-layer architecture (Von Mises plastic strain contour).

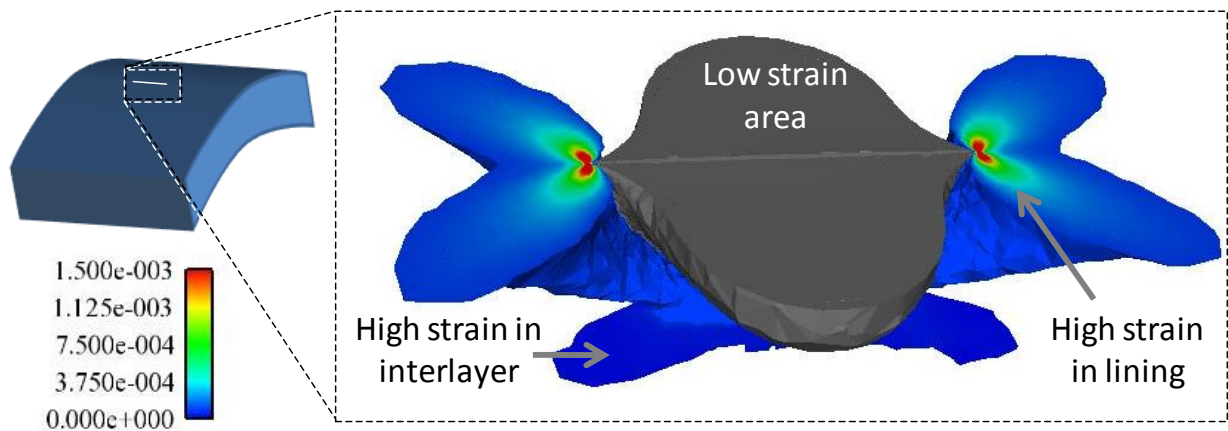


Figure 79. Plastic zone shape and low strain area next to the crack in tri-layer architecture (Von Mises plastic strain contour).

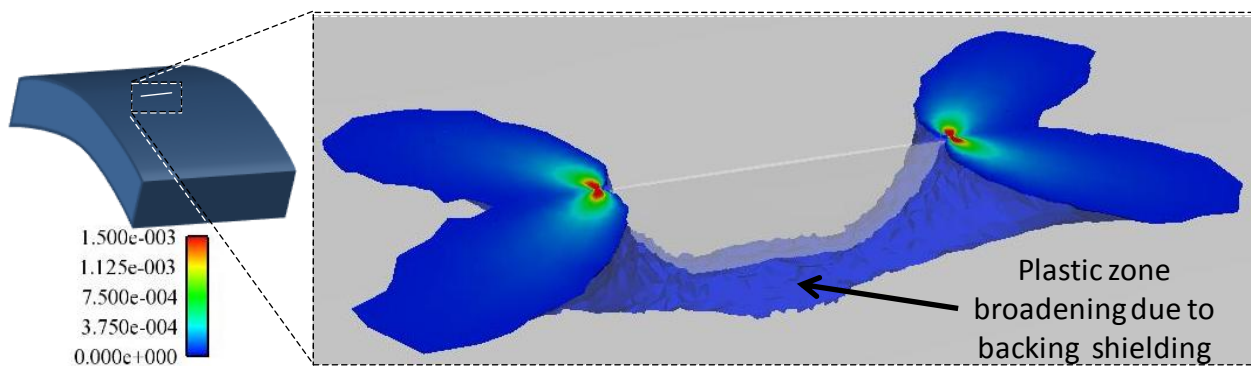


Figure 80. Plastic zone broadening at the deepest point of the crack due to backing shielding in bi-layer architecture (Von Mises plastic strain contour).

## **5.7. Discussion**

The adopted methodology put emphasis on the evolution of the crack front as it approached a dissimilar layer to evaluate shielding and anti-shielding effects on half-penny cracks. Modelling crack growth in dissimilar layers with elastic and plastic mismatch made the analysis complex and time consuming.

The three-dimensional elastic FE models showed acceptable accuracy when compared to respective exact solutions for a specimen containing an elliptical or circular crack. These results gave confidence in the reliability of the meshing and solution methodology. The application of spider-web crack-tip meshes showed a better performance than blunted tip arrangements based on the comparison of their predictions with axisymmetric analytical solutions. Blunted tips still appear to be better suited to detailed stress and strain analysis around the crack tip but at a higher computational cost.

The use of experimental results allows the validation of numerical models and their application to solve engineering problems. The development of a crack growth law provided the necessary link to the observed crack growth behaviour of the material increasing the applicability of the developed models. Computationally expensive analyses led to a crack growth law in which the crack driving force is the key parameter. Some microstructural features of the material that reproduce short fatigue crack behaviour were also accounted for. More experimental and numerical analysis would be necessary to include other loading parameters such as load frequency and ratio that have shown a significant impact on crack growth processes.

The effect of tri-axiality on the deformation of the material has been accounted for through the development of 3D FE models. However, its effect on crack propagation has not been accounted for so far. The crack growth laws based on the Modified Chan and Lankford and Modified Miller relation do not follow the similitude principle, but the fitting process of these relations to

experimental data assumed that the growth deep into the material would be identical to that at the surface when equal values of CDF were considered. Further efforts to quantify the effect of crack tip tri-axiality on growth would be also beneficial for this work due to the change of the state of stress as the crack approached a stiffer material. Accounting for tri-axiality in the growth model would require crack growth experiments at different tri-axiality conditions and the development of a different crack growth law. This expansion would be an interesting path to pursue bearing in mind that additional testing and detailed stress analysis should be required and appears a sound option for future work.

Another issue related to the tri-axial behaviour of crack growth is the free surface effect discussed by Lin and Smith [135]. The change of singularity observed at the intersection of the free surface and the crack front has presented an unusual behaviour of estimations of crack growth and values of CDF, especially with  $K$  and  $J$ , leading to forecasted crack fronts of irregular shapes. The estimations of CTOD obtained in this work based on elasto-plastic material models did not show any sign of the free surface effect at crack tips that develop blunting. The absence of free surface effects on the obtained results was attributed to the development of plasticity and the use of a CDF parameter which is not based on plane strain or stress assumption. The overall behaviour predicted by the numerical models followed the trends predicted in previous work [134, 135] giving confidence about the methods followed.

The analysis of shielding and anti-shielding effects was forecasted to be less significant in three-dimensional crack growth in comparison to through-width cracks in two-dimensional specimens. This conclusion can be drawn from the similarity between forecasted CDF estimates and crack fronts in bi-layer and tri-layer architectures despite the existence of contrasting shielding and anti-shielding behaviour. The crack front segments affected most intensively by shielding and anti-shielding in 3D are expected to accelerate or decelerate, respectively, the crack growth of the

neighbouring crack front material. At the same time, the neighbouring material obstructs the disproportional growth of the most affected areas.

Occurrences of deflection and bifurcation observed experimentally still remain to be investigated due to their interesting development through the interlayer. The crack extension into the interlayer offers great challenges: from the creation of a surface crack that extends in 3D in deflected and bifurcated arrangements to the high level of refinement necessary due to the thinness of the interlayer. The development of such analyses with elastic materials would simplify significantly the task; however, deflections and bifurcations were only identified using elasto-plastic material models as shown in Section 3.6.

### **5.8. Summary**

Initial simulations of crack growth in monolithic components under tension showed that the spider-web crack tip configuration was more suitable than blunted tip modelling for the analysis of 3D crack propagation since it resulted in lower computational cost and faster convergence. The comparison of predicted CODs with those obtained by an exact solution was considered appropriate for the studies being carried out.

The development of a crack growth law using experimental data obtained from previous work at the University of Southampton provided the link between the numerical simulations and the observed crack growth rate. In this way, it is possible to estimate the number of cycles necessary for a surface crack to reach the interlayer in a tri-layered architecture. The crack growth simulation showed small differences between the bi-layer and tri-layered architectures in terms of CDF estimates and crack front shapes. This difference was examined previously with 2D analyses which showed more clearly the effects of shielding and anti-shielding. The crack front segments affected most intensively by shielding and anti-shielding in 3D are expected to accelerate or decelerate,

respectively, the crack growth of the neighbouring crack front material. At the same time, the neighbouring material obstructs the disproportional growth of the most affected areas.

## **6. Chapter Six: Fatigue life estimation and the effect of co-linear coalescence**

### **6.1. Introduction**

The objective of this chapter is the assessment of the crack growth methodology described in Section 5 through its application to a layered architecture subjected to severe yielding and the suitability of the failure criterion used for total life tests to reflect lining detachment, as described in Section 1.4.5. The first part of the objective is focused on the evaluation of shielding effects at higher loads and assessing the applicability of the developed crack growth law presented in the previous chapters.

The second part of this objective is concerned with the comparison of numerical models developed in this thesis and total life experiments limited by a failure criterion representing a particular measure of damage in bearing architectures. This measure of damage is expected to represent, approximately, the number of cycles required for a lining particle to detach. In contrast, the numerical models developed estimate the time required for a single crack to reach the interlayer and how the interaction with co-linear cracks would contribute to or affect such a process. By comparing numerical and experimental life estimations, it should be possible to estimate the importance of crack growth processes within the lining and steel according to the adopted failure criterion.

### **6.2. Background**

Crack propagation studies deal with complexities related to crack interaction, loading and materials, among others. This section focuses particularly on literature related to crack interaction

in 3D following on from previous literature reviews and relevant discussion found in earlier chapters. Some relevant work is also cited in the areas of 3D modelling of homogeneous and heterogeneous materials subjected to LSY at the end of this section.

Initial studies of crack interaction and coalescence [121] based on experimental observations formulated the basis for 2D numerical studies in this field [119, 120]. Experimental and numerical works in 3D by Soboyejo *et al.* [125] showed the importance of this phenomenon for large cracks analysed under LEFM conditions. Soboyejo *et al.* [125] reported higher crack growth rates of coalescing cracks at a given  $K$  value on the surface than those indicated by previous material characterisation for a single crack. The rate of increase of the stress intensity factor and crack growth rate was difficult to quantify given that load increasing and load shedding schemes were used before and during coalescence. Soboyejo *et al.* [125] also mentioned that co-linear cracks, as those shown in Figure 81a, grew almost independently before contact and that the just coalesced region showed high  $K$  values promoting the re-formation of a quasi semi-elliptical front. The front evolution was defined by the beachmarks found on the fracture surface.

Subsequent work based on FE used more refined numerical models to study the effect of multiple co-linear cracks [155], loading configurations [123] and crack orientations [156, 157]. The work by Lin and Smith [123] tested various degrees of bending in a flat plate with a quasi semi-elliptical crack and showed that the quasi ellipse aspect ratio was substantially influenced by the type of loading. At the same time, their work describes how cracks gradually reshape into a more natural crack front form according to the applied loading and material conditions.

Soboyejo and Knott [158] also worked with co-linear (Figure 81a), parallel-oblique (Figure 81b) and parallel-aligned (Figure 81c) crack arrangements describing effects of anti-shielding, out of plane growth and shielding, respectively. Kamaya [156, 157] studied non-coplanar oblique cracks in ductile materials finding that the crack area, before and after coalescence, may be used as an

alternative parameter of CDF. This work did not estimate the front progression and simulated various crack fronts obtained from the fractured specimen.

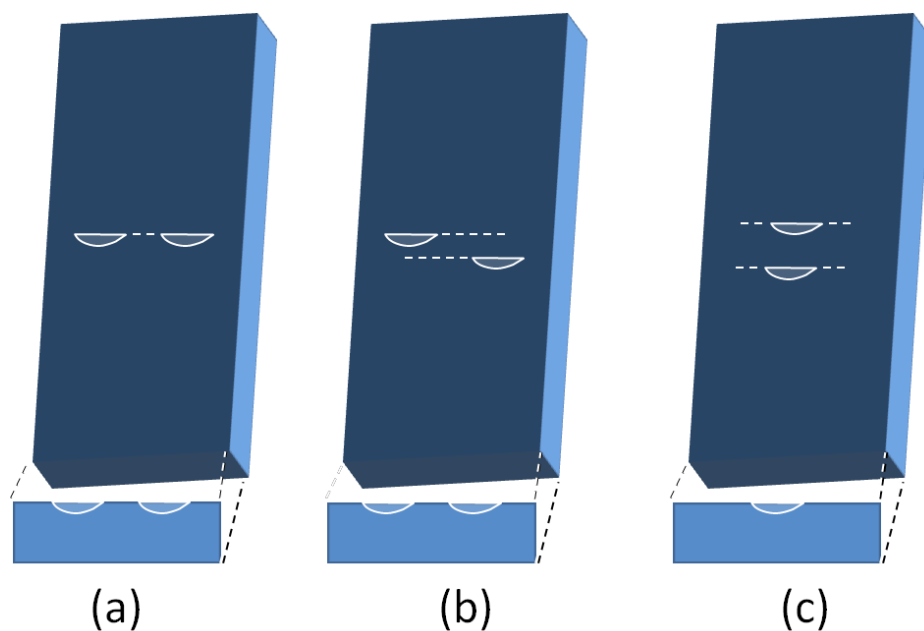


**Figure 81. Co-linear (a), parallel-oblique (b) and parallel-aligned (c) crack arrangements.**

The simulations presented in this literature review were based on numerical models representing pre or post coalescence conditions. The moment at which coalescence occurs represents the end of a two-crack analysis and the beginning of a new evaluation with a single odd shaped (coalesced) crack. This transition produces a sudden rise in crack length that influences the CDF estimates. The instant at which both cracks come into contact is a problem that has been largely studied in the context of fracture. The critical distance at which coalescence occurs has been studied in terms of the force magnitude in the remaining ligament between cracks and interaction of the plastic zones [128, 129], among others.

On the other hand, the generation of 3D numerical models to study fracture and fatigue has been extended to assess LSY conditions in homogeneous materials [159-162]. The use of inhomogeneous materials in engineering applications has promoted the generation of numerical models to assess their performance. These studies have included the application of damage tolerance approaches to

such materials. Significant progress has been made in fibre reinforced materials [163], particle reinforced composites [164] and layered architectures [7, 165].

### **6.3. *Elasto-plastic analyses replicating experimental data***

The application of elasto-plastic material models to the analysis of propagating cracks in the MAS-20S architecture (tri-layer) was carried out to replicate experimental data obtained during previous work at the University of Southampton in the Materials Research Group [8]. These experimental data included total life experiments using different load levels in a three-point bending test in flat strips, shown in Figure 18. Specific information on the experimental data used for this comparison is given next along with further information on crack propagation evolution across the layers.

#### **6.3.1. Total life experimental data**

Previous work [8] studied the fatigue performance of the architecture MAS-20S through three-point bending tests of in flat strip specimens, shown in Figure 18. These fatigue tests were carried out at a maximum load equal to 720 N (causing a maximum plastic strain of approximately 0.003), a load ratio  $R$  equal to 0.1 and a frequency of 10 Hz on a digitally controlled 50 KN Instron Servo Hydraulic fatigue testing machine (8502). The failure criterion for these bending tests was set to a maximum absolute vertical displacement of the loading cross-head 0.5 mm greater than the maximum absolute vertical displacement in the first loading cycle.

Tests on these roll-bonded flat strips subjected to three-point bending loading were also carried out for the assessment of the rolling direction effect on the total life [10]. These tests showed that the orientation of rolling with respect to the loading axes had minimal effect on the lifetime over a range of loads. The only discrepancy was found at a maximum load of 840 N where a life time difference of approximately 10% was observed. Total life estimates of the architecture of interest were extracted from [10] and are shown in Figure 82.

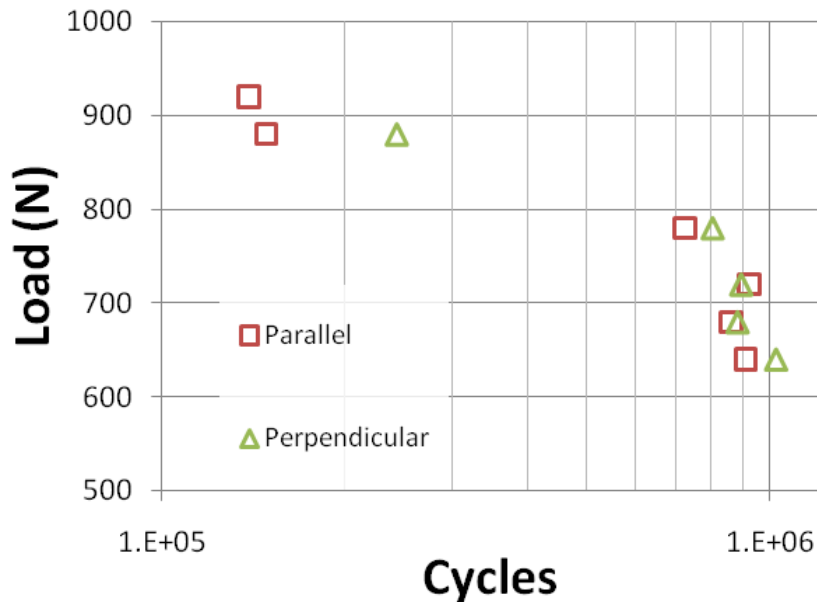


**Figure 82. Total life tests of flat strips MAS-20S in parallel and perpendicular orientations of the loading axis to rolling.**

Along with total life tests, crack initiation observations (via replica observations) were carried out showing a total life fraction of approximately 14% for initiation at a maximum load of 840 N. Data regarding initiation at 720 N was not available; therefore, in this work the total life fraction for initiation was assumed to be equal at both load levels considering that the load magnitude difference between them was 15 %. The detection of initiating cracks was carried out through acetate strips manually pressed against the polished surface in interrupted fatigue tests. These acetate strips were applied and removed at intervals of 1000 cycles to identify the onset of crack initiation, with typical initial crack lengths being observed between 7  $\mu\text{m}$  and 13  $\mu\text{m}$ . Subsequent crack growth was tracked through replicas taken at intervals of 500 cycles [10].

### 6.3.2. Crack propagation phases within MAS-20S

The analysis of the micrograph shown in Figure 12 (corresponding to a cross section of a flat strip specimen MAS-20S subjected to three-point bending) led to the consideration of five phases in the damage process: crack initiation on the lining surface, crack propagation through the lining, crack propagation within the interlayer and initiation and crack propagation within the steel.

The existence of the latter was corroborated by the results from 2D models, identical to the ones analysed in Section 2.3 but with longer cracks penetrating the backing layer. These models simulated crack growth into the backing layer and showed that a width-through crack of approximately 0.8 mm (that is, 0.38 mm long within the steel) was necessary to achieve the vertical displacement set by the failure criterion in experiments. The estimated concomitant flat strip deflection according to the crack length analysed are compared in Table 7.

**Table 7. Maximum absolute vertical deformation at various crack lengths.**

Crack length	Crack tip containing layer	Max deflection	Difference with initial deflection
0.127 mm	Lining	0.393 mm	0.211 mm
0.27 mm	Lining	0.397 mm	0.215 mm
0.52 mm	Steel	0.399 mm	0.217 mm
0.7 mm	Steel	0.437 mm	0.255 mm
0.805 mm	Steel	0.681 mm	0.5 mm (interpolated)
0.87 mm	Steel	0.897 mm	0.712 mm

Figure 12 also shows that the crack growth in the interlayer commenced from a crack originated in the lining that crossed the lining-interlayer interface and continued its growth. This is in contrast to the cracks observed in the backing layer since cracks in the interlayer deflect and extend parallel to the layers orientation. Figure 12 illustrated that cracks in the backing may initiate at a separate point from where the principal crack reaches the interface.

Based on these observations of initiation in the backing, it can be assumed that the stages of propagation through the interlayer and initiation at the steel boundary occur almost

simultaneously. In fact, micrographs of layered architectures, such as Figure 11 and Figure 12, showed that extensive crack propagation within compliant interlayers had occurred before significant growth was observed in the backing.

High stress and strain concentrations arise as cracks penetrate the interlayer accelerating the initiation process in the backing. The initiation and propagation process within the backing is a complex problem that offers further opportunities for research and this work can only show its importance through a comparison between numerical estimations of cycles for crack growth through the lining and those from total life experiments, the latter shown in Figure 82. The difference between these two would reveal the importance, in terms of proportional total life, of crack initiation and propagation in the backing layer at the particular load level considered. Initiation and propagation within the backing depends on the complex state of stress at the interlayer-backing interface that is greatly affected by bifurcated and deflected cracks extending within the interlayer. According to the available experimental data and computational resources, it was not possible to account for this crack growth stage in the current project.

### **6.3.3. Crack growth analysis across the MAS-20S lining**

The crack growth developing in a bi-layer architecture was also simulated for comparison purposes. A lower load equal to 720 N was chosen to perform analyses in both architectures due to the high computational cost involved using the crack growth law developed in Section 5.5. The methodology to develop a fatigue crack growth analysis described in Section 5.3 is used here and the crack is propagated up to a crack depth of 0.35 mm due to the excessive mesh refinement needed to come any closer to the materials interface. A maximum crack growth step of 0.03 mm is used in this analysis for the first 13 steps and later reduced to 0.01 mm to capture with greater detail the shielding and anti-shielding effects that occur in this Section.

The application of greater loads, 780 N and 840 N, was initially planned; but their computational costs were higher than expected and only crack depths below 0.18 mm were reached. These partial results were far from adequate to be presented here and the additional extension of plasticity required significantly higher computational costs. It is the intention of the author to extend these analyses until crack depths are reached near the interlayer for assessing the loading magnitude effect in future work.

The crack front evolution in bi-layer and tri-layer architectures showed indistinguishable differences below crack depths of 0.27 mm; small differences can be observed at greater depths as observed at lower loads. The crack driving force evolution in both architectures at 720 N also showed a very similar pattern during the whole simulation. Figure 83 shows the evolution of CDF distribution along the crack front in both architectures. Small differences can only be noted at crack depths close to the interface (especially in the contour plot in the top right corner of the bases in Figure 83).

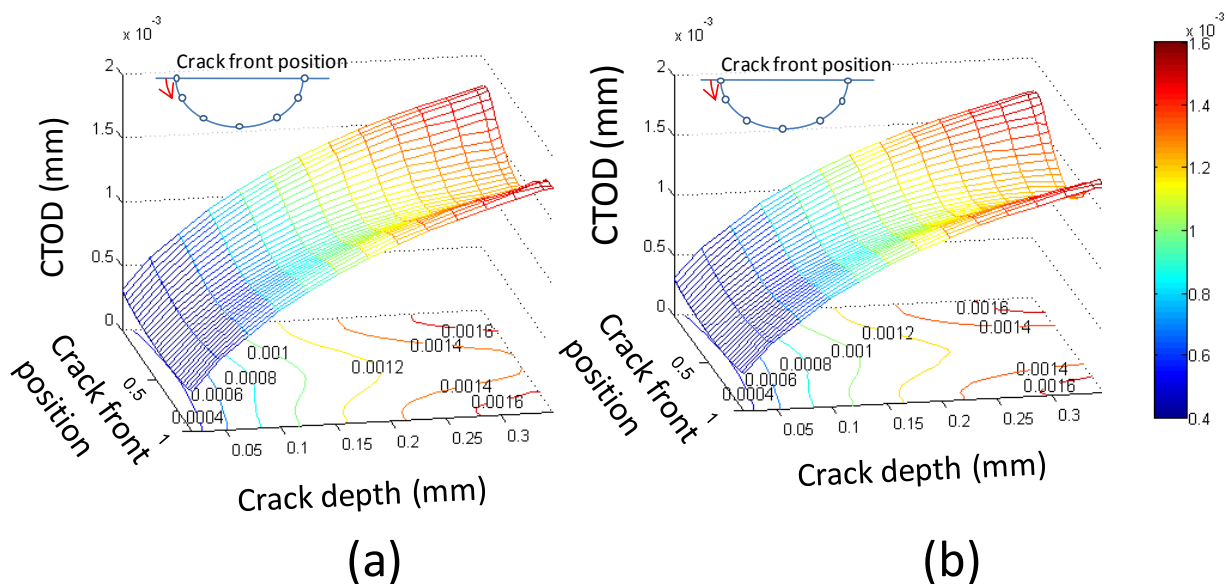
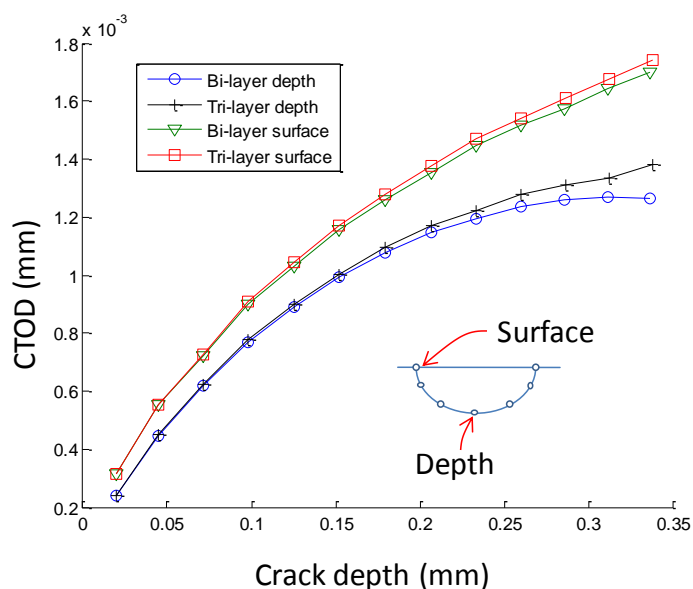


Figure 83. Crack driving force evolution in bi-layer (a) and tri-layer (b) architectures.

The CDF evolution observed at 720 N also showed a clear difference between the values obtained at the surface and the deepest crack front point when the front came near to the layers interface. Figure 84 shows that the crack growth at the free surface of the flat strip was not affected significantly by shielding or anti-shielding, in contrast to the deepest point of the crack front.



**Figure 84. Estimated crack driving force values evaluated at the free surface and deepest point of the crack in bi-layer and tri-layer architecture in 3D models.**

Throughout this work, the CTOD has been used as the crack driving force to evaluate the crack growth conditions. Recent advances in the latest release of the FE code ANSYS (version 11.0) has simplified the computation of the  $J$  integral in collapsed spider web mesh configurations. Its implementation to initially blunted crack tips in 2D could however not be developed satisfactorily. The evolution of the  $J$ -integral estimates, shown in Figure 85a, presented a similar trend to that observed for the CTOD with one major difference at the lining free surface. The estimates obtained at the free surface were not the maximum values at each evaluated step as observed in the CTOD estimation. The  $J$  integral values drop suddenly near the surface reaching their minimum values along the whole crack front. This effect previously discussed by Lin and Smith [135] can be attributed to the numerical computation of the  $J$  integral and the change of the singularity on the

stress and strain fields as the estimation of the CDF is developed over crack front portions located deeper into the material.

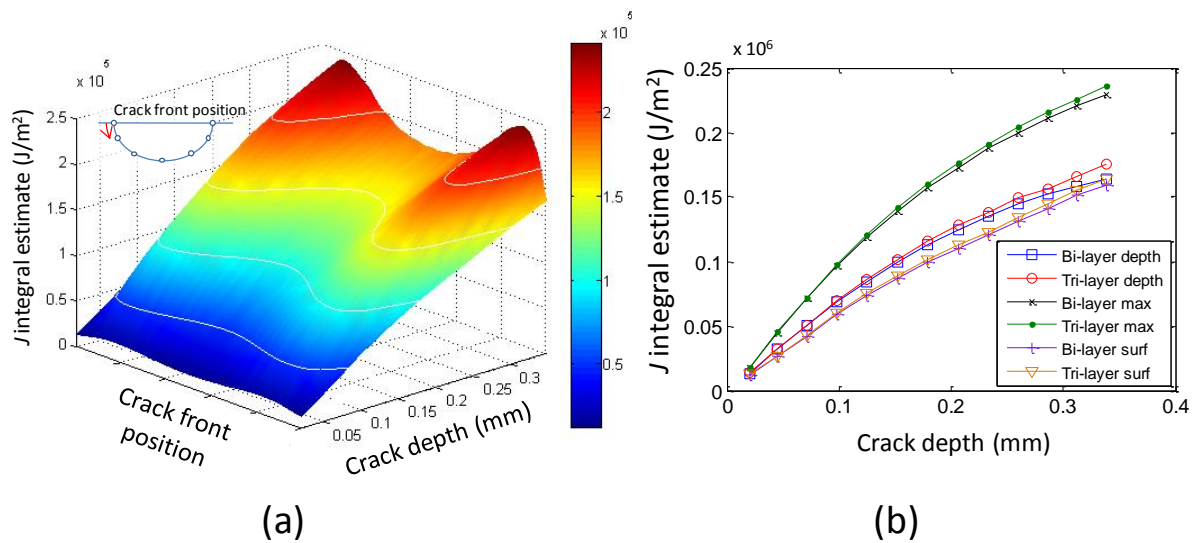


Figure 85. Estimated J-integral values along the crack front (a) and at particular positions for clarity (b) in bi-layer and tri-layer architectures in 3D models.

#### 6.3.4. Lining life numerical estimations

Numerical crack growth analyses within the lining were performed here with the objective of estimating the required number of cycles for a crack to reach the interlayer after its initiation process at lining surface. Based on the sensitivity of the initiation detection method, the growth process was initiated through a half-penny crack with a diameter of  $10\ \mu\text{m}$ . Since the initiation proportion of total life was identified in previous work [10] at approximately 14% at a slightly higher load, it can be assumed that the approximate number of cycles for initiation  $N_i=129,500$ , from a total experimental life  $N_T=925,000$  according to the adopted failure criterion. The numerical life estimations carried out in this chapter were focused on the analysis of crack growth and estimation of load cycles elapsed within the lining  $N_L$ . The estimation of  $N_L$  could be then compared to the number of cycles  $N_B$  required to propagate the crack from lining-interlayer interface until the failure criterion was reached. The comparison of  $N_L$ ,  $N_B$  and the experimentally obtained total life of

the specimen  $N_f$  should reveal the suitability of the adopted failure criterion in experimental tests to represent the number of cycles necessary to cause lining detachment. For the study of this relative importance it is assumed that

$$N_f = N_i + N_L + N_B = N_i + N_P \quad (24)$$

Thus the estimation of  $N_B$  depends on the numerically estimated value of  $N_L$ .

The number of cycles  $N_L$  necessary to propagate the crack after initiation to a depth where the crack front came into contact with the interlayer interface was estimated through a numerical integration using the Tanaka and Modified Chen and Lankford (MCL) relations, equations ( 20 ) and ( 22 ) presented in Section 5.2, and the CTOD estimations shown in Figure 83. A single fatigue life estimate  $N_L$  was obtained for the relationship proposed by Tanaka for short cracks; in contrast to the MCL relation which is dependent on the microstructural features of the material.

The introduction of lower and upper bounds to the MCL relationship showed the possible influence of the chosen model on the estimated life  $N_L$  as the crack growth rate takes maximum and minimum values. The numerically obtained life estimations for  $N_L$  are presented in Table 8 as well as the percentages of experimental propagation life  $N_p$  (experimental total life minus initiation life). The comparison between the estimates based on Tanaka and MCL (which included the barrier average distribution) showed that the latter was more conservative irrespective of the chosen value of  $D$  (with a difference between Tanaka and MCL estimates of around 30%).

The effect of the chosen  $D$  value on the predicted number of cycles was not very significant relative to the total life obtained experimentally (less than 2%). The maximum difference observed between these life predictions for various values of  $D$  was around 4%. The estimated crack growth in the lining was affected by the number of barriers to be overcome, which is inversely proportional to the value of  $D$ ; more barriers represented slightly lower values of crack growth and, consequently,

more cycles to reach the interlayer. However, accounting for this behaviour leads to the assumption of a faster crack growth when the crack tip is away from the barrier which may result in higher estimations of growth rate in comparison to Paris type laws.

During the life estimation process using the MCL relation, it was observed that the initial crack position, or initiation location, of the crack between microstructural barriers could influence the final outcome. The reason for this is that at small crack lengths, the impact of the microstructural barrier, represented in Eq. ( 22 ) by  $\omega(D - 2X/D)$  which varies between 0 and 0.96, is greatest (shown in Figure 73b). In order to assess this effect, five different locations for crack initiation were selected at distances equal to 0 D, 0.05 D, 0.225 D and 0.45 D and when the crack actually initiated at the barrier (distance equal to 0.5 D), which according to crack initiation studies [8] was identified as crack pinning points. The results from this parametric study are shown in Table 9.

**Table 8. Life estimation using Tanaka and modified Chan and Lankford (MCL) relation with upper and lower bounds.**

	Estimation type	Estimated number of cycles $N_L$	% of propagation life $N_p$
Tanaka		247,240	31.1%
Chen and Lankford	Upper bound	45,923	5.8%
	Lower bound	765,396	96.3%
	D= 16 $\mu\text{m}$	177,271	22.3%
	D= 28 $\mu\text{m}$	173,748	21.9%
	D= 41 $\mu\text{m}$	170,262	21.4%

**Table 9. Impact of crack initiation position in relation to hard intermetallics on fatigue life estimate.**

Distance between intermetallics ( $\mu\text{m}$ )	Centred $N_L$	0.05D $N_L$	0.225D $N_L$	0.45D $N_L$	At the barrier $N_L$
16	177,271	177,332	171,924	171,953	170,370
28	173,748	174,003	172,459	164,515	167,420
41	170,262	170,425	170,528	158,394	164,440

The effect of crack initiation location between the microstructural barriers proved to be as high as 8%, larger than the overall effect of the selection of  $D$ . The effects of the selection of  $D$  and the location initiation become more evident when the estimated period of growth considers crack sizes smaller or equal to  $D$ , where smaller CDF values are usually observed. The maximum difference observed between the estimations of  $N_L$  obtained by the MCL relationship, at any tested scenario, and Tanaka was around 36% with the former being less conservative. Similar estimations were made for the bi-layer architecture for comparison purposes. The life estimates of bi-layer and tri-layer architecture did not show a significant difference (around 2%) since out of plane propagation was not accounted for and only propagation within the lining was assessed.

In general terms, the estimations of crack growth based on cracks nucleated at hard intermetallics showed that the fraction of total life necessary to reach the interlayer, accounting for initiation  $(N_i + N_L)/N_f$ , was between 31% and 34% for a maximum load equal to 720 N. In contrast, the relation used by Tanaka estimated that 40% of the total life would be spent on such a process. The estimations made so far only include the growth of a single independent crack. However, previous experimental work [8] has identified coalescence as an important mechanism within the total failure process and, therefore, this is discussed next.

#### **6.4. *Co-linear cracks coalescence***

The occurrence of co-linear crack coalescence has been identified as an important mechanism in the extension of cracks. The use of advanced 3D in-situ monitoring techniques, such as computed tomography [166], may be able to trace the evolution of the crack front as loading occurs. However, such techniques are expensive (limited equipment access) and their applicability depends on the specimen size, type of material used and appropriate geometry of the scanned volume. Optical monitoring processes depend on interrupted tests to detect the appearance of cracks on the component surface. However, the evolution of cracks at their deepest point into the material can

also be estimated through numerical analyses or a post-mortem evaluation of the crack path and possibly fracture surface features (e.g. beachmarks or striations).

The collection of data describing fatigue crack growth, presented in Section 5.5.1, was based on interrupted surface replication tests of individual small cracks aimed at reducing the effects of coalescence and shielding on the fatigue crack growth estimates and, hence, focusing on evaluating the lining fatigue resistance (for alloy comparison purposes).

The impact of coalescence on the current problem was assessed through modelling the growth of twin cracks in a tri-layer architecture subjected to a max load of 720 N. These cracks were extended to interact with each other until the crack front elements, shown in Figure 56, came into contact. A coalesced crack, based on the shape of the twin cracks as shown in Figure 86, was then generated and extended according to the crack growth law obtained in Section 5.5 and the estimated CDF values along the front.

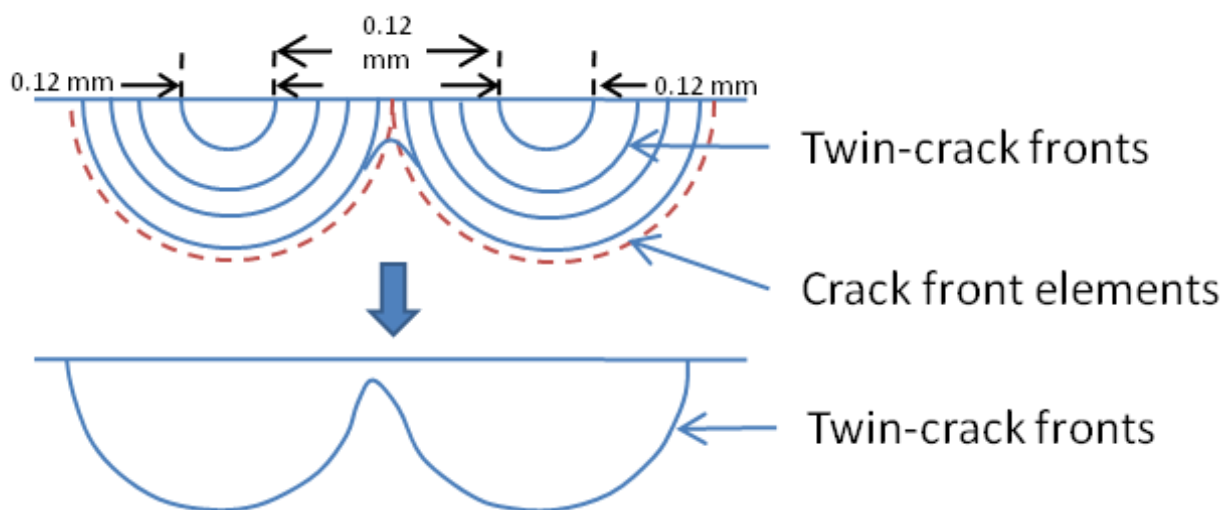


**Figure 86. Coalesced crack progression.**

This simulation consisted of two parts involving pre and post coalescence cracks in order to assess its effect on fatigue life. This thesis replicated the smallest coalesced crack observed experimentally in [10] at a load of 920 N (with a distance of 0.24 mm between the two initiation points). The initial

depth of the twin cracks was set at 0.06 mm and the simulation stopped when the coalesced crack recovered its quasi semi-elliptical shape. Unfortunately, experimental data on crack growth and coalescence was not available at 720 N and the plasticity developed at 920 N required greater computational costs, as shown in the development of the crack growth law where crack depths up to only 40 % of the lining were reached. However, the analysis of a typical crack coalescence geometry in this system at lower loading loads, that could be assessed computationally, was considered useful.

### 6.4.1. CTOD and crack front evolution

The crack growth assessment of co-linear twin cracks showed an identical behaviour to that of single-crack specimens while the separation between cracks remained larger than approximately 0.08 mm or  $1.33a_0$  (initial crack length). The evaluation of crack growth behaviour at smaller separations showed CDF increments for the approaching portions of the crack fronts. The overall CDF evolution along the front and a comparison between CDF at coalescing, non-coalescing surface points and the deepest crack point are shown in Figure 87a and b, respectively.

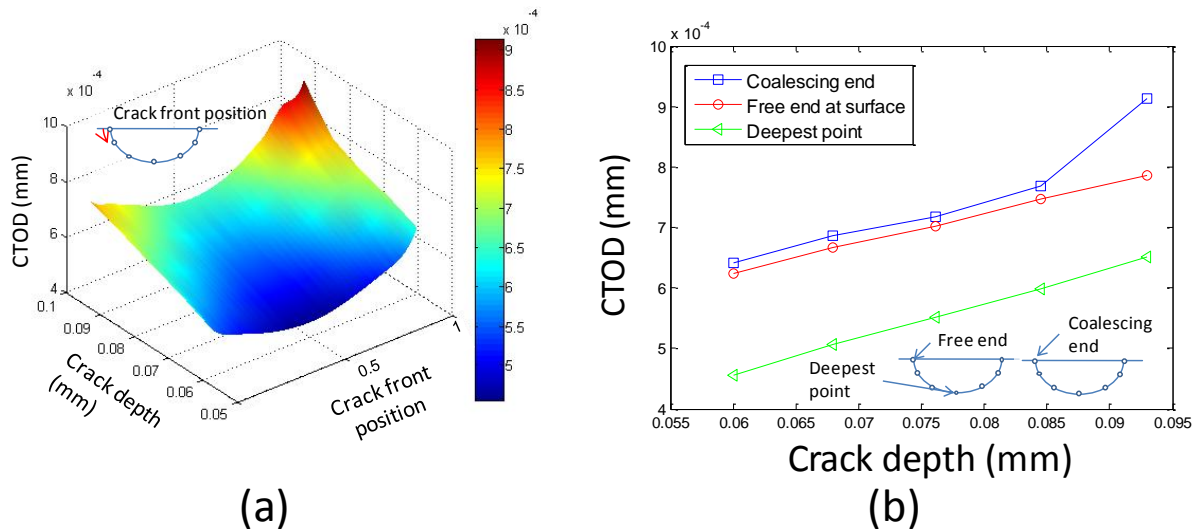


Figure 87. Pre-coalescence CDF evolution in twin cracks beyond the effect of layered anti-shielding.

The interaction between twin cracks was expected to modify the crack front shape locally due to the higher CDF estimates at the coalescing crack front ends. The forecasted crack front shapes did not however show a significant distortion arising from the CDF variation, not even at the last tested model (restricted by the size of the crack front elements). However, greater values of CDF would arise as the distance between crack fronts is reduced further leading to a greater CDF mismatch along the front. Furthermore, a sudden growth promoted by fast ductile fracture would occur when a critical CDF value is reached.

The transition to the post-coalesced model was carried out when the elements forming the crack front, shown in Figure 56, of both twin cracks overlapped. The post-coalesced crack growth showed contrasting results to the crack growth behaviour obtained from single crack specimens. The maximum CDF estimate shifted to the middle of the crack front at the coalesced cracks intersection. This maximum value was significantly higher than the estimates at the surface while the minimum values were observed at the deepest points along the crack front. The overall CDF evolution along the front and a comparison between the middle, surface and deepest crack point are shown in Figure 88a and b, respectively.

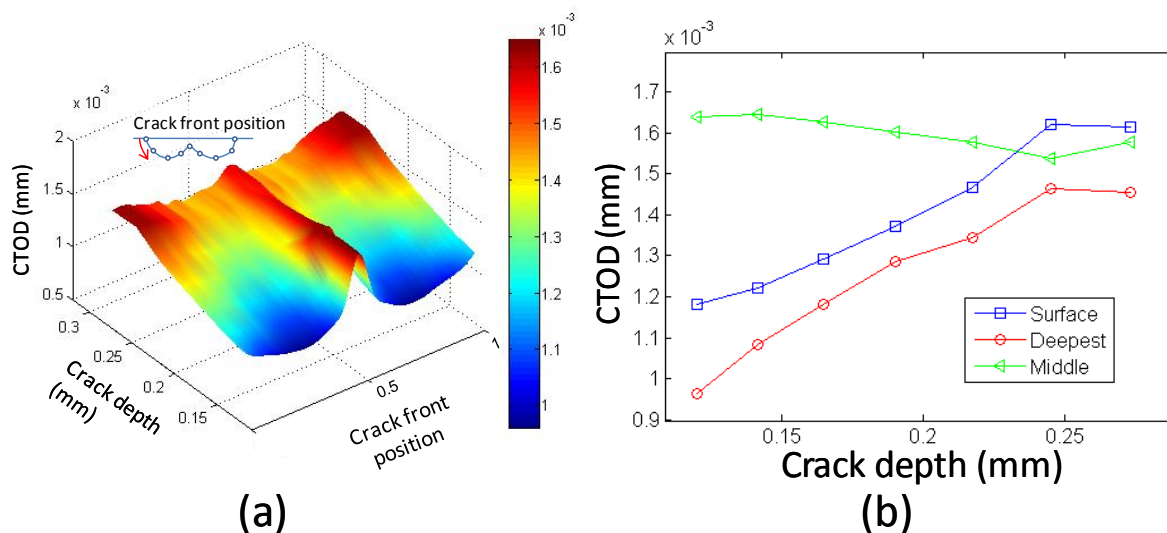
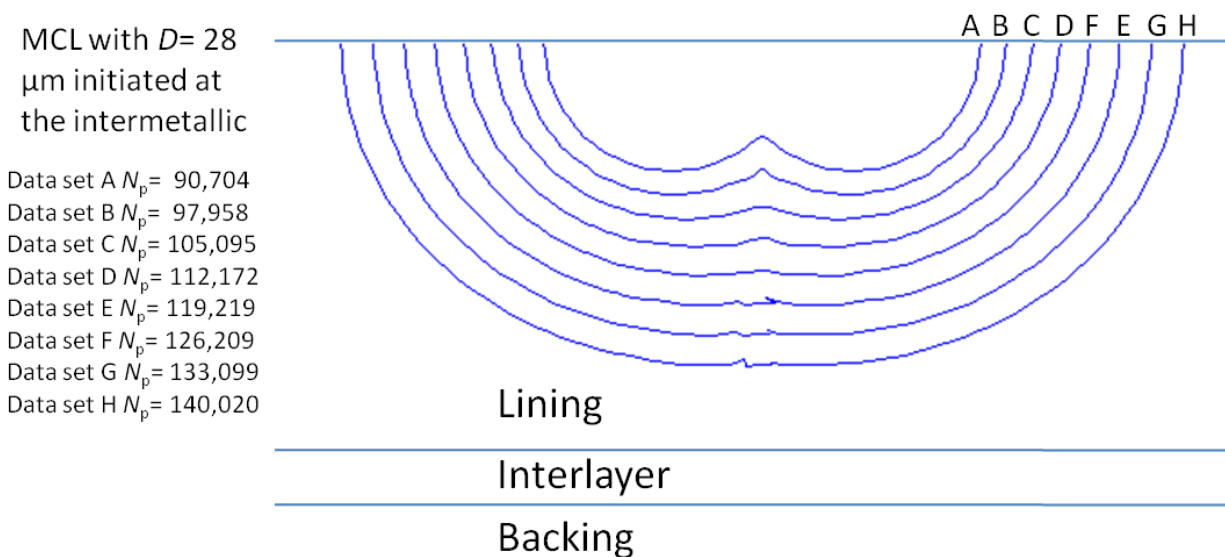


Figure 88. Post-coalescence CDF evolution in twin cracks beyond the effect of layered anti-shielding.

The high CDF estimates observed in the middle of the specimen reshaped the crack into a quasi semi-elliptical form. This change occurred in a gradual manner and as the crack shape approximated a quasi semi-elliptical form, the CDF values in the middle of the specimen dropped in relation to the other CDF estimates along the crack front.



**Figure 89. Post-coalescence cracks affected by shielding.**

Experimental data obtained through interrupted fatigue tests [10] showed the impact of coalescence processes on the crack growth rate and crack length. In contrast, the assessment of crack depth requires more sophisticated experimental procedures to be evaluated. The developed FE analyses estimated crack front shape evolution according to CTOD estimates and a crack growth law based on lining surface data.

The CTOD estimates obtained in pre and post coalescence models can be compared in Figure 90a, where crack depths smaller than approximately 0.1 mm only show values for half of the scale representing just one of the pre-coalescence twin cracks. The points located in the middle of the scale correspond to the coalescent front end (Figure 90a Point A) and showed greater CTOD values before coalescence ( $CTOD_{PRE}$ ) than that of the front end at the other side of the crack (Figure 90a

Point B). CTOD values after coalescence ( $CTOD_{POST}$ ), at crack depths greater than approximately 0.12, mm cover the whole scale along the coalesced crack front position showing the twin crack overlap in the middle (Figure 90a Point C). Points at the ends of the crack front are at the specimen surface (Figure 90a Point D).

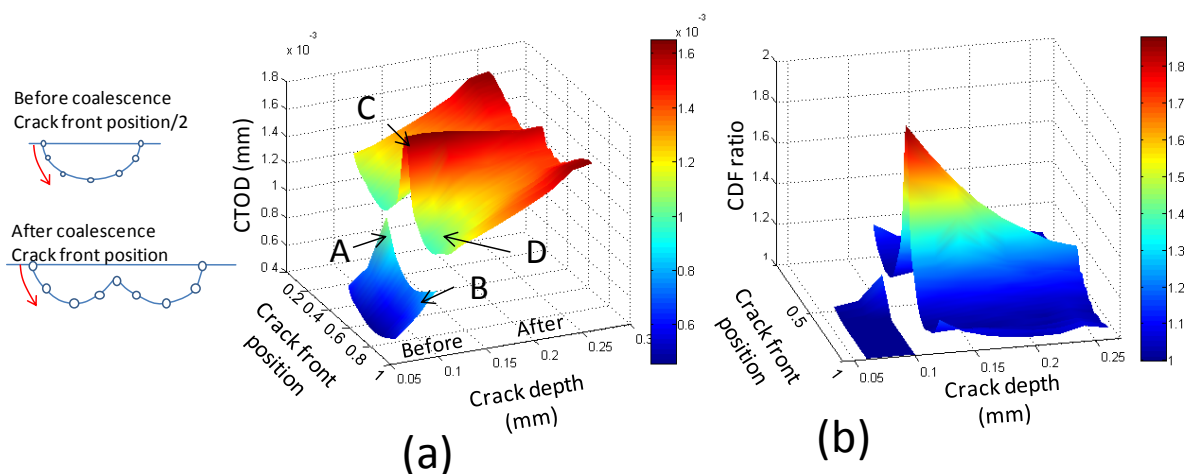


**Figure 90. CTOD estimates (a) and CDF ratio with half penny crack of equivalent depth.**

Figure 90a showed a sudden CTOD increase at the middle position (Figure 90a Point C) as the twin cracks became one, which is in contrast to the CTOD values of a specimen containing a single crack ( $CTOD_{SINGLE}$ ). The  $CTOD_{PRE}$  values at the free crack front end did not show a significant rise, despite the significant crack length increment. The impact of coalescence on the CDF can be better evaluated through the values of  $CTOD_{PRE}/CTOD_{SINGLE}$  at an equal crack depth, shown Figure 90b.  $CTOD_{PRE}/CTOD_{SINGLE}$  values appeared to be very close to 1 along most of the crack front.  $CTOD_{PRE}/CTOD_{SINGLE}$  estimates at the coalescing front end and close neighbours showed slight rises due to the attraction between both twin cracks. More evident rises were observed at the crack front middle after coalescence where the irregular shape of the crack promoted greater CDF to reshape the crack front into a more “natural” quasi semi-elliptical shape. As the crack grew towards a quasi semi-elliptical shape, the values of  $CTOD_{POST}/CTOD_{SINGLE}$  in the middle of the crack front dropped. The values  $CTOD_{POST}/CTOD_{SINGLE}$  were equal or greater than 1.1 showing a general rise along the

whole front, which shows that the coalesced crack had faster crack growth rates in comparison to a single quasi semi-elliptical crack.

The modelling of cracks fronts that were very close to, before and after, the coalescence point was a complex task due to the stress concentrations arising from the locally distorted crack front shape. The behaviour observed at the middle of the crack front displayed asymptotic trends for the CDF, especially in Figure 90b, that could be linked to the coalescence process and the coalesced crack front shape recovery. The crack penetration into lining (crack depth grow) was not affected to such an extent. Evaluated CTODs in twin cracks were higher than single crack estimates by only 15%; this maximum difference occurred at the surface at the coalescing end.

#### **6.4.2. Impact on fatigue life**

Crack interaction and coalescence has showed a significant impact on the CTOD magnitude and distribution along the front. Naturally, this impact should be observed on the crack growth. The most evident consequence is a sudden rise in the crack length (by addition of two cracks). Previous analyses have shown that as soon as coalescence occurred, a process to reshape the crack took place. This process showed substantial rates of CDF increase in the recently coalesced zone; however, its overall effect on the crack growth speed through the depth of the lining has not been quantified.

In order to quantify this effect, the growth was divided into four stages: cracks growing without interaction, interacting twin cracks, reshaping process of just coalesced cracks and crack growth that reaches the interlayer. The duration of the first and last stage was assessed through previous analyses of growing cracks within the lining in Section 6.3.1. The life estimation related to interacting twin cracks covered the extension to depths ranging from 0.06 mm to 0.12 mm. CTOD estimations could only be directly obtained up to a crack depth of approximately 0.1 mm due to the overlapping of the crack front mesh. The estimation of life between 0.1 mm and 0.12 mm was based

on an extrapolation of CTOD values obtained for smaller twin cracks. The life estimation of the coalesced crack during its reshaping process covered the change in crack depth from 0.12 mm to 0.27 mm. The duration of the stages described above is shown in Table 10 for a  $D$  equal to 28  $\mu\text{m}$ .

**Table 10. Comparison between single and coalesced crack growth based on the Modified Chan and Lankford (MCL) relation using a  $D=28 \mu\text{m}$  initiated at the microstructural barrier.**

	Crack depth (mm)	Number of cycles at independent crack	Number of cycles at coalesced crack	Difference %
Initiation	0-0.005	129,500	129,500	0
Independent twin cracks	0.005-0.06	60594	59,892	0
Interacting cracks	0.06-0.012	39,794	30,812	22.4
Just coalesced cracks	0.12-0.27	55,962	49,497	11.4
Reshaped crack	0.27-0.38	11,070	10,942	0
Total	0-0.38	296,920	280,771	5.4%

The difference between the total life estimation for single and coalesced cracks showed a difference of 5.4 %. This difference may appear not to be substantial but this is due to the initiation and crack growth stages that remained unaffected. However, a closer look at the stages where coalescence occurred showed that reductions in the number of cycles of 22% and 11% took place while cracks interacted and the coalesced crack was reshaped, respectively. The life reduction observed during the stage of interacting cracks appeared to be more significant. It is noteworthy that a fraction of the analysed crack extension was done by extrapolating CTOD values over a depth equal to 0.02 mm following rising CDF trends. This extrapolation may have overestimated CTOD values and, in consequence, crack growth; however, this overestimation may be used to account to some extent for the expected fast ductile fracture occurring at the precise moment of coalescence.

### 6.4.3. Development of the plastic zone

The proximity to stress concentrators, crack shape and orientation are key factors that determine the form and size of the plastic zone surrounding the crack front. The development of the plastic zone in twin cracks was only affected by coalescence at crack separations smaller than 0.02 mm, similar to the effect on CDF. The irregular crack front shape post-coalescence led to uncharacteristic plastic zone shapes. Figure 91 shows the volume around the crack where the plastic strain is equal or greater than  $4e-3$ , demonstrating the irregular shape of the high strain volume around the crack tip.

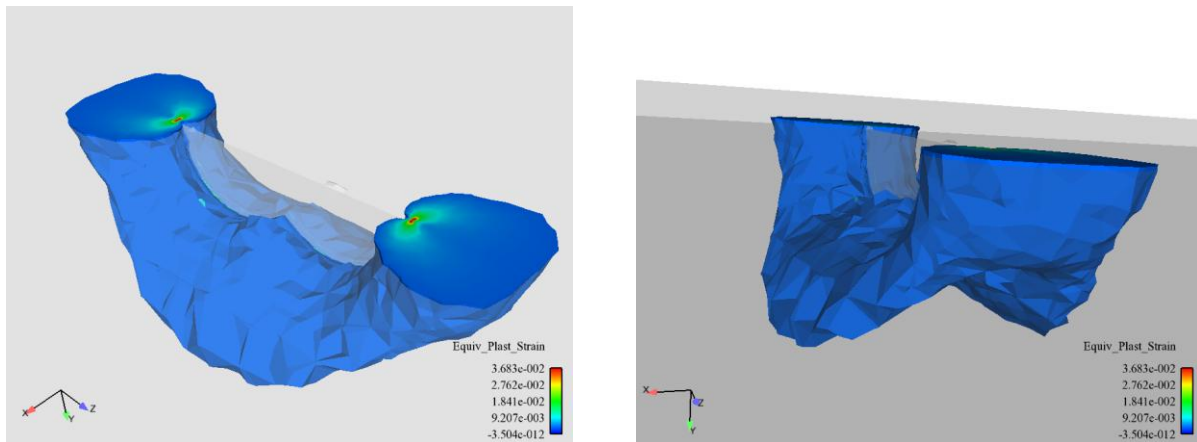


**Figure 91. Post-coalesced plastic zone shapes at a crack depth equal to 0.12 mm under a load of 720 N (volume experiencing strains higher than  $4e-3$  is shown).**

## 6.5. Discussion

In this chapter, FE models simulated large amounts of plastic deformation promoted by the layer architecture. The use of stress-strain curves and automatic updating of the compliance matrix during the solution of the simulations were suitable for the simulation of large deformations. The analysis of out of plane crack propagation was not accounted for in these simulations and remains an area of opportunity for future work.

In the context of the damage tolerance approach and life, the current methodology used for fatigue life estimation accounted for the mechanical properties of layered architectures and the lining layer heterogeneity through the implementation of a crack growth law based on experimental data. Accounting for microstructural barriers in the life estimation process provided a better insight of the possible impact of short crack fatigue behaviour. In contrast, it is believed that a more thorough analysis of the selection of the cracks to be included into the development of the crack growth law would have showed a clearer effect of CDF and microstructural barriers on crack growth. The experimental data used for the crack growth law development did not exclude cracks in parallel-aligned arrangements, as shown in Figure 81. This kind of arrangement leads to shielding due to a dominant parallel crack, as shown in Section 4.4.2, and, consequently, reduced values of crack growth were related to a given crack size affecting the crack growth law development. This would lead to underestimations of crack growth.

The comparison between Tanaka and the modified Chan and Lankford relation showed that the latter was more conservative. The inclusion of microstructural barriers showed a more conservative life estimate for the small fatigue crack growth behaviour observed, in comparison to a Paris type relationship, such as the one proposed by Tanaka, as previously discussed in the literature review [144]. The initiation and growth processes in the lining, given by  $N_i + N_L$ , in the MAS-20S architecture subjected to a maximum cyclic load of 720 N and a load ratio of 0.1 varied from  $0.32N_f$  to  $0.4N_f$ , depending on the crack growth law used.

According to these estimates of proportional life, it can be said that a greater proportion of the loading cycles applied corresponded to crack initiation and growth within the backing layer. The crack penetration into the backing necessary to achieve an additional maximum absolute deflection of 0.5 mm was estimated to be  $\sim 0.4$  mm, similar to lining thickness (in a 2D model with a through-width crack). Therefore, it seems consistent that a growing crack within stronger and stiffer

material would require a substantial number of cycles despite stress concentrations arising from cracks within the interlayer that may have accelerated the initiation process.

The detachment of a lining particle is a complex process that requires a number of conditions to be fulfilled, such as initiation and growth of two different cracks originated on the lining surface and deflection and coalescence at the interlayer, parallel to the layers orientation. The numerical analyses have estimated the number of cycles  $N_L$  necessary for a single independent crack to reach the interlayer; nevertheless, the growth of a second crack, affected by a larger and more dominant crack, is expected to be slower. Two-dimensional analyses in Section 4 showed that parallel-dominant and oblique crack orientations were affected by other cracks according to the separation  $h$  between them. However, it is believed that the second crack would exhibit similar values of  $N_L$  according to experimental observations [10] showing simultaneous growth of multiple cracks despite having parallel-dominant or oblique orientations and high deformation levels near the crack faces in 3D analyses (see Figure 69). The crack propagation phase within the interlayer is not expected to contribute significantly towards  $N_f$  due to its compliance, weaker mechanical properties and high CDF values obtained in comparison to the lining in 2D models. This reasoning is also supported by Figure 12, which shows that two independent cracks have reached the interlayer before substantial growth existed in the backing.

The results obtained from total life experiments,  $N_f$ , under three-point bending did not appear to be representative of the number of cycles necessary for a lining fragment to detach and, therefore, were not expected to be useful as a measure of the detachment likelihood for lining material. The analyses developed with a maximum load of 720 N showed that at least 60% of the applied cycles seemed to be dedicated to processes developing at the steel. It could be argued that a constant proportion of life is spent to initiate and propagate cracks to the interlayer and, thus, assume that total life, propagation life, propagation life within the lining and propagation life within the backing

estimates are proportional at any given load level. However, the application of a different level of loading determines the state of strain and stress within the interlayer and is dependent on the position and trajectory of the crack, as shown in Section 3.3.1 with 2D analyses. This state of stress influences the period of initiation and growth within the backing in a manner that is difficult to predict. A constant proportional life is not expected to hold due to the differences between the lining, interlayer and backing materials of the MAS-20S architecture. Therefore, this measure is expected to be load dependent and unable to give a single value per tested architecture.

However, total life experiments provided valuable information regarding the importance of crack initiation and growth within the lining and clearly showed the importance of the backing layer in terms of structural support for the whole architecture. It is true that the detachment of lining fragments reduces the engine performance; however, the amount of damage that this architecture can hold without a critical failure is substantial which indicates the need for future 3D in-situ experimental analysis of failure.

The effect of coalescence on the fraction of total life necessary to reach the interlayer had an overall effect around 5%. This effect did not appear to be substantial in comparison to the crack extension observed at the surface. This is partially caused by the fact, that coalescence did not double the crack depth but only accelerated the depth growth process due to the enlargement of the crack observed from the surface. This enlargement forced the material located deep into the lining to accelerate its growth to achieve a more natural shape of the crack and, in this way, accelerated the depth growth.

The overall effect of coalescence did not appear to be substantial due to the apparent importance of the initiation process on the number of cycles to reach the interlayer. However, the analysis of every particular stage of growth for twin co-linear cracks, in comparison to a single independent crack, showed crack growth rises around 20% which could be considered more substantial.

## **6.6. Summary**

The crack growth analysis under LSY conditions in multi-layered architectures is a time consuming activity for the analyst and a computationally expensive process. Nevertheless, the development of such analyses show clearly the influence of shielding and anti-shielding when quasi semi-elliptical cracks are analysed. In contrast to 2D analyses simulating width-through cracks, the growth of quasi semi-elliptical cracks in 3D analyses did not show such a substantial effect under LSY conditions; this is consistent with previous analyses at more moderated conditions of yielding in Section 5.

The number of cycles for a crack to reach the interlayer, including the initiation process, showed values between 290,000 and 370,000 cycles equivalent to a 32% and 40% of the experimentally determined total life under three-point bending test of a flat strip of MAS-20S with a failure criterion set to an additional maximum absolute deflection of 0.5 mm. These life estimates were obtained using the relationships proposed by Chan and Lankford and Tanaka. The former, accounting for microstructural barriers, showed a more conservative prediction of fatigue life based on the analysis of short fatigue crack growth behaviour. Due to the reduced number of cycles required for a crack to reach the interlayer, it was determined that the experimental tests could not be used as a representative measure of the number of cycles necessary for a lining fragment to detach.

Crack coalescence effects showed an overall moderate effect on reaching the interlayer. Coalescence did not occur in the direction of depth and, therefore, the only acceleration observed was caused by the crack reshaping process towards a more natural shape according to loading and architecture. Comparisons with single independent cracks showed crack growth accelerations up to 20 % at particular stages.

## 7. Chapter Seven: Stress analysis of plain bearings

### 7.1. *Introduction*

The objective of this chapter is to study the effects of bearing service conditions on the material and, thus, understand the conditions under which crack initiation and propagation may occur. Bearing service conditions involve cyclic loading patterns with complex profiles over the lining surface and change rapidly as the engine cycle goes through the different combustion stages. Stress and strain estimations at the lining surface are used as key indicators of the deformation arising in the component.

### 7.2. *Background*

Pure fatigue failure events in bearings in service are difficult to find. Usually a combined set of mechanisms, such as fatigue, cavitation erosion, wear and corrosion damage bearings. A typical failure observed in bearing is the lining detachment that releases free fragments into the hydrodynamic film, which damages the surface of the journal or the bearing. The deterioration of the surface modifies the EHL profile causing larger pressure gradients and, consequently, greater tendency to fatigue damage.

The lining detachment occurs through a three-dimensional crack growth process that is influenced by the layered architecture of the bearing and the EHL profile. The principal trend observed in this process is the alignment of the crack path to run parallel to the layers orientation (as shown in Figure 12). At the same time, characteristic interaction mechanisms between cracks and mixed mode loading may cause coalescence in the plane parallel to the bearing surface (as shown in Figure 52). An example of lining detachment can be observed in Figure 92 [62].

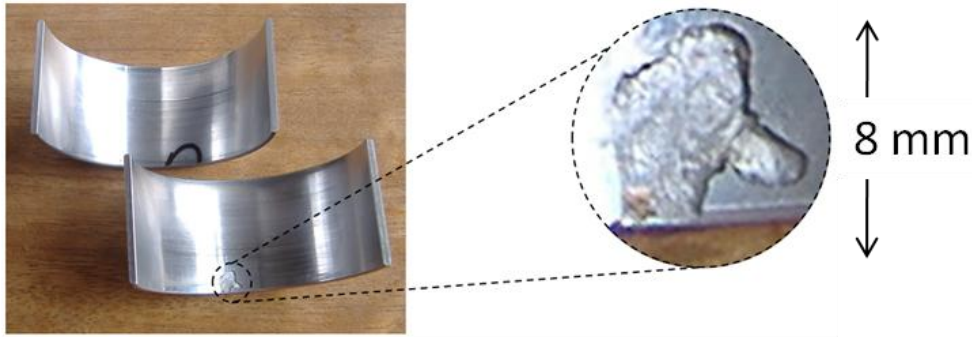


**Figure 92. Lining detachment caused by fatigue mechanisms.**

Early work related to the study of fatigue damage in plain bearings has mainly involved semi-empirical approaches aiming at the estimation of total life of service. Studies in the 1970s by Lang [167] and Hardbordt [168] on journal shells related their fatigue resistance to estimations of the surface tensile stress. Their observations concurred that the position of maximum stress corresponds to that of the maximum pressure gradient, leading to possible crack initiation. Their findings were supported by previous experimental work by Blount [169], who found that cracks tend to propagate axially and radially due to circumferential stresses. McCallion & Lofti [170] studied the effect of oil pressure inside the bearing chamber on fatigue life and suggested that higher elasto-hydrodynamic lubrication (EHL) pressures cause a bearing life reduction since the oil is forced into the crack increasing its opening.

Finite element analyses have extended the understanding of fatigue processes in bearings and the relation between the EHL pressure and crack propagation. McCallion and Lofti [170] and Martin *et al* [171] used 2D finite element analyses to study the stress distribution over the lining. These independent studies showed a good correlation between fatigue crack initiation in test specimens from the work of Gyde [172] and Blundell [173] with their estimations of the maximum circumferential stress. In the early 1990s, Bahai and Xu [174] predicted the EHL pressure over a bearing based on an axisymmetric elasto-plastic finite element model; they examined the influence of the deviatoric circumferential stress and strain as well as the hydrostatic stress. Their work

concluded that tensile deviatoric circumferential stresses at crack initiation sites are present during the whole cycle while their hydrostatic counterpart ruled the overall stress state in a compressive environment. Circumferential stresses were reported as compressive along the whole loading cycle; however, smaller negative values were obtained through the unloading process. Hacifazlioglu and Karadeniz [175] developed a three dimensional finite model and studied the effects of the housing rigidity on fatigue life in relation to the opening bending strains generated as the housing deforms. Little information on the effect of residual stresses caused by forming operations or cyclic loading was found in this literature review.

### **7.2.1. Bearing design procedures at MAHLE Engine Systems**

The manufacture of plain bearing architectures for the automotive industry has been carried out by various companies; MAHLE Engine Systems is one such established company. MAHLE was founded in 1920, originally dedicated to the manufacture of pistons. Nowadays, MAHLE is one of 50 largest automotive suppliers in the world and one of the top three piston system suppliers [176]. The design process developed in MAHLE Engine Systems provided important information related to service and accelerated fatigue test conditions for this work. This data along with experimental results obtained by MAHLE promote the analysis of more realistic service conditions and their validation.

The design process carried out in MAHLE Engine Systems introduces assembly and operating conditions into their analysis leading to the selection of a suitable architecture and materials for the desired application. The design analysis in its comprehensive form consists of three main stages as shown in Figure 93: Bolt-up analysis, calculation of the bearing loads and EHL analysis through the SABRE-EHL software (in-house code developed by MAHLE Engine Systems).

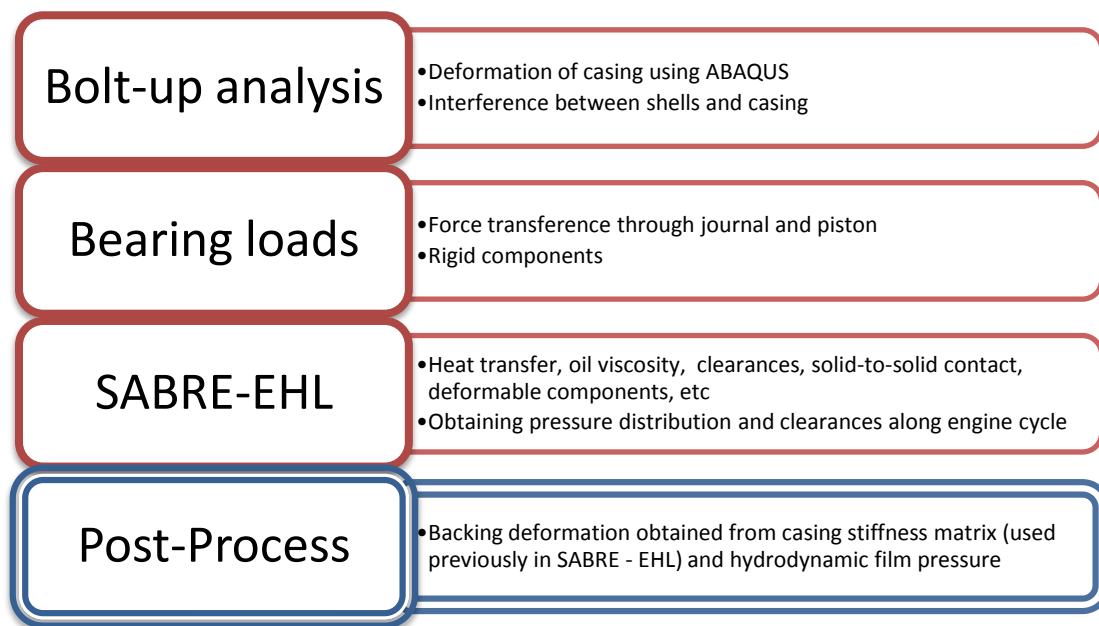


**Figure 93. Design stages for MAHLE Engine Systems (Post-processing operations are only carried out in this research project, not currently required for MAHLE Engine Systems).**

The bolt-up analysis predicts the bearing deformation caused by the process of fitting the bearing into the housing. This is a non-linear FE analysis developed on ABAQUS that models contact between components and estimates the bearing shape and clearances between the bearing and journal surfaces. A quasi semi-elliptical shape of the fitted bearing instead of a perfect circle is usually observed in practice and adopted in EHL analyses of experimental arrangements. It is noteworthy that the bolt-up FE analysis is applied only in order to estimate the clearance between the journal and the bearing. Simpler analyses are applied to assure that the bolt-up process does not cause excessive deformation and stress on the component.

The next analysis step consists of the calculation of the applied forces on each bearing according to its position in the engine. These forces, usually given as specific loads, that is, force applied to the bearing over the projected lining area, are used to compute the EHL pressure distribution over the bearing surface, shown schematically in Figure 94, during the cyclic motion of the crankshaft.

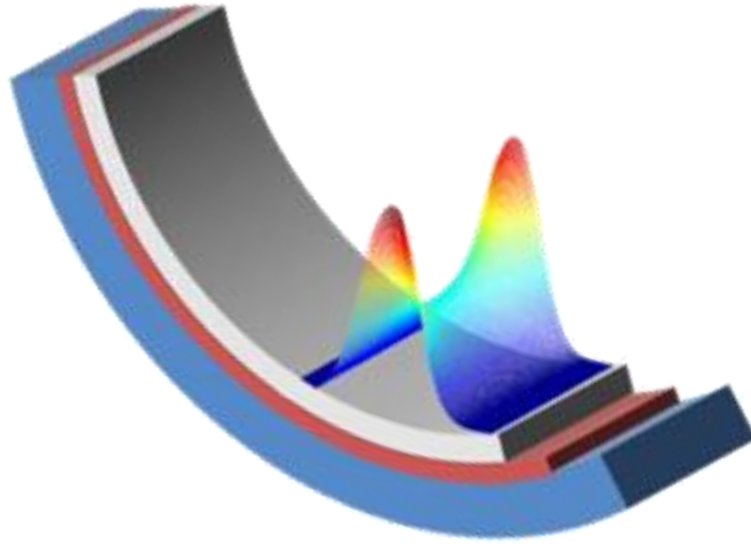


**Figure 94. Representative EHL pressure over bearing surface.**

In order to estimate the EHL pressure, the behaviour of the EHL film is studied through a coupled analysis involving structural and thermal responses. This analysis is the most elaborate step in the design process and involves a heat balance analysis to determine the oil viscosity and material expansion in order to estimate the clearances between bearing and journal. An extended analysis using the in-house code SABRE-EHL may include the modelling of oil feed, journal profile (including grooves and elliptical shapes) and solid-to-solid contact with flexible components. SABRE-EHL is based on the finite difference method and accounts for the elastic deformation of both journal and bearing-rod assembly. SABRE-EHL analyses by MAHLE engine systems assume elastic deformations, Newtonian fluids and the absence of bubble collapse within the fluid. The estimations of pressure, film thickness and other relevant factors are compared to those of previous successful designs to determine their suitability for the operational conditions to be met.

The EHL pressure as well as the housing deformation is the output from SABRE – EHL that is mainly relevant to this research project. It is noteworthy that fatigue crack initiation has also been traced to the position of maximum pressure gradients [167, 168]. The minimum film thickness is also

relevant in order to investigate if contact and its resulting shear over the lining surface may be responsible for crack initiation.

Several operations that affect the final stress and strain state can be indentified during bearings' manufacture, as described in Figure 9, and under service conditions. In a chronological order, the first operation causing residual stresses is the concave shell forming operation; this operation is carried out after a thermal treatment that alleviates previous residual stresses from previous layer bonding. Secondly, fitting operations into the casing reduce the effective radius of the concave shell. Finally, service conditions are assumed to be governed by EHL pressure and the concomitant casing deformation; both estimated through SABRE – EHL.

### ***7.3. Residual stresses from forming operation***

The estimation of residual stresses was carried out by simulating the forming operation of a flat strip into a concave shell. This operation consists of a punch that drives a flat strip into a die until the concave shell is formed and two secondary processes designated coining and broaching. The “coining” process consists of a membrane deformation of approximately 0.5 mm applied to the concave shell ends when the punch is located at its lowest or deepest position in contact with most of the lining surface. This operation is aimed at reducing the intensity of the residual stresses. The broaching process consists of the material removal of approximately 0.1 mm from the top of the lining layer and its aim is to fulfil the geometrical tolerances of the part and remove a pure aluminium protective layer.

The forming process appears to be essentially independent of the bearing width, that is, two-dimensional. In order to test this hypothesis, a 3D FE model of the multi-layered strip was initially developed accounting for three different types of non-linearities: elasto-plastic material, large deformations and contact between the forming tools and the strip. Friction between the surfaces was characterised by a dynamic coefficient whose value was assumed comparable to that for two

lubricated components of steel [177], that is, approximately equal to 0.1. Analyses presented later in this chapter assessed the effect of varying this coefficient on the results of the simulation.

For the sake of computational efficiency, both die and punch were modelled as rigid due to their stiffness being much larger than that of the deformable flat strip. For this reason only the punch contact areas were modelled. The radius of the punch and die were set at 27.105 and 28.215 mm, respectively. The bearing consists of two shells with a diameter ( $D_b$ ) of 56.43 mm made of a strip of length ( $L$ ) of 95.61 mm, a width ( $W_b$ ) of 29.49 mm, a lining thickness  $t_{l,2}$  of 0.42 mm and a backing thickness  $t_b$  of 1.8 mm. Other computational costs of the 3D simulation led to neglecting the effect of the coining and broaching process at this stage. The mesh of the flat strip was consistent with that used in the SABRE - EHL analysis to simplify the application of boundary conditions in later analyses and transfer residual stress information, which was based on the elements and their internal integration points. The complete model is shown in Figure 95.

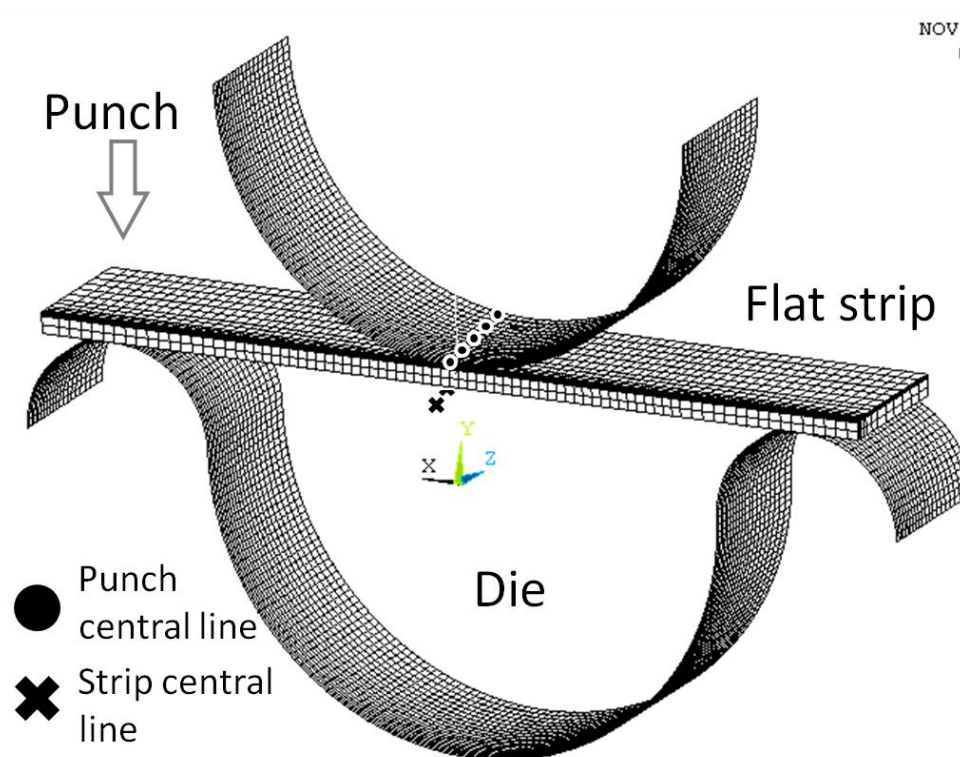


Figure 95. Forming process components.

Initial simulations that modelled the tri-layered architecture MAS-20S showed an unstable solution behaviour caused by the large deformation of the compliant and thin interlayer leading to excessive computational costs. This problem also arose later in the initial modelling attempts at bearing analysis under service conditions. For this reason, the analysis was applied to a bi-layer architecture with a lining thickness  $t_{L2}$  equal to  $t_{L1}+t_i$ , whose behaviour at early stages of propagation under three-point bending conditions in 2D and 3D was shown to be identical to its tri-layer counterpart.

The forming simulation was initially carried out in 4 different steps: initial contact, main deformation, punch removal and extraction of the shell overcoming friction. The punch travelled gradually towards the die deforming the flat strip into a concave shape until the punch was removed. Spring back forces existed at this point of the simulation. In consequence, a partial removal of the punch caused the concave shell to rise away from the central part of the die. Taking advantage of this event, the DoFs in the vertical direction of the punch and strip central lines (shown in Figure 95) were coupled so that the formed bearing would be extracted from the die and, thus, retrieve the residual stresses.

Previous studies [169] have shown the importance of the circumferential stresses on the bearing service life and how they may relate to crack initiation and propagation. The residual circumferential normal stress was particularly significant due to the nature of the forming process. The stress over the lining surface at the end of the main deformation and punch removal stages appeared to be highly compressive, as shown in Figure 96. Compressive and tensile stresses in the backing reflected the expected behaviour of a beam subjected to a moment, shown Figure 96 Substep 1, while stresses in the lining remain compressive across its thickness. The evolution of stresses at the lining surface during the extraction step is also shown Figure 96 at steps 1, 2 and 3,

corresponding to at 15%, 50 % and 85%, respectively, of the vertical travel to release the concave shell from the die.

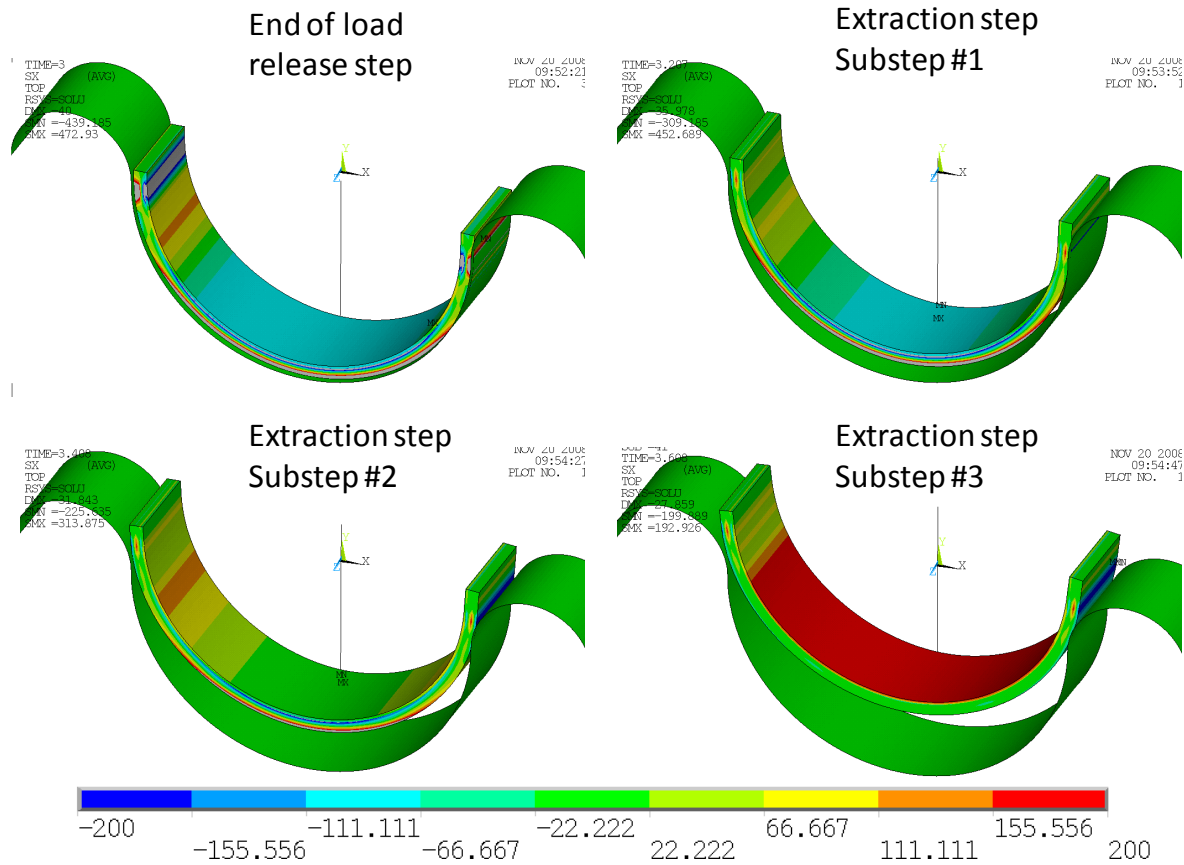


Figure 96. Circumferential stress evolution during the forming process.

Figure 96 Substep 3 shows the tensile residual circumferential stresses after the bearing was extracted from the die. A constant stress can be observed over most of the lining surface, especially in the lowest central part of the concave shell where the greatest values of EHL pressure are usually found. According to the analyses developed so far the magnitude of the residual stresses was around 180 MPa. The stresses arising from the forming analysis were constant across the bearing width, as expected from the constant bearing cross section and the applied deformation.

Based on these results, 2D models with a greater mesh density were developed to increase the resolution of the obtained results, especially in the backing where only two elements through-

thickness were used in 3D models. At the same time, the impact of the assumed friction coefficient  $\mu$  was assessed by using different values in the range from 0 to 0.25. The comparison between 2D and 3D analyses using a  $\mu = 0.1$  showed very similar results, especially in the lining where greater mesh density was used in contrast to the backing layer. A more significant difference was observed in the latter where less refined meshes in the 3D model appeared not to be sufficient to capture accurately the resultant residual stresses. The cross-sectional residual stresses in the 3D model and the residual stress distribution comparing 2D and 3D models are shown in Figure 97. The predicted residual stresses in the circumferential direction are shown to be affected negligibly by the variation of the assumed coefficient of friction within the range 0.03 to 0.25, shown in Figure 97. Neglecting friction led to a significantly different deformation process; this was especially evident in the location of contact points between the punch and the lining. Any model that assumed friction showed that contact remained mostly at the central line. This is in contrast with the frictionless simulations which showed that contact shifted to two outer positions as the punch was driven downwards. The estimates of residual stress also showed a significant difference when friction was assumed not to exist.

More detailed simulations that included the coining and the broaching process were then performed for  $\mu = 0.1$ . The coining process was modelled using a rigid surface that applied a deformation equal to 0.5 mm to the bearing edges. This step was included before the punch was released resulting in a stress alleviation in the circumferential direction. The broaching operation was modelled after the bearing shell was extracted removing a single layer of elements at the lining surface through the “kill” functionality in ANSYS 11 [55]. These simulations assumed that the machining carried out in the broaching process did not produce any additional residual stresses caused by shearing during the material removal. The introduction of coining and broaching operations only resulted in a small drop of the residual circumferential stresses by about 20 MPa

(9.5%). This is in contrast to the total simulation time which almost doubled. The evolution of the circumferential stresses at the centre of the bearing is shown in Figure 98.

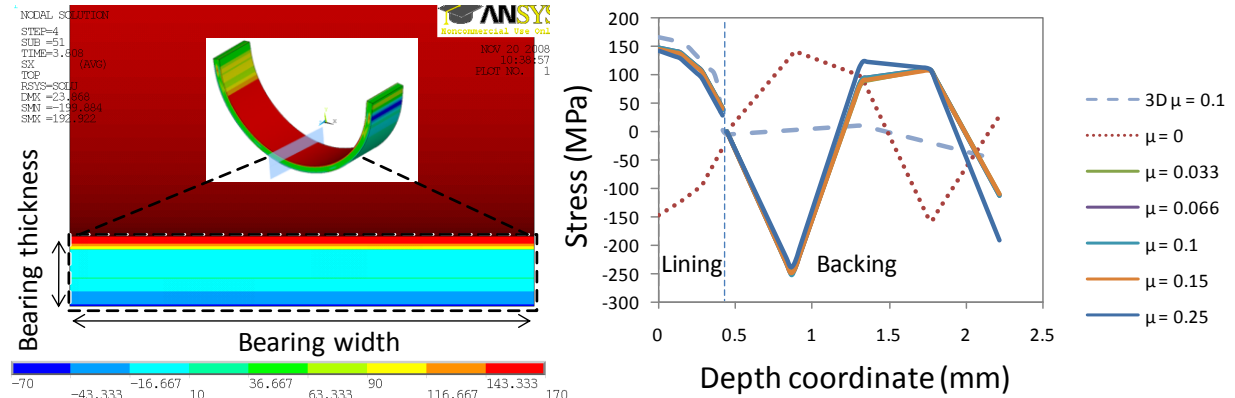


Figure 97. Cross Section of the bearing showing residual circumferential stresses resulting from forming (left) and residual circumferential stresses from 2D and 3D model showing the influence of friction (right).

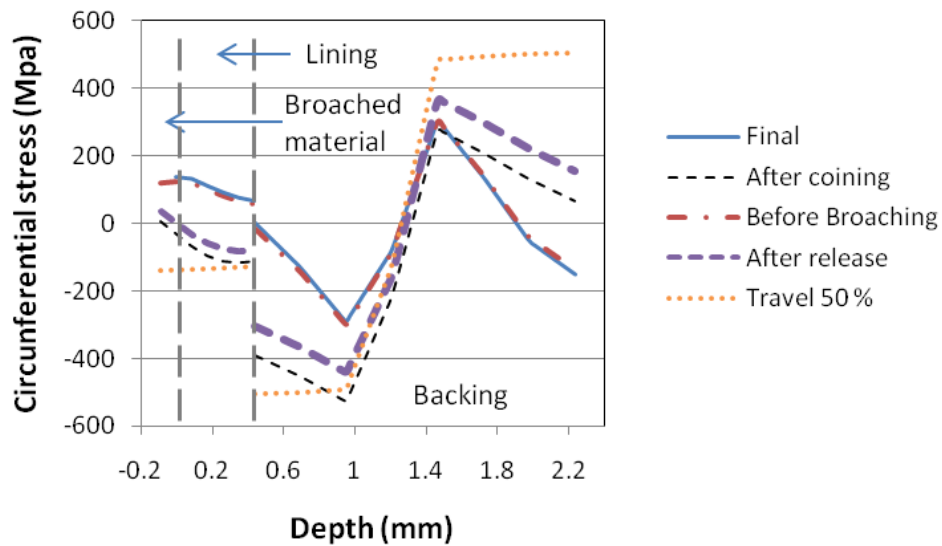


Figure 98. Evolution of the circumferential stresses when coining and broaching operations are included.

The magnitudes of the residual stresses observed in these simulations were 200% higher than the yield stress of the lining material. Such residual stresses would be expected to be detrimental to the fatigue life of the component due to their magnitude and direction. Given the established long life of

the component it appears unrealistic that such values remain on the lining surface during extended cyclic loadings. The hardness evaluations of the lining materials [10] as-received bearings of flat strip material showed very little variation. Some apparent hardness variation would be expected if such high tensile residual stresses remained. This indicates that the values of residual stresses may have been significantly overestimated.

#### **7.4. Full bearing analysis**

Typical bearing design analyses in MAHLE Engine Systems are based on the comparison between EHL pressure and clearance estimates of successful and new designs. EHL pressure is a good indicator of the bearing loading capacity while the clearance between journal and bearing has been used as a measure of possible solid to solid contact. At the same time, low clearance values and high pressure gradients have also been related to cavitation erosion that promotes the explosion of air bubbles that damage the bearing surface. However, these measures do not consider the bearing mechanical properties. The estimation of strain and stress arising from service conditions, obtained through the SABRE-EHL software, is a more representative measure of the material cyclic deformation and, in consequence, a clear indicator of possible fatigue damage promoted by that deformation.

The estimation of EHL pressure arising from the service conditions was based on the design process developed at MAHLE Engine Systems. Realistic loading conditions are vital to the reliable determination of circumferential stresses. This stress analysis is a key indicator of the position, circumferentially and axially, in the bearing where cracks are expected to initiate and develop. The bearing service conditions encompass structural, thermal and fluid mechanics features that result in a complex multi-physics problem. SABRE-EHL transforms the input into forces and deformations which only show the overall estimated structural behaviour. Local effects, such as bubble collapse promoted by high gradient pressures, were not accounted for.

Some post-processing operations are necessary in order to convert the data obtained from the SABRE-EHL software to “ready to use” boundary conditions for FE analyses. These boundary conditions consist of the EHL pressure and the deformation of the bearing casing. The former is obtained directly from SABRE-EHL; while the latter is indirectly used in the EHL computation but not stored during the solution process. However, the casing deformation can be obtained by multiplying the EHL pressures (in its nodal force form) by the compliance matrix of the housing and bearing to produce the total deformation that the bearing lining  $d_b$  experiences.

Using the lining deformations obtained from the SABRE-EHL  $d_b$ , it is possible to estimate the radial deformation at the interface between backing and casing  $d_c$

$$d_c = d_b - d_f + d_n \quad (25)$$

where  $d_f$  represents the bearing deformation caused by the fitting operations and  $d_n$  the normal shell deformation caused by EHL pressure as shown in previous work by Bahai and Xu [174].

The normal shell deformation was assumed to be equal to the EHL pressure multiplied by the bearing architecture radial compliance  $C_{norm}$ . Applying superposition, the concave shell compliance in the radial direction is obtained as

$$C_{norm} = \frac{t_b}{E_b} + \frac{t_{L2}}{E_{lin}} \quad (26)$$

This assumption of elastic response is consistent with EHL analyses, which are only based on elastic material models and accounted only for the radial displacements and the EHL pressure. An additional source of deformation was introduced by the fitting operation forcing the bearing effective radius to shrink. This deformation can be extracted from the initial clearance profile introduced into SABRE – EHL ( $\sim 28 \mu\text{m}$ ). The FE boundary conditions for the developed analyses are schematically shown in Figure 99.

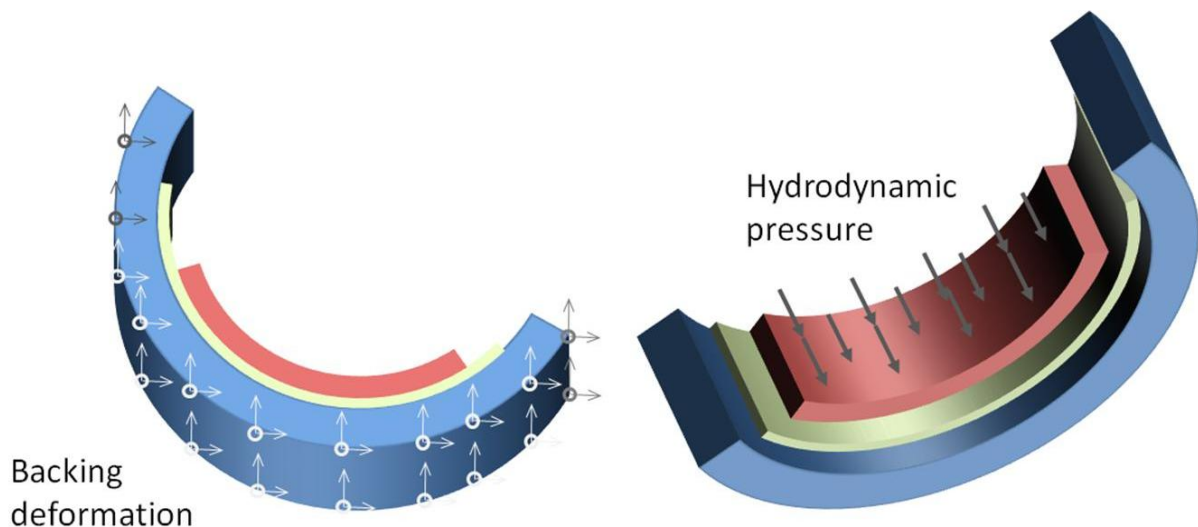


Figure 99. Boundary conditions application.

#### 7.4.1. Accelerated fatigue test conditions

The loading conditions analysed in this section corresponded to those arising during accelerated fatigue tests developed by MAHLE Engine Systems (the test rig is known as the Sapphire rig schematically shown in Figure 100). The Sapphire rig consists of an eccentric shaft that forces a piston to travel in the vertical direction through a connecting rod. At the same time, the rig applies some resistance to the movement of the piston due to the oil present in the chamber of a hydraulic ram. This oil is forced into another chamber and its flow is regulated by valves to obtain the desired resistance of travel or specific load applied to the bearing. The measurement of the load applied to the bearing is carried out through strain gauges positioned on the connecting rod. This rig also measures the bearing temperature, which has been used as a parameter to identify failure (through a measurement spike of  $5^{\circ}$  interpreted as a performance drop). A great amount of experimental fatigue data are generated under such conditions; this makes the Sapphire rig output an ideal candidate for comparison with the results of numerical simulations. The bearing casing used in these accelerated fatigue tests is stiffer than the regular casings used in automotive engines leading to conditions that promote the bearing extended lives. At the same time, the simulations of

accelerated fatigue tests can be supported by more detailed experimental information and, thus, lead to the development of a future benchmark for the materials used by this company.

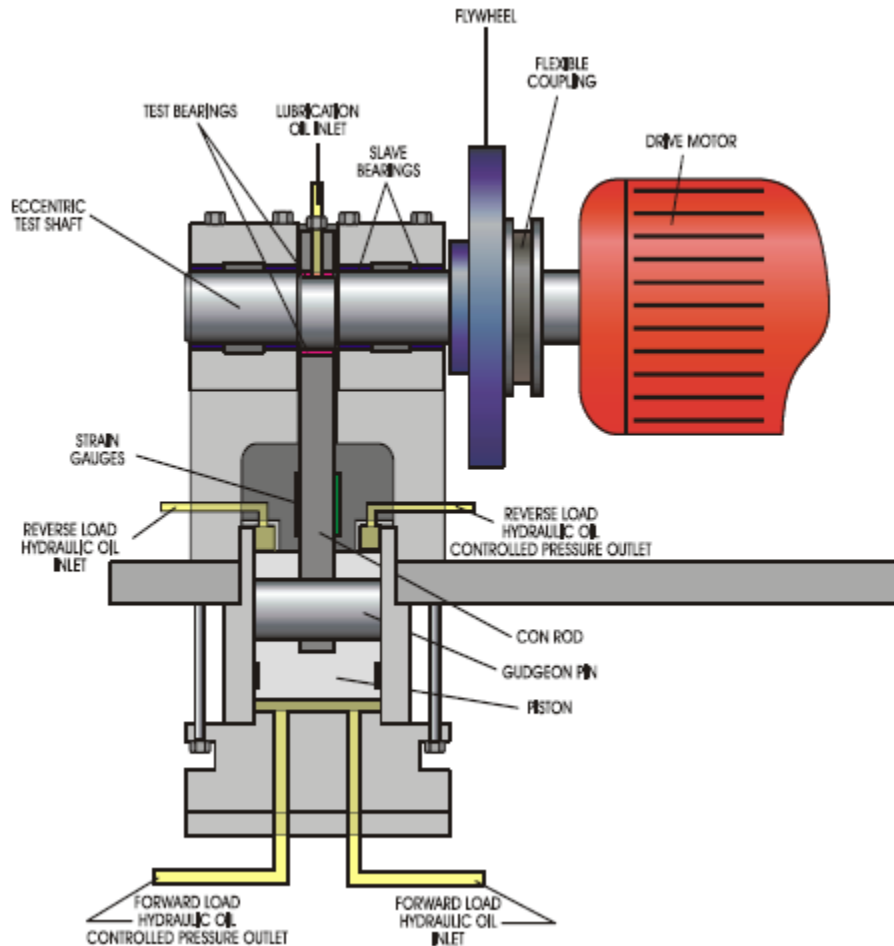


Figure 100. Sapphire rig.

Due to the way the Sapphire rig operates, the specific load is applied on the bottom shell (as shown in Figure 101a); however, casing deformations also occur on the side of the upper bearing shell as well. Figure 101b shows the associated deformation at maximum specific load and the contours of strain in the circumferential direction. The evolution of deformation and pressure during the engine cycle is shown in Figure 102a and Figure 102b, respectively, along the bearing symmetry line (see Figure 101b). The evolution of EHL pressure showed that despite the absence of specific load applied over the upper shell, EHL pressure existed due to the inertial forces and the pressure

difference between Sapphire rig chambers. However, the magnitude of the observed EHL pressure on the top shell was found to be insignificant in comparison to that applied on the bottom shell. This is consistent with experimental observations that damage only occurs on the bottom shell. The EHL pressures and bearing housing deformations, shown in Figure 102, correspond to accelerated fatigue tests in MAHLE Engine Systems at 3000 RPM with a specific load of 97 MPa.

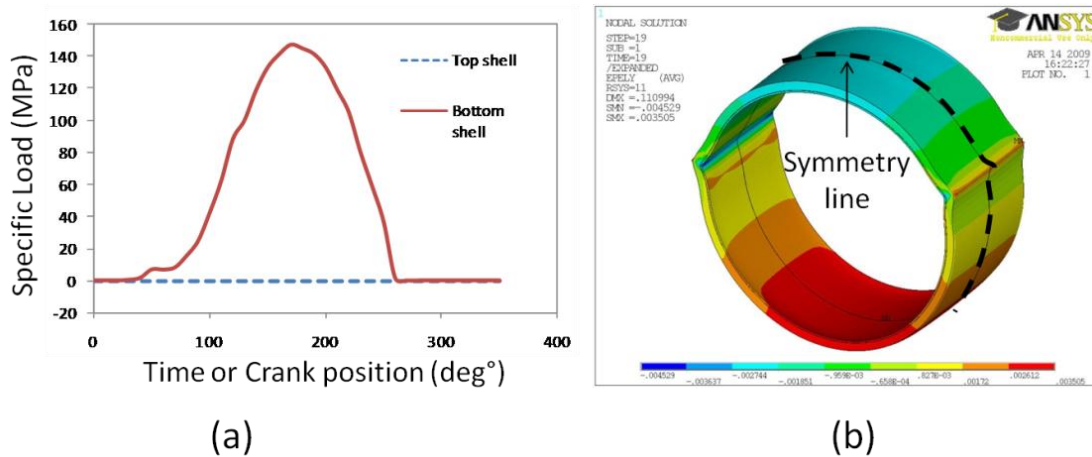


Figure 101. Specific load applied to upper top and bottom shell (a) and circumferential strain (MPa) in the bearing lining (neglecting fitting and forming operations and assuming linear elastic material models) at the cycle peak pressure (b).

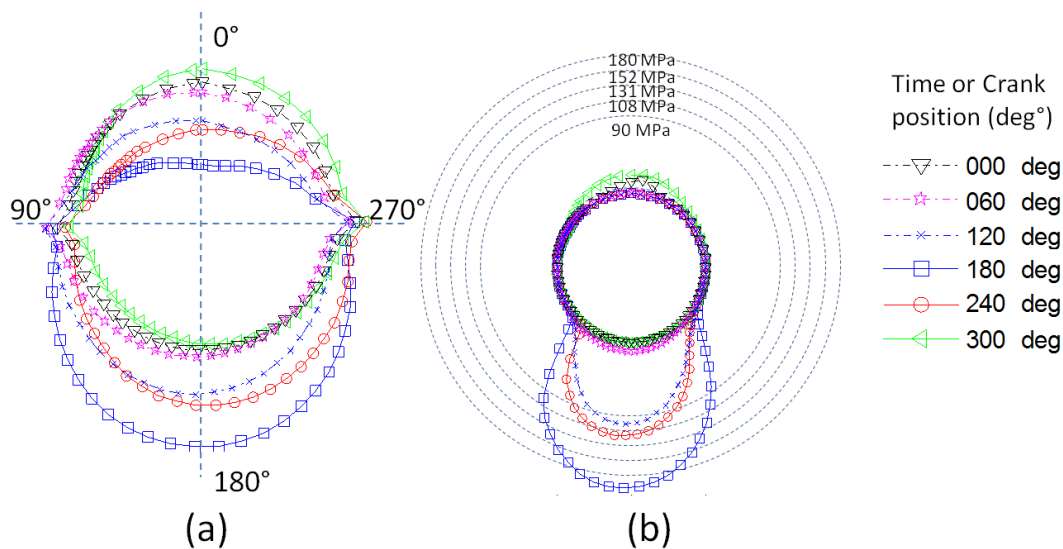


Figure 102. Bearing casing deformed shape (a) and EHL pressure evolution (b) during engine cycle (not to scale).

For the assessment of stress and strain, four different analyses were developed. These analyses evaluated the implications of neglecting the residual stresses arising from forming and fitting (F&F RS) and accounting for plastic deformations within the simulation. In total, four different simulations were developed: (1) elastic material model neglecting F&F RS, (2) elastic material model accounting for F&F RS, (3) elasto-plastic material model neglecting F&F RS and (4) elasto-plastic material model accounting for F&F RS.

F&F RS into the analyses described above were included through two different sources. First, the effect of the fitting operations on the bearing service condition was included or neglected through the computation of the bearing casing deformation  $d_c$ , shown in Eq. ( 25 ), and the parameter  $d_f$ . The value of  $d_f$  was set to 28  $\mu\text{m}$  when the effects of F&F RS were included; otherwise set to 0. The effect of forming residual stresses was applied into the numerical simulation by the functionality INISTATE [55] of ANSYS, which defines the initial state of the material according to normal and shear stresses in every direction. The elasto-plastic analysis accounting for F&F RS had an additional solution step at the beginning of the simulation to achieve equilibrium before the service conditions were applied.

The development of four different analyses is justified by the possible effects of the service temperature (around 150° C) on the material mechanical behaviour. Such a high temperature may cause stress relief reducing the impact of forming and fitting operations (temperature applied in annealing processes on aluminium alloys has been reported as low as 220° C [178]). At the same time, the high cycle fatigue life observed in this bearing did not match the levels of plasticity estimated in preliminary FE analyses (as high as  $4 \sigma_y$ ). The work hardening process occurring in the first few cycles may cause an elastic shakedown and be followed by elastic deformations in subsequent cycles. Therefore, it can be argued that accounting for F&F RS and plastic deformation

would not be representative of the deformation process affected by the service temperature and shakedown, respectively.

Linear-elastic analyses consisted of 36 steps (one every 10° of crank angle) to study stress and strain fluctuations over the test cycle. The results obtained from elastic FE analyses only depend on the currently applied step (which may also include additional radial deformation arising from fitting and residual stresses from forming). In contrast, elastic-plastic analyses that simulate plastic deformations would also depend on the previous load history. Therefore, the estimation of cyclic strain amplitudes was carried out at the third loading cycle involving a total of 108 service conditions' steps. This was aimed at reducing the influence of the initial deformation process at the first cycle and converging to a stable hysteresis loop. In this particular case and material model, three full loading cycles was found to be sufficient to reach such a stable deformation cycle. The discussion of results from these analyses was focused on circumferential stress and strains; however, other parameters such as Von Mises and the maximum principal stress were also considered for the sake of comparison.

#### **7.4.1.1. Stress and strain results**

The full bearing analyses, based on data generated by SABRE-EHL, were performed on the same computing facilities used for the bearing forming simulation. Typical stress and strain analyses over a complete crank cycle lasted about 24 hrs for elastic and 84 hrs for elasto-plastic analyses.

The analyses performed showed that lining stresses varied substantially during the cycle depending on the EHL pressure magnitude and the associated housing deformation. The results for total circumferential stresses and strains over the bearing surface at an axial section 1.8 mm from the edge were used to explain the different trends observed and compare the estimates obtained through elastic and elasto-plastic analysis accounting for or neglecting F&F RS. Sections at greater separations from the border were also examined showing similar trends.

The estimations of stress and strain presented next are plotted against two variables: the angular position around the bearing, describing the position where stress or strain was estimated, and crank angle, describing the time or crank position during the engine cycle ( $360^\circ$ ). The generated models predicted greater deformations and stresses in the central part of the bottom bearing shell near the EHL pressure peak (see Figure 102b). For this reason, the studied angular positions ranged from  $120^\circ$  to  $240^\circ$ . It is also noteworthy that the maximum EHL pressure occurs at a crank angle close to  $180^\circ$ .

General trends were difficult to find among the four tested models, especially when stress was analysed. Stress estimations appeared to be very sensitive to the inclusion of F&F RS while strain estimations were affected to lesser extent. The bearing angular position of maximum stress varied according to the model analysed but always appeared at a crank angle corresponding to the moment of maximum EHL pressure, shown in Figure 103a and b for elastic analyses only. In contrast, the bearing angular position and crank angle of maximum strain was consistent for every analysis performed, shown in Figure 104a and b for elastic analyses only. It is also important to mention that the angular position and crank angle at which the maximum EHL pressure occurred was consistent with that of the maximum radial casing deformation.

For the assessment of fatigue performance, the same stress and strain results were also plotted versus the crank angle. Figure 105a and b shows the difference between the estimates neglecting and accounting for F&F RS at four key circumferential locations. These plots show the existence of higher stresses at a bearing angular position equal to  $180^\circ$  when F&F RS were accounted for, in comparison to those obtained neglecting F&F RS. This stress rise was expected due to the highly positive values of F&F RS. At the same time, the behaviour of the stresses at bearing angular positions of  $140^\circ$  and  $220^\circ$  changed from minimum to maximum at a crank angle of  $180^\circ$ ; stress

estimations at these angular positions were almost identical to the one of 180°. The same behaviour was observed in strain data.

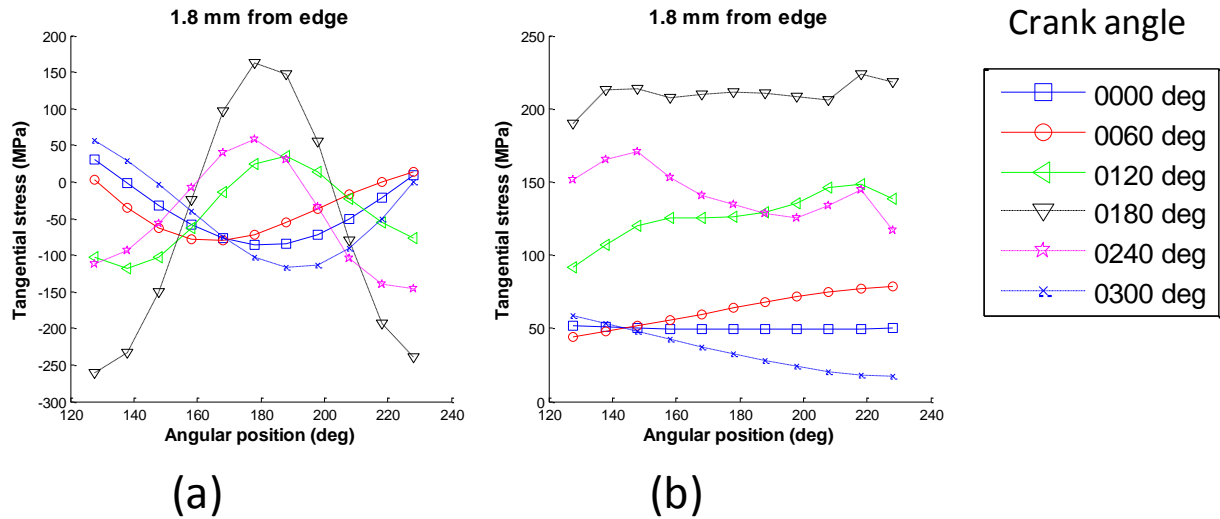


Figure 103. Total circumferential stress vs. position at various crank angles (or time steps) assuming linear elastic material model neglecting (a) and accounting for F&F RS (b).

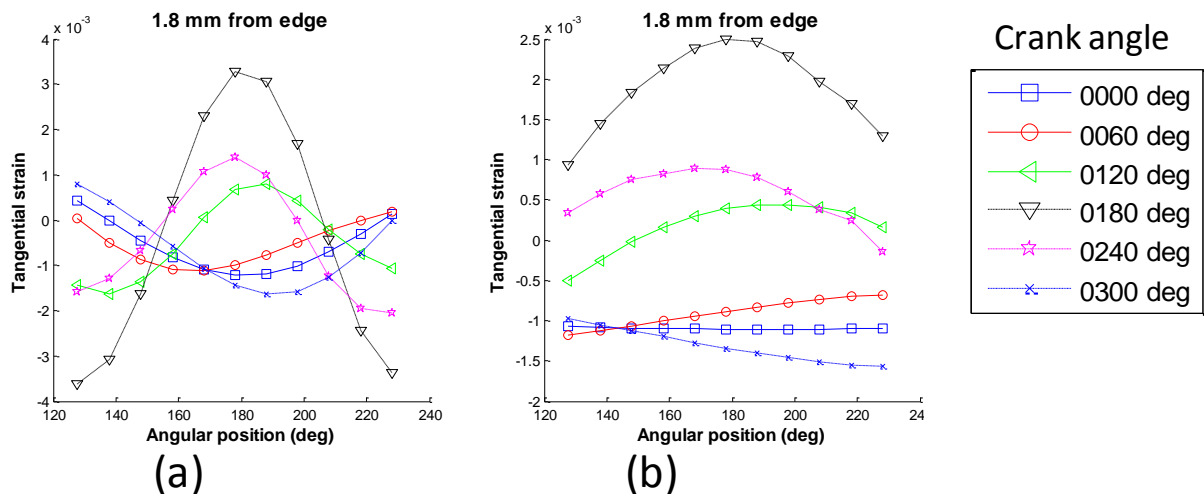
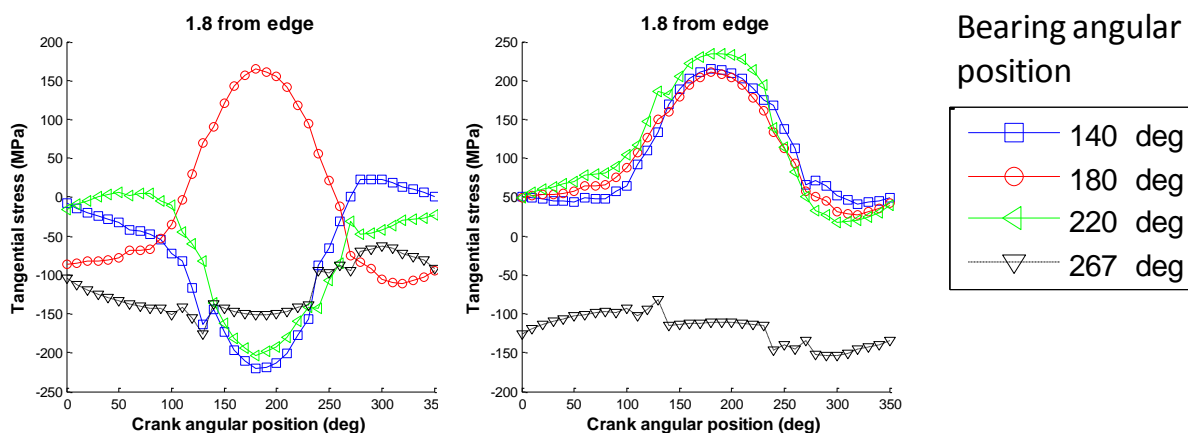


Figure 104. Total circumferential (or tangential) strain vs. angular position at various crank angles (or time steps) assuming linear elastic material model neglecting (a) and accounting for F&F RS (b).

Figure 105a and b revealed that there was, essentially, one representative deformation cycle per engine or crank cycle in the accelerated performance test. On the other hand, it is worth noting that the cyclic variation of stress developed in tensile-compressive and purely tensile scenarios when

F&F RS were neglected and accounted for, respectively, in elastic analyses. The amount of cyclic stress and deformation amplitude appeared to match a low cycle fatigue component with amplitudes greater than  $4 \sigma_y$ . However, tests in the Sapphire rig revealed high cycle fatigue lives of the order of millions of cycles.



**Figure 105. Total circumferential stress vs. crank angle at various angular position assuming linear elastic material model neglecting (a) and accounting for F&F RS (b).**

Similar to elastic analyses, elasto-plastic models showed that the maximum deformation was attained at an angular position equal to  $180^\circ$ , close to the peak of the EHL pressure. On the other hand, elasto-plastic models showed that most of the deformation cycle developed under compressive stresses, especially when F&F RS were accounted for. Despite the existence of mainly compressive stresses during the deformation process, positive circumferential strains of slightly greater magnitude than the ones observed in the linear elastic model were estimated, shown in Figure 106 and Figure 107. The difference between stress estimates was also notable between both elasto-plastic analyses, in contrast to strain estimates where a single peak of similar shape was observed when the maximum EHL pressure was applied.

The data produced by the simulations describing elastic and elasto-plastic behaviour neglecting or accounting for F&F RS was extensive and difficult to analyse. The analysis of data through stress or strain vs. bearing angular position or crank angle allowed the identification of some trends and

differences between the models. However, the analysis of stress and strain amplitude over the lining surface through the engine cycle (crank angle), seemed to be a better approach for assessing the fatigue performance of the lining and in the generation of damage maps that would provide a different view of the data previously presented.

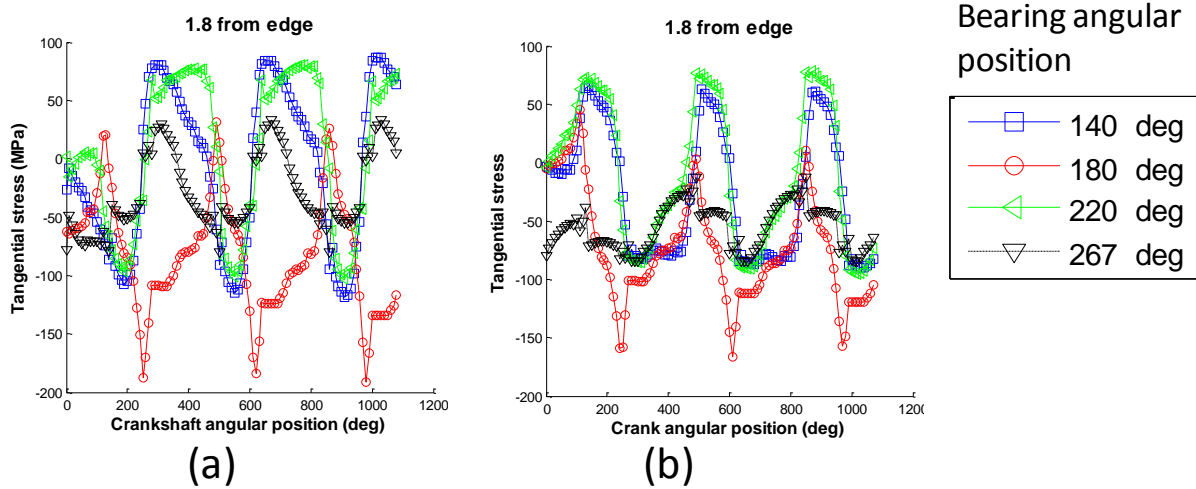


Figure 106. Total circumferential stress vs. crank angle at various angular positions assuming elastic-plastic model neglecting (a) and accounting for F&F RS (b).

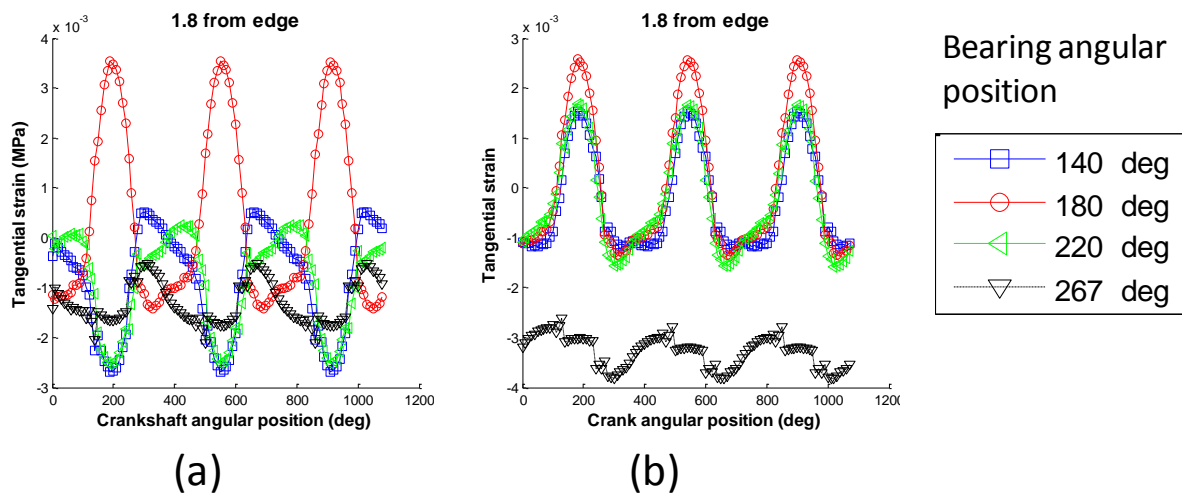
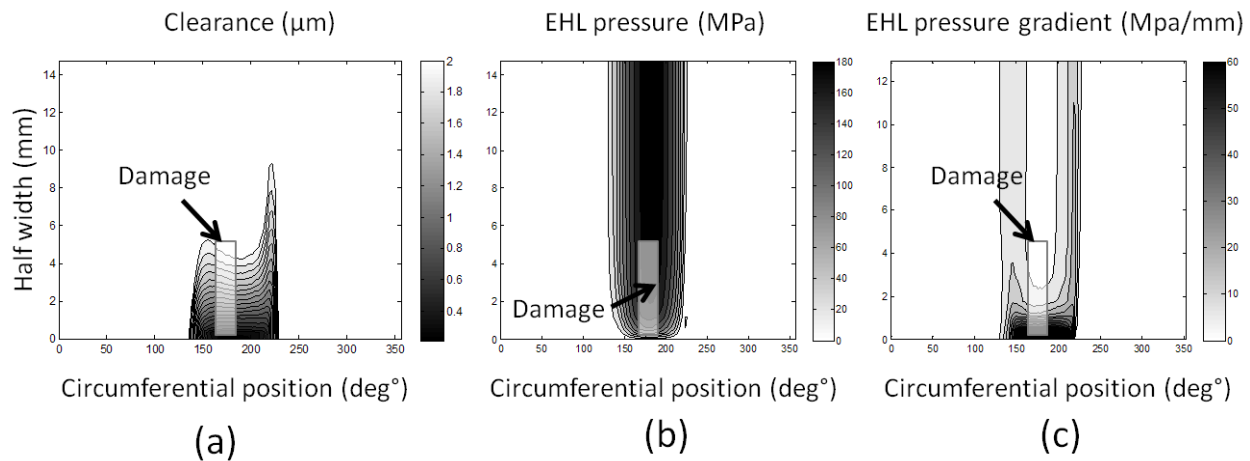


Figure 107. Total circumferential strain vs. crank angle at various angular positions assuming elastic-plastic model neglecting (a) and accounting for F&F RS (b).

### 7.4.1.2. Damage maps

The use of contour maps allowed the visualisation of distributions of clearance, EHL pressure, EHL pressure gradient and cyclic strain or stress. These maps display the value of the selected variable over the lining surface relative to a cylindrical coordinate system ( $z$  coordinate along the bearing width, the  $\theta$  coordinate along the circumference and  $r$  along the radial coordinate). Maps describing the EHL pressure, EHL pressure gradient and clearance between the journal and the bearing at the peak specific load are shown in Figure 108a, b and c, respectively.



**Figure 108. EHL pressure and clearance at 97 MPa at the cycle peak pressure.**

Of equal importance is the distribution of the stress or strain amplitudes, which were systematically evaluated over the whole lining surface as a measure of potential damage. As shown previously, the EHL pressure cycle consisted of a single peak and preliminary stress analyses showed the same trend with a maximum and a minimum point defining the whole deformation cycle. The amplitude of these peaks was used to create these maps and identify the most probable locations of crack initiation. The damage maps generated using circumferential, principal and Von Mises stress and strain are presented in Figure 109.

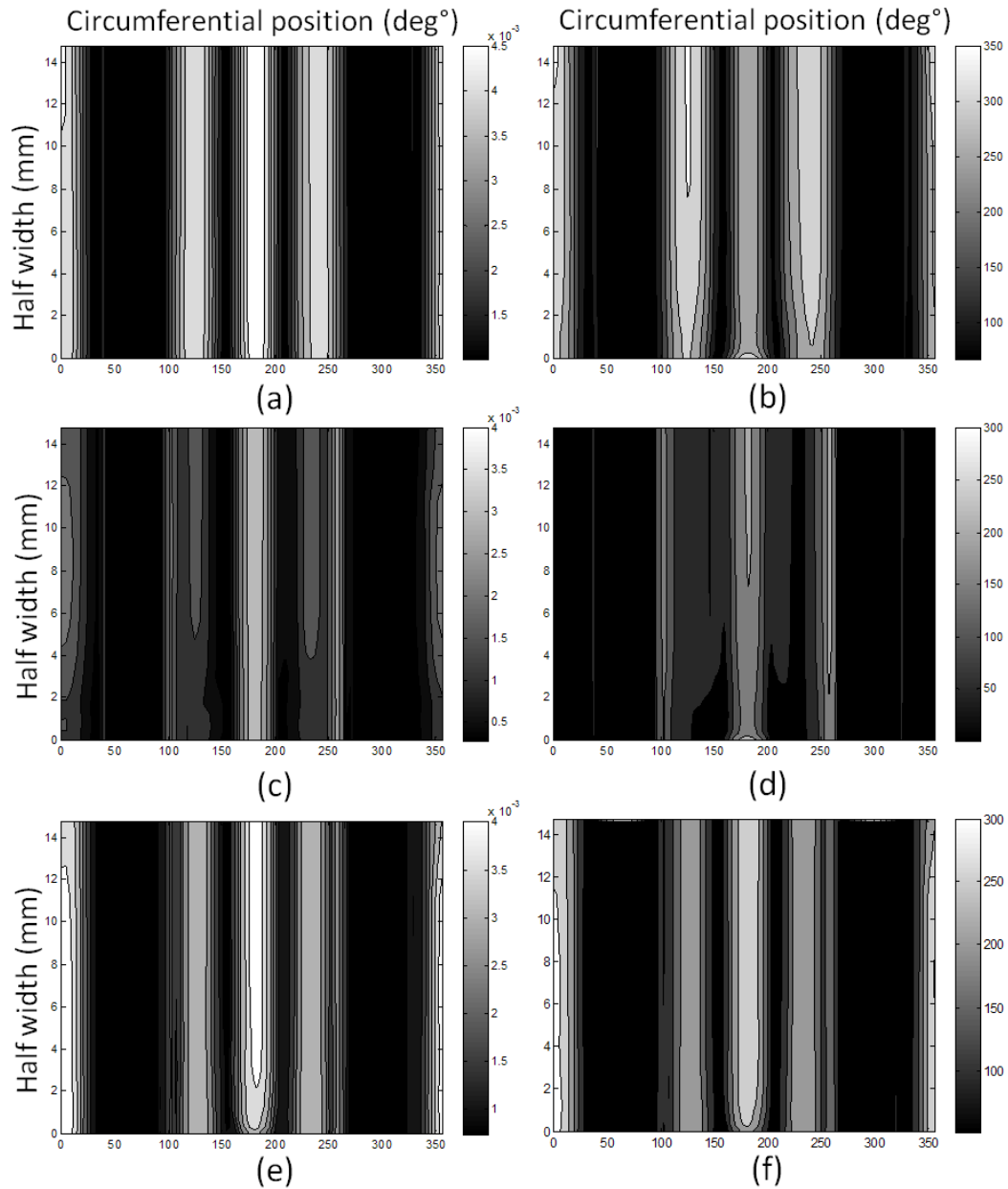


**Figure 109. Amplitude maps of elastic and no residual stress analysis. Circumferential strain (a) and stress (b), principal strain (c) and stress (d) and Von Mises strain (e) and stress (f)**

The damage maps presented in Figure 109 showed similar trends and some distinctive features. All the maps presented below show three clearly identified columns at around 130°, 190° and 240°. The middle column clearly corresponds to the position of maximum EHL pressure while the other two are often related to a bending effect caused by the casing deformation according to the design

team in MAHLE Engine Systems. It is also evident that strain maps place the greatest amplitudes at the location of maximum EHL pressure values while stress generated maps show similar values at the three columns. Circumferential stress damage maps, obtained from analysis with elasto-plastic material models, even showed that high amplitude areas caused by the bending effect were more significant than the one observed at the location of the maximum EHL pressure values.

The damage maps based on circumferential strain and stress assuming linear-elastic material models did not appear to be influenced by the addition of F&F RS, as observed in Figure 110 and Figure 111. This result was expected considering the superposition of two independent elastic analyses: service conditions and F&F RS. The application of F&F RS would not vary along the Sapphire test cycle and, consequently, would not affect the amplitude of estimated deformation.

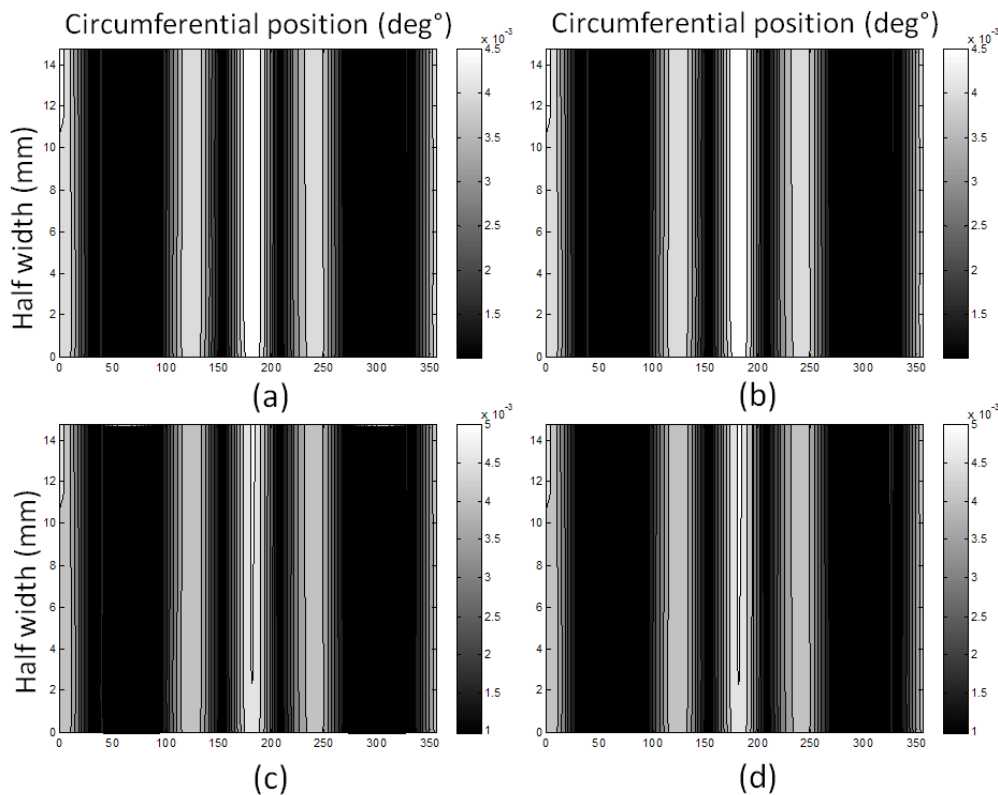


**Figure 110. Circumferential strain amplitude maps for elastic and no residual stress case (a), elastic and residual stress case (b), elasto-plastic and no residual stress case (c) and elasto-plastic and residual stress case (d).**

The damage maps based on circumferential strain and stress assuming elasto-plastic material models only consider the deformation amplitude of the stabilised cycle (third cycle). The damage map obtained from elasto-plastic analyses showed contrasting results regarding their sensitivity to F&F RS. Figure 110 shows that the generated maps based on strain amplitudes were not significantly affected by the considerations of residual stresses. In contrast, Figure 111 shows that the damage maps based on circumferential stress amplitudes were affected by the consideration of residual stresses.

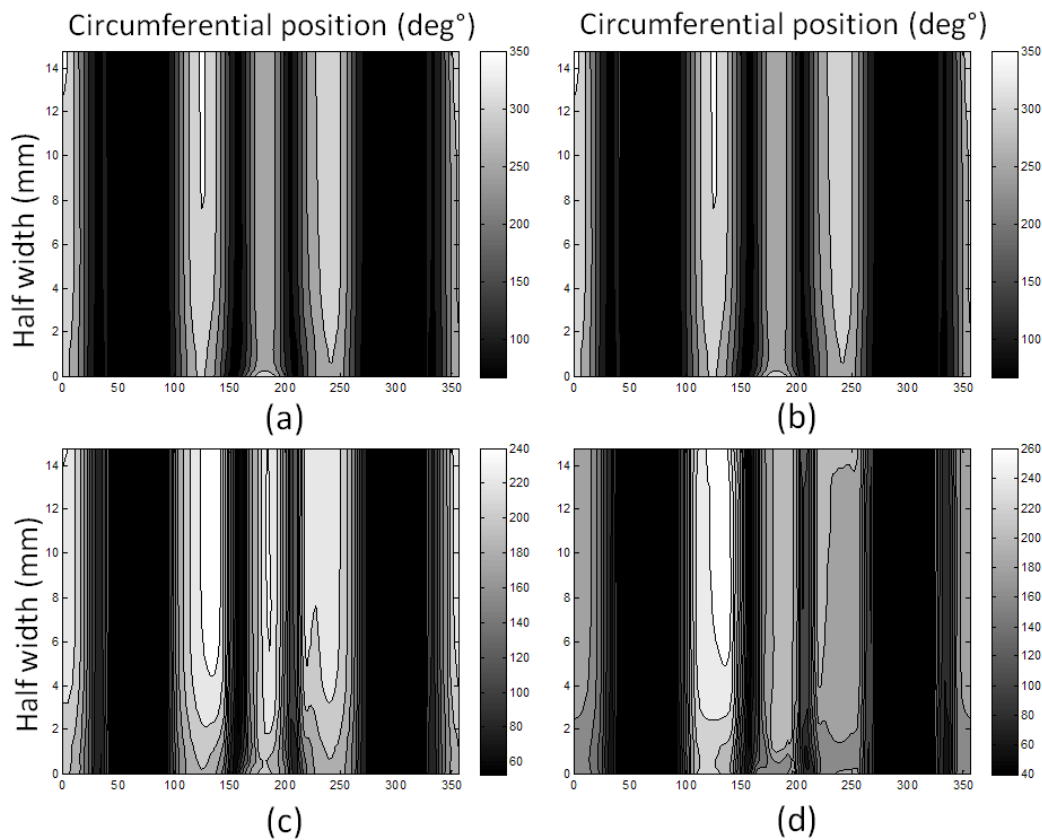


**Figure 111. Circumferential stress amplitude maps for elastic and no residual stress case (a), elastic and residual stress case (b), elasto-plastic and no residual stress case (c) and elasto-plastic and residual stress case (d).**

The difference between stress and strain based damage maps can be attributed to the extensive plastic deformation undergoing in the loading process and the casing deformation. The bearing deformation process, or strain estimation, is governed by the casing deformation obtained from

SABRE-EHL. Lining deformation was observed to be mainly dependent on the associated casing deformation irrespective of the initial state of stress. In contrast, the stress computation to achieve force equilibrium according to the applied deformations depends on the initial point on the strain-stress curve, which is defined by initial residual stresses.

### 7.4.2. Real engine conditions

The methodology of the previous section was also applied to a bearing designated “Real A” subjected to real engine service conditions arising from an engine speed equal to 1800 RPM and a specific load described in Figure 112. These details as well as SABRE-EHL output were also provided by MAHLE. As shown in Figure 113, the computed EHL pressures at various circumferential locations around the bottom shell, which is subjected to the piston force, also varied with the position of the crankshaft. It is evident from Figure 112 that the top shell is subjected to higher loads and prone to damage, as previous experiments have shown. The bi-layer architecture analysed consisted of an aluminium alloy MAS-15 with a thickness  $t_{L2}$  equal to 0.49 mm and yield strength of 60 MPa. The backing layer had a thickness of 1.49 mm and yield strength of 552 MPa. The bearing geometry for this scenario was set at a diameter ( $D_b$ ) of 56.43 mm and a width ( $W_b$ ) of 22.2 mm. The analysis developed for this bearing assumed elastic properties and did not include the effect of F&F RS.

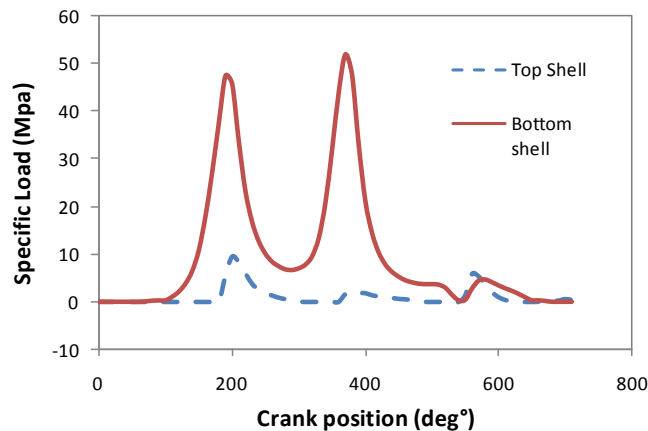


Figure 112. Specific load variation with crankshaft position.

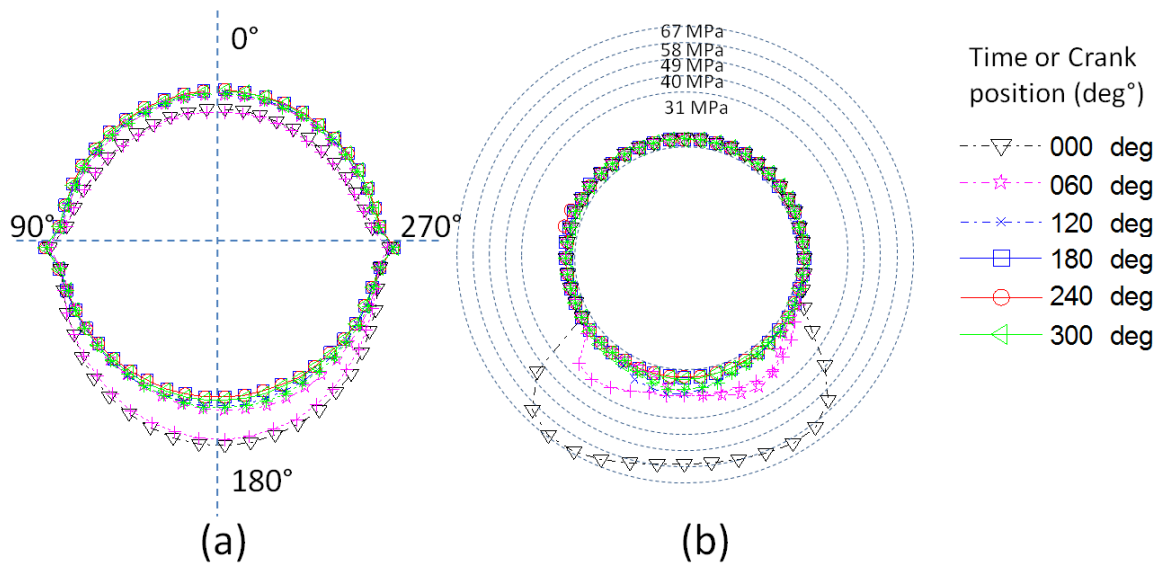


Figure 113. Bearing deformed shape (a) and EHL pressure (b) evolution along engine cycle for real case scenario (not to scale).

#### 7.4.2.1. Stress and strain analysis

An elastic stress analysis was carried out here consisting of 36 load steps equally spaced along the 720° of crankshaft rotation. Preliminary examination of EHL pressure and clearance data files showed that the highest pressure was applied close to a distance of 21 mm from the edge (1.2 mm away from the other edge). Therefore, stress results at this  $z$  coordinate were obtained and plotted in Figure 114a and Figure 115a focusing on the circumferential strain. These results showed that most of the top bearing shell was subjected to positive circumferential strains which could accelerate the fatigue initiation process. The maximum circumferential strains were observed at a time or crankshaft angular position near 400° and a bearing angular position near 180°. Significant circumferential strains are also observed as we draw farther from the bearing centre (at 180°) where greater shear stresses in the  $z\theta$  plane were observed (circumferential-axial direction) as shown in Figure 114b and Figure 115b.

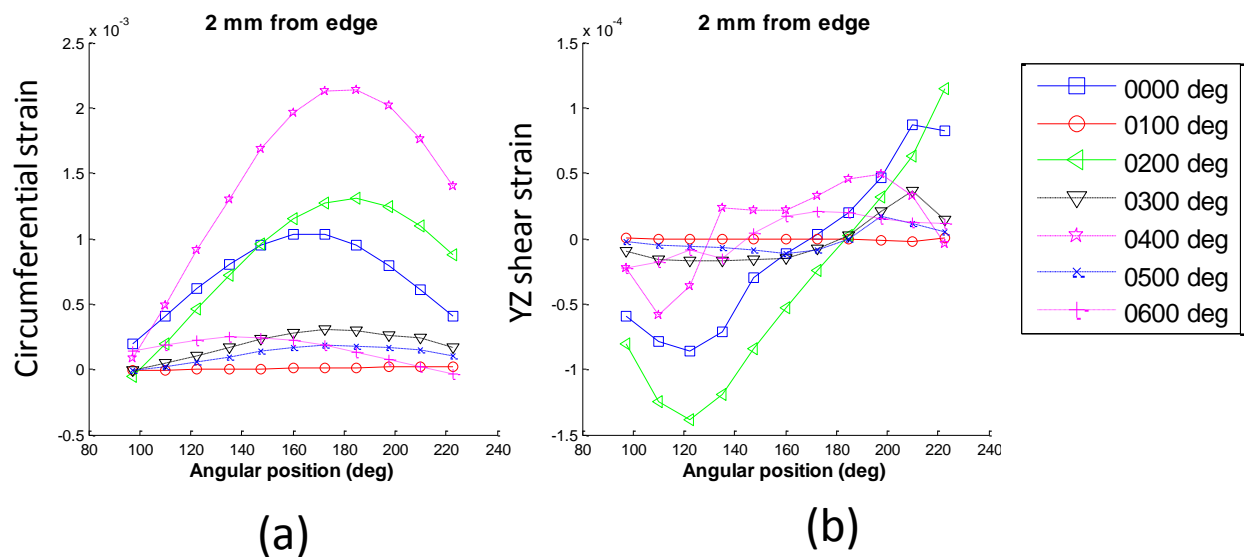


Figure 114. Circumferential or tangential (a) and YZ shear strain (b) vs. bearing angular position in “Real A”.

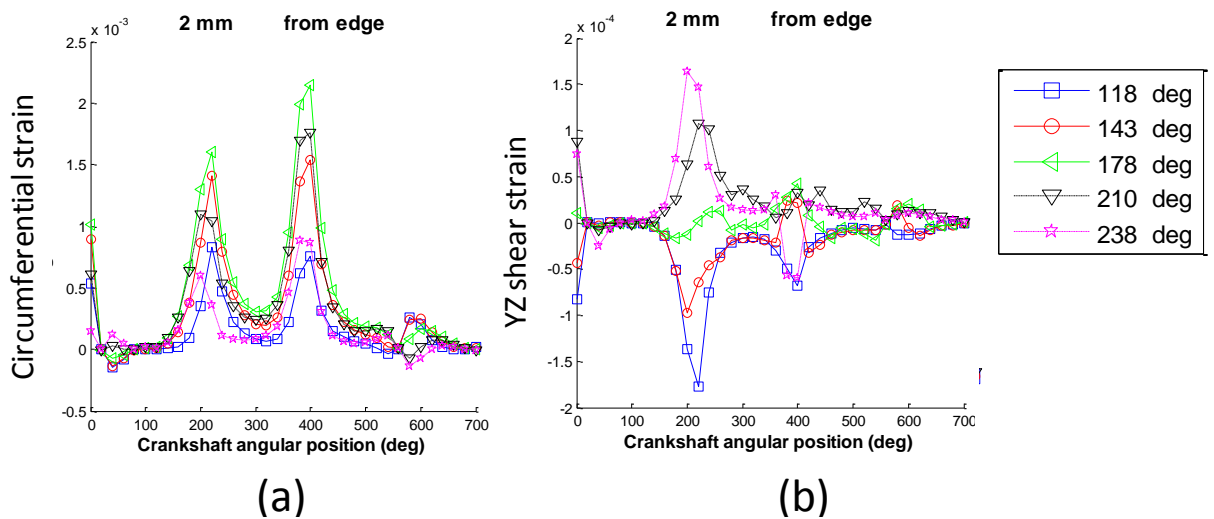


Figure 115. Circumferential or tangential (a) and YZ shear strain (b) vs. crankshaft angular position in “Real A”.

#### 7.4.2.2. Damage maps

The position of maximum pressure and gradient has a good correlation with damage observations, made by MAHLE Engine Systems, as shown in Figure 116b and c in this bearing at a crank position of 372°. The located damage was also associated with low clearance values, as shown in Figure 116a, which may accelerate the fatigue damage process through cavitation mechanisms.

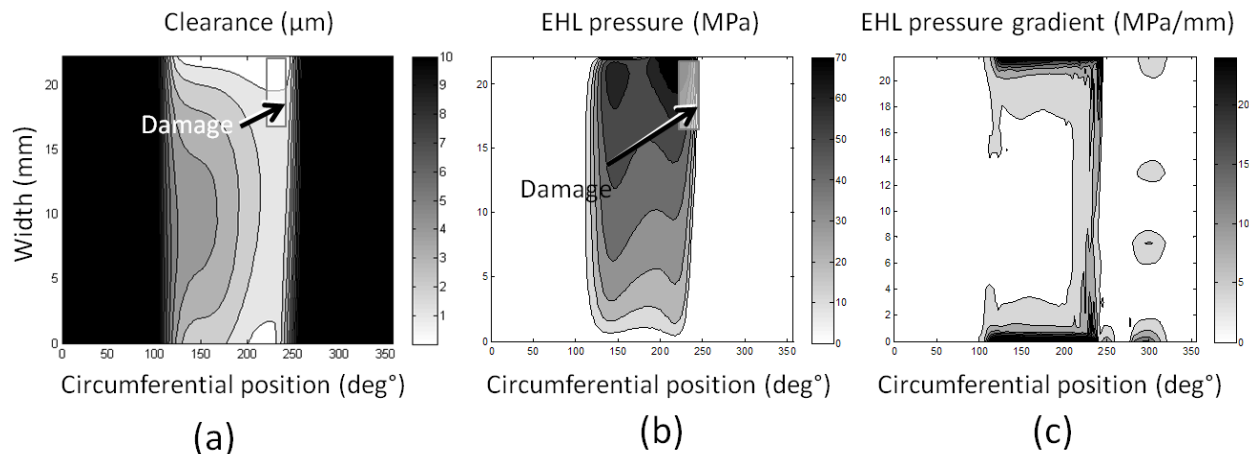


Figure 116. EHL pressure (a) and clearance at peak load in “Real A”.

The generation of damage maps based on the amplitude of any calculated parameter does not give an accurate representation of the local cycles found within the engine cycle of the real case. For the sake of comparison with the Sapphire rig, these maps were developed and the description of a more extensive methodology accounting for damage accumulation is given in Appendix A. A damage map based on the circumferential strain amplitude was generated in order to predict possible damage locations, shown in Figure 117a. The potential damage locations indicated by this map were not consistent with experimental observations. According to the stress analyses developed, higher amplitudes of circumferential strains can be found at the middle of the bearing around  $180^\circ$  or  $190^\circ$ . In contrast, a damage map based on  $r\theta$  (radial-circumferential direction) shear strain showed a better correlation, shown in Figure 117b. This agreement however may be accidental and needs to be investigated further since no significant correlation to experimental observations was found under the Sapphire rig conditions.

### 7.4.3. Discussion

The developed damage maps using elastic and elasto-plastic material models are capable of identifying the principal zones, shown in Figure 108, where crack initiation has been observed during the Sapphire rig testing of the MAS-20S architecture. Assuming elastic or elasto-plastic

material behaviour was found to favour one or another of the main zones of damage identified previously in the industrial environment. More complex damage contours were estimated when elasto-plastic material models and F&F RS were accounted for.

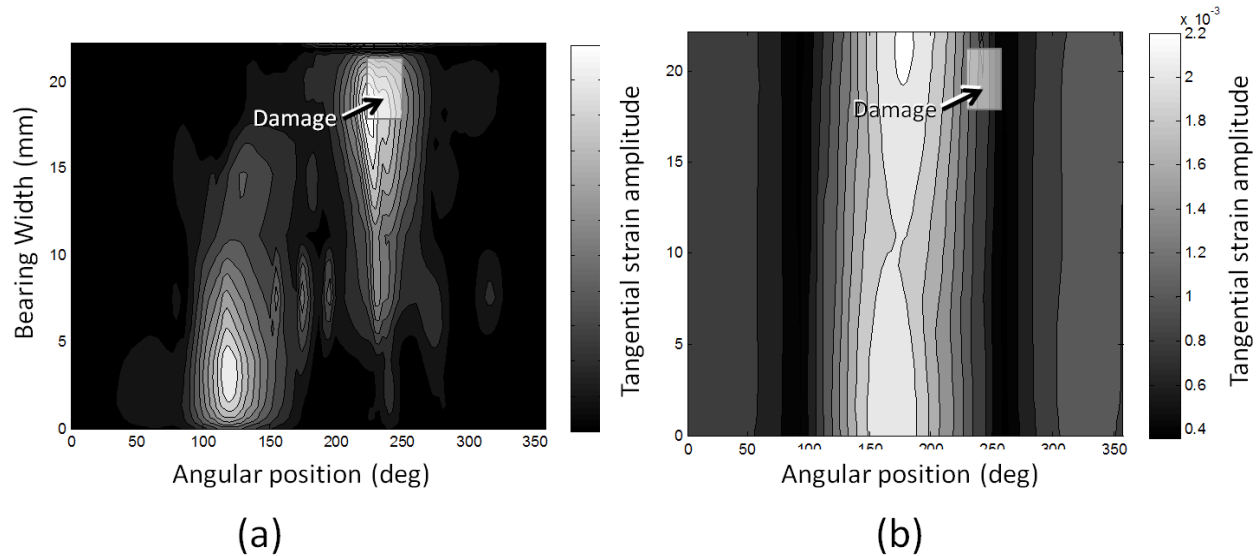


**Figure 117. Damage map based on circumferential or tangential (a) and XY shear (b) strain amplitude in “Real A”.**

The application of elasto-plastic material models appeared to be suitable for the assessment of crack growth under the scope of EPFM for future analyses. However, it is important to bear in mind that more demanding material characterisation is necessary to reproduce the conditions or characteristic behaviour observed in components’ service. At the same time, the computational cost for elasto-plastic analyses is higher especially in the development of damage tolerant analyses. The application of submodelling could be a valuable tool for the local evaluation of the deformation conditions, which seems to be suitable for the development of cheaper crack growth analyses. The exploration of this possibility was developed in Appendix B.

The characteristic behaviour of the material in service was simulated through a work hardening material model based on an isotropic hardening rule. Kinematic hardening models appeared however more suitable for the range of analysed deformations; nevertheless, the available material

models within ANSYS could only incorporate either large deformations or kinematic hardening. The simulation of large deformations through material models that accounted for kinematic hardening could not cope with the unloading process associated with EHL pressures, which were higher than the yield stress of the lining by a factor of three. Accounting for the elasto-plastic deformation may require additional assumptions regarding the  $\sigma$ - $\epsilon$  curves under cyclic loading and somewhat elevated temperature. At the same time, it can be argued that elasto-plastic analyses are inconsistent with the method used for the estimation of boundary conditions obtained by SABRE-EHL which is based on elastic compliance models due to the large plastic deformations experienced by the lining (around 0.1). The application of linear-elastic materials assumes that the applied deformation would not exceed the proportional limit of the material. The application of such models can be justified by the idea that cyclic deformation could lead the bearing material to a saturation point at the hysteresis loop where the deformation process, or most of it, is elastic.

Damage maps based on the tangential strain correlated well to the position of damage observed experimentally in accelerated fatigue tests. This correlation did not appear in the analysis of the case study "Real A". The two cases showed distinctive deformation patterns; the latter promoting greater radial displacements (by around 60%) at equal specific load levels. Another source of discrepancy can be attributed to the estimation of casing deformation obtained from SABRE-EHL and its application as direct boundary conditions to the backing of the bearing. The deformations applied to FE models were of such magnitude that strain maxima were located at an angular position near 180°, where maximum radial displacement was found. It appears that the casing compliance matrix developed for the SABRE-EHL analysis predicts the maximum radial displacement at this position irrespective of the position and profile of the EHL pressure applied. This can be either attributed to the topology of the bearing casing or the computation of the stiffness matrix by ABAQUS (in MAHLE Engine Systems) which only takes into account the radial deformation.

It is believed that the existence of multiple specific load peaks within the engine cycle did not affect the estimation of the most probable damage position according to the experienced cyclic deformation. The application of damage accumulation methodologies would also designate the circumferential position close to  $180^\circ$  as the most prone to damage, according to the tangential strain maps. The material located at circumferential position close to  $180^\circ$  showed higher strain estimates in comparison to those at any point on the lining surface during the simulation, as shown in Figure 115a. Experimental observations showed damage around  $240^\circ$ , as observed in Figure 116. It is evident that accounting for damage accumulation caused by both strain cycles during a single engine cycle would be a better representation of the evolution of cyclic damage, but it would require experimental data to observe the influence of cyclic loading factors such as amplitude, mean and frequency (RPMs)

Design methodologies based on linear elastic or elasto-plastic models for the study of bearing fatigue showed the complexity of the analysed problem. The applied analyses showed that additional investigation and the inclusion of other relevant conditions related to the service conditions may be necessary to predict the service life for these components. For such a task, it is believed that a simpler approach based on elastic models would initially promote further development of other issues related to the bearing damage. The damage generation process in bearings depends on various interacting mechanisms such as corrosion, cavitation erosion, foreign particles and wear. A case in point of this requirement is made by the analysis of a real case scenario, shown in Section 7.4.2, which showed that the estimation of stress and strain cycles based on elastic material cannot fully explain the position of crack initiation on the lining surface. The primary damage location predicted by the present analyses was not consistent with experimental observations. The location of damage observed experimentally corresponded to a secondary area of high cyclic deformation reinforcing the idea of the important role of cyclic deformation on damage.

It is also believed that the application of damage tolerance methodologies as presented in previous chapters of this work would not suit the industrial needs of bearing design. The greatest strength of the current crack growth analysis methodology is the extensive analysis of the material cyclic deformation experienced by the bearing. Its greatest weakness is not to account for other important damage mechanisms developing over the bearing life which modified the mechanical properties of the material or were previously ignored on the computation of the EHL pressure, i.e. cavitation erosion and bubble collapse.

### **7.5. Summary**

Bearing design involves the study of multi-layer architectures that cannot be analysed through exact solutions of standard specimens, especially when the elasto-hydrodynamic layer (EHL) pressure is involved. Fatigue studies in the literature of such components have established that the position of the maximum circumferential stress matches the location of crack initiation and growth occurs in the axial and radial direction.

MAHLE Engine Systems is dedicated to the design and manufacture of automotive bearings. Its design process involves the analysis of assembly and service conditions. Such service conditions are estimated through the finite difference software SABRE-EHL that considers the journal and bearing profile, clearances, heat transfer, contact and stiffness of the involved components. Using the estimations of deformation caused by the EHL pressure it is possible to assess the fatigue performance of bearing architectures including the elasto-plastic behaviour of the materials used within the different layers.

The analysis of a plain bearing subjected to accelerated fatigue tests showed an interesting deformation cycle that may contribute to the generation of fatigue damage. Accounting for forming and fitting residual stresses showed a significant impact on the analysis of stress. Strains were affected to a lesser extent. The plastic deformations observed in these numerical analyses did not

correspond to high cycle fatigue lives which led to the consideration that temperature and elastic shake down could justify the use of simpler elastic analyses.

The use of damage maps based on strain and stress amplitude was consistent with experimental observations in the case of the Sapphire rig. Such consistency did not hold when a real scenario was tested leading to the idea that simpler structural analyses incorporating other related damage mechanisms observed in bearings could be more efficient tools for the prediction of damage location and fatigue life.

## 8. Chapter Eight: Conclusions, contributions and future work

### 8.1. *Conclusions*

The crack propagation studies developed in this thesis incorporated relevant features in the context of fatigue and fracture in order to assess the impact on crack growth of a multi-layered architecture and its associated mechanical properties mismatch. The analysed problem involved large scale yielding along with shielding, anti-shielding and coalescence effects on the crack front evolution in two and three dimensions. Other features such as crack deflection, bifurcation and interaction between cracks were investigated only in 2D. The main conclusions drawn from this work are described next:

- It was confirmed that FE packages, such as ANSYS, are powerful tools for the study of crack propagation [46]. The use of scripting procedures, known as Ansys Parametric Design Language, allows the development of automated routines that simulate crack propagation effectively through remeshing schemes. The propagation path and crack front evolution can be estimated during this extension process leading to realistic estimates of crack driving force, stresses and strains, which are stored for further analysis and post-processing.
- The prediction of significant crack driving force accelerations and decelerations in straight paths as the crack tip approached more compliant or stiffer layers confirmed trends observed in previous work [7]. Crack deflection in width-through cracks was predicted under shielding conditions as the crack approached the stiff backing following a straight path and being subjected to pure opening-mode loading. The estimation of the crack path, according to the maximum tangential strain criterion, showed that the crack would extend

in the direction which offers the least resistance. In this case, that path was parallel to the layers orientation through the interlayer which maximised the crack driving force value or CTOD per crack extension length, in comparison to straight cracks. Anti-shielding phenomena showed an opposite effect by attracting the crack tip to a more compliant layer in a straight path.

- The strength of shielding in width-through cracks has been previously related to the yield strength or Young's modulus mismatch between the layers. The evaluation of this effect in relation to these two material constants does not always provide a complete problem description given that the actual stiffness mismatch also depends on the extent of plasticity developed and the degree of strain hardening. The local stiffness of the material located between the crack tip and the layer to be approached varies according to the post-yield properties of the materials involved, applied loading and the crack position and orientation. The introduction of true stress-strain curves into the numerical model simulates a more realistic behaviour but increases substantially the computational cost of the analyses.
- Crack path evaluations in width-through cracks analyses can be translated into bearing design where lining detachment is an issue of interest. CTOD and tangential strain estimations in bi-layer architectures confirmed previous findings related to deflected paths in the lining [7] which may promote early fragment detachment in bearings. This is in contrast to tri-layer designs where lining detachment usually occurs after the crack penetrates the interlayer and propagates in a plane parallel to the layers orientation. The existence of the compliant interlayer was predicted to reduce substantially the variability of the path to be followed by the crack within the lining where early detachment could occur in bi-layer architectures. The attraction effect caused by the interlayer's lower compliance appears to delay lining detachment despite promoting faster crack growth just before the crack reaches the interlayer.

- The interaction between thickness-through cracks in a simplified representation of the top surface of the lining as a plate under tension showed the effects of parallel, co-linear and oblique crack arrangements. The crack driving force estimations for co-linear cracks confirmed significant increments during coalesce processes [118], these estimations grew asymptotically as both tips approach. Parallel crack arrangements showed that shielding phenomena may result in arrest as a dominant crack extends and blocks smaller cracks, confirming trends obtained in previous work [118]. Oblique arrangements analyses forecasted that cracks located within an area of influence around the crack tips (approximately 4 times the initial crack length) were likely to result in coalescence and may enhance lining detachment processes. Deflections that promote coalescence in the oblique overlapped cracks became more pronounced as the applied load increased. Shielding and anti-shielding phenomena in different crack configurations are dependent on the extent of plasticity and separation between cracks, the latter being more influential in determining whether coalescence would occur between oblique cracks.
- An effective methodology for the study of crack propagation in multi-layered architectures was developed here based on the concepts described in previous work [46, 47, 50, 143]. This methodology allowed the study of the effects of a multi-layered architecture on the crack path and crack front evolution in 3D. The successful implementation of this methodology faced three major challenges: the generation of automated meshing processes for the crack front elements (node by node generation), a subsequent meshing procedure focused on the element size transition from the crack front to volumes with low stress gradients and the estimation of crack driving force along the crack front for the prediction of a subsequent crack front shape. The challenges described above allowed the study of the crack front evolution and the simulation of irregular front shapes, as shown in coalescence, and were faced by coupling powerful tools like ANSYS and MATLAB.

- In contrast, the major drawback of the developed methodology is their computational cost. Automatisation processes developed here have liberated the designer from time consuming tasks during the crack growth analyses. However, it is still believed that the required times were excessive. To some extent, the computational cost can be attributed to the non-linearity exhibited in the analysed problem and the need of refined meshes to evaluate shielding and anti-shielding close to the layers' interface. Other drawbacks of this methodology can be found in the step by step crack growth simulation, which accounted for neither residual stresses nor out-of plane growth as cracks extended due to cyclic loading.
- The effects of shielding and anti-shielding on 3D half penny cracks growing in multi-layer architectures were not as strong as those predicted in 2D width-through cracks. The crack front shape appeared to be constrained by the growth of the crack as a whole; this growth was governed by global and local mechanisms. The effects of layered architectures on small segments of the crack front proximate to the layers' interface seemed to be averaged or diluted along the whole crack front leading to barely noticeable changes on the front shape and crack driving force when contrasting shielding and anti-shielding behaviours were analysed through the crack growth in tri-layer and bi-layer architectures, respectively.
- Life estimations of bi-layer and tri-layer (MAS-20S) systems did not show a significant difference (considering only the number of cycles that a straight crack would take to reach the position of the interlayer). The estimated crack driving force difference between width-through cracks growing in tri-layer and bilayer architectures was not observed in quasi semi-elliptical cracks. This reinforces the idea that the addition of the compliant interlayer would be beneficial for the architecture since it was predicted to avoid the development of early deflection within the lining and keep fairly constant the number of cycles required for a crack to reach the interlayer interface.

- For the particular load level analysed, it was found that the number of cycles for a crack to reach the interlayer, including the initiation process, corresponded to a 32% (Chan and Lankford) and 40% (Tanaka) of the total life in three-point bending test with a failure criterion set to an additional maximum absolute displacement of 0.5 mm. The life estimations developed here confirmed trends obtained in previous work [144, 147] related to the possibility of higher life estimations when a Paris law type, such as the one proposed for Tanaka, is used. The Chan and Lankford relation, accounting for microstructural barriers, showed a more conservative prediction in the analysis of short fatigue crack growth behaviour.
- Since the predicted life for crack initiation and propagation within the lining only corresponded to a small proportion of the total number of cycles to failure, it was suggested that the three-point fatigue tests with the specified failure criterion could not be used as an indication of the likelihood of a lining fragment to detach. However, further analysis taking into account additional important factors, such as the level of loading, are necessary to confirm this hypothesis.
- FE simulations studying crack coalescence predicted an overall moderate effect on the crack growth in the depth direction. The only acceleration predicted was caused by the crack reshaping process just after coalescence towards a quasi semi-elliptical shape. Comparisons with single independently growing cracks estimated that at particular stages of crack growth accelerations of up to a 22 % were achieved.
- The stress and strain analysis of shell bearings operating in engine environments showed the estimated effects of the EHL pressure and concomitant casing deformation on the lining. Potential damage maps based on the cycle amplitude of circumferential stresses or strains were not always consistent with experimental observations, especially when realistic engine conditions were tested. The location of damage observed experimentally was

assessed as secondary potential area on the bearing; this correlation shows that cyclic loading plays an important role in the damage process but cannot characterise by itself such damage. Further analysis in this area is needed to account for other factors involved and to investigate sources of discrepancy with experimental information.

## **8.2. Contributions**

It is believed that the work carried out in this research project has contributed, in particular, to the existing knowledge on FE modelling fatigue behaviour in multi-layered systems and bearings.

These contributions are listed here:

- The use of the CTOD as a CDF parameter to assess shielding and anti-shielding effects in multi-layered specimens under three point-bending. Similar trends are observed in previous work [7] that used the  $J$  integral. At the same time, the generated models allowed the study of the impact of large extents of plasticity and the analysis of crack growth with crack tips closer to the layers interface in comparison with previous work in the literature.
- The use of a blunted tip that simulates the observed crack tip profiles in ductile materials allowed the investigation of the near-tip material conditions while shielding or anti-shielding phenomena occur. The blunted tip also allows the unambiguous and direct estimation of tangential strains on the blunted crack tip surface. The study of these strains, during the shielding phenomena, shows that the preferential propagation direction shifts to greater deflections as the crack tip approaches a stiffer interface. This shift occurs in a symmetrical manner, which is consistent with experimental observations of crack bifurcation.
- The study of shielding effects showed that despite the absence of far field mixed mode loading or any micro-structural feature, it is possible to obtain deflected paths according to the estimations based on the maximum tangential strain criterion. Furthermore, these

deflected paths in multi-layered architectures showed greater crack driving force estimates, when compared to straight cracks, maximising the CDF and satisfying the maximum crack driving force principle.

- Accounting for the proportional crack growth involving the analysed crack tips, assuming that crack growth rate varies linearly with the CTOD [126], showed a more realistic view of interacting cracks. Previous work in the literature [120] only analysed a single initial state at particular orientations and crack sizes. Tracking this crack growth provided a more appropriate assessment of coalescence or arrest, especially when deflected paths arise due to this interaction.
- The study of shielding and anti-shielding effects had been mainly studied in through-thickness cracks observing significant crack growth and driving force increments. Its study on quasi semi-elliptical cracks did not predict such a significant acceleration in crack driving force estimates since the affected region was small and only occurred close to the interface. At the same time, the evolution of the crack front shape developed as whole and the localised effects of shielding or anti-shielding did not affect significantly the overall evolution of the crack front. Therefore, the shape of the crack did not suffer a significant transformation.
- A procedure for the assessment of a damage tolerance approach to estimate the fatigue life of a multi-layered component was developed. This assessment was compared to previous experimental work in the University of Southampton and showed the relative importance on the total life of propagation processes within different layers [63].
- A detailed evaluation of cyclic stresses and strains arising from bearing service conditions and including previous stress history related to manufacturing was developed here. Forming, coining and fitting operations were modelled to estimate the possible initial state of the material. Elasto-hydrodynamic film pressure and concomitant deformation were

applied cyclically on elastic and elasto-plastic material models leading to the conclusion that the occurrence of damage could not be only characterised through the analysis of cyclic structural conditions only.

### **8.3. Future work**

The work carried out for this thesis helped in the identification of possible areas of research where similar approaches and studies could be developed to contribute to the understanding of crack propagation processes and heterogeneous materials. The most evident and logical area of opportunity of this work is the optimisation of the numerical analyses in order to reduce the computational costs during the crack propagation analysis, especially in 3D.

In the context of crack propagation, a deeper analysis of bifurcated cracks in multi-layered systems is another area of opportunity. Bifurcated kinks in monolithic specimens have been shown to propagate for a limited distance after which arrest occurs at one kink. The growth of bifurcated cracks in layered architectures has shown a different behaviour where both kinks keep propagating. The comparison between layered and monolithic materials may clarify the factors that cause this difference.

Two-dimensional assessments of such path instabilities have been carried out in through-thickness specimens; however, work on the evolution of these cracks in 3D from elliptical or quasi semi-elliptical cracks has not been detected in the literature. The study of crack driving force along the complex crack front would provide a deeper understanding of deflected crack growth.

The extension of the developed methodology to account for out of plane crack growth is another logical step according to the developed research. Previous 2D analyses validated and implemented a deflection criterion based on blunted crack tips. The current 3D methodology also considers blunted tips; however, its refinement is not considered to be sufficient to obtain accurate strain

estimations around the tip. The implementation and validation of a different deflection criterion and the numerical implementation for automated model regeneration are challenging tasks that would allow specialised elasto-plastic analyses.

On the other hand, a simplified and more economical methodology based on linear elastic fracture mechanics concepts would improve its applicability to industrial design processes. Damage tolerance approaches, such as the one implemented here, are currently too time consuming to be occupied on a daily bases. Computational power development and appropriate changes to the methodology would provide a robust tool for the design process of layered architectures.

In the context of bearing design, the application of this methodology leads to the consideration of other important factors in the analysis of growing cracks. The crack front extension under disproportional loading is a case in point. Complex loading patterns show maximum and minimum CDF estimates within every cycle and the adoption of an appropriate method for the selection of the effective magnitude is another area of opportunity. This is especially important when out of plane growth is accounted for since deflection estimations will vary along the cycle and step by step extension requires a single direction of propagation.

It is understood that most of the methodologies and techniques used here cannot be used directly in industrial environments. However, it is believed that translating the academic knowledge gained in this thesis into industrial design processes could contribute to the development of better products. The development of empirical rules or formulae to be used in a daily basis has been done in previous research and appears as a sound option to assist the industrial sector.

## Appendix A

### *Proposed methodology for fatigue damage assessment*

The analysis of a real bearing in a given engine design presents more difficulties than the Sapphire rig. These difficulties consist in the greater compliance displayed by the casing and the existence of multiple specific load peaks with significant amplitudes. Greater compliance reduces significantly the bearing life, in comparison to stiffer casings at the same specific load level. The existence of multiple peaks also accelerates the occurrence of damage. The product development also complicates from the designer point of view since the accumulation of damage has to be assessed.

The proposed design methodology, shown in Figure 118, for real cases must feed numerical models with experimental data regarding the fatigue life of the bearing. Such tests are typical in industry; the Sapphire rig being a case in point (marked 01 in Figure 118). This rig is used at various specific loads to determine the carrying capacity of the bearing and allow the comparison with other bearing architectures. However, these tests evaluate the bearing under favourable conditions of casing rigidity, loading alignment and cyclic loading configuration. The numerical replication of these tests provides the resulting stresses and strains that cause the damage evolution (02).

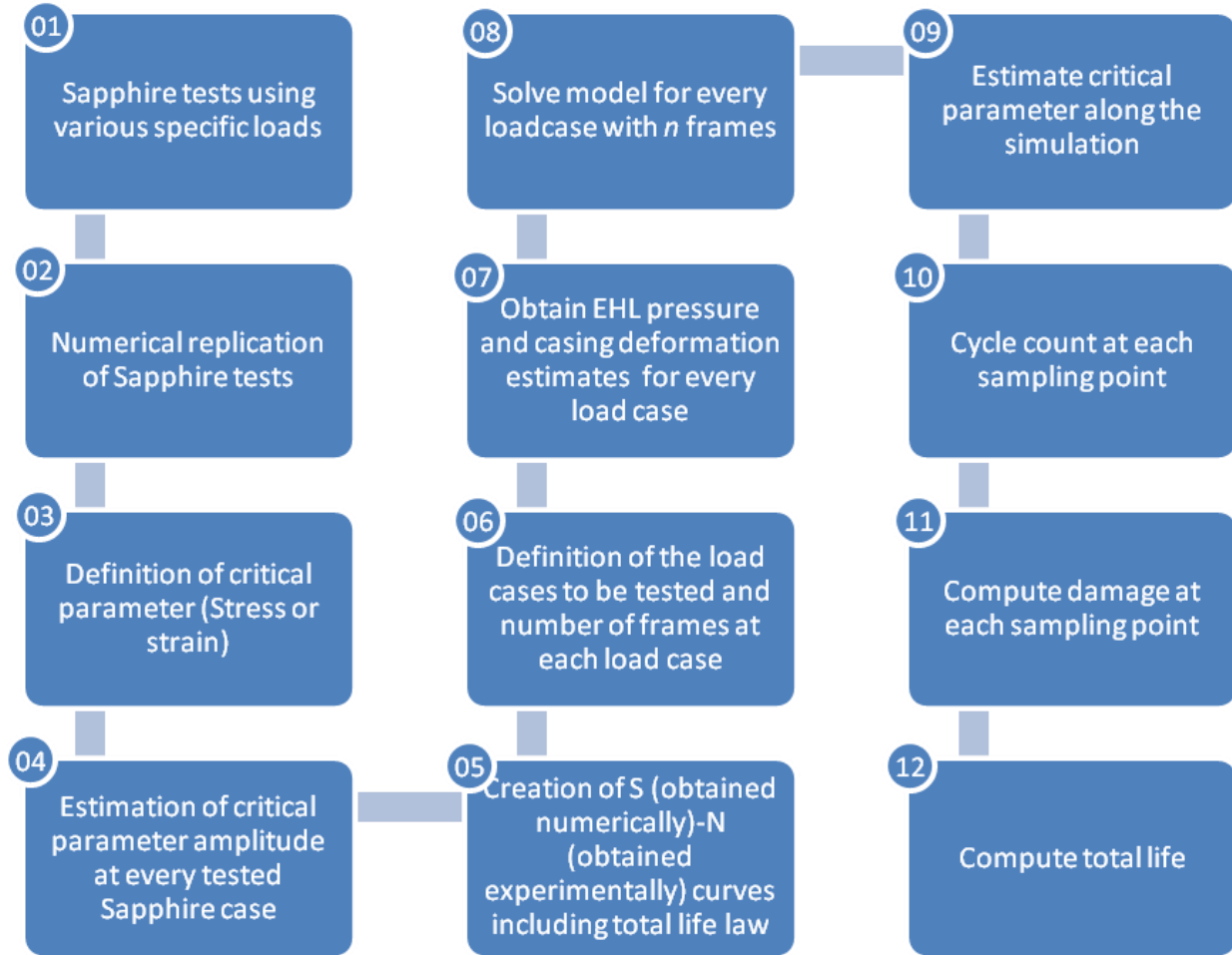


**Figure 118. Proposed methodology for bearing design**

Stress and strain estimates indicate the loading effects on the material. Failure criteria such as Von Mises or Tresca have been widely used, but for this particular case the circumferential stress and strain have been correlated to crack initiation (03). The use of the EHL pressure as a critical parameter is also a sound option, which would not require any FE analyses but only the replication of experimental conditions in SABRE-EHL. The loading applied in Sapphire tests only consists of a single peak cycle, in contrast to real case scenarios. The application of a single peak loading histogram usually produces a simple peak of the critical parameter to evaluate simplifying the estimation of the critical parameter cycle amplitude (04). The creation of S-N curve (05) plots the numerically obtained amplitudes  $\sigma_a$  against the experimentally obtained life  $N_f$  and the Basquin

relationship, shown in equation ( 27 ), is obtained for a particular bearing architecture with material constants  $q$  and  $r$ .

$$N_f = q(\sigma_a)^r \quad ( 27 )$$

The number of loadcases to be tested is defined according to the bearing service conditions and engine requirements, in contrast to the available product development time (06). The computation of EHL pressure and casing deformation according to the specific load and engine speed (07) are essential for the development of realistic models (08). The estimation of the critical parameter through the numerical model (09) generates a significant amount of data to be post processed. A matrix of a size  $a \times b \times c$  is generated with  $a$  representing the number of sampling points on the bearing surface,  $b$  the number of loadcases to be investigated and  $c$  the number of frames or snapshots taken at each loadcase. Cycle counting techniques are carried out along the  $c$  dimension obtaining cycle amplitude, mean and relative frequency in a single engine cycle (10). The damage per peak cycle is calculated using equation ( 27 ) and the equivalent damage per engine cycle is obtained through the Palmgren-Miner relationship of linear accumulation of damage, shown in equation ( 28 ).

$$\sum_1^i \frac{n_i}{N_{fi}} \leq 1 \quad ( 28 )$$

This relationship specifies that the component will remain in service while the equivalent damage is smaller than 1. The equivalent damage per engine cycle is formed by the sum of  $I$  loadcases which have an individual total life  $N_{fi}$  and  $n_i$  cycles are applied per engine cycle. The inverse of the equivalent damage per engine cycle represents total number of engine cycles to be sustained.

## Appendix B

### *Sub-modelling stress analysis*

The full model presented before appears to be a suitable tool for determining the lining surface stress analysis. However, a more complete understanding of the effect of stress and strain state on crack growth within this layer would be also desirable since the crack evolves accordingly. Sub-modelling appears to be a suitable tool for such a task, since the region of interest is limited to a particular area where damage is most likely. This initial work is aimed at contributing to a crack growth analysis under bearing service conditions on which future work may be carried out. The elastic analyses neglecting F&F RS are used for the development of these analyses.

#### **1. Methodology**

The development of a sub-modelling analysis consists of several steps involving a full and sectioned model. A brief summary of the required actions is given here. The first step is the development of a coarse model of the complete component assessing the areas of interest. After the region of interest has been selected and a sub-model mesh is built ensuring that the node numbering at the boundary, where connecting material is located in the full model, would remain fixed. Then, nodes placed at the border are selected and exported along with their coordinates. The node number and their coordinates are imported into the solution of the full analysis. Full and sub-model should share a common origin and coordinate system. Finally, it is necessary to check that the results at the boundary are consistent.

The sub-modelling technique is mainly based on elastic material models. Therefore, 36 steps obtained from the elastic analysis were exported into the sub-modelling version. For each time step, the displacement components at each of the sub-model nodes placed at the boundary were

calculated through interpolation routines based on the full analysis solution. The estimated displacements at the specified locations were exported to a file ready to be included as an input file in the sub-model. This file includes the node number, magnitude and direction of the boundary condition to be applied.

ANSYS sub-modelling tools facilitate extensively the estimation of the boundary conditions (displacements) over the interface between full and sub model. The application of EHL pressure was carried out by dividing the bearing surface into a grid through a MATLAB routine. Using ANSYS APDL tools, an average pressure value was applied to the nodes found within the grid section. This process, along with the application of the boundary conditions, was developed for every particular time step (crank angle) in a consecutive manner. Full and sub-modelling analyses are schematically represented in Figure 119. It is important to mention that estimations of stress and strain near the borders, where boundary conditions from the full model were applied, do not usually provide accurate values. The region of interest should be placed away from these sub modelled interfaces [55].

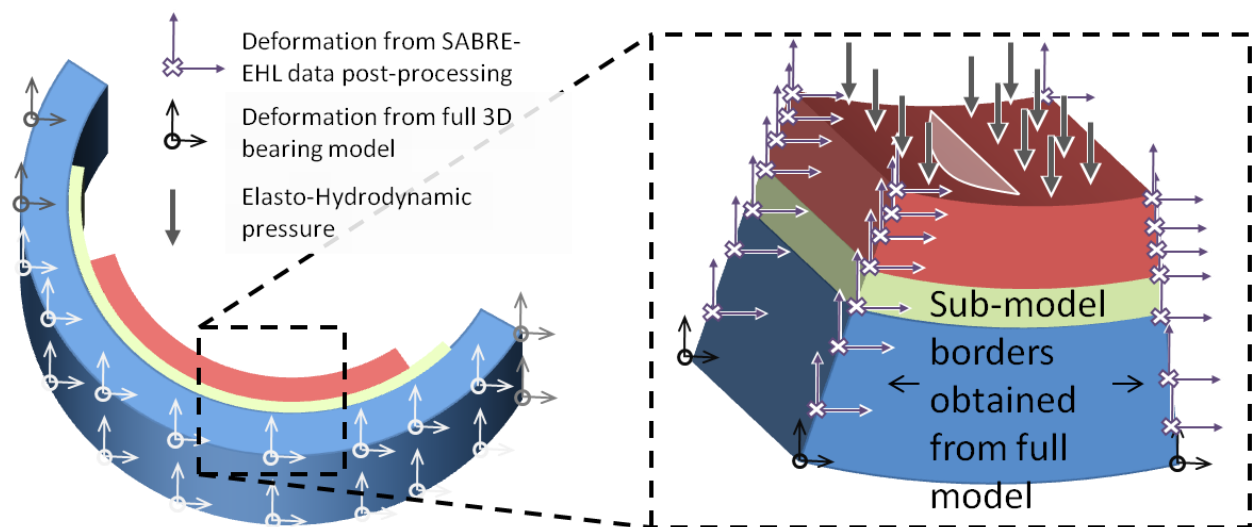


Figure 119. Sub-modelled analysis using EHL and deformations estimated from SABRE-EHL.

## 2. Results

The results obtained from the sub-modelling analyses were initially compared to the full model developed for simulating the Sapphire rig test stress fields in order to identify differences between them. The observed trends and magnitudes at the lining surface were very similar. The volume chosen to be sub modelled consisted of a width  $W_s$  equal to 7.6 mm, an arc length  $L_s$  equal to 19.5 mm and the whole thickness of the layered architecture. The value for  $W_s$  was chosen according to the damage observed in Figure 92 and previous research by Bahai and Xu [174] that found initiation damage between 5-7 mm away from the border in a different architecture but similar loading. The value of  $L_s$  was chosen due to its proximity to the specimen used for three-point bending tests.

Figure 120 shows the circumferential strains on the lining surface from the full and sub-modelled analyses obtained when the peak pressure is applied. Further comparisons are presented next in order to validate and assess the limitations of the submodelling technique in this particular application. Tangential strain comparison on the lining surface showed similar results along the whole engine cycle.

In contrast, strains estimated at the interface of the sub-model with the full model showed very different results, as shown in Figure 121. This difference can be related to the application of boundary conditions which caused significant local deformation to a mesh with different size and element type (full model mesh used only hexahedral elements while the submodel combines hexahedral and tetrahedral elements) and the possible change of node numbering of the mid nodes at the sub-model mesh. Uneven contours with particularly high values near the border were found here, especially in the radial direction along which large deformations were applied. The estimates of stress and strain become more similar as the point compared was further from the sub modelled interface.

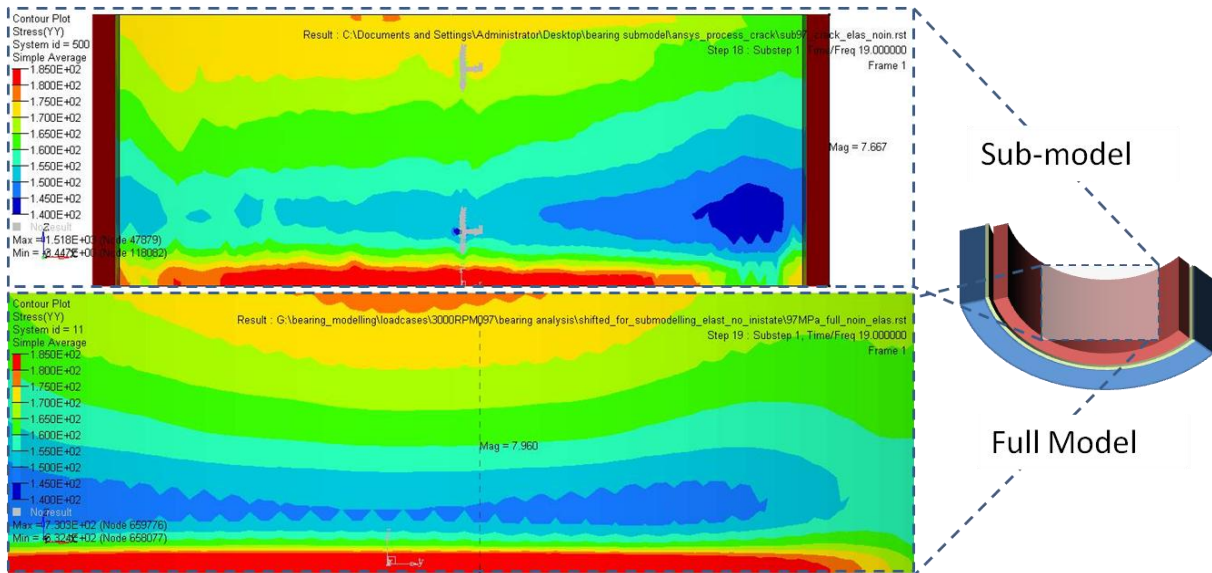


Figure 120. Circumferential strain comparison between full and sub-modelled analysis.

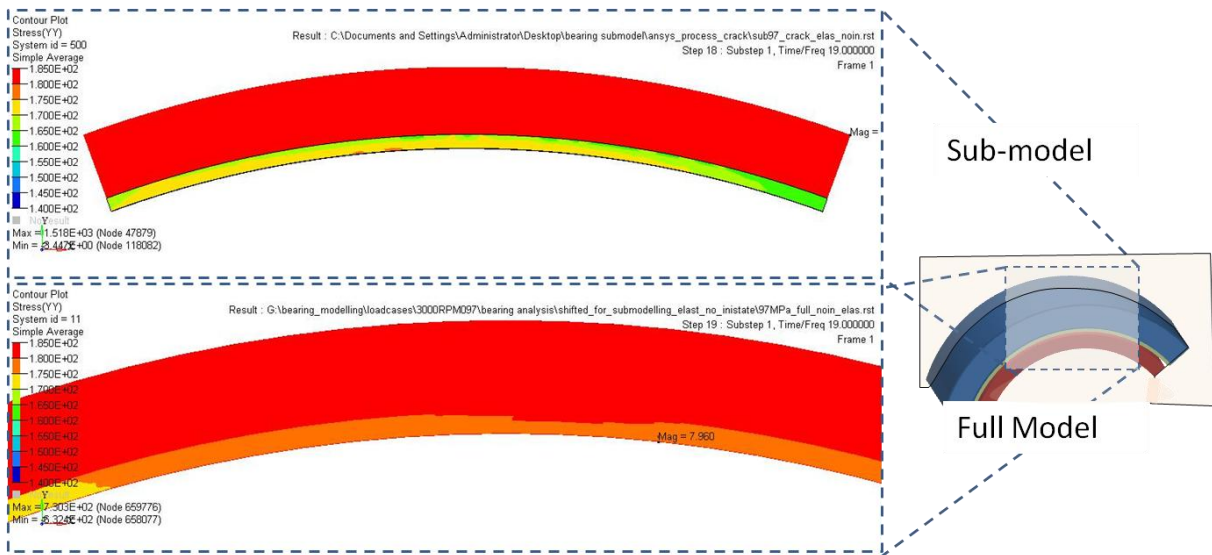


Figure 121. Circumferential strain comparison between sub-model and full analysis (using a cross section defined as the sub-model border for the latter one).

Strains in the circumferential direction from full and sub-model simulations showed very consistent outcomes, as shown in Figure 122. The highest strains were found near the edge of the bearing (Figure 122 Point C) corresponding to the position of the maximum EHL gradient. As we move towards the middle line of the bearing a strain drop could be observed (Figure 122 Point D) followed by a rise consistent with the gradual increase of EHL (Figure 122 Point E).

Strains in the width direction showed similar contours to those in the circumferential direction with lower values, however. The distribution of strains near the border and the greatest EHL pressure gradient could be observed as well. In contrast to strains in the circumferential direction, higher strains in the backing were observed below the low strain area in the lining, as shown in Figure 123 Point F. This particular behaviour was only captured by the more refined sub-model analysis.

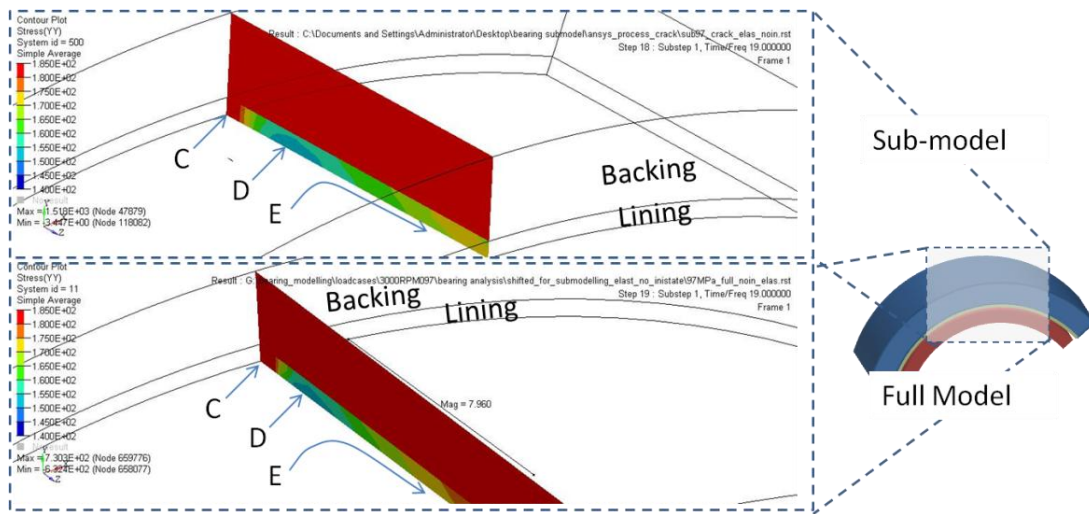


Figure 122. Circumferential strain comparison between sub-model and full analysis (using a cross section at 180°)

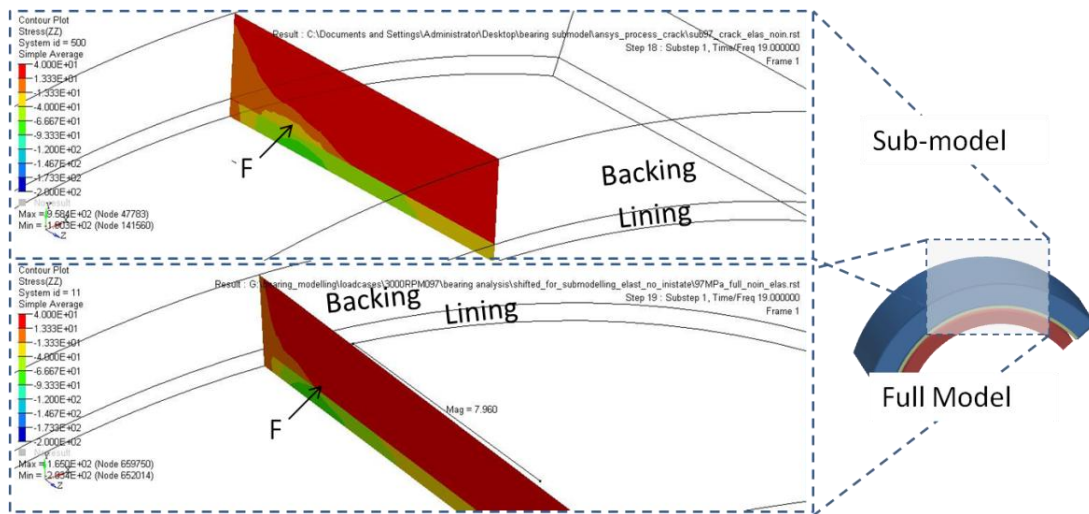
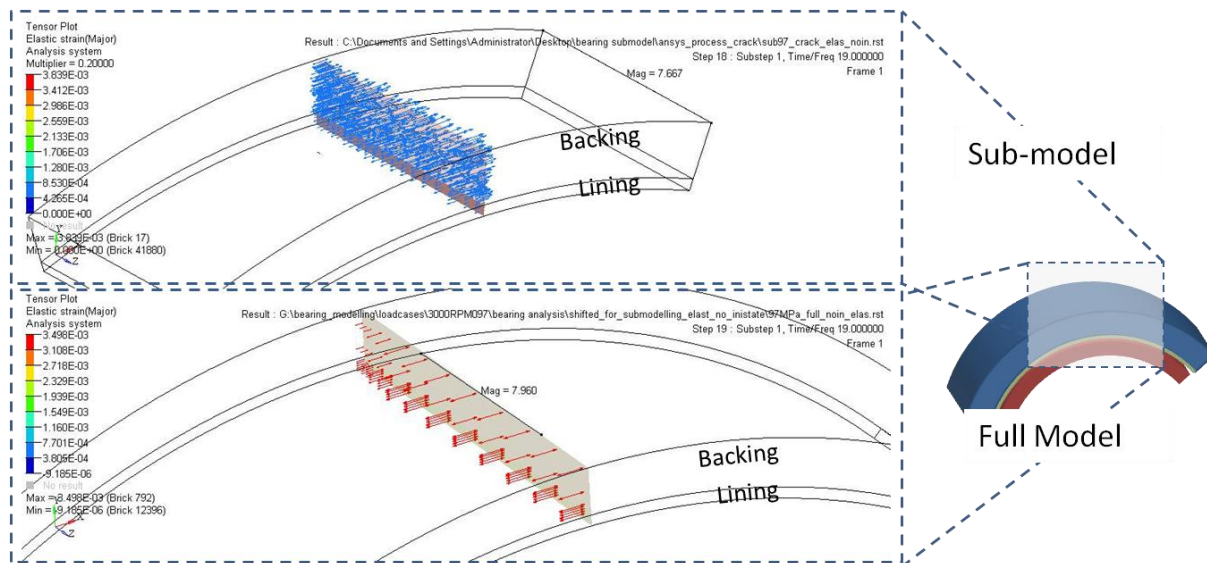


Figure 123. Strain ZZ (width direction) comparison between sub-model and full analysis (using a cross section at 180°)

Similar cross sections were considered to investigate the maximum principal strain direction. Both models showed very consistent outcomes showing that principal strains were almost aligned with the circumferential direction, as shown in Figure 124. The arrow density corresponds to the element density and the existing difference of element refinement was evident. The solution from the whole loading cycle was also inspected to ensure that these conditions existed during the whole simulation. Figure 125 shows the evolution of the principal strain along the loading cycle. This transition showed that before the peak pressure was applied, the principal strain was parallel to the bearing width direction. As the Sapphire rig peak pressure started to emerge, the principal strain aligned with the circumferential direction. This shows that crack growth that occurs during the damage process in the Sapphire rig occurs essentially under mode I loading conditions.



**Figure 124. Principal strain comparison between sub-model and full analysis (using a cross Section at 180°).**

### 3. Discussion

Previous damage tolerance analyses developed for flat strips under three-point bending showed how cracks would propagate according to that simple state of stress. Three-point bending tests mainly generate stresses in one direction in a perfect specimen. The stress magnitude in any other

direction was negligible. This is in contrast to the actual state of stress observed in bearings. It is evident that circumferential or longitudinal stresses are critical and cracks grow according to their magnitude and distribution. However, normal and shear stresses in any other direction were observed to be greater in comparison to those generated by three-point bending tests. The tri-axiality observed under both loading scenarios was observed to be quite different. This issue may reduce the applicability of the crack growth law developed from three-point bending results and analysis, in addition to other factors such as service temperature, penetration of oil into the crack, solid to solid contact to mention but a few.

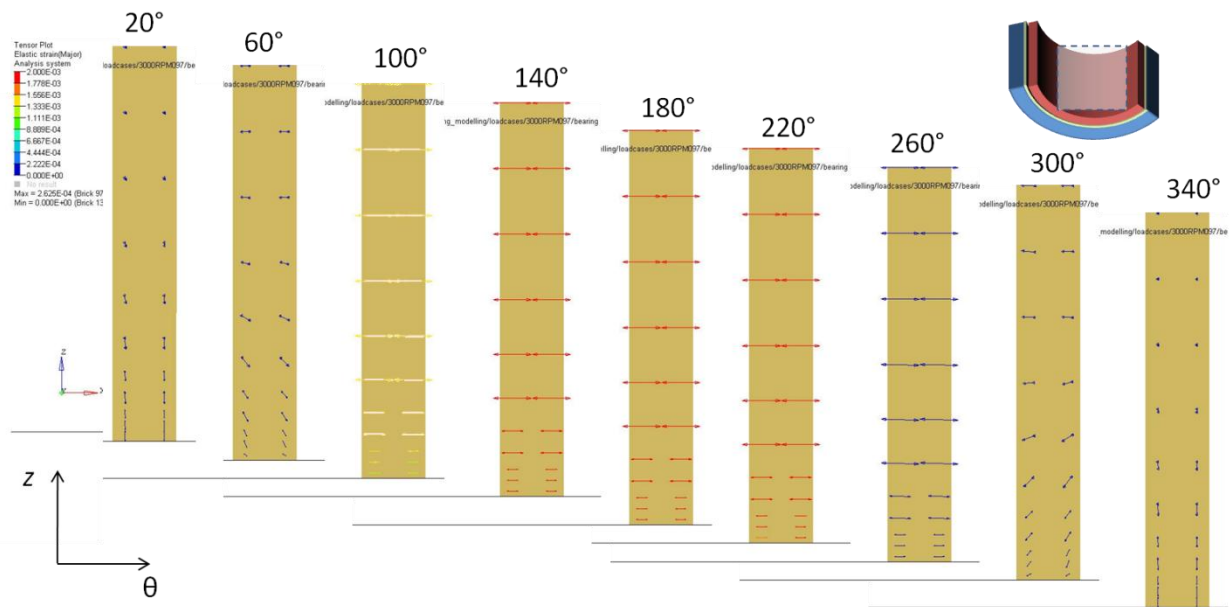


**Figure 125. Maximum strain reorientation as loading is applied (Full model used for clarity showing values at the lining surface).**

The use of the sub-modelling technique reproduced the behaviour of the full model through the transfer of deformation data to a partial volume. The development of numerical analyses for assessing fracture mechanics would be greatly enhanced by this technique in terms of computational cost as long as the introduction of a crack does not affect the behaviour of the component outside the sub-modelled region. This kind of analysis appears as the next logical step

in this research and could lead to a greater insight of the crack propagation process in bearing components.

However, it is believed that the application of damage tolerance methodologies as presented in this work would not suit the industrial needs of bearing design. The greatest strength of the current methodology is the extensive analysis of the material cyclic deformation experienced by the bearing. Its greatest weakness is not to account for other important damage mechanisms developing over the bearing life which modified the mechanical properties of the material or were previously ignored on the computation of the EHL pressure, i.e. cavitation erosion and bubble collapse.

## Appendix C

### ***1. Two dimensional flat strip with single tip crack model under three-point bending***

The code shown next is an input file to be used directly in ANSYS coded with APDL tools.

```
/batch

/CWD,'C:\Documents                    and                    Settings\burke.CEDGUSERS\My
Documents\PhD_project\current_analysis\ansys_working_folder'
*cfopen,crack_intensity.txt

!          input variables

wback=1.8
wlin=.38
wint=.04
winteperc= .15          !crack depth into lining or interlayer
xdivposy=.04/.38      ! first layer thickness % of lining
kinklth=.05
indefangle=0          !angle of initial crack
artdefangle=0        !angle of artificial deflectionradial=18
radial=36
layers=30
rratio=5
bitri=3
wbacke=wback
winte=wint
wline=wlin
*SET,force, 19.5*10/19.5 ! force
*SET,lth,40 ! length of the specimen 40 mm
*SET,wth,40 ! width of the specimen
*SET,ccx1, -wth/2 ! x coordinate for the first corner of block
*SET,wline, .38      ! thickness lining
*SET,winte, .04      ! thickness interlayer
*SET,els, .005       ! element size parameter
*SET,qpes,.0025 ! quarter point element size
bluntirad= 0.00012
radnum=16
ratio=1.3
elemradnum=18

DEFANGLE=INDEFANGLE

!          array size
*dim, angle, array,80
*dim, ldist, array,80
*dim, lkp1, array,80
```

```
*dim, lkp2, array,80
*dim, kpsize, array,280
*dim, ctod, array,80
*dim, ctsd, array,80
*dim, ctod1, array,80
*dim, ctsd1, array,80
*dim, dxcrp, array,80
*dim, dycrp, array,80

!      Loop for crack extensions

*do, m,1,80,1
angle(m,1,1)=0
*enddo

!      plastic analysis variables

load=3000
nlstps = load/60
/nerr, , , 0,0

!      Preprocessing

/prep7
seltol, 1e-12

!      Plasticity data: multi-linear isotropic hardening
! Lining material properties (Ref. no. 1)

/input,20Slining.txt

!properties for linear analysis
!MPTEMP,,,,,,,,
!MPTEMP,1,0

!mp,ex,1,70e3      ! elastic properties
!mp,nuxy,1,0.33

! Backing properties (Ref. no. 2)
/input,20Ssteel.txt

!      properties for linear analysis
!MPTEMP,,,,,,,,
!MPTEMP,1,0
!mp,ex,2,210e3    ! elastic properties
!mp,nuxy,1,0.3

! Interlayer properties (Ref. no. 3)
/input,Alfoil.txt
!properties for linear analysis
!MPTEMP,,,,,,,,
!MPTEMP,1,0
!mp,ex,3,70e3    ! elastic properties
```

!mp,nuxy,1,0.33

!solid element of 8 nodes  
 et,1,82,,,2

!////////////////////////////////////

! define initial crack position

!////////////////////////////////////

```

*SET,angle1, indefangle      ! first crack deflection angle degrees
*SET,extx1, (kinklth+.01)*wint*sin(indefangle/180*3.1416)      ! extension in x direction
*SET,fxcrp, extx1      ! new crack position in x
*SET,exty1, (kinklth+.01)*wint*cos(indefangle/180*3.1416)      ! extension in x direction
*SET,fycrp, wback+(1-winteperc)*wlin+wint-exty1
local,12,0,fxcrp,fycrp,0,+indefangle+90
local,13,1,fxcrp,fycrp,0,+indefangle+90
ydivposx=wth/40+fxcrp
!////////////////////////////////////
! permanent geometry creation
!////////////////////////////////////
csys,0
k,1,-wth/160
k,2,fxcrp
k,3,wth/160
k,4,wth/160,wbacke
k,5, fxcrp,wbacke

k,6, -wth/160,wbacke
k,7,-wth/160, wbacke+winte
k,8, fxcrp, wbacke+winte
k,9, wth/160, wbacke+ winte
k,10, wth/160, wback+wint+wlin*.9
k,11, bluntirad, wback+wint+wlin*.9
k,12, -bluntirad, wback+wint+wlin*.9
k,13, -wth/160, wback+wint+wlin*.9
k,14, -wth/160,+ wback+wint+wlin
k,15, -bluntirad,+ wback+wint+wlin
k,16, bluntirad,+ wback+wint+wlin
k,17, wth/160,+ wback+wint+wlin
l,1,2      !bottom left backing #1
l,2,3
l,3,4
l,4,5
l,5,6
l,6,7
l,7,8
l,8,9
l,9,10
l,10,11
l,12,13
l,13,14
l,14,15
l,16,17
l,12,15
l,11,16
l,5,8
    
```

l,1,6  
l,2,5  
l,4,9  
l,7,13  
l,10,17  
csys,12  
k, 18, 3\*qpes, bluntirad  
k,19, 3\*qpes, -bluntirad  
csys, 13  
k, 20, 3\*qpes,90  
k,21, 3\*qpes,270  
csys, 13  
k,22, bluntirad,180  
k,23, 3\*qpes,180  
k,24, bluntirad,270  
k,25,bluntirad,90  
csys,12  
k,26, 3\*qpes, 3\*qpes  
k,27, 3\*qpes, -3\*qpes  
l, 20,26

l,26,18  
l,19,27  
l,27,21  
l,20,25  
l,24,21  
l,18,25  
l,19,24  
csys, 13  
l, 20,23  
l,23,21  
l,25,22  
l,22,24  
csys,12  
l,12,18  
l,11,19  
l,23,8  
csys,0  
k,101,-wth/2  
k,103,wth/2  
k,104,wth/2,wbacke  
k,106, -wth/2,wbacke  
k,107,-wth/2, wbacke+winte  
k,109, wth/2, wbacke+ winte  
k,110, wth/2, wback+wint+wlin\*.9  
k,113, -wth/2, wback+wint+wlin\*.9  
k,114, -wth/2,+ wback+wint+wlin  
k,117, wth/2,+ wback+wint+wlin  
l,1,101  
l,6,106  
l,7,107  
l,13,113  
l,14,114  
l,17,117  
l,10,110  
l,9,109  
l,4,104  
l,3,103  
l, 103,104  
l,104,109  
l,109,110

l,110,117  
 l,101,106  
 l,106,107  
 l,107,113  
 l,113,114  
 l, 10,17  
 l,1,101  
 l,6,106  
 l,7,107

l,13,113  
 l,14,114  
 l,17,117  
 l,9,109  
 l,4,104  
 l,3,103  
 l,22,23

csys, 13  
 k,201,bluntirad,135  
 k,202, bluntirad,225  
 k,203,3\*qpes,135  
 k,204, 3\*qpes,225  
 l, 25,201  
 l, 201,22  
 l,22,202  
 l,202,24  
 l,20,203  
 l,203,23  
 l,23,204,  
 l,204,21  
 !ldele, 33  
 !ldele,34  
 csys, 0  
 l,202,204  
 l,201,203

!////////////////////////////////////  
 ! AREA CREATION  
 !////////////////////////////////////

al, 1,19,5,18  
 al,19,2,3,4  
 al,17,4,20,8  
 al, 17,5,6,7  
 al,7,21,11,35,24,23,61,62,37  
 al, 37,63,64,26,25,36,10,9,8  
 al,10,22,14,16  
 al,15,13,12,11  
 al, 28,30,25,26  
 al,27,29,24,23  
 al,28,60,65,64  
 al,3,47,48,46  
 al,20,46,49,45  
 al,50,45,9,44  
 al,22,44,51,43  
 al,38,18,39,52  
 al,6,39,53,40  
 al,21,40,54,41  
 al,12,41,55,42  
 al,65,63,56,59  
 al, 56,62,58,66

```

al, 66,57,27,61
!////////////////////////////////////

!      Element size calculation
!////////////////////////////////////

lsel,all
*GET,lnum,LINE,,COUNT,,,
*do, l, 1,lnum,1
*GET,ldist(l,1,1),LINE,l,LENG
*GET,lkp1(l,1,1),LINE,l,KP,1
*GET,lkp2(l,1,1),LINE,l,KP,2
*enddo

*do, g,1,279,1
p=g
kpsize(g,1,1)=10
*enddo

kpsize(1,1,1)=1
kpsize(2,1,1)=.5
kpsize(3,1,1)=1
kpsize(4,1,1)=.005
kpsize(5,1,1)=.014
kpsize(6,1,1)=.005
kpsize(7,1,1)=.009
kpsize(8,1,1)=.0045
kpsize(9,1,1)=.009
*if, fycrp,le,1.9,then
kpsize(8,1,1)=.002
*endif
kpsize(10,1,1)=.015
kpsize(11,1,1)=.01
kpsize(12,1,1)=.01
*if, fycrp,ge,2.1,then
kpsize(11,1,1)=.0045
kpsize(12,1,1)=.0045
*endif
*if, fycrp,ge,2.14,then
kpsize(11,1,1)=.002
kpsize(12,1,1)=.002
*endif

kpsize(13,1,1)=.015
kpsize(14,1,1)=.015
kpsize(15,1,1)=.015
kpsize(16,1,1)=.015
kpsize(17,1,1)=.015
kpsize(18,1,1)=40e-5
kpsize(19,1,1)=40e-5
kpsize(20,1,1)=3e-5

kpsize(21,1,1)=3e-5
kpsize(22,1,1)=3e-5
kpsize(23,1,1)=40e-5
kpsize(24,1,1)=3e-5
kpsize(25,1,1)=3e-5
kpsize(26,1,1)=3e-5
kpsize(27,1,1)=3e-5
kpsize(28,1,1)=3e-5
kpsize(101,1,1)=2

```

```
kpsize(103,1,1)=2
kpsize(104,1,1)=2
kpsize(106,1,1)=2
kpsize(107,1,1)=2
kpsize(109,1,1)=2
kpsize(113,1,1)=2
kpsize(114,1,1)=2
kpsize(117,1,1)=2
!////////////////////
! meshing parameter calculation
!////////////////////
allsel, all
*do, s, 1, lnum, 1
L=l dist(s, 1, 1)
*if ,kpsize(lkp1(s, 1, 1), 1, 1), ge, kpsize(lkp2(s, 1, 1), 1, 1), then
emax=kpsize(lkp1(s, 1, 1), 1, 1)
emin=kpsize(lkp2(s, 1, 1), 1, 1)
*endif
*if ,kpsize(lkp1(s, 1, 1), 1, 1), le, kpsize(lkp2(s, 1, 1), 1, 1), then
emin=kpsize(lkp1(s, 1, 1), 1, 1)
emax=kpsize(lkp2(s, 1, 1), 1, 1)
*endif
tolerance=2
fratio=emax/emin
fesize=(emin+emax)/2
fne=nint(l/fesize)
nratio=fratio
*if, fne, eq, 0, then
fne=1
*endif
nne=fne
*if, fratio, ne, 1, then
*if, fne, ne, 1, then
nemin=L*(1-(fratio)**(1/(fne-1)))/(1-(((fratio)**(1/(fne-1)))** (fne)))
nemax=nemin*fratio
*endif
*endif

*do, m, 1, 200, 1

*if, kpsize(lkp1(s, 1, 1), 1, 1), eq, 10, exit
*if, fratio, eq, 1, exit
*if, nne, eq, 1, exit
*if, emin, lt, nemin, then
*if, emax, lt, nemax, then
nratio=nratio+.1
nne=nne+1
*if, emax, gt, nemax, then
nratio=nratio+1
*endif
*endif
*if, emin, gt, nemin, then
*if, emax, gt, nemax, then
nne=nne-1
*endif
*if, emax, lt, nemax, then
nratio=nratio-.5
*endif
*endif
*if, emin, lt, 1.1*nemin, then
*if, emin, gt, .9*nemin, then
```

```
*if, emax,lt,1.1*nemax, then
*if, emax,gt,.9*nemax, exit
*endif
*endif
*endif
*endif

nemin=L*(1-(nratio)**(1/(nne-1)))/(1-(((nratio)**(1/(nne-1)))**nne))
nemax=nemin*nratio
*enddo
*if,kpessize(lkp1(s,1,1),1,1),ge,kpessize(lkp2(s,1,1),1,1),then
nratio=1/nratio
*endif

lesize,s,,nne,nratio,1
*enddo
lsel, all
lesize,57,,radial/2,,1
lesize,58,,radial/2,,1
lesize,59,,layers,rratio,1
lesize,60,,layers,rratio
lesize,27,,layers,rratio,1
lesize,28,,layers,1/rratio,1
lesize,56,,layers,1/rratio,1
lesize,66,,layers,1/rratio,1
lesize,65,,layers,1/rratio,1

lesize,24,,layers,,1
lesize,23,,layers,,1
lesize,25,,layers,,1
lesize,26,,layers,,1
lesize,29,,layers,1/40,1
lesize,30,,layers,1/40,1
csys,0
lsel, s, loc, x, wth/2
lsel,a, loc,x, -wth/2
lsel, u, loc, y, wback-wint, wback+wint*2
lsel, u, line,,54
lsel, u, line,,50
lesize,all,,8,1/6,1
lsel, s, loc, x, wth/160
lsel,a, loc,x, -wth/160
lsel, u, loc, y, wback-wint, wback+wint*2
lsel,u,line,,21
lsel,u,line,,12
lsel,u,line,,9
lsel,u,line,,22
lesize,all,,8,1/6,1,1
lsel, s, loc, x, wth*.20,wth*.30
lsel,a, loc,x, -wth*.20,-wth*.30
lesize,all,,30,50,1
allsel, all
lesize,55,,1,1/3,1
lesize,51,,1,1/3,1
lesize, 50,,1,1/3,1
lesize, 54,,1,1/3,1
lesize,57,,radial/2
lesize,58,,radial/2
lesize,59,,radial/2
```

```

lesize,60,,,radial/2
lesize,61,,,radial/2
lesize,62,,,radial/2
lesize,63,,,radial/2
lesize,64,,,radial/2
!////////////////////////////////////
!meshing
!////////////////////////////////////
asel, all
mopt, expnd, 1.2
mopt, trans, 1.3
mat, 1
MSHKEY,1
csys,0
mat,1
amesh,20

amesh,21
amesh,10
amesh,9
amesh,11
amesh,22
mopt, expnd, 1.1
mopt, trans, 1.3
mshkey,0
amesh,14
amesh,18

mat,2
mshkey,1
amesh,16
amesh,12
mshkey,0
mat,bitri
amesh,13
amesh,17
mat,1
amesh,19
amesh,15
MSHKEY,2
mat,2
amesh,1
amesh,2
mat,bitri
amesh,3
amesh,4
mat,1
amesh,5
amesh,6
mat,1
amesh,8
amesh,7
!////////////////////////////////////
!boundary conditions
!////////////////////////////////////
csys, 0
allsel, all
nset, s, loc, x, 0
nset, r, loc, y, 0
F,all,FY,force
d, all, ux

```

```
nset, s, loc, x, wth/2
nset, r, loc, y, wback+wlin+wint
D,all,uy
nset, s, loc, x, -wth/2
nset, r, loc, y, wback+wlin+wint
D,all,uy
allsel, all
!////////////////////////////////////
! solution controls loading
!////////////////////////////////////
finish
/nerr, , , 0,0
allsel, all
/solu
solcontrol, on
!autots, on
antype,stat
nlgeom,1
time,100
OUTRES,ERASE
OUTRES,ALL,-1
deltim,2/force,.00003,4/force
solve
```

## ***2. Two dimensional flat strip with bifurcated tip crack model under three-point bending***

The code shown next is an input file to be used directly in ANSYS coded with APDL tools.

```

/batch
/CWD,'C:\Documents and Settings\burke.CEDGUSERS\My Documents\thesis\deflection_model\test1'
*SET,force,19.5*20/19.5 ! force
*SET,lth,40 ! length of the specimen 40 mm
*SET,wth,40 ! width of the specimen
*SET,ccx1,-wth/2 ! x coordinate for the first corner of block
*SET,wback,1.8 ! thickness backing
*SET,wlin,.38 ! thickness lining
*SET,wint,.04 ! thickness interlayer
*SET,els,.005 ! element size parameter
*SET,qpes,wint/50! quarter point element size
bluntirad=0.00012
radnum=16
ratio=1.3
nratio=7
mratio=5
layers=10
elemrad=18
wintperc=.81 !crack depth into lining or interlayer
kinklth=.0150
indefangle=25
DEFANGLE=INDEFANGLE

*dim, angle, array,80
*dim, ldist, array,80
*dim, lkp1, array,80
*dim, lkp2, array,80
*dim, kpesize, array,80
*dim, ctod, array,80
*dim, ctsd, array,80
*dim, dxcrp, array,80
*dim, dycrp, array,80

! \\\\
! Crack extension loop
! \\\\
*do, m,1,80,1
angle(m,1,1)=0
*enddo

!plastic analysis variables
load=3000
nlstps = load/60

/nerr, , , ,0,0

/prep7
seltol,1e-12
! Plasticity data: multi-linear isotropic hardening

```

```

! Lining material properties (Ref. no. 1)
/input,20Slining.txt
!properties for linear analysis
!MPTEMP,,,,,,,,
!MPTEMP,1,0
!mp,ex,1,70e3      ! elastic properties
!mp,nuxy,1,0.33
! Backing properties (Ref. no. 2)
/input,20Ssteel.txt
!properties for linear analysis
!MPTEMP,,,,,,,,
!MPTEMP,1,0
!mp,ex,2,210e3    ! elastic properties
!mp,nuxy,1,0.3
! Interlayer properties (Ref. no. 3)
/input,Alfoil.txt
!properties for linear analysis
!MPTEMP,,,,,,,,
!MPTEMP,1,0
!mp,ex,3,70e3     ! elastic properties
!mp,nuxy,1,0.33
!solid element of 8 nodes
et,1,82,,2

!////////////////////////////////////

! define initial crack position

!////////////////////////////////////

*SET,angle1, indefangle      ! first crack deflection angle degrees
*SET,extx1, (kinklth+.03)*wlin*sin(indefangle/180*3.1416)      ! extension in x direction
*SET,fxcrp, extx1      ! new crack position in x
*SET,exty1, (kinklth+.01)*wlin*cos(indefangle/180*3.1416)      ! extension in x direction
*SET,fycrp, wback+(1-wintperc)*wlin+wint-exty1
local,12,0,fxcrp,fycrp,0,+indefangle+90
local,13,1,fxcrp,fycrp,0,+indefangle+90
xdivposy=.9      ! first layer thickness % of lining
ydivposx=wth/40+fxcrp
!////////////////////////////////////

! permanent geometry creation

!////////////////////////////////////
csys,0
k,1
k,2,ydivposx
l,1,2      !bottom left backing #1
k,3, , wback
l,1,3      !backing left #2
k,4,ydivposx,wback
l,4,2      !backing middle #3
k,5,wth/2
k,6,wth/2, wback
l,4,6      !backing top right #4
l,2,5,      !backing bottom right #5
l, 5, 6      !backing right #6
k,7, ,wback+wint
k,8, ydivposx,wback+wint
k,9, wth/2,wback+wint
l,3,7      !!interlayer left #7

```

```

l,8,9                !interlayer top right #8
l, 9,6              !interlayer right #9
l,8,4               !interlayer middle #10
k,10, ,wback+wint+xdivposy*wlin
k,11, ydivposx, wback+wint+xdivposy*wlin
k,12, wth/2, wback+wint+xdivposy*wlin
l,11, 12           !cracklya top right #11
l, 12, 9           !!cracklya right #12
k,13,, wback+wint+wlin
k,14,ydivposx, wback+wint+wlin
k,15, wth/2, wback+wint+wlin
l,12,15           !lin right #13
l,14,15           !lin top right #14
l,13,10           !lin left #15
l, 8, 11           !cracklay middle #16
l, 11,14          !lin middle #17
al,3,5,6,4       ! back right ##1
al,4,9,8,10      ! int right ##2
al,8,12,11,16    ! cracklay right ##3
al,11,13,14,17   ! lining right ##4
lsel, s, loc, x, wth/4, wth/2*.99
lesize, all,,50,5,1
!////////////////////
! particular geometry
!////////////////////

k,19,fxcrp, wback
k,20,fxcrp, wback+wint
k,21, fxcrp, wback+wint+xdivposy*wlin
k,22, fxcrp, wback+wint+wlin
l, 19,3           ! top backing crack left #18
l,19,4           ! top backing crack right #19
l,20,7           ! bottom cracklay crack left #20
l,20,8           ! bottom cracklay crack right #21
l,21,10          ! bottom lining crack left #22
l,21,11          ! bottom lining crack right #23
l,22,13          ! top lining crack left #24
l,22,14          ! top lining crack right #25
k,23,, fycrp+fxcrp*tan((90-indefangle)*3.1416/180)-bluntirad/cos((90-indefangle)*3.1416/180)
k,24,, fycrp+fxcrp*tan((90-indefangle)*3.1416/180)+bluntirad/cos((90-indefangle)*3.1416/180)
l,7,23           !crack lay left bottom #26
l,24,10          !crack lay left top #27
csys,12
k, 25, 3*qpes, bluntirad
k,26, 3*qpes, -bluntirad
csys,0
l, 23,25         !crack lower #28
l,24,26         !crack upper #29
csys, 13
k, 27, 3*qpes,90
k,28, 3*qpes,270
csys, 0
csys, 13
k,29, bluntirad,180
k,30, 3*qpes,180
l, 28,30 !qpes arc #30
l,30,27 !qpes arc2 #31
k,31, bluntirad,270
k,32,bluntirad,90

```

```

l, 29,32 !blunti arc #32
l,31,29 !blunti arc2 #33
csys, 0
l, 27,32 !upper base circ #34
l,31,28 !lower base circ #35
csys, 12
k,33, 3*qpes, 3*qpes
k,34, 3*qpes, -3*qpes
l, 28,34 ! upper crack area side #36
l,26,34 ! upper crack area contrabase #37
l,26,31 ! upper crack area crack side #38
l,33,27 ! lower crack area side #39
l,33,25 ! lower crack area contrabase #40
l,25,32 ! lower crack area crack side #41
l, 34,21 !crack lay division top #42
l, 30,20 !crack lay divisions bottom #43
l, 29,30 ! middle ring #44

lsel,all
*GET,lnum,LINE,,COUNT,,,
*do, l, 1,lnum,1
*GET,l,ldist(l,1,1),LINE,l,LENG
*GET,lkp1(l,1,1),LINE,l,KP,1
*GET,lkp2(l,1,1),LINE,l,KP,2
*enddo
! \\\
! Element size
! \\\

*do, g,1,79,1
p=g
kpsize(g,1,1)=10
*enddo

kpsize(1,1,1)=.14
kpsize(2,1,1)=.14
kpsize(3,1,1)=3.5e-3
kpsize(4,1,1)=.12
kpsize(7,1,1)=8e-3
kpsize(8,1,1)=1.2e-1
kpsize(10,1,1)=8e-3
kpsize(11,1,1)=1.2e-1
kpsize(13,1,1)=5.83e-3
kpsize(14,1,1)=1.2e-1
kpsize(19,1,1)=5.25e-3
kpsize(20,1,1)=5.25e-3
kpsize(21,1,1)=5.25e-3
kpsize(22,1,1)=5.25e-3
kpsize(23,1,1)=2.79e-4
kpsize(24,1,1)=2.79e-4
kpsize(25,1,1)=7e-5
kpsize(26,1,1)=7e-5
kpsize(27,1,1)=7e-5
kpsize(30,1,1)=7e-5
kpsize(34,1,1)=8.37e-5
! \\\

! meshing parameter calculation

! \\\

```

```
*do,s,1,lnum,1

L=lDist(s,1,1)

*if ,kpesize(lkp1(s,1,1),1,1),ge,kpesize(lkp2(s,1,1),1,1),then
emax=kpesize(lkp1(s,1,1),1,1)
emin=kpesize(lkp2(s,1,1),1,1)
*endif

*if ,kpesize(lkp1(s,1,1),1,1),le,kpesize(lkp2(s,1,1),1,1),then
emin=kpesize(lkp1(s,1,1),1,1)
emax=kpesize(lkp2(s,1,1),1,1)
*endif

tolerance=2
fratio=emax/emin
fesize=(emin+emax)/2
fne=nint(l/fesize)
nratio=fratio
*if,fne,eq,0,then
fne=1
*endif

nne=fne
*if, fratio,ne,1,then
*if, fne,ne,1,then
nemin=L*(1-(fratio)**(1/(fne-1)))/(1-(((fratio)**(1/(fne-1)))**fne)))
nemax=nemin*fratio
*endif
*endif

*do, m,1,200,1

*if,kpesize(lkp1(s,1,1),1,1),eq,10, exit
*if,fratio,eq,1, exit
*if,nne,eq,1, exit

*if, emin,lt,nemin,then
*if, emax, lt, nemax, then
nratio=nratio+.1
nne=nne+1
*if,emax, gt,nemax, then
nratio=nratio+1
*endif
*endif

*if, emin,gt,nemin, then

*if, emax, gt, nemax, then
nne=nne-1
*endif

*if,emax, lt,nemax, then
nratio=nratio-.5
*endif

*endif

*if, emin,lt,1.1*nemin, then
```

```

*if, emin,gt,.9*nemin, then
*if, emax,lt,1.1*nemax, then
*if, emax,gt,.9*nemax, exit
*endif
*endif
*endif
*endif

nemin=L*(1-(nratio)**(1/(nne-1)))/(1-(((nratio)**(1/(nne-1)))**(nne)))
nemax=nemin*nratio
*enddo

*if,kpysize(lkp1(s,1,1),1,1),ge,kpysize(lkp2(s,1,1),1,1),then
nratio=1/nratio
*endif

lesize,s,,,nne,nratio,1

*enddo

lsel, all
lesize,3,,15,,,1
lesize,17,,,1
lesize, 16,,1,,,1
lesize, 10,,,1
lesize, 12,,1,,,1
lesize,13,,,1
lesize,6,,15,,,1
lesize, 9,,,1
csys,0
lsel, s, loc, x, wth/4, wth/2*.99
lesize, all,,,50,5,1
lsel,all
lesize,30,,,elemrad
lesize,33,,,elemrad
lesize,32,,,elemrad
lesize,31,,,elemrad
lesize,39,,,layers,1/mratio
lesize,36,,,layers,mratio
lesize,37,,,layers,,1
lesize,40,,,layers,,1
lesize,38,,,layers,1/mratio,1
lesize,41,,,layers,1/mratio,1

lesize,44,,,layers,1/nratio,1
lesize,34,,,layers,nratio,1
lesize,35,,,layers,1/nratio,1
!////////////////////////////////////

! particular geometry area creation

!////////////////////////////////////

al, 39,40,41,34    !left small square ##5
al,34,31,44,32    !ring ##6
al,37,36,35,38    !right small square ##7
al,31,39,40,28,26,20,43    !inferior left cracklay ##8
al, 29,37,42,22,27    !superior right cracklay ##9
al,20,7,18,19,10,21    !interlayer left ##10
al,21,16,23,42,36,30,43    !crack lay middle ## 11
al,23,17,25,24,15,22    !lining left ##12

```

```

al,1,3,19,18,2      !backing right ##13
al,35,33,44,30     !ring ##14
asel, all
aglua, all
!ldiv,33,,3
!csys, 13
!lsl, s,loc,x,bluntirad*.99,bluntirad*1.01
!lsl, r, loc, y, 210,270
!lesize, all,,2
!lsl, s,loc,x,bluntirad*.99,bluntirad*1.01
!lsl, r, loc, y, 180,210
!lesize, all,,6
!lsl, all
!ldiv,32,,3
!lsl, s,loc,x,bluntirad*.99,bluntirad*1.01
!lsl, r, loc, y, 90,150
!lesize, all,,2
!lsl, s,loc,x,bluntirad*.99,bluntirad*1.01
!lsl, r, loc, y, 150,180
!lesize, all,,6
!lsl, all
!ldiv,30,,3
!lsl, s,loc,x,qpes*3*.99,qpes*3*1.01
!lsl, r, loc, y, 210,270
!lesize, all,,2
!lsl, s,loc,x,qpes*3*.99,qpes*3*1.01
!lsl, r, loc, y, 180,210
!lesize, all,,6
!lsl, all
!ldiv,31,,3
!lsl, s,loc,x,qpes*3*.99,qpes*3*1.01
!lsl, r, loc, y, 90,150
!lesize, all,,2
!lsl, s,loc,x,qpes*3*.99,qpes*3*1.01
!lsl, r, loc, y, 150,180
!lesize, all,,6
!lsl, all
!lesize,44,,2,1/2,1
!////////////////////////////////////
meshing

!////////////////////////////////////
asel, all
mopt, trans, 1.12
mat, 1
MSHKEY,1
csys,15
amesh,6
amesh, 14
amesh,3
amesh,4
MSHKEY,2
amesh,5
amesh,7
amesh, 8
amesh, 9
amesh, 11
mopt, trans, 1.15
amesh, 12
mat, 2

```

```

amesh,1
amesh, 13
mopt, trans, 1.12
MSHKEY,1
amesh, 2
mopt, trans, 1.15
MSHKEY,2
amesh, 10
!////////////////////////////////////

!boundary conditions

!////////////////////////////////////
csys, 0
nset, s, loc, x, 0
nset, r, loc, y, 0
F,all,FY,force
nset, s, loc, x, wth/2
nset, r, loc, y, wback+wlin+wint
D,all,uy
nset, s, loc, x, 0
nset, r, loc, y, -1, fycrp+fxcrp*tan((90-indefangle)*3.1416/180)-bluntirad/cos((90-indefangle)*3.1416/180)
d, all, ux
!////////////////////////////////////

! solution controls

!////////////////////////////////////
finish
/nerr, , , 0,0
allsel, all

/solu
solcontrol, on
!autots, on
antype,stat
nlgeom,1
time,100
OUTRES,ERASE
OUTRES,ALL,-1
deltim,3/force,.00003,6/force
solve
finish

```

### ***3. Three dimensional flat strip with quasi semi-elliptical crack under three-point bending***

The code shown next correspond to the file that wraps a number of smaller files with particular functions developed for the creation, solution and extension of crack models. All the necessary files are stored in the CD attached.

```
inputdata;
for cc200=6:25 %      Extension loop
restartfile=sprintf('restart%02.0f.mat',curextstep); % restart files
save(restartfile);
  folderstructure; %      File name system
cracknodes; %      Position of the nodes along the front
keypoint; %      Position of keypoints
lines; %      Line connectivity
esize; %      Element size
surfaces; %      surface connectivity
volume; %      Volume connectivity
printinputdata; %      .m files commencing with "print" save the date into a text file
printkeypoint;
printkeypointscrack;

printlines;
printlinescrack;

printsurface;

printsurfacescrack;
printlesize;
printvolume;
printvolumescrack;
cracknodes_spiderweb; %      Reposition of nodes along the front
printareameshing;
printvolumemeshing;
printsolution; %      Solution commands
printpostproc; %      Postprocessing commands
fclose('all');
  pause (5);
  system(executeansys);

lockstatus= exist(lockfile,'file');

loopcounter=0;
while lockstatus~=0
  loopcounter=loopcounter+1;
  lockstatus= exist(lockfile,'file');
  warning('lockstatus pause');
  pause(30);
  if loopcounter==60
    exit
  end
```

```
end

flagstatus= exist('ansys_process/flag.txt','file');

while flagstatus~=2
    loopcounter=loopcounter+1;
    flagstatus= exist('ansys_process/flag.txt','file');
    warning('flagstatus pause');
    pause(5);
end                                     %      launch ANSYS in batch mode and wait for solution

readresultsspid;                       %      Open text files and import results
crackextension;                       %      Post process data for new model

!cp -rf /tmp/31autoextspid/input_files/*.out /home1/utp-71/burke/31autoextspid/results1/
!cp -rf /tmp/31autoextspid/ansys_process/*.rstt /home1/utp-71/burke/31autoextspid/results1/
!cp -rf /tmp/31autoextspid/ansys_process/*.rst /home1/utp-71/burke/31autoextspid/results1/
!cp -rf /tmp/31autoextspid/*.mat /home1/utp-71/burke/3dcrack/results1/

save ('workspace.mat');                 % File management
delete('ansys_process/*.rst');
delete('ansys_process/*.rstt');
delete('ansys_process/*.rdb');
delete('ansys_process/*.full');
delete('ansys_process/*.esav');
delete('ansys_process/*.emat');
delete('ansys_process/*.BCS');
delete('ansys_process/*.esav');
delete('ansys_process/*.osav');
delete('ansys_process/*.r001');
delete('ansys_process/*.mntr');
delete('ansys_process/*.stat');
delete('ansys_process/*.pce');
delete('ansys_process/*.pcs');
delete('ansys_process/*.err');
delete('ansys_process/*.ldhi');
delete('ansys_process/*.mntr');
delete('ansys_process/*.db');
delete('ansys_process/flag.txt');

end
```

#### 4. Three dimensional full bearing analysis

The code shown next correspond to the file that wraps a number of smaller files with particular functions developed for the creation, solution and extension of crack models. All the necessary files are stored in the CD attached.

```

!////////////////////////////////////
Input data
!////////////////////////////////////

bearinggrad=56.43/2;
bearingwidth=29.49;
wlin=.38;
wint=.04;
wback=1.8;
totth=wback+wint+wlin;
llin=4;
lint=1;
lback=2;
ang1=57;
ang2=77;
zcoord1=1;
zcoord2=9;
meshang=154;
meshwidth=13;

angrange=angle(ang2)-angle(ang1);
lth=sind(angrange/2)*bearinggrad*2;

radcoord(1:1+llin)=[bearinggrad:wlin/llin:bearinggrad+wlin];
radcoord(2+llin:llin+lint+1)=[bearinggrad+wlin+wint/lint:wint/lint:bearinggrad+wlin+wint];
radcoord(2+llin+lint:llin+lint+lback+1)=[bearinggrad+wlin+wint+wback/lback:wback/lback:bearinggrad+wlin+wint+wback];

fid=fopen('bearing_stress_shifted_no_inis_elas_no_fit.txt','w');
%////////////////////////////////////
% Ansys elements and material types
%////////////////////////////////////

fprintf(fid,'\n\n\n!   input data\n\n ');
fprintf(fid,'\n\n\n')
fprintf(fid,'/prep7\n\n ');

fprintf(fid,'ET,1,SOLID185\n ');
fprintf(fid,'ET,2,SOLID186\n ');
fprintf(fid,'SHPP,OFF\n ');
%Backing properties (Ref. no. 2)
fprintf(fid,'/input,20Slining.txt\n ');
fprintf(fid,'/input,20Ssteel.txt\n ');
fprintf(fid,'/input,Alfoil.txt\n ');
%
fprintf(fid,'MPTEMP,,,,,,,, \n');
fprintf(fid,'MPTEMP,1,0 \n');
fprintf(fid,'MPDATA,EX,4,,70e3 \n');
fprintf(fid,'MPDATA,PRXY,4,,.33\n');

```

```

fprintf(fid,'MPTEMP,,,,,,,, \n');
fprintf(fid,'MPTEMP,1,0 \n');
fprintf(fid,'MPDATA,EX,5,,210e3 \n');
fprintf(fid,'MPDATA,PRXY,5,,.29\n');

fprintf(fid,'MPTEMP,,,,,,,, \n');
fprintf(fid,'MPTEMP,1,0 \n');
fprintf(fid,'MPDATA,EX,6,,50e3 \n');
fprintf(fid,'MPDATA,PRXY,6,,.33\n');

%////////////////////////////////////
% Coordinate systems
%////////////////////////////////////

fprintf(fid,'local,%3.0f,1, %8.7f , %8.7f , %8.7f , %4.2f ,%4.2f,%4.2f \n',11,bearinggrad*sind(angrange/2),-
bearinggrad,0,272,0,0)%-4-(270-(angle(ang2)-angle(ang1))/2-angle(ang1))-180,0,0);
fprintf(fid,'local,%3.0f,0, %8.7f , %8.7f , %8.7f , %4.2f ,%4.2f,%4.2f \n',12,bearinggrad*sind(angrange/2),-
bearinggrad,0,272,0,0)%-4-(270-(angle(ang2)-angle(ang1))/2-angle(ang1))-180,0,0);

angle1(1:89)=angle(66:154);
angle1(90:154)=angle(1:65)
% angle1=angle(-4-(270-(angle(ang2)-angle(ang1))/2-angle(ang1))+180-angrange);

% fprintf(fid,'csys,1\n');
fprintf(fid,'csys,11\n');

fprintf(fid,'type,1\n');
% fprintf(fid,'mat,2\n');
fprintf(fid,'mat,5\n');

for cc3=1:llin+lint+lback+1
for cc1=1:154
    for cc2=1:13
        fprintf(fid,'n,,%6.2f,%6.2f,%6.2f\n',radcoord(cc3),angle(cc1),zcoord(cc2)*bearingwidth);
    end
end
end
%
%////////////////////////////////////
% Node and element creation
%////////////////////////////////////

for cc3=1:llin+lint+lback
for cc1=1:153
    for cc2=1:12
        fprintf(fid,'e,%6.2f,%6.2f,%6.2f,%6.2f,%6.2f,%6.2f,%6.2f,%6.2f\n',1+(cc2-1)+(cc1-1)*13+(cc3-1)*2002,2+(cc2-
1)+(cc1-1)*13+(cc3-1)*2002,15+(cc2-1)+(cc1-1)*13+(cc3-1)*2002,14+(cc2-1)+(cc1-1)*13+(cc3-1)*2002,2003+(cc2-
1)+(cc1-1)*13+(cc3-1)*2002,2004+(cc2-1)+(cc1-1)*13+(cc3-1)*2002,2017+(cc2-1)+(cc1-1)*13+(cc3-
1)*2002,2016+(cc2-1)+(cc1-1)*13+(cc3-1)*2002);
    end
end
for cc2=1:12
    fprintf(fid,'e,%6.2f,%6.2f,%6.2f,%6.2f,%6.2f,%6.2f,%6.2f,%6.2f\n',1+(cc2-1)+(cc3-1)*2002,2+(cc2-1)+(cc3-
1)*2002,1991+(cc2-1)+(cc3-1)*2002,1990+(cc2-1)+(cc3-1)*2002,2003+(cc2-1)+(cc3-1)*2002,2004+(cc2-1)+(cc3-
1)*2002,3993+(cc2-1)+(cc3-1)*2002,3992+(cc2-1)+(cc3-1)*2002);
end
end

fprintf(fid,'nsel,s,loc,z,%5.4f\n',zcoord(13)*bearingwidth);

```

```
fprintf(fid,'d,all,uz,0\n');

% fprintf(fid,'nset,s,node,%.7f,%.7f\n',2002*(llin+lint+lback)+1,2002*(llin+lint+lback)+2002)
% fprintf(fid,'d,all,uy,0\n');

fprintf(fid,'esel, s, elem,%.6f,%.6f\n',1,1848*llin);
% fprintf(fid,'emodif,all, mat, 1\n');
fprintf(fid,'emodif,all, mat, 4\n');
fprintf(fid,'esel, s, elem,%.6f,%.6f\n',1848*llin+1,1848*(llin+lint));
% fprintf(fid,'emodif,all, mat, 1\n');
fprintf(fid,'emodif,all, mat, 4\n');
fprintf(fid,'esel, s, elem,%.6f,%.6f\n',1848*(llin+lint)+1,1848*(llin+lint+lback));
% fprintf(fid,'emodif,all, mat, 2\n');
fprintf(fid,'emodif,all, mat, 5\n');

fprintf(fid,'nset,s,loc,z,%.5f\n',0);
fprintf(fid,'esln\n');

fprintf(fid,'EGEN,2,600000,all,,,,,,,,,%.5f\n',-(zcoord(2)-zcoord(1))*bearingwidth);
fprintf(fid,'allsel, all\n');

fprintf(fid,'nummrg,node,1e-2,,,low\n');
%
fprintf(fid,'emodif,all, type, 2\n');

fprintf(fid,'emid,add,all\n');

% %////////////////////////////////////
%
% % number of steps to be solved
%

% %////////////////////////////////////
% including stress history
%////////////////////////////////////
fprintf(fid,'/sol\n');
cc200=0;

fprintf(fid,'time,%.4f\n',cc200);
fprintf(fid,'INISTATE,set, csys, 1\n');
%
% inistate=[-0,-0,-2.8649,37.4564,167.5479,0.4877;-0,-0,-2.4386,31.1964,162.6096,0.5695;-0,-0,-
1.8316,21.2292,152.0197,0.7125;-0,-0,-1.557,11.7552,125.6447,0.9656;-0,-0,-1.7234,3.1326,97.8095,1.6143;-0,-0,-
1.3706,-77.7407,-5.6151,1.0735;-0,0,0.0286,59.537,10.7766,6.3511;-0,0,2.6063,103.0705,-47.4177,0.1889]; %xz yz xy z
y x
inistate=[0,0,-2.86490000000000,37.45640000000000,135,0.4877000000000000;0,0,-
2.4386000000000000,31.19640000000000,124,0.5695000000000000;0,0,-
1.8316000000000000,21.22920000000000,109,0.7125000000000000;0,0,-
1.5570000000000000,11.75520000000000,93,0.9656000000000000;0,0,-1.72340000000000,-
77.74070000000000,80,1.61430000000000;0,0,-1.37060000000000,59.537000000000,-
124,1.07350000000000;0,0,0.02860000000000,103.070500000000,75,6.35110000000000];

%////////////////////////////////////
% Loading import
%////////////////////////////////////
```

```

backdispfile='totaldef/totdef109.txt';
pressurefile='pressure/pressure001.txt';
backdisp=load(backdispfile);

    fprintf(fid,'csys,0\n');
    cc200=cc200+1;
%////////////////////////////////////
% loading application form and fitting
%////////////////////////////////////

for cc1=1:154
    for cc2=1:13
fprintf(fid,'d,%5.0f,ux,%5.6f\n',2002*(llin+lint+lback)+cc2+(cc1-1)*13,backdisp(cc1,cc2)*cosd(angle(cc1)+272));
fprintf(fid,'d,%5.0f,uy,%5.6f\n',2002*(llin+lint+lback)+cc2+(cc1-1)*13,backdisp(cc1,cc2)*sind(angle(cc1)+272));
fprintf(fid,'d,%5.0f,uz,%5.6f\n',2002*(llin+lint+lback)+cc2+(cc1-1)*13,0);

        end
    end
    fprintf(fid,'time,%4.0f\n',cc200);

    fprintf(fid,'NSUBST,20,200,1\n');
    fprintf(fid,'allsel, all\n')
    fprintf(fid,'csys,12\n');
    fprintf(fid,'solve\n');

for cc101=1:1
if cc101==1
    mg=5;
    mh=176;
else
    mg=5;
    mh=176;
end

for cc100=1:mg:mh
cc200=cc200+1

    cc300=cc100+90
    if cc300>=181
        cc300=cc300-180;
    end
    fprintf(fid,'time,%4.0f\n',cc200);
    pressurefile(18:20)=num2str(cc300,'%03.0f');
    backdispfile(16:18)=num2str(cc300,'%03.0f');
    fprintf(fid,'allsel, all\n');

%////////////////////////////////////
% Loading application service conditions
%////////////////////////////////////

    pressure=load(pressurefile);
    backdisp=load(backdispfile);
    for cc1=1:153
        for cc2=1:12
% fprintf(fid,'SFE,%5.0f,1,PRES, %6.4f, ,
% \n',cc2+(cc1-1)*12,(pressure(cc1,cc2)+pressure(cc1+1,cc2)+pressure(cc1,cc2+1)+pressure(cc1+1,cc2+1))/4);
        fprintf(fid,'SFE,%5.0f,1,PRES, %6.4f,%6.4f ,%6.4f ,%6.4f\n',cc2+(cc1-1)*12, pressure(cc1,cc2+1), pressure(cc1,cc2),
        pressure(cc1+1,cc2), pressure(cc1+1,cc2+1)); % node order for sfe correspond to face node numbering jilk

```

```
    end
end

for cc2=1:12
%
%                               fprintf(fid,'SFE,%5.0f,1,PRES,           ,%6.4f,
,\n',cc2+(153)*12,(pressure(154,cc2)+pressure(154,cc2+1)+pressure(153,cc2+1)+pressure(153,cc2))/4);
    fprintf(fid,'SFE,%5.0f,1,PRES, %6.4f,%6.4f %6.4f %6.4f\n',cc2+(153)*12, pressure(153,cc2+1), pressure(153,cc2),
pressure(154,cc2), pressure(154,cc2+1));
    end
% fprintf(fid,'csys,0\n');

    fprintf(fid,'csys,0\n');

    for cc1=1:154
    for cc2=1:13
fprintf(fid,'d,%5.0f,ux,%5.6f,\n',2002*(llin+lint+lback)+cc2+(cc1-1)*13,backdisp(cc1,cc2)*cosd(angle(cc1)+272));
fprintf(fid,'d,%5.0f,uy,%5.6f,\n',2002*(llin+lint+lback)+cc2+(cc1-1)*13,backdisp(cc1,cc2)*sind(angle(cc1)+272));
fprintf(fid,'d,%5.0f,uz,%5.6f,\n',2002*(llin+lint+lback)+cc2+(cc1-1)*13,0);
% fprintf(fid,'d,%5.0f,ux,%5.6f,\n',2002*(llin+lint+lback)+cc2+(cc1-1)*13,backdisp(cc1,cc2));
% fprintf(fid,'d,%5.0f,uy,%5.6f,\n',2002*(llin+lint+lback)+cc2+(cc1-1)*13,0);
% fprintf(fid,'d,%5.0f,uz,%5.6f,\n',2002*(llin+lint+lback)+cc2+(cc1-1)*13,0);

    end
    end
% fprintf(fid,'csys,0\n');
fprintf(fid,'csys,12\n');
% fprintf(fid,'d,%5.0f,uy,%5.6f,\n',2002*(llin+lint+lback)+cc2+(cc1-1)*13,0);
% fprintf(fid,'d,%5.0f,uz,%5.6f,\n',2002*(llin+lint+lback)+cc2+(cc1-1)*13,backdisp(cc1,cc2)/1000);
    fprintf(fid,'allsel, all\n');

%////////////////////////////////////
% solution controls
%////////////////////////////////////
    if cc101==1
        fprintf(fid,'outres, nsol, last\n');
    else
        fprintf(fid,'outres, nsol, last\n');
    end
% fprintf(fid,'lswrite,\n');
%

if cc101==1
% fprintf(fid,'NSUBST,20,40,1\n');
% fprintf(fid,'esel, s, mat,,1\n');
    fprintf(fid,'NSUBST,1,1,1\n');
    fprintf(fid,'nropt,init\n');
else
    fprintf(fid,'NSUBST,30,40,1\n');
end
% fprintf(fid,'sbctran\n');
fprintf(fid,'nset, s, loc, z,%5.7f\n',bearingwidth/2);
fprintf(fid,'d,all, uz,0\n');
fprintf(fid,'allsel, all\n');
fprintf(fid,'solve\n');
end
end

fprintf(fid,'allsel, all\n');
fprintf(fid,'antype,stat\n');
fprintf(fid,'OUTRES,BASI,LAST\n');
```

```
fprintf(fid,'NLGEOM,OFF\n');

maxtime=1.5;
normaltime=1;
%
%

%////////////////////////////////////
% print results
%////////////////////////////////////
fprintf(fid,'/post1\n');

fprintf(fid,'SET,1\n');
fprintf(fid,'/format,20,,18,10\n');
fprintf(fid,'allsel,all\n');
fprintf(fid,'nsel,s,node,,1,2002\n');
% fprintf(fid,'rsys,1\n');
fprintf(fid,'rsys,11\n');
for cc1=1:37
    fprintf(fid,'allsel,all\n')
    fprintf(fid,'CBDOF,"submodel_boundary_nodes","dat","","submodeloutput_%03.0f","dat","","0,,0\n',cc1)
    fprintf(fid,'nsel,s,node,,1,2002\n');
    fprintf(fid,'/OUTPUT,bearing_stress%03.0f,rstt,\n',cc1);
    fprintf(fid,'PRNSOL,S,COMP \n');
    fprintf(fid,'/OUTPUT,bearing_stresp%03.0f,rstt,\n',cc1);
    fprintf(fid,'PRNSOL,S,prin \n');
    fprintf(fid,'/OUTPUT,bearing_strain%03.0f,rstt,\n',cc1);
    fprintf(fid,'PRNSOL,epto,COMP \n');
    fprintf(fid,'/OUTPUT,bearing_straip%03.0f,rstt,\n',cc1);
    fprintf(fid,'PRNSOL,epto,prin \n');
    fprintf(fid,'/OUTPUT,\n');
    fprintf(fid,'/nsel,s,node,,1,500000\n');
    fprintf(fid,'/OUTPUT,bearing_disps%03.0f,rstt,\n',cc1);
    fprintf(fid,'PRNSOL,U,COMP \n');
    fprintf(fid,'/OUTPUT,\n');
    fprintf(fid,'allsel,all\n');
    fprintf(fid,'/EFACET,1 \n');
%
% fprintf(fid,'/dscale,all,off\n');
% fprintf(fid,'rsys,1\n');
fprintf(fid,'rsys,11\n');

fprintf(fid,'/RGB,INDEX,100,100,100,0 \n');
fprintf(fid,'/RGB,INDEX,80,80,80,13 \n');
fprintf(fid,'/RGB,INDEX,60,60,60,14 \n');
fprintf(fid,'/RGB,INDEX,0,0,0,15 \n');
fprintf(fid,'/REPLOT \n');

% fprintf(fid,'SET,NEXT\n');
% fprintf(fid,'SET,NEXT\n');
% fprintf(fid,'SET,NEXT\n');
fprintf(fid,'/PLOPTS,MINM,0\n');
% fprintf(fid,'PLNSOL,EPPL,EQV,0,1.0 \n');
% fprintf(fid,'/contour,,30,,00005,,005\n');
% fprintf(fid,'PLNSOL,S,EQV,0,1.0\n');
% fprintf(fid,'/contour,,30,0,,130\n');
    fprintf(fid,'PLNSOL,s,y,0,1.0 \n');
    fprintf(fid,'/contour,,30,-50,,140\n');

% fprintf(fid,'/AUTO,1 \n');
% fprintf(fid,'/REP,FAST \n');
```

```
% fprintf(fid,'/AUTO,1 \n');
% fprintf(fid,'/REP,FAST \n');
% fprintf(fid,'ESEL,R,TYPE,,1 \n');
% fprintf(fid,'FLST,5,20,2,ORDE,2 \n');
% fprintf(fid,'FITEM,5,2084\n');
% fprintf(fid,'FITEM,5,-2103 \n');
% fprintf(fid,'ESEL,U,, ,P51X \n');

% fprintf(fid,'/EXPAND,2,RECT,HALF,0.00001 \n');
% fprintf(fid,'/REPLOTT \n');
%
% fprintf(fid,'/AUTO,1 \n');
% fprintf(fid,'/REP,FAST \n');
fprintf(fid,'/dscale,,120 \n');
% fprintf(fid,'/AUTO,1 \n');
% fprintf(fid,'/REP,FAST \n');
% fprintf(fid,'/ZOOM,1,RECT,0.286817,0.162336 ,0.379928764425 ,0.0758968303231 \n');
% fprintf(fid,'/ZOOM,1,RECT,-0.268527,0.594532 ,0.981828991704 ,-0.682108329453\n');
fprintf(fid,'/EXPAND,2,RECT,HALF,,,29.49/2 \n');
fprintf(fid,'/ANG,1 \n');
fprintf(fid,'/AUTO,1 \n');
fprintf(fid,'/REP,FAST \n');
fprintf(fid,'/ANG,1 \n');
fprintf(fid,'/REP,FAST \n');
fprintf(fid,'/VIEW,1,1,2,3 \n');
fprintf(fid,'/ANG,1 \n');
fprintf(fid,'/ANG,1,-30,ZS,1 \n');
fprintf(fid,'/ANG,1,-30,ZS,1 \n');
fprintf(fid,'/ANG,1,-30,ZS,1 \n');
fprintf(fid,'/REP,FAST\n');

% fprintf(fid,'esel, s, mat,,1\n');
fprintf(fid,'esel, s, mat,,4\n');

fprintf(fid,'/show,JPEG \n');
fprintf(fid,'/REP,FAST \n');
fprintf(fid,'/show, close\n');
fprintf(fid,'SET,next\n');
end

fclose('all'
```

## References

1. Darrow, K. and Pagnotta, G., *Method of manufacture of cooled turbine or compressor buckets in Free Patents online*, U.P. office, Editor. 1980: US.
2. Torres-Villaseñor, G. and Negrete-Sánchez, J., *Aluminum clad zinc bimetallic planchet*. Materials & Design, 2008. **29**(4): p. 798-800.
3. Marzouki, M., Kowandy, C., and Richard, C., *Experimental simulation of tool/product interface during hot drawing*. Wear, 2007. **262**(3-4): p. 235-241.
4. Polyanskii, S.N. and Kolnogorov, V.S., *Cladded Steel for the Oil and Gas Industries*. Chemical and Petroleum Engineering, 2002. **38**(11): p. 703-707.
5. Yutani, N. and Reynolds, T., *Survey of fastening techniques for ship building* S.S. Comitee, Editor. 1976, Naval Sea Systems Command: Washington, US.
6. Mwanza, M.C., Joyce, M.R., Lee, K.K., Syngellakis, S., and Reed, P.A.S., *Microstructural characterisation of fatigue crack initiation in Al-based plain bearing alloys*. International Journal of Fatigue, 2003. **25**(9-11): p. 1135-1145.
7. Joyce, M.R., Reed, P.A.S., and Syngellakis, S., *Numerical modelling of crack shielding and deflection in a multi-layered material system*. Materials Science and Engineering A, 2003. **342**(1-2): p. 11-22.
8. Ali, M., Syngellakis, S., and Reed, P.A.S., *A comparison of fatigue performance of HVOF spray coated and conventional roll bonded aluminium bearing alloys*. Materials Science Technology, 2008. **25**(5): p. 575-581.
9. Joyce, M.R., Lee, K.K., Syngellakis, S., and Reed, P.A.S., *Quantitative assessment of preferential fatigue initiation sites in a multi-phase aluminium alloy*. 2004. **27**(11): p. 1025-1036.
10. Ali, M., *Microstructural modelling of fatigue in layered bearing architectures*, in *Materials Research Group. PhD Thesis*. 2007, University of Southampton: Southampton. p. 275.
11. Suresh, S., *Fatigue of materials*. 2nd ed. 1998, Cambridge University Press, Cambridge. 679.
12. Duga, J.J., Fisher, W.H., Buxbaum, R.W., Rosenfield, A.R., Buhr, A.R., Honton, E.J., and McMillan, S.C., *The Economic Effects of Fracture in the United States*, U.S.D.o. Commerce, Editor. 1983, NBS Special Publication.
13. Griffith, A.A., *The Phenomena of Rupture and Flow in Solids*. Philosophical Transactions, 1921. **A221**: p. 163-198.
14. Gol'dstein, R.V. and Salganik, R.L., *Brittle fracture of solids with arbitrary cracks*. International Journal of Fracture, 1974. **V10**(4): p. 507-523.
15. Inglis, C.E., *Stresses in a Plate due to the Presence of Cracks and Sharp Corners*. Transactions of the Institute of Naval Architects, 1913. **55**: p. 219-241.
16. Irwin, G.R. *Onset of Fast Crack Propagation in High Strength Steel and Aluminum Alloys*. in *Sagamore Research Conference Proceedings*. 1956.
17. Irwin, G.R., *Analysis of Stresses and Strains near the End of a Crack Traversing Plate*. Journal of Applied Mechanics, 1957. **24**: p. 361-364.
18. Westergard, H., *Bearing Pressures and cracks*. Journal of Applied Mechanics, 1939. **61**: p. 49-53.
19. BS7448, *Fracture mechanics toughness tests: Method for determination of  $K_{Ic}$ , critical CTOD and critical  $J$  values of metallic materials*, B.S. Institution, Editor. 1991: London.

20. E399-90, *Standard test method for plane-strain fracture toughness of metallic materials*. . Annual book of ASTM Standards, Metals test method and analytical procedures, 2003. **v. 03.01**: p. 451-482.
21. Dugdale, D.S., *Yielding in Steel Sheets containing Slits*. Journal of Mechanics and Physics of Solids, 1960. **8**: p. 100-104.
22. Barenblatt, G.I., *The Mathematical Theory of Equilibrium Cracks in Brittle Fracture*. Advances in Applied Mechanics, 1962. **7**: p. 55-129.
23. Anderson, T.L., *Fracture Mechanics. Fundamentals and Applications*. 3 ed. 2005: CRC Press Inc. 448 pp.
24. Narasimhan, R. and Rosakis, A.J., *Three Dimensional Effects Near a Crack-Tip in a Ductile Three Point Bend Specimen - Part I: A Numerical Investigation*. 1988, California Institute of Technology: Pasadena, California.
25. Rice, J.R., *A Path Independent Integral and the Approximate Analysis of Strain Concentration by Notches and Cracks*. Journal of Applied Mechanics, 1968 **35** p. 379-386.
26. Eshelby, E., *The Elastic Field Outside an Ellipsoidal Inclusion*. Proceedings of Royal Society, 1959. **A252**: p. 561-569.
27. Rice, J.R. and Rosengreen, G.F., *Plane Strain Deformation near a Crack Tip in a Power Law Hardening Material*. Journal of Mechanics and Physics of Solids, 1968. **16**: p. 1-12.
28. Hutchinson, J.W., *Singular Behaviour at the End of a Tensile Crack in a Hardening Material*. . Journal of Mechanics and Physics of Solids, 1968. **16**: p. 13-31.
29. Ramberg, W. and Osgood, W., *Description of stress strain curve by three parameteres*, N.A.C.f. Aeronautics, Editor. 1943: Washington D.C.
30. Wells, A.A. *Unstable Crack Propagation in Metals: Cleavage and fast Fracture*. in *Proceedings of the Crack Propagation Symposium*. 1961. Cranfield, UK.
31. Irwin, G.R. *Plastic Zone Near a Crack and Fracture Toughness*. in *Sagamore Research Conference Proceedings*. 1961.
32. Burdekin, F.M. and Stone, D.E.W., *The Crack Opening Displacement Approach to Fracture Mechanics in Yielding Materials*. Journal of Strain Analysis, 1966. **1**: p. 145-163.
33. Tvergaard, V., *On fatigue crack growth in ductile materials by crack-tip blunting*. Journal of the Mechanics and Physics of Solids, 2004. **52**(9): p. 2149-2166.
34. Wöhler, A., *Zeitschrift Bauwesen 20*, in *Spalten*. 1870. p. 3-106.
35. Paris, P.C. and Erdogan, F., *Stress Analysis of Cracks. Fracture Toughness and Testing and its Applications*. American Society for Testing and Materials, 1965. **STP 381**: p. 30-83.
36. Ritchie, R.O., *Influence of Microstructure on Near Threshold Fatigue Crack Propagation in Ultra High Strength Steel*. Metal Science, 1977.
37. Ritchie, R.O., *Mechanisms of fatigue crack propagation in metals, ceramics and composites: Role of crack tip shielding*. Materials Science and Engineering, 1988. **103**(1): p. 15-28.
38. Donehoo, P., Yu, W., and Ritchie, R.O., *On the growth of cracks at the fatigue threshold following compression overloads: Role of load ratio*. Materials Science and Engineering, 1985. **74**(1): p. 11-17.
39. Pearson, S., *Initiation of Fatigue Cracks in Commercial Aluminum Alloys and the Subsequent Propagation of Very Short Cracks*. Engineering Fracture Mechanics, 1975. **7**: p. 235-247.
40. Lankford, J., *The Growth of Small Fatigue Cracks in 7075-T6 aluminum*. Fatigue & Fracture of Engineering Materials and Structures, 1982. **5**(233-248).
41. Tanaka, K. and Nakai, Y., *Propagation and No Propagation of Fatigue Cracks at a sharp Notch*. Fatigue & Fracture of Engineering Materials and Structures, 1983. **6**: p. 315-327.
42. Courant, R., *Variational Methods for the Solution of Problems of Equilibrium and Vibrations*. Bulletin of the American Mathematical Society, 1943. **49**: p. 1-23.
43. Clough, R.W. *The finite element method in plane stress analysis*. in *Proceedings of second ASCE Conference on electronic computation*. 1960.

44. Barsoum, R., *Triangular Quarter point Elements as elastic and perfectly plastic crack tip elements*. International Journal for numerical Methods in engineering, 1977. **11**: p. 85-98.
45. McMeeking, R.M. and Parks, D.M., *On the Criteria for J Dominance of Crack Tip Fields in Large Scale Yielding*. ASTM, 1979. **STP 668**: p. 175-194.
46. Bittencourt, T.N., Wawrzynek, P.A., Ingraffea, A.R., and Sousa, J.L., *Quasi-automatic simulation of crack propagation for 2D LEFM problems*. Engineering Fracture Mechanics, 1996. **55**(2): p. 321-334.
47. Riddell, W.T., Ingraffea, A.R., and Wawrzynek, P.A., *Experimental observations and numerical predictions of three-dimensional fatigue crack propagation*. Engineering Fracture Mechanics, 1997. **58**(4): p. 293-310.
48. Singh, R., Carter, B.J., Wawrzynek, P.A., and Ingraffea, A.R., *Universal crack closure integral for SIF estimation*. Engineering Fracture Mechanics, 1998. **60**(2): p. 133-146.
49. Chen, C., Wawrzynek, P.A., and Ingraffea, A.R., *Crack Growth Simulation and Residual Strength Prediction in Airplane Fuselages*. 1999, NASA Langley Technical report. p. 172.
50. Carter, B.J., Wawrzynek, P.A., and Ingraffea, A.R., *Automated 3-D crack growth simulation*. International Journal for Numerical Methods in Engineering, 2000. **47**(1-3): p. 229-253.
51. Spievak, L., Wawrzynek, P.A., and Ingraffea, A.R., *Simulating Fatigue Crack Growth in Spiral Bevel Gears*. 2000, NASA. p. 116.
52. Neto, J.C.B., Wawrzynek, P.A., Carvalho, M.T.M., Martha, L.F., and Ingraffea, A.R., *An Algorithm for Three-dimensional Mesh Generation for Arbitrary Regions with Cracks*. Engineering with Computers, 2001. **17**(1): p. 75-91.
53. Ural, A., Heber, G., Wawrzynek, P.A., Ingraffea, A.R., Lewicki, D.G., and Neto, J.B.C., *Three-dimensional, parallel, finite element simulation of fatigue crack growth in a spiral bevel pinion gear*. Engineering Fracture Mechanics, 2005. **72**(8): p. 1148-1170.
54. ABAQUS, *Abaqus Reference Manual*. 2008.
55. Ansys, *Ansys reference manual*. 2005.
56. Sutton, M.A., Deng, X., Ma, F., Newman Jr, J.C., and James, M., *Development and application of a crack tip opening displacement-based mixed mode fracture criterion*. International Journal of Solids and Structures, 2000. **37**(26): p. 3591-3618.
57. Panontin, T.L., Makino, A., and Williams, J.F., *Crack tip opening displacement estimation formulae for C(T) specimens*. Engineering Fracture Mechanics, 2000. **67**(3): p. 293-301.
58. Wilcock, D.F., *Bearing design and application*. First ed. 1957, New York: McGraw-Hill.
59. Mian, O., *MAHLE Engine Systems*. 2008: Rugby, UK.
60. van Basshuysen, R., ed. *Internal Combustion Engine Handbook: Basics, Components, Systems, and Perspectives*. 2004, SAE International: Warrendale, USA.
61. Joyce, M.R., *Fatigue of Aluminium Lining in Plain Automotive Bearings*, in *Materials Research Group. PhD Thesis*. 2000, University of Southampton: Southampton, UK. p. 251.
62. Burke-Veliz, A., D., W., Wahdy, N., Reed, P.A.S., Merritt, D., and Syngellakis, S., *Plain bearing stresses due to forming and oil film pressure*. Journal of Physics: Conference Series, 2009. **181**: p. 12010
63. Ali, M.S., Reed, P.A.S., Reed, P.A.S., Syngellakis, S., Moffat, A., and Perrin, C., *Microstructural factors affecting fatigue initiation in various Al based bearing alloys*. Materials Science Forum, 2006. **519-521**: p. 1071-1076.
64. Zienkiewicz, O.C. and Taylor, R.L., *The finite element method. The Basis*. 5th edition ed. 2002: McGraw Hill. 689.
65. Sugimura, Y., Lim, P.G., Shih, C.F., and Suresh, S., *Fracture normal to a bimaterial interface: Effects of plasticity on crack-tip shielding and amplification*. Acta Metallurgica et Materialia, 1995. **43**(3): p. 1157-1169.
66. Sugimura, Y., Grondin, L., and Suresh, S., *Fatigue crack growth at arbitrary angles to bimaterial interfaces*. Scripta Metallurgica et Materialia, 1995. **33**(12): p. 2007-2012.

67. Suresh, S., Sugimura, Y., and Tschegg, E.K., *Growth of a Fatigue Crack Approaching a Perpendicularly Oriented Bimaterial Interface*. Scripta Metallurgica et Materialia, 1992. **27**: p. 1189-1194.
68. Hbaieb, K., McMeeking, R.M., and Lange, F.F., *Crack bifurcation in laminar ceramics having large compressive stress*. International Journal of Solids and Structures, 2007. **44**(10): p. 3328-3343.
69. Pippan, R., Flechsig, K., and Riemelmoser, F.O., *Fatigue crack propagation behavior in the vicinity of an interface between materials with different yield stresses*. Materials Science and Engineering A, 2000. **283**(1-2): p. 225-233.
70. Jiang, F., Deng, Z.L., Zhao, K., and Sun, J., *Fatigue crack propagation normal to a plasticity mismatched bimaterial interface*. Materials Science and Engineering A, 2003. **356**(1-2): p. 258-266.
71. Pippan, R. and Riemelmoser, F.O., *Fatigue of bimetals. Investigation of the plastic mismatch in case of cracks perpendicular to the interface*. Computational Materials Science, 1998. **13**(1-3): p. 108-116.
72. Henshell, R.D. and Shaw, K.G., *Crack tip finite elements are unnecessary*. International Journal of Numerical Methods in Engineering 1975. **9** p. 495-507.
73. Barsoum, R., *Triangular Quarter point Elements as elastic and perfectly plastic crack tip elements*. International Journal for Numerical Methods in Engineering, 1977. **11**: p. 85-98.
74. Laird, C. and Smith, G.C., *Crack propagation in high stress fatigue*. 1962, Taylor & Francis. p. 847 - 857.
75. Pelloux, R.M.N., *Crack extension by alternating shear*. Engineering Fracture Mechanics, 1970. **1**(4): p. 697-700.
76. BS5447, *Methods for testing for plane strain fracture toughness (KIC) of metallic materials*. 1974, British Standards Institution.
77. E399-90, *Standard Test Method for Plane strain Fracture Toughness of Metallic Materials*. 1990, American Society for Testing and Materials.
78. Chang, K.J., *On the maximum strain criterion--a new approach to the angled crack problem*. Engineering Fracture Mechanics, 1981. **14**(1): p. 107-124.
79. Suresh, S., *Micromechanisms of Fatigue Crack Growth Retardation Following Overloads*. Engineering Fracture Mechanics, 1983. **18**: p. 577-593.
80. Sih, G.C., *Strain Energy Density Factor Applied to Mixed Mode Crack Problems*. International Journal of Fracture, 1974. **10**: p. 305-321.
81. Sih, G.C., *Mixed Mode Fatigue Crack Growth Predictions*. Engineering Fracture Mechanics, 1973. **5**(365-377).
82. Cotterell, B. and Rice, J.R., *Slightly curved or kinked cracks*. International Journal of Fracture, 1980. **16**(2): p. 155-169.
83. Erdogan, F. and Sih, G.C., *On the Crack Extension in Plates Under Plane Loading and Transverse Shear*. Journal of Basic Engineering, 1963. **85**: p. 519-527.
84. Hussain, M. and Pu, S., *Strain energy release rate for a crack under combined mode I and II*. Fracture Analysis Transactions, 1974. **STP 560**: p. 2-28.
85. Palaniswamy, K. and Knauss, W.G., *Propagation of a crack under general, in-plane tension*. International Journal of Fracture, 1972. **V8**(1): p. 114-117.
86. Ramulu, M. and Kobayashi, A., *Numerical and Experimental Study of Mixed Mode Fatigue Crack Propagation*, in *Handbook of Fatigue Crack Propagation in Metallic Structures*, A. Carpinteri, Editor. 1994, Elsevier: Amsterdam. p. 1073-1124.
87. Chambers, A.C., Hyde, T.H., and Webster, J.J., *Mixed mode fatigue crack growth at 550[deg]C under plane stress conditions in Jethete M152*. Engineering Fracture Mechanics, 1991. **39**(3): p. 603-619.

88. Mageed, A.A.M. and Pandey, R.K., *Mixed Mode Crack Growth under Static and Cyclic Loading in Al Alloy Sheets*. Engineering Fracture Mechanics, 1991. **40**(2): p. 371-375.
89. Broek, D., *Elementary Engineering Fracture Mechanics*. 1974, Leyden, Netherlands: Noordhoff International.
90. Lugovy, M., Orlovskaya, N., Slyunyayev, V., Gogotsi, G., Kubler, J., and Sanchez-Herencia, A.J., *Crack bifurcation features in laminar specimens with fixed total thickness*. Composites Science and Technology, 2002. **62**(6): p. 819-830.
91. Maiti, S.K. and Smith, R.A., *Criteria for brittle fracture in biaxial tension*. Engineering Fracture Mechanics, 1984. **19**(5): p. 793-804.
92. Pontin, M.G. and Lange, F.F., *Crack Bifurcation at the Surface of Laminar Ceramics That Exhibit a Threshold Strength*. 2005. p. 1315-1317.
93. Kitagawa, H., Yuuki, R., and Ohira, T., *Crack-morphological aspects in fracture mechanics*. Engineering Fracture Mechanics, 1975. **7**(3): p. 515-520.
94. Suresh, S. and Shih, C.F., *Plastic near-tip fields for branched cracks*. International Journal of Fracture, 1986. **30**(4): p. 237-259.
95. Meggiolaro, M.A., Miranda, A.C.O., Castro, J.T.P., and Martha, L.F., *Stress intensity factor equations for branched crack growth*. Engineering Fracture Mechanics, 2005. **72**(17): p. 2647-2671.
96. Suzuki, S., Sakaue, K., and Iwanaga, K., *Measurement of energy release rate and energy flux of rapidly bifurcating crack in Homalite 100 and Araldite B by high-speed holographic microscopy*. Journal of the Mechanics and Physics of Solids, 2007. **55**(7): p. 1487-1512.
97. Ho, S., Hillman, C., Lange, F.F., and Suo, Z., *Surface Cracking in Layers Under Biaxial, Residual Compressive Stress*. 1995. p. 2353-2359.
98. Katz, Y., Bussiba, A., and Mathias, H., *Micromechanisms of fatigue crack growth retardation following overloads*. Met. Sci., 1981. **15**: p. 317-319.
99. Xie, D. and Biggers, J.S.B., *Progressive crack growth analysis using interface element based on the virtual crack closure technique*. Finite Elements in Analysis and Design, 2006. **42**(11): p. 977-984.
100. Unosson, M., Olovsson, L., and Simonsson, K., *Failure modelling in finite element analyses: Element erosion with crack-tip enhancement*. Finite Elements in Analysis and Design, 2006. **42**(4): p. 283-297.
101. Pang, H.L.J., *Linear elastic fracture mechanics benchmarks: 2D finite element test cases*. Engineering Fracture Mechanics, 1993. **44**(5): p. 741-751.
102. Simandjuntak, S., Alizadeh, H., Smith, D.J., and Pavier, M.J., *Three dimensional finite element prediction of crack closure and fatigue crack growth rate for a corner crack*. International Journal of Fatigue, 2006. **28**(4): p. 335-345.
103. O'Donoghue, P.E., Kanninen, M.F., Leung, C.P., Demofonti, G., and Venzi, S., *The development and validation of a dynamic fracture propagation model for gas transmission pipelines*. International Journal of Pressure Vessels and Piping, 1997. **70**(1): p. 11-25.
104. Borst, R.d., Remmers, J.J.C., and Needleman, A., *Mesh-independent discrete numerical representations of cohesive-zone models*. Engineering Fracture Mechanics, 2006. **73**(2): p. 160-177.
105. Yoshimura, A., Nakao, T., Yashiro, S., and Takeda, N., *Improvement on out-of-plane impact resistance of CFRP laminates due to through-the-thickness stitching*. Composites Part A: Applied Science and Manufacturing, 2008. **39**(9): p. 1370-1379.
106. Cook, G., Timbrell, C., and Browning, B., *The Application of 3D Finite Element Analysis to Engine Life Prediction*, in *AeroMat 2001 - 12th Advanced Aerospace Materials & Processes Conference & Exhibition*. 2001: Long Beach, CA, U.S.A.
107. Zencrack. 2008; Available from: <http://www.zentech.co.uk/zencrack.htm>.

108. Belytschko, T. and Black, T., *Elastic crack growth in finite elements with minimal remeshing*. International Journal for Numerical Methods in Engineering, 1999. **45**(5): p. 601-620.
109. Moës, N., Dolbow, J., and Belytschko, T., *A finite element method for crack growth without remeshing*. International Journal for Numerical Methods in Engineering, 1999. **46**(1): p. 131-150.
110. Bordas, S., Rabczuk, T., and Zi, G., *Three-dimensional crack initiation, propagation, branching and junction in non-linear materials by an extended meshfree method without asymptotic enrichment*. Engineering Fracture Mechanics, 2008. **75**(5): p. 943-960.
111. Giner, E., Sukumar, N., Tarancón, J.E., and Fuenmayor, F.J., *An Abaqus implementation of the extended finite element method*. Engineering Fracture Mechanics, 2009. **76**(3): p. 347-368.
112. Iida, S. and Kobayashi, A., *Crack-propagation rate in 7075-T6 plates under cyclic tensile and transverse shear loadings*. Journal of Basic Engineering, 1969: p. 764-769.
113. Li, C., *Vector CTD Criterion Applied to Mixed Mode Fatigue Crack Growth*. Fatigue & Fracture of Engineering Materials and Structures, 1989. **12**(1): p. 59-65.
114. Wawrzynek, P.A. and Ingraffea, A.R., *An interactive approach to local remeshing around a propagating crack*. Finite Elements in Analysis and Design, 1989. **5**(1): p. 87-96.
115. Colombo, D. and Giglio, M., *A methodology for automatic crack propagation modelling in planar and shell FE models*. Engineering Fracture Mechanics, 2006. **73**(4): p. 490-504.
116. Chang, K.J., *Further studies of the maximum stress criterion on the angled crack problem*. Engineering Fracture Mechanics, 1981. **14**(1): p. 125-142.
117. Sih, G.C. and Hartranft, R.J., *Variation of strain energy release rate with plate thickness*. International Journal of Fracture, 1973. **V9**(1): p. 75-82.
118. Murakami, Y., *Stress Intensity Factors handbook*. 1987, New York, USA: Pergamon Press.
119. Meyer, Diegele, Bruckner, F., and Moslang, *Crack interaction modelling*. Fatigue & Fracture of Engineering Materials and Structures, 2000. **23**(4): p. 315-323.
120. Wang, Y.Z., Atkinson, J.D., Akid, R., and Parkins, R.N., *Crack Interaction, Coalescence and Mixed Mode Fracture Mechanics*. Fatigue & Fracture of Engineering Materials and Structures, 1996. **19**(1): p. 51-63.
121. Forsyth, P.J.E., *A unified description of micro and macroscopic fatigue crack behaviour*. International Journal of Fatigue, 1983. **5**(1): p. 3-14.
122. Soboyejo, W.O., Knott, J.F., Walsh, M.J., and Cropper, K.R., *Fatigue crack propagation of coplanar semi-elliptical cracks in pure bending*. Engineering Fracture Mechanics, 1990. **37**(2): p. 323-340.
123. Lin, X.B. and Smith, R.A., *Fatigue growth analysis of interacting and coalescing surface defects*. International Journal of Fracture, 1997. **85**(3): p. 283-299.
124. Jones, R., Peng, D., and Pitt, S., *Assessment of multiple flat elliptical cracks with interactions*. Theoretical and Applied Fracture Mechanics, 2002. **38**(3): p. 281-291.
125. Soboyejo, W.O., Kishimoto, K., Smith, R.A., and Knott, J., *A study of the interaction and coalescence of two coplanar fatigue cracks in bending*. Fatigue & Fracture of Engineering Materials and Structures, 1989. **12**(3): p. 167-174.
126. Tomkins, B., *Fatigue crack propagation: an analysis*. Philosophical Magazine, 1968. **18**(155): p. 1041 - 1066.
127. Cisilino, A.P. and Aliabadi, M.H., *Dual boundary element assessment of three-dimensional fatigue crack growth*. Engineering Analysis with Boundary Elements, 2004. **28**(9): p. 1157-1173.
128. Moon, S.-I., Chang, Y.-S., Kim, Y.-J., Lee, J.-H., Song, M.-H., Choi, Y.-H., and Hwang, S.-S., *Assessment of plastic collapse behavior for tubes with collinear cracks*. Engineering Fracture Mechanics, 2006. **73**(3): p. 296-308.

129. Chang, Y.-S., Huh, N.-S., Kim, Y.-J., Lee, J.-H., and Choi, Y.-H., *Coalescence evaluation of collinear axial through-wall cracks in steam generator tubes*. Nuclear Engineering and Design, 2007. **237**(12-13): p. 1460-1467.
130. Irwin, G.R., *Crack extension force for a part-through crack in a plate*. ASME Transactions. J. App. Mech, 1962. **29**: p. 651-654.
131. Shah, R.C. and Kobayashi, A.S., *Stress intensity factor for an elliptical crack under arbitrary normal loading*. Engineering Fracture Mechanics, 1971. **3**(1): p. 71-96.
132. Green, A.E. and Sneddon, I.N. *The distribution of stress in the neighbourhood of a flat elliptical crack in an elastic solid*. in *Proc. Cambridge. Philosophical Society*. 1950.
133. Newman Jr, J.C. and Raju, I.S., *An empirical stress-intensity factor equation for the surface crack*. Engineering Fracture Mechanics, 1981. **15**(1-2): p. 185-192.
134. Raju, I.S. and Newman, J.C., *Stress-intensity Factors for a Wide Range of Semi-Elliptical Surface Cracks in Finite-Thickness Plates*. Engineering Fracture Mechanics, 1979. **11**: p. 817-829.
135. Lin, X.B. and Smith, R.A., *Finite element modelling of fatigue crack growth of surface cracked plates: Part II: Crack shape change*. Engineering Fracture Mechanics, 1999. **63**(5): p. 523-540.
136. Gonzalez-Herrera, A. and Zapatero, J., *Tri-dimensional numerical modelling of plasticity induced fatigue crack closure*. Engineering Fracture Mechanics, 2008. **75**(15): p. 4513-4528.
137. Schuller, T. and Lauke, B., *Finite-element simulation of interfacial crack propagation: Methods and tools for the complete failure process under large scale yielding*. Engineering Fracture Mechanics, 2006. **73**(16): p. 2252-2263.
138. Schöllmann, M., Fulland, M., and Richard, H.A., *Development of a new software for adaptive crack growth simulations in 3D structures*. Engineering Fracture Mechanics, 2003. **70**(2): p. 249-268.
139. Guagliano, M., Vergani, L., and Vimercati, M., *Sub-surface crack propagation analysis in hypoid gears*. Engineering Fracture Mechanics, 2008. **75**(3-4): p. 417-426.
140. Joyce, J.A. and Link, R.E., *Application of two parameter elastic-plastic fracture mechanics to analysis of structures*. Engineering Fracture Mechanics, 1997. **57**(4): p. 431-446.
141. Benthem, J.P., *State of stress at the vertex of a quarter-infinite crack in a half space*. International Journal of Solids and Structures, 1977. **13**: p. 479-492.
142. Wu, S.-X., *Shape change of surface crack during fatigue growth*. Engineering Fracture Mechanics, 1985. **22**(5): p. 897-913.
143. Lin, X.B. and Smith, R.A., *Finite element modelling of fatigue crack growth of surface cracked plates: Part I: The numerical technique*. Engineering Fracture Mechanics, 1999. **63**(5): p. 503-522.
144. Hussain, K., *Short fatigue crack behaviour and analytical models: A review*. Engineering Fracture Mechanics, 1997. **58**(4): p. 327-354.
145. Tanaka, K., Hoshide, T., and Sakai, N., *Mechanics of Fatigue Crack Propagation by Crack Tip Plastic Blunting*. Engineering Fracture Mechanics, 1984. **19**: p. 805-825.
146. Pearson, S., *Initiation of fatigue cracks in commercial aluminium alloys and the subsequent propagation of very short cracks*. Engineering Fracture Mechanics, 1975. **7**(2): p. 235-240, IN15-IN18, 241-247.
147. Miller, K.J., *The behaviour of short fatigue cracks and their initiation part II. A general summary*. Fatigue & Fracture of Engineering Materials & Structures, 1987. **10**(2): p. 93-113.
148. Hobson, P., *The formulation of a crack growth equation for short cracks*. Fatigue & Fracture of Engineering Materials & Structures, 1982. **5**(4): p. 323-327.
149. Navarro, A. and De los Rios, E.R., *A Microstructurally-short fatigue crack growth equation*. Fatigue & Fracture of Engineering Materials & Structures, 1988. **11**(5): p. 383-396.

150. Chan, K.S. and Lankford, J., *A crack-tip strain model for the growth of small fatigue cracks*. Scripta Metallurgica, 1983. **17**(4): p. 529-532.
151. Tanaka, K., Akiniwa, Y., Nakai, Y., and Wei, R.P., *Modelling of small fatigue crack growth interacting with grain boundary*. Engineering Fracture Mechanics, 1986. **24**(6): p. 803-819.
152. Singh, K.D., Khor, K.H., and Sinclair, I., *Roughness- and plasticity-induced fatigue crack closure under single overloads: Finite element modelling*. Acta Materialia, 2006. **54**(17): p. 4393-4403.
153. BS7910, *Guide to methods for assessing the acceptability of flaws in metallic structures*. 2005, British Standards Institution: London.
154. Lin, X.B. and Smith, R.A., *Finite element modelling of fatigue crack growth of surface cracked plates: Part III: Stress intensity factor and fatigue crack growth life*. Engineering Fracture Mechanics, 1999. **63**(5): p. 541-556.
155. Lin, X.B. and Smith, R.A., *A numerical simulation of fatigue growth of multiple surface initially semicircular defects under tension*. International Journal of Pressure Vessels and Piping, 1995. **62**(3): p. 281-289.
156. Kamaya, M., *Growth evaluation of multiple interacting surface cracks. Part I: Experiments and simulation of coalesced crack*. Engineering Fracture Mechanics, 2008. **75**(6): p. 1336-1349.
157. Kamaya, M., *Growth evaluation of multiple interacting surface cracks. Part II: Growth evaluation of parallel cracks*. Engineering Fracture Mechanics, 2008. **75**(6): p. 1350-1366.
158. Soboyejo, W.O. and Knott, J.F., *The propagation of non-coplanar semi-elliptical fatigue cracks*. Fatigue & Fracture of Engineering Materials & Structures, 1991. **14**(1): p. 37-49.
159. Zhao, J., Guo, W., and She, C., *Three-parameter approach for elastic-plastic fracture of the semi-elliptical surface crack under tension*. International Journal of Mechanical Sciences, 2008. **50**(7): p. 1168-1182.
160. Levy, N., Marcal, P.V., and Rice, J.R., *Progress in three-dimensional elastic-plastic stress analysis for fracture mechanics*. Nuclear Engineering and Design, 1971. **17**(1): p. 64-75.
161. Brocks, W. and Olschewski, J., *On J-dominance of crack-tip fields in largely yielded 3D structures*. International Journal of Solids and Structures, 1986. **22**(7): p. 693-708.
162. Nakamura, T. and Parks, D.M., *Three-dimensional crack front fields in a thin ductile plate*. Journal of the Mechanics and Physics of Solids, 1990. **38**(6): p. 787-812.
163. Sirivedin, S., Fenner, D.N., Nath, R.B., and Galiotis, C., *Effects of inter-fibre spacing and matrix cracks on stress amplification factors in carbon-fibre/epoxy matrix composites. Part I: planar array of fibres*. Composites Part A: Applied Science and Manufacturing, 2003. **34**(12): p. 1227-1234.
164. Ayyar, A. and Chawla, N., *Microstructure-based modeling of crack growth in particle reinforced composites*. Composites Science and Technology, 2006. **66**(13): p. 1980-1994.
165. Burke-Veliz, A., Reed, P.A.S., and Syngellakis, S., *A numerical study of crack shielding and deflection under extensive plasticity*. Engineering Fracture Mechanics, 2009. **76**(9): p. 1345-1356.
166. Wright, P., Fu, X., Sinclair, I., and Spearing, S.M., *Ultra High Resolution Computed Tomography of Damage in Notched Carbon Fiber--Epoxy Composites*. Journal of Composite Materials, 2008. **42**(19): p. 1993-2002.
167. Lang, O.R. *Bearing fatigue*. in *Limits of lubrication* 1975.
168. Harbordt, J., *Stresses and material fatigue in bi-metal shells of journal bearings* 1976, University of Karlsruhe.
169. Blount, E.A. *Design Factors Influencing the Fatigue Resistance of Connecting Rod Big End Bearings*. in *International Mechanical Engineering*. 1961.
170. McCallion, H. and Lotfi, M., *Tensile surface stresses and fatigue in plain journal bearings*. Tribology International, 1992. **25**(4): p. 247-257.

171. Martin, F.A., Garner, D.R., and Adams, D.R., *Hydrodynamic Aspects of Fatigue in Plain Bearings*. Transactions of ASME, Lubricants Technology, 1981. **103**: p. 150-156.
172. Gyde, N., *Fatigue Fractures in Babbitt Lined Journal Bearings*. 1969, Technical University of Denmark.
173. Blundell, J.K., *The Fatigue of Dynamically Loaded Journal Bearings*. 1977, University of Nottingham.
174. Bahai, H. and Xu, H., *Three-dimensional elastoplastic finite element and elastohydrodynamic analyses of journal bearings*. Proceedings of the I MECH E Part C Journal of Mechanical Engineering Science, 1997. **211**: p. 143-152.
175. Hacifazlioglu, S. and Karadeniz, S., *A parametric study of stress sources in journal bearings*. International Journal of Mechanical Sciences, 1996. **38**(8-9): p. 1001-1015.
176. *150 Suppliers 2007*, in *Automotive News*. 2008.
177. Avallone, A.E., Baumeister, T., Sadegh, A., and Marks, L., *Marks' Standard Handbook for Mechanical Engineers*, ed. M.-H. Professional. 2006.
178. Romhanji, E., Popovic, M., Glisic, D., Dodok, R., and Jovanovic, D., *Effect of annealing temperature on the formability of Al-Mg4.5-Cu0.5 alloy sheets*. Journal of Materials Processing Technology, 2006. **177**(1-3): p. 386-389.